Operation of Multiple Accelerating Structures in an X-Band High-Gradient Test Stand

William Lee Millar

Supervisor: Professor G.C. Burt

Department of Engineering
University of Lancaster

This thesis is submitted for the degree of
Doctor of Philosophy

April 2021

Declaration

I hereby declare that the contents of this dissertation have not been submitted in whole or in part for consideration for any other degree or qualification in this, or any other university. This dissertation is my own work and contains nothing which is the outcome of work done by or in collaboration with others except where specifically indicated in the text.

William Lee Millar
April 2021

Acknowledgements

I would like to express my sincerest gratitude to both Professor Graeme Burt and Dr. Walter Wuensch for providing me with the opportunity to undertake a PhD in such an exciting environment and for their supervision throughout. Their guidance and discourse have proved invaluable during my studies and led to the development of many of the ideas presented herein. In particular it is to Graeme, who delivered my first lecture in electromagnetism in 2015 and has been supervising me since, that much of my knowledge of RF engineering and professional development may be attributed. Equally, I'd like to convey my appreciation to Walter for his continued advice and for the many interesting anecdotes.

I would also like to thank those at Lancaster University and Daresbury Laboratory who have provided guidance and greatly contributed to expanding my knowledge, particularly Dr. Amos Dexter for his excellent lecture series and for the stimulating discussions throughout my time at university.

Additionally, I would like to express my thanks to all those at CERN who made operating the test stands not only possible, but a thoroughly enjoyable aspect of my time spent there. In particular, I would like thank Dr. Benjamin Woolley for sharing his knowledge of the facility and for the substantial technical support provided. Similarly, I would like to thank Dr. Nuria Catalán-Lasheras and Gerard McMonagle for facilitating all experimental work and for the significant time spent solving all problems modulator, klystron, or otherwise test stand related and without either of whom the collection of the experimental data within this thesis would not have been possible.

Abstract

This thesis describes the operation of two high-gradient accelerating structures in a high-power klystron based X-band test stand simultaneously and the phenomena observed in such an arrangement. The LLRF (Low Level Radio Frequency), interlock, and control systems of the test stand are modified to accommodate a dual structure arrangement and the designs are presented. Following this, numerical methods and CST Microwave Studio's PIC solver are used to model the interactions which may manifest in a multi-structure high-gradient arrangement, namely the signal propagation during breakdown and the behaviour of field emitted current in high-gradient structures. Several implications for modern high-gradient facilities are then provided.

In the upgraded test stand the high-gradient accelerating structures were conditioned simultaneously to gradients of approximately 90MV/m and 45MV/m respectively and the aforementioned simulations were validated experimentally. Finally, the development of a Monte Carlo model of high-gradient conditioning and operation is presented and compared with existing test stand data. The model is then used to investigate the effects of modifying the conditioning algorithm currently in use in CERN's X-band test stands.

Contents

List of figures **xiii**

List of tables **xxxi**

1 Introduction **1**

1.1 Electromagnetic Theory 1

1.1.1 Maxwell's Equations 2

1.1.2 Electromagnetic Fields in a Cylindrical Waveguide 4

1.1.3 Floquet Theorem and Space Harmonics 8

1.2 Characteristics of Travelling Wave Linear Accelerators 11

1.2.1 Energy Gain in an RF Gap 11

1.2.2 Power Loss and Coupling 13

1.2.3 Practical Design Considerations 17

1.3 Applications of High-Gradient Technology 20

1.3.1 Light Sources 20

1.3.2 Radiation Therapy 21

1.3.3 Next Generation Linear Colliders 22

1.4 Thesis Outline 23

2 RF Conditioning and Breakdown in High-Gradient Accelerators **25**

2.1 Field Electron Emission 25

2.2 Overview of Breakdown 29

2.3 Constraints and Underlying Physical Phenomena in Breakdown 32

2.3.1 Surface Electric Field 32

2.3.2 Power Flow and the Modified Poynting Vector 33

2.3.3 Nottingham Heating 36

2.3.4 Dislocation Dynamics and Breakdown Nucleation 38

2.4 Empirical Scaling Laws and Material Dependencies 39

2.5 Surface Conditioning in High-Gradient RF Structures 42
2.5.1 Evolution of Surface Properties during Conditioning 43
2.5.2 Observations on Field Emission during Conditioning 45
2.6 Conclusion 47

3 CERN's High-Gradient Test Facility 49
3.1 High-Power RF Generation 49
3.1.1 Klystron and Modulator 50
3.1.2 Pulse Compressor 51
3.2 Low-Level RF System 54
3.2.1 LLRF Generation 54
3.2.2 Signal Acquisition 56
3.3 Test Stand Operation 58
3.3.1 Vacuum Conditioning 59
3.3.2 Breakdown Rate Conditioning 60
3.4 Conclusion 61

4 Expansion of an X-Band Test Stand 63
4.1 LLRF System Upgrade 63
4.1.1 System Requirements 64
4.1.2 New Down-Conversion Scheme 66
4.1.3 LLRF System Test and Installation 68
4.2 Actuator Control System 73
4.3 New Pulse Compression Scheme 75
4.3.1 BOC Design 75
4.3.2 Correction Cavity Chain Design 78
4.3.3 Tuning and Installation 82
4.4 Commissioning of the Upgrade 85
4.4.1 Calibration of the RF Signal Chains 85
4.4.2 High-Power Test 86
4.5 Conclusion 87

5 Simulation of Interactions in Coupled Accelerating Structures 89
5.1 Motivation of the Study 89
5.2 The Modelled Experiment Setup 90
5.3 Simulation of Power Flow During Breakdown in Coupled Structures . . 91
5.3.1 Solving Signal Flow Graphs 93

5.3.2 Pulse Shape Variance . . . 99
5.3.3 Simulation of Power Flow During Breakdown . . . 102
5.4 Simulation of Field Emission in a Multi-Structure System . . . 108
5.4.1 Simulation Setup and Approximation of Emission Characteristics 111
5.4.2 Capture Efficiency of a Single Structure Arrangement . . . 116
5.4.3 Energy Spectrum of a Single Structure Arrangement . . . 123
5.4.4 Capture Efficiency and Energy Spectrum of a Multi-Structure Arrangement . . . 129
5.5 Dark Current Considerations for High-Gradient Facilities . . . 138
5.6 Conclusion . . . 139

6 High-Power Test of a Multi-Structure High-Gradient System 141
6.1 Structure Overview . . . 141
6.1.1 TD26CCR05 Design . . . 142
6.1.2 Endoscopy and Tuning . . . 144
6.2 High-Power Test . . . 151
6.2.1 Conditioning History . . . 151
6.2.2 Breakdown Distribution . . . 157
6.2.3 Interactions Between Structures During Breakdowns . . . 162
6.2.4 Comparative Analysis of Constituent Structures . . . 169
6.3 Multi-Structure Emission Measurements . . . 175
6.3.1 Phase Calibration . . . 175
6.3.2 Variation of Capture and Radiation with Relative Phasing . . . 178
6.4 Conclusion . . . 181

7 Monte Carlo Model of High-Gradient Conditioning and Operation 183
7.1 General Description of the Model . . . 183
7.1.1 Definition of the Model's Quantities . . . 184
7.2 Conditioning Algorithm . . . 185
7.3 Quantification of Conditioning . . . 186
7.4 Stochastic Modelling of Breakdown . . . 188
7.4.1 Two-Rate Model Approach . . . 190
7.4.2 Grid-Based Approach . . . 194
7.5 Results of the Model . . . 200
7.5.1 Simulation of Spatially Resolved Conditioning . . . 200
7.5.2 Simulation of a Multi-Structure System . . . 207
7.5.3 Effect of the BDR Setpoint on Conditioning . . . 209

7.5.4 Effect of the Algorithm Loop Settings on Conditioning 212
7.6 Conclusion 216

8 Conclusion and Future Work **219**
8.1 Overview of Work Presented 219
8.1.1 High-Power Test of a Multi-Structure Arrangement 219
8.1.2 Simulation of a Multi-Structure Arrangement 220
8.1.3 Monte Carlo Model of High-Gradient Conditioning 220
8.2 Future Work 221
8.2.1 Completion of the Multi-Structure High-Power Test 221
8.2.2 Expansion of the Multi-Structure Simulations 222
8.2.3 Verification and Expansion of the Monte Carlo Model 222

References **225**

Appendix A Published Work **241**
A.1 Co-Author Publications 241
A.1.1 Peer Reviewed Journal Articles 241
A.1.2 Non-Peer Reviewed Conference Proceedings 241
A.2 Invited and Contributed Talks 242

List of figures

1.1 Illustration of a cylindrical waveguide section of radius a. 5
1.2 A Brillouin diagram showing the dispersion relations for a perfect transmission line (dashed red line) and an infinite uniform cylindrical waveguide (solid black line). It can be seen that a uniform cylindrical waveguide will always have a phase velocity which exceeds the speed of light, c. . . 8
1.3 A cylindrical waveguide section which has been periodically loaded with discs. The length of a period is given as L. 8
1.4 A Brillouin diagram illustrating the dispersion relations for a perfect transmission line (dashed red line) and for an infinite, disc-loaded cylindrical waveguide (solid black line). A passband of permissible operating frequencies exists in the range of ω_c to ω_p. The dispersion curve for a disc-loaded waveguide crosses the red dashed line, indicating that operation with $v_p = c$ is possible when $k_z = 2\pi/3L$. 10
1.5 Rendering of the vacuum space of a dual-feed waveguide coupler for a TW LINAC (a) and the electric field profile during operation (b). . . . 16
1.6 Plan showing the footprint of the proposed 380 GeV, 1.5 TeV and 3 TeV energy stages for CLIC relative to the LHC [35]. 23

2.1 The potential barrier, V(z), (blue) seen by the conduction band electrons in the metal with Fermi energy, W_F, as a consequence of the interaction with the image charge on the surface (green) and the surface electric field, E_S, in the vacuum (red)[46]. The effective potential height is reduced by the field as $V_m - \sqrt{\frac{e^3 E_s}{4\pi\epsilon_0}}$. 26
2.2 Dark current vs surface electric field (a) and $\log_{10} \frac{I_f}{E_s^{2.5}}$ plotted against $\frac{1}{E_s}$ (b) for a T24 accelerating structure for the first (yellow), central (orange) and final (blue) accelerating cells in the structure respectively [41]. . . . 28
2.3 Post-mortem SEM images of the CLIC crab cavity showing breakdown sites [57]. 30

2.4 Breakdown locations determined via an array of acoustic sensors in a SLAC H90VG5 structure showing a clear hot cell [59]. Post-mortem examination revealed a small piece of foil inside the structure. 31
2.5 The Paschen curves for hydrogen, nitrogen, helium, neon, and argon respectively [64]. 32
2.6 Kilpatrick's limit showing the region in which arcing was likely to occur and below which operation without arcing was thought to be possible. . 33
2.7 Time dependent electric field (dashed black), active power flow (blue), reactive power flow (red), and field emission power flow (green) [16] . . 35
2.8 Comparison of calculated (solid curves) and measured (points) of the power transfer, H_N, during emission over a range of emission site temperatures (a) and emission currents (b). Negative values of H_N indicate a net cooling effect [75]. 37
2.9 The average birth, $\dot{\rho}_+$, (solid lines), and death rates, $\dot{\rho}_-$, (dashed lines) for electric fields of 150, 190, 230, 270, and 310 MV/m respectively from bottom to top (a). Also shown is an SEM image from a fully-conditioned OFHC soft Cu electrode in which several dislocation cells are visible (b) [36]. 39
2.10 Results of novel material structures high-gradient testing. Note the CLIC goals are given as 150MV/m and 170MV/m as this was the goal for the previously considered 30 GHz design [85]. Each sample was operated with a 15 ns RF pulse at a repetition rate of 5 Hz, "no. of shots" refers to the cumulative number of RF pulses. 41
2.11 The processing history of the T24 N2 structure tested in CERN's Xbox-2 test stand. 42
2.12 Conditioning curves of a TD26CC (blue) and TD24R05 (cyan) tested in CERN's Xbox-1 test, and two TD24R05s (red and green) tested at NEXTEF showing the accelerating gradient scaled to a pulse length of 200 ns and a BDR of 1×10^{-6} bpp/m plotted against the cumulative number of RF pulses (a) and breakdowns (b) [46]. Image axes have been rescaled for improved readability. 43
2.13 Comparison of the breakdown probabilities for two accelerating structures, one prepared via conventional methods (normal clean) and one prepared under conditions similar to those implemented in the preparation of superconducting cavities (ultra clean) at SLAC [90]. 44

2.14 TEM images of a copper sample (left),a work hardened sample (centre) and the surface of a copper cavity conditioned under RF pulses (right) [91]. Images have been rescaled for improved readability. 45
2.15 Conditioning history of a T24 structure tested in Xbox-2. The top plot show the operating gradient and cumulative number of breakdowns plotted against pulse number. The bottom plot shows the evolution of the peak upstream and downstream Faraday cup signals during testing. 46

3.1 The exterior of CERN's high-gradient test facility (a) located in building 354 at CERN and two structures installed in the Xbox-3 test slots inside the bunker (b). 50
3.2 Diagram showing the working principle of a klystron. 50
3.3 Diagram of a SLED-I type pulse compressor. 51
3.4 Diagram showing the operation of a 3dB hybrid in a pulse compressor. When a wave of amplitude V is introduced at the input, half the power i.e 3dB (corresponding to $\frac{1}{\sqrt{2}}$ times the voltage) is transmitted to outputs 1 and 2 with a phase shift. When a wave returns from the cavities, the process is repeated leading to complete destructive interference at the source, and all of the power being directed towards the fourth port. . . 52
3.5 Simulation of a pulse compressor with β=6 and $Q_0 = 1.8 \times 10^5$ showing the exponential decay resulting from operation with a fixed 180° phase flip (a) and a pulse with a flat top region achieved via phase modulation of the klystron pulse (b). 54
3.6 The Xbox-2 modulator and klystron enclosure located outside the test bunker (a) and the SLED-I pulse compressor situated on the bunker wall within the enclosure (b). 55
3.7 Diagram showing how modulated signals are produced within the NI-5793 card. 55
3.8 The current Xbox-2 up-conversion scheme. 56
3.9 CAD model of an X-Band 60dB direction coupler showing external geometry (left) and internal geometry with coupling slots (right). . . . 57
3.10 The current Xbox-2 down-mixing scheme. 58
3.11 Block diagram of the Xbox-2 LLRF system. 59
3.12 Vacuum plots showing globally elevated but stable vacuum levels associated with the first high-power RF in a recently installed structure and a small non-BD outgassing event occurring several days into testing after vacuum levels have dropped. 60

3.13 Graphical representation of the conditioning algorithm as shown on the Xbox-2 GUI. 61

4.1 Diagram of an example dual structure test arrangement. 64
4.2 The measured phase noise of the QuickSyn FSW-0020 when programmed to produce an 11.8 GHz signal (a) and the phase noise for different frequencies as specified on the datasheet (b). 67
4.3 Diagram showing how the 2.4 GHz CERN PLL and synthesizer are locked to the PXI crate's built-in 10 MHz oscillator. 67
4.4 Diagram of the new XB2 down-mixing scheme. 68
4.5 The new down-mixing arrangement installed in the crate. The QuickSyn FSW-0020 is located on the right beneath the large black heat sink. Only four RF channels are visible, with the remaining channels being located in the lower layer of the crate. 69
4.6 Results of the phase noise measurement of the assembled mixing crate. 70
4.7 Diagram showing how the 2.4 GHz CERN PLL and PXI crate are locked to the synthesizer's built-in 10 MHz oscillator. 71
4.8 The signal distribution scheme in Xbox-2 test stand. 72
4.9 Arrangement of the multiplexers in Xbox-2 showing how any channel may be read and calibrated non-invasively, minimising the potential for error introduction. 72
4.10 Mechanical design and CST simulations of the variable power splitter (a,c,e) and variable phase shifter (b,d,f). 74
4.11 The final stepper motor driver circuit complete with motion limiting contact switches. 75
4.12 Field Distributions of C-band BOC developed and in use in the SwissFEL LINAC showing a top down view (a) and a side on view (b) of the "Whispering Gallery" $TM_{18,1,1}$ mode. It should be noted that view (b) shows only the spherical cavity and excludes the surrounding waveguide section visible in (a) [111]. 76
4.13 Parameterised elliptical cross section of the BOC storage cavity. 77
4.14 Cross section showing the mechanical design of the BOC (a) and the final assembly at PSI, prior to being shipped to CERN for installation and high-power testing (b) [118]. 79

4.15 Simulated S_{21} of an X-band SLED-II pulse compressor designed to operate with a compressed pulse length of 250ns (left) and the output produced by a klystron pulse with a 180° phase flip at time t=1250ns (right). It should be noted that in reality the device is reciprocal, i.e. $S_{12} = S_{21}$. 80
4.16 The mechanical design (a) of the correction cavity chain showing the waveguide flanges on the lower left and lower right and the vacuum pumping ports on top. Shown on the right (b) is the field patterns and operating modes in a single unit comprised of two spherical cavities and a coupling cell are also shown [122, 123]. 80
4.17 Geometry of the polariser which couples the waveguide section to the cavities showing the magnitude of the E-field distribution in an arbitrary colour scale (a) and the gield patterns seen in a section of the spherical resonant cavities with TE_{012} and two TE_{112} modes [122, 123]. 81
4.18 The frequency response of the SLED-I pulse compressor with correction cavities (a) and simulated waveforms at the output of the CCC and SLED pulse compressor when operating with a 1.5μs klystron pulse with a phase flip (b). The central frequency of the spectrum is 11.994 GHz and the nearby peaks are situated 4 MHz apart [122]. 82
4.19 Arrangement of the BOC and CCC during VNA measurement at CERN prior to installation in the Xbox-2 test stand (a) and results of the VNA measurement of the assembled pulse compression scheme after tuning via temperature (b) [119]. 83
4.20 Simulated waveforms produced by a an arrangement comprised of the CCC and the SLED-I pulse compressor and the CCC and BOC respectively [119]. 84
4.21 The final installation of the CCC (a) and the BOC (b) in the Xbox-2 test stand prior to high-power testing. 84
4.22 Arrangement used for calibration in Xbox-2. The grey arrow shows the only place the signal chain must be unscrewed in order to measure the attenuation prior to operation. 86
4.23 First compressed high-power RF pulses as shown on the GUI and the power meter situated in the Xbox-2 rack during calibration for the PolariX-TDS test. Details of the full test have been reported previously [118]. 87

5.1 Diagram of the planned dual structure test arrangement. 91

5.2 Diagram showing how a breakdown in structure A may result in a reflection towards the klystron and to structure B. 91
5.3 CST MWS rendering of the vacuum space in a 3dB waveguide splitter with waveguide ports in red (a) and an equivalent signal flow graph representation showing nodes as dots and the paths between them as arrows (b). 93
5.4 All possible paths and loops for S21 on the 3dB splitter signal flow graph. 95
5.5 Comparison of the S21 of a 3dB splitter with a short circuit placed on the third port as calculated by 3D electromagnetic simulation in CST Microwave Studio and the SFG method respectively. Shorts were placed at distances corresponding to fractions of the wavelength of the 11.9942 GHz operational frequency. 97
5.6 Signal flow graph of the entire RF network planned for installation in Xbox-2. 97
5.7 Diagram showing the manner and order in which the recursive function would map out an arbitrary network. 98
5.8 Simulation results showing the pulses directed to port 2 (a and b) and port 3 (c and d). A full 1.5 μs klystron pulse has been used with phase modulation which has been tuned to provide an approximately flat pulse at port 3. 100
5.9 S-parameters of the variable phase shifter with the piston in the central position showing relatively wideband transmission. 101
5.10 S-parameters of the power splitter with the piston in the central position. 101
5.11 The vacuum geometry of the variable power splitter (a) and a cross section of the variable piston which acts as a short for a section of circular waveguide (b). The piston positions for which S-parameters for the SFG model were retrieved in CST MWS are also shown. 102
5.12 The transmitted and reflected pulses during a non-breakdown pulse (a) and a pulse in which a breakdown has occurred immediately upon arrival of the RF pulse (b). Both examples have been taken from the results of the CLIC crab cavity test. 103

5.13 Peak Power normalised to the klystron pulse directed to the neighbouring structure and back towards the klystron as a function of reflection phase and hence breakdown location. The power splitter piston was in the central position and hence split the power equally between port 2 and port 3. Also shown is the peak power delivered to the port during a non-BD pulse. 104
5.14 Pulses (normalised to the klystron power) directed to the neighbouring structure and back towards the klystron for the short length in port 3 which results in the maximum and minimum value of each. The power splitter piston was in the central position and hence split the power equally between port 2 and port 3. 105
5.15 Peak Power directed to the neighbouring structure and back towards the klystron as a function of reflection phase and hence breakdown location. 106
5.16 Pulse reflected towards the klystron. Note the secondary discharges following the main compressed pulse which occur due to the inclusion of the BOC and CCC in the simulated RF network. 107
5.17 Pulse reflected towards the klystron (a) and the S_{11} of both the power splitter and the full RF network when both power splitter ports are shorted (b). 108
5.18 Rendering showing a cross section of the simulation geometry (a) and a close-up of the irises showing an emission area highlighted in red (b). . 112
5.19 CST results showing poor meshing of the iris (a) and the heavy aliasing caused by the interpolation of the imported field (b) likely to result in emission on the left side only. Field values in (b) are normalised to a structure input power of 1W. 112
5.20 CST rendering showing the voids included within the copper iris (a) and the resulting increase in mesh density localised to the iris (b). As the voids are located within the copper iris they are isolated from the relevant simulation volume and have no effect on the results. 113
5.21 The T24 PSI2 structure under test in the Xbox-2 test slot. Planes shown by the red and blue dashed lines indicate where the 2D monitors in simulation representing the structure output and Faraday cup detection surface correspond to experimentally. 114

5.22 Scan showing the downstream current averaged over eight RF periods when steady state has been reached versus the correction factor to account for fact only a small portion iris is thought to emit at a given time. Typical downstream measurements of the dark current lie in the milliAmp regime at 100MV/m and so an adjustment factor of 5.6×10^{-7} is found to be appropriate for future simulations. 115
5.23 Simulation results showing the average current reaching the downstream and upstream monitors as a function of accelerating gradient (a) and the ratio between them (b). 116
5.24 Experimental data recorded during the conditioning of the T24 PSI2 accelerating structure at CERN showing a ramp in operating gradient after a pause in operation (a) and the corresponding amplitudes of the downstream and upstream Faraday cup signals and the ratio between them (b). 117
5.25 Trajectories taken by particles emitted at various phases during the RF period. A phase of 90° corresponds to when the field in the middle cell is at its maximum. In the final two images (e, f) the current is emitted on the other side of the cell due to the reversed polarity of the field at these phases. 118
5.26 Simulation results showing the fraction of emitted current from each iris which exits the structure (a) and reaches the upstream and downstream Faraday cups (b). Electrons emitted adjacent to the input/output of the structure do not require capture to reach the 2D monitors meaning a larger fraction of current emitted in these areas reaches them. 120
5.27 The total current emitted from each iris in simulation (a) and the contribution to that observed in the downstream monitor (b). The sporadic behaviour is caused by imperfect meshing, leading to irregularities in the emission properties however the trends are presumed to be correct. 121
5.28 Surface electric field on the iris of the first and final regular accelerating cells in the TD26CCR05 Structure. Fields are normalised to an input power of 1W. 122

5.29 Downstream dark current signal and local β value for the T24 PSI1 structure plotted as a function of spatial position when operating at 100MV/m for different days [135]. Plots were derived by sending a short RF pulse through the structure and are hence in units of signal propagation time, where 0 represents the RF input of the structure and 60ns corresponds to the RF output. 123
5.30 The energy spectra of dark current emitted from every fourth iris reaching the downstream monitor in a single structure simulation with an accelerating gradient of 100MV/m. Results were taken over the course of a single RF period after the simulation had reached a steady state solution. 124
5.31 Cross section of bunched dark current approaching the 2D monitor representing the structure output (red line) in CST MWS. All particles are shown in (a) while only those with an energy greater than 1MeV, corresponding to a velocity of 0.8c or higher are shown in (b). 125
5.32 Phase space diagrams (a-b) and the transverse profile (c) of the macroparticles which reach the downstream monitor over the course of a full RF Period when the simulation has reached a steady state solution. A 200×200 grid was used to generate the bins in each plot. The radius of the beam pipe at the structure output is 4mm, and so no current is observed with a displacement beyond this. 125
5.33 The phase at which the current emitted from different irises exits the structure relative to a fully relativistic beam phased for maximum acceleration (shown by the red line) for various energies. 127
5.34 The variation in charge density (a) and mean and max energies (b) of the dark current at the output of a single structure during a single 11.9942 GHz RF period compared to the arrival time of a bunch phased for maximum acceleration. The resolution with which the structure of the current is viewed is determined by the particle monitor time step in simulation, which was set to one twelfth of the RF period. The current which arrives within the 30-60° bin is plotted as a data point at 45°. . . 128
5.35 Cross section of the full superstructure assembly (a) and a close up of the section outlined in red showing the spacing between the final cell of the first structure and the first cell of the second (b). 130

5.36 Cross section of the PIC simulation showing the propagation of the imported current through the second accelerating structure at 0.1ns (a), 0.5ns (b) and 1ns (c) respectively. The second structure was phased at 60° relative to the first. 132
5.37 Attenuation of the current emitted from the first structure as a function of longitudinal position in the second (a) and the total current observed reaching the output of the second structure normalised to the max value (b) for various phasing arrangements. A phase of 90° corresponds to the second structure being phased at 90° relative to the first. 133
5.38 The average (a) and peak (b) particle energies in the dark current bunches observed at the output of a dual structure arrangement as a function of relative phasing. A phase of 90° corresponds to the second structure being phased at 90° relative to the first and this is the phasing in which a relativistic beam would receive the maximum energy gain. The maximum energy is governed by the arrival time of high energy particles from the first structure. 133
5.39 PIC Simulation of 2nd Structure 135
5.40 Phase space and transverse profile of the macroparticles emitted in the first structure which reached the output of the second over a full RF Period when the second structure is phased at 60°(a-c), and 90°(d-f) relative to the first. A 200×200 grid was used to generate the bins in each plot. The radius of the final iris in the structure is 2.35mm and so most of the particles have a transverse displacement within this range. . 137

6.1 Basic cell geometry of the accelerating structure showing the waveguide damping (a) and a full structure assembly (b) [33]. 142
6.2 Rendering showing a row of silicon carbide inserts (a) and their final position inside the structure manifolds (b). 143
6.3 Key RF parameters for each cell for the unloaded (a) and loaded (b) design powers. In plot b the dashed lines represent unloaded operation and solid lines are beam-loaded conditions. 144
6.4 Reflection from the superstructures observed during operation in CTF3 [141]. Note that structures ACS3 and ACS4 refer to the first and second constituents of the superstructure which was removed and later installed in Xbox-2 for high-power testing. 146
6.5 Images captured during the superstructure endoscopy showing an iris (a) and a view of the silicon carbide in the damping waveguide section (b). 146

6.6 The arrangement used for the VNA measurement and bead-pull of the superstructure in CERN's high-gradient test area (a) and the dielectric wire used to move the bead through the structure (b). 148
6.7 The initial bead pull result for structure B. Shown are the field profile on the beamline axis (a) and a polar plot of S_{11} (b). The cells are counted with the bead pulled in the downstream direction i.e. from the input coupler to the output. 148
6.8 The final bead pull results for structure A showing the field profile (a) and a polar plot of S_{11} (b) with the bead pulled in the downstream direction. 149
6.9 The final bead pull results for structure B after tuning showing the field profile (a) and a polar plot of S_{11} (b) with the bead pulled in the downstream direction. 150
6.10 The S-parameters of structure A (a) and B (b) in air at 20.6°C prior to installation in the Xbox-2 test slot. 150
6.11 Schematic of the superstructure test arrangement and diagnostic equipment. The green and red arrows represent the forward and reflected RF signals while the Faraday cup signals are shown in blue. The positions of the ion pumps throughout the waveguide network are shown by the grey squares with arrows. 152
6.12 The pulse compressor arrangement at the klystron output (a) and the final installation inside the bunker prior to testing (b) showing the superstructure, power splitter and a partial view of the phase shifter. The coaxial cables for the acquisition system had not yet been connected to the directional couplers. 153
6.13 Two numerical solutions 154
6.14 The incident, transmitted and reflected waveforms associated with structure A (a) and B respectively (b) when using a 50ns klystron pulse. The correction cavities are tuned to 32, 16, 8 and 4 MHz respectively and so discharges in and following the main pulse are observed at 31.25, 62.5, 125 and 250ns in the time domain. 155
6.15 The incident, transmitted and reflected waveforms associated with structure A (a) and B respectively (b) when a 700ns klystron pulse is compressed to 50ns. 156

6.16 Illustration showing how the difference in the propagation times of the rising edge of the reflection and the truncation in the transmitted signal may be used to infer the breakdown location. The resulting t_d value in this exampled would be equal to half the fill time of the structure, indicating the arc occurred in the central cell. 159
6.17 The t_d values and group velocity for each cell in the TD26CC R05 structure (a) and the transmitted and reflected waveforms on a non-BD and BD pulse (b). The truncation in the transmitted signal and rising edge on the reflected signal are shown by the vertical red and green dashed lines respectively. 160
6.18 Distribution of breakdown sites within each constituent structure as calculated via the edge method. A time of 0ns corresponds to the structure input while 65ns (approximately one fill time) corresponds to the output coupler. 161
6.19 Diagram showing how a breakdown in structure A may result in a large reflection (red) being sent back towards the klystron and to structure B, the latter being capable of provoking a secondary breakdown in structure B if constructive interference occurs. 162
6.20 The PSRA (a), PEIA (b), PSIB (c) and PEIB (d) waveforms during a normal pulse and a pulse in which a breakdown has occurred in structure A. The reflection from the breakdown in structure A has resulted in a power surge in structure B. The region which is integrated to calculate the gain factors is shown by the vertical green (t_{ref}) and red (t_c) lines respectively. 164
6.21 The change in power in structure B during breakdowns in structure A relative to a non-breakdown pulse as function of breakdown phase for the incident (a) and transmitted (c) signals and the difference between them (d). The simulation results with the power splitter in the relevant position are also shown (b). Experimental results are plotted as a heat map for improved readability and the colour scale is indicative of the number of data points lying within a given area. High density areas are shown in red and dark blue regions effectively show the noise floor of the measurement. 165

6.22 Example of a breakdown in structure A (top) inducing a breakdown in structure B (bottom) on the same pulse. Note the surge in the incident (PSIBBD) and transmitted (PEIBBD) signals in the second structure followed by immediate truncation and a large reflection. The waveforms from the previous pulse are also shown in blue for comparison. 167
6.23 Example showing the reflected signal from a breakdown in structure A (PSRABD) destructively interfering with the structure B incident signal (PSIBBD) causing a reduction in the incoming and transmitted power. The waveforms from the previous pulse are also shown in blue for comparison. 168
6.24 Waveforms during a pulse in which three separate arcs have occurred. PEIA truncates first resulting in a large reflected signal. Following this, PEIB truncates and a large rise in PSRB is observed. Finally, tens of nanosends later both incident channels truncate suggesting the either the power splitter or a component earlier in the line has also arced. . . 169
6.25 Conditioning history of a T24-open tested at CERN's X-band test facility showing the established gradient (blue), the structure BDR (magenta), the pulse length (green) and the cumulative breakdowns (red). 171
6.26 The conditioning history of a T24-open structure tested in CERN's X-band test facility as calculated by Equation 6.10. 171
6.27 The conditioning history of a T24-open test at CERN scaled to a pulse length scaled to a pulse length of 200ns and BDR of 1×10^{-6} with Equation 6.11. 172
6.28 Normalised 174
6.29 Evolution of the scaled peak surface electric field (E_{Surf}) of superstructure constituent A (SS A) and B (SS B) when plotted against the cumulative breakdowns. Five other high-gradient prototype structures are also plotted for comparative purposes. 175
6.30 Block diagram illustrating the setup used to calibrate the electrical length of the signal chains relative to one another. 176

6.31 Raw amplitude and phase data logged from the PSIA and PSIB channels when both are measuring the incident pulse on structure A (top left and top right respectively) with a close-up (bottom) illustrating the difference in electrical length of each signal chain manifesting as a phase and time discrepancy. Note, although the same signal is being sampled there is nonetheless a difference in the measured amplitude due to the difference in attenuation of each respective signal chain. 177
6.32 Diagram showing the position of the ion chamber during the dose rate measurements. 179
6.33 The dark current waveforms logged in each position (a) and the normalised average downstream dark current signal plotted as a function of relative phasing between structures for the simulation results and experimental data (b) for structures operating at 85 and 42.5MV/m respectively. A phase of 90° corresponds to structure B leading in phase by 90° relative to structure A. The phasing arrangement in which a fully relativistic beam would receive the maximum energy gain is shown by the black line. 179
6.34 The dose rate immediately outside the downstream Faraday cup as a function of relative phasing between the two structures. 181

7.1 Simplified block diagram showing the how the conditioning process and test stand behaviour may be simulated. 184
7.2 Graphical representation of the conditioning algorithm in CERN's high-gradient test stands where the loop length is set to 10,000 pulses, the ramp length is set to 5000 pulses, and the step size is 10kW. 185
7.3 The measured BDR as a function of peak surface electric field for the T24 PSI2 structure tested in CERN's Xbox-2 test stand at a pulse lengths 200ns. Error bars have been calculated as the square root of the number of breakdowns for each data point and the measurements are compared to the empirical E^{30} scaling. Details of the full test are available elsewhere [157]. 189
7.4 Cumulative number of breakdowns as a function of cumulative RF Pulses for a TD26CC structure tested in Xbox-1 with insets showing close-ups of the breakdown accumulation (a) and a distribution showing the number of pulses between breakdowns with a double fit in red (b) [58].191

7.5 Preliminary conditioning of several high-gradient prototypes plotted as a function of cumulative RF pulses (a) and breakdowns (b). Only the preliminary conditioning is included and so the pulse length is for 50ns for the data shown. 192
7.6 Results of the model using the two-rate approach i.e. Equation 7.12 plotted as a function of cumulative RF pulses (a) and breakdowns (b). Results are overlaid on the conditioning curves of several high-gradient prototypes for comparative purposes. Also shown is a distribution of the number of pulses between breakdowns with a bin size of 200 pulses (c). 193
7.7 Diagram showing an array of grid elements, each with a unique ψ value. If a breakdown is recorded in a grid element, the element is then assigned a new ψ value. 196
7.8 Results of the model when using the grid-based approach shown in Figure 7.7 instead of Equation 7.12. Results are plotted as a function of cumulative RF pulses (a) and breakdowns (b) and overlaid on the conditioning curves of several high-gradient prototypes for comparative purposes. Also shown are distributions of the number of pulses between breakdowns for all grid elements (c) and for a single element (d). A bin size of 200 pulses is used in each. 197
7.9 Sections of the CLIC crab cavity after high-power testing (a) and the breakdown crater locations in the input cell (marked as number 1 in the photograph) plotted over the electric field distribution from HFSS (b). The cavity was cut via electrical discharge machining (EDM) [57]. . . . 200
7.10 The breakdown sites on cell 2, iris 2 of the CLIC crab cavity (a) the total number of breakdown craters as a function of angle (b) [57]. The direction in which the sites were counted and hence, corresponding angular position is also labelled in (a). A total of 1305 breakdown sites were counted on the surface. 201
7.11 The CLIC crab cavity surface field distribution normalised to an input power of 1W in CST MWS showing the convention in which angular positions were assigned (a) and the calculation surfaces produced by sweeping the lines radially (b). An isometric view of the calculation surfaces is also shown (c) alongside the corresponding k_n values calculated as the integrated electric field on each calculation surface normalised to the maximum (d). 202

7.12 Conditioning history of the CLIC crab cavity showing the peak surface electric field (blue), the structure BDR (magenta), the pulse length (green) and the cumulative breakdowns (red) as a function of cumulative RF pulses. 203
7.13 Conditioning history of the CLIC crab cavity showing the peak surface electric field scaled to a pulse length of 100ns (blue), the structure BDR (magenta), and the cumulative breakdowns (red) as a function of cumulative RF pulses. 204
7.14 Results of the simulation showing the nominal $E_{Operate}$ value (blue), the total BDR (magenta), and the cumulative breakdowns (red) as a function of cumulative pulses. 205
7.15 The progression of E_{State}, E_{Op} and the ratio between them for several grid elements of interest (a,b,c) followed by the total accumulated breakdowns for each grid element normalised to the maximum and compared with experimental data (d). Finally, the breakdown accumulation and progression of E_{State} as a function of breakdowns are shown (e,f). . . . 206
7.16 Results of the multi-structure simulations in which the initial E_{State} value of one cavity was set $20MV/m$ higher (a,c,e) and the $E_{Operate}$ value in one cavity was held 10% higher than the other (b,d,f). 208
7.17 The scaled surface electric field plotted against the cumulative RF pulses (a) and cumulative breakdowns (b) for the CLIC crab cavity and the Polarix-TDS. The blue and red lines show the number of breakdowns accumulated by each structure after having reached a scaled peak surface electric field of 80MV/m. 210
7.18 Conditioning curves produced by the model plotted as a function of cumulative RF pulses (a) and cumulative breakdowns (b) for various BDR setpoint values. The conditioning histories are also plotted as a function of cumulative breakdowns (c) with the number of breakdowns required to reach operation at 220MV/m for each case indicated by a vertical line. Also plotted is the cumulative number of breakdowns vs the cumulative pulses required to reach operation at 220 MV/m for each setpoint (d). 211

7.19 Conditioning curves produced by the model plotted as a function of cumulative RF pulses and cumulative breakdowns for various loop lengths, ramp lengths, and step sizes. In Figures(a-b) the loop length was swept with the ramp length and step sizes fixed at 15000 pulses and 10kW respectively. In Figures(c-d) the ramp length was swept with the loop length and step size fixed at 5000 pulses and 10kW respectively. In Figures(e-f) the step size was swept with the loop length and ramp length fixed at 15000 pulses and 5000 pulses respectively. In all cases the BDR setpoint was set to 4×10^{-5} bpp. 213

7.20 The number of pulses and cumulative breakdowns required to reach operation at a surface electric field of 220MV/m for different step size and loop length combinations at a BDR setpoint of 1×10^{-5} (a,c) and 4×10^{-5} (b,d). It was shown previously in Figure 7.19 that the ramp length had little effect on the preliminary conditioning and so this value was fixed at 5000 pulses for all cases. For readability the 4D results are also compiled and presented as a 3D histogram for where the colour is indicative of the cumulative number of breakdowns for BDR setpoints of 1×10^{-5} (e) and 4×10^{-5} (f). 215

List of tables

3.1 Nomenclature for the forward and reflected signals sampled at each directional coupler in Xbox-2. 57

4.1 Signals to be monitored on a pulse-to-pulse basis in Xbox-2 when running two structures simultaneously. Note that the structure reflections appear twice, this is because while a direct feed is necessary for IQ demodulation the signal must also be split and sent to a log detector for hardware interlocking. 65

4.2 Key geometric and measured RF parameters of the XBOC working with a $TM_{18\,1\,1}$ mode. It should be noted that the measurement was performed at a temperature of 41.2 °C while the design temperature is 40 °C [118]. 78

6.1 Key RF and geometric design parameters of the TD26CC R05 structure for the CLIC main LINAC [138]. 145

6.2 Summary of key test parameters for each superstructure constituent. Values shown correspond to the maximum achieved during the test period and where relevant the values at which each structure terminated the test are also included in brackets. 182

7.1 Initial settings for the Monte Carlo model which produce the results shown in Figure 7.8. 199

Chapter 1

Introduction

The idea of using time dependent electric fields to accelerate particles was first proposed in 1924 by Gustav Ising [1]. Although not implemented in practice, this publication served as the inspiration for Rolf Widerøe, who in 1928 accelerated potassium ions to an energy level of 50 keV through the use of oscillating electromagnetic fields, thereby creating the first linear accelerator (LINAC) and the progenitor for many modern devices [2]. To circumvent the limits associated with establishing high DC voltages, the majority of modern accelerators use radio frequency (RF) fields, and can be classified according to a number of criteria including their material (normal conducting or superconducting), geometry, and the electromagnetic field patterns established within them (operating mode). In preparation for the discussion of the simulation and test of two high-gradient travelling (TW) LINACS in this thesis, the following section outlines the principles by which accelerators of this kind function.

1.1 Electromagnetic Theory

In the presence of an electric or magnetic field, a charged particle is subjected to the Lorentz force, expressed:

$$\vec{F} = q\left(\vec{E} + \vec{v} \times \vec{B}\right) \tag{1.1}$$

Where $\vec{E}$ is the electric field strength, $\vec{B}$ is the magnetic flux density, q is the particle charge, and $\vec{v}$ is its velocity. It follows, that only the electric field component is capable of transferring energy to the particle in the direction of its propagation, whilst the magnetic field's utility lies primarily in the deflection of moving particles. For a

charged particle to continuously gain energy in an oscillatory electromagnetic field, two conditions must be satisfied. Firstly, there must be a component of the electric field which acts in the direction of the particle's motion. Secondly, the particle must remain synchronous with the field, requiring that its velocity is equal to the velocity at which the crest of the wave travels. In accelerators, appropriate fields are often established via the use of a specially designed radiofrequency (RF) cavity. As much of the work carried out in subsequent sections is related to these devices, several important concepts and formulae pertaining to the theory of electromagnetic fields are presented following.

1.1.1 Maxwell's Equations

Classical electrodynamics at the macroscopic level is described Maxwell's equations. First introduced by James Clerk Maxwell in the nineteenth century [3], these equations have since been reformulated several times and in their differential form are given [4]:

$$\nabla \times \vec{E} = -\frac{\partial \vec{B}}{\partial t} \tag{1.2}$$

$$\nabla \times \vec{H} = \vec{J} + \frac{\partial \vec{D}}{\partial t} \tag{1.3}$$

$$\nabla \cdot \vec{D} = \rho \tag{1.4}$$

$$\nabla \cdot \vec{B} = 0 \tag{1.5}$$

Where the Nabla operator (∇) is used to express curl and divergence of the vector fields, $\vec{D}$ is the electric flux density, $\vec{H}$ is the magnetic field strength, $\vec{J}$ is the electric current density, ρ is the enclosed charge density, and ϵ_0 and μ_0 are the permittivity and permeability of free space respectively. Taking into account the properties of matter, the electric and magnetic field strengths are related to their corresponding flux densities as:

$$\vec{D} = \epsilon_0 \epsilon_r \vec{E} \tag{1.6}$$

$$\vec{B} = \mu_0 \mu_r \vec{H} \tag{1.7}$$

Where ϵ_r and μ_r are the relative permittivity and permeability respectively. In a homogeneous, isotropic medium these quantities adopt a scalar value but in practice both generally have a spatial dependence, and take the tensor form for anisotropic materials [5]. As Equations 1.2 and 1.5 contain no charge or current source terms, they

are often referred to as the homogeneous Maxwell equations whilst the remainders are known as the inhomogeneous equations. In free space however, the current and charge terms vanish and so Equations 1.2 to 1.5 reduce to:

$$\nabla \times \vec{E} = -\frac{\partial \vec{B}}{\partial t} \tag{1.8}$$

$$\nabla \times \vec{B} = \mu_0 \epsilon_0 \frac{\partial \vec{E}}{\partial t} \tag{1.9}$$

$$\nabla \cdot \vec{E} = 0 \tag{1.10}$$

$$\nabla \cdot \vec{B} = 0 \tag{1.11}$$

With these terms, the electric and magnetic fields' propensities for propagation may then be illustrated for the simplest case. Taking the curl of Equations 1.2 and 1.3 yields:

$$\nabla \times (\nabla \times \vec{E}) = -\frac{\partial}{\partial t}(\nabla \times \vec{B}) \tag{1.12}$$

$$\nabla \times (\nabla \times \vec{B}) = \mu_0 \epsilon_0 \frac{\partial}{\partial t}(\nabla \times \vec{E}) \tag{1.13}$$

However, for an arbitrary vector field, $\vec{A}$, it has been shown that [6]:

$$\nabla \times (\nabla \times \vec{A}) = \nabla(\nabla \cdot \vec{A}) - \nabla^2 \vec{A} \tag{1.14}$$

Simplifying Equations 1.12 and 1.13 via this identity and substituting Equations 1.4 and 1.5, the wave equations for the electric and magnetic fields in the absence of matter then arise as:

$$\left(\epsilon_0 \mu_0 \frac{\partial^2}{\partial t^2} - \nabla^2\right) \vec{E} = 0 \tag{1.15}$$

$$\left(\epsilon_0 \mu_0 \frac{\partial^2}{\partial t^2} - \nabla^2\right) \vec{B} = 0 \tag{1.16}$$

These equations describe the propagation of electromagnetic waves in free space, predicting that the crest of the wave travels at a speed, typically denoted c, related to the permittivity and permeability as:

$$c = \frac{1}{\sqrt{\epsilon_0 \mu_0}} \tag{1.17}$$

Unguided electromagnetic waves in free space can be described as single, or the superposition of several, plane waves which are of the so-called transverse electromagnetic (TEM) type, meaning that both the electric and magnetic field vectors act perpendicular to the direction of propagation [7]. Through the imposition of boundary conditions, it is possible to efficiently ensure that a longitudinal electric field component remains superimposed on trajectory of a charged particle during transit, and this is the premise by which RF cavities generally function. The manner in which this is accomplished in TW LINACS is described in the sections which follow, alongside several important concepts related to the operation of RF cavities in general.

1.1.2 Electromagnetic Fields in a Cylindrical Waveguide

On a boundary of infinite conductance, generally known as a perfect electric conductor (PEC), only the normal electric-field component and the tangential magnetic-field component can be non-zero at the conductor surface, or more formally [4]:

$$\hat{n} \times \vec{E} = 0 \tag{1.18}$$

$$\hat{n} \cdot \vec{H} = 0 \tag{1.19}$$

Where $\hat{n}$ is the unit vector normal to the surface. In practice, perfect conductors do not exist however for materials with a sufficiently high conductance a reasonable approximation of the behaviour may still be obtained via Equations 1.18 and 1.19. A perfect magnetic conductor (PMC) boundary may also be defined in similar fashion as:

$$\hat{n} \cdot \vec{E} = 0 \tag{1.20}$$

$$\hat{n} \times \vec{H} = 0 \tag{1.21}$$

As before, no such material exists in practice however these terms often employed in the simulation of electromagnetic fields, where PMC boundaries may be inserted as symmetry planes to simplify field calculations in regions where the terms are adhered to. Generally, RF cavities are manufactured from highly conductive media and so

Equations 1.18 and 1.19 are of particular interest. Since the guides used in accelerators are generally tubular, it is most intuitive to model the fields within using a cylindrical co-ordinate system. A cross section of a simple cylindrical waveguide section is shown in Figure 1.1.

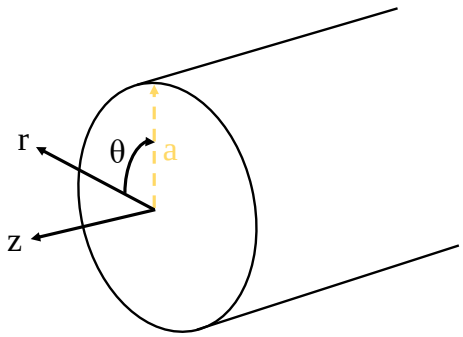

Fig. 1.1 Illustration of a cylindrical waveguide section of radius a.

The electromagnetic fields in a waveguide section manufactured from a highly conductive medium must then satisfy the wave equation and the boundary conditions defined in Equations 1.18 and 1.19. Several sets of solutions which meet these requirements exist, and so it is then convenient to define a means of categorising the field patterns which emerge. Two such sets are the transverse electric (TE) modes (in which the longitudinal component of the electric field is zero) and transverse magnetic (TM) modes (in which the longitudinal component of the magnetic field is zero). In a cylindrical coordinate system, these modes are typically denoted TE_{mnp} and TM_{mnp} respectively where m is the number of full period variations of the field components in the azimuthal (θ) direction, n is the number of zero point crossings in the radial direction (r) between the boundaries, and p is the number of half period variations in the longitudinal direction (z). As a longitudinal electric field component is required for acceleration in the direction of travel, particular attention will be paid to the TM mode solutions in the sections following. The wave equation in cylindrical coordinates is given as [4]:

$$\left(\frac{\partial^2}{\partial z^2} + \frac{1}{r}\frac{\partial}{\partial r} + \frac{\partial^2}{\partial r^2} - \frac{1}{c^2}\frac{\partial^2}{\partial t^2}\right) E_z = 0 \tag{1.22}$$

Where c is the speed of light, t refers to the time, and as in Figure 1.1, r and z are the radial and longitudinal positions respectively. The general expressions for the electric

and magnetic field components of a TM mode in a cylindrical waveguide section may be expressed [4, 8]:

$$E_z = E_0 J_m\left(k_{mn} r\right) \cos(m\theta) \cos(\frac{p\pi z}{L_{cavity}}) e^{j\omega t} \tag{1.23}$$

$$E_r = \frac{p\pi}{L_{cavity}} \frac{a}{x_{mn}} E_0 J_m^{'}\left(k_{mn} r\right) \cos(m\theta) \sin(\frac{p\pi z}{L_{cavity}}) e^{j\omega t} \tag{1.24}$$

$$E_\theta = \frac{p\pi}{l} \frac{ma^2}{x_{mn}^2 r} E_\theta J_m\left(k_{mn} r\right) \sin(m\theta) \sin(\frac{p\pi z}{L_{cavity}}) e^{j\omega t} \tag{1.25}$$

$$B_z = 0 \tag{1.26}$$

$$B_r = -j\omega \frac{ma^2}{x_{mn}^2 c^2} E_0 J_m\left(k_{mn} r\right) \sin(m\theta) \cos(\frac{p\pi z}{L_{cavity}}) e^{j\omega t} \tag{1.27}$$

$$B_\theta = -j\omega \frac{a}{x_{mn} c^2} E_0 J_m^{'}\left(k_{mn} r\right) \cos(m\theta) \cos(\frac{p\pi z}{L_{cavity}}) e^{j\omega t} \tag{1.28}$$

Where J_m is a Bessel function of the first kind of order m, $J_m^{'}$ is the derivative of the Bessel function, x_{mn} refers the zero crossings of the corresponding Bessel function and k_{mn} is equal to the zero crossing of the corresponding Bessel function divided by the cavity radius. The cavity length and radius are given as L_{cavity} and a respectively while ω is the angular frequency. From the boundary conditions given in Equations 1.18 and 1.19 it is clear that the longitudinal electric field must vanish at the radial extremity, and so:

$$E_z(r, \theta) = 0 \qquad \text{at} \qquad r = a \tag{1.29}$$

Thus, it can also be seen that the corresponding Bessel function must be zero at this position, or:

$$J_m(k_{mn} a) = 0 \tag{1.30}$$

Hence, each Bessel function root corresponds to a different TM mode and modes in which $m = 0$ are referred to as monopole modes, with $x_{01} = 2.405$. To ensure the boundary conditions remain satisfied, a mode in a given guide has a corresponding cutoff wavenumber, k_c, below which the wave will be exponentially damped. The cutoff wavenumber of the TM_{01p} family of modes is given:

$$k_c = \frac{2.405}{a} \tag{1.31}$$

The operating frequency of the TM_{01p} modes is then determined only by the guide radius, and the angular cutoff frequency, ω_c, can be given as:

$$\omega_c = k_c c = \frac{2.405\, c}{a} \tag{1.32}$$

By operating in a TM mode, an electric field component may be established in the direction of particle travel, and so the simplest solution for acceleration may then seem to be a simple cylindrical waveguide section. However, the particle must also be synchronous with the fields during transit or else deceleration will occur. In a guide, the free space and cutoff wavenumbers are related to the guide wavenumber, also occasionally known as the propagation constant, k_z, by the dispersion relation, which for a cylindrical waveguide section takes the form [4, 9]:

$$\frac{\omega^2}{c^2} = k^2 = k_c^2 + k_z^2 \tag{1.33}$$

Where k_z then corresponds to the periodicity of the field in the longitudinal direction and thus, for the TM_{010} mode would be zero. If the axial wavenumber is plotted as a function of temporal frequency in radians the result is the so-called dispersion or Brillouin diagram, and this diagram is shown for the TM_{01p} family of modes in Figure 1.2.

The velocity at which the crest of the wave travels is known as the phase velocity, and for a given mode may calculated as [4, 7]:

$$v_p = \frac{\omega}{k_z} = \frac{c}{\sqrt{1 - (\omega_c/\omega)^2}} > c \tag{1.34}$$

Whilst the velocity at which the energy propagates, a quantity known as the group velocity, may be defined [4, 7]:

$$v_g = \frac{d\omega}{dk_z} \tag{1.35}$$

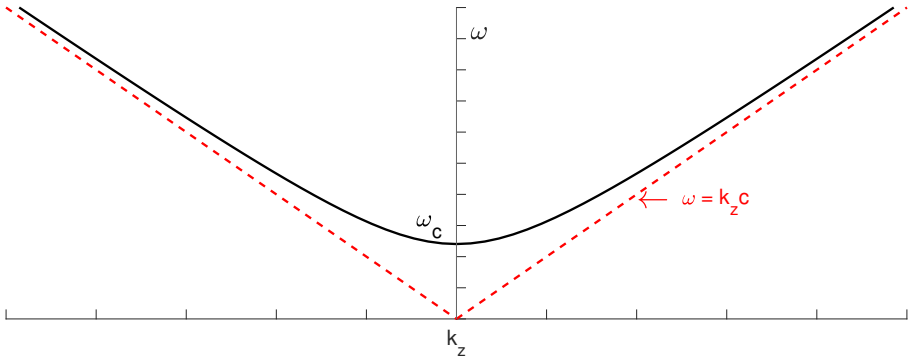

Fig. 1.2 A Brillouin diagram showing the dispersion relations for a perfect transmission line (dashed red line) and an infinite uniform cylindrical waveguide (solid black line). It can be seen that a uniform cylindrical waveguide will always have a phase velocity which exceeds the speed of light, c.

From Equations 1.33 and 1.34 it can be seen that in a cylindrical guide the phase velocity of a TM_{01p} mode always exceeds the speed of light, meaning that longitudinal synchronism with a relativistic particle over any appreciable distance, and hence continuous energy gain, are not possible.

1.1.3 Floquet Theorem and Space Harmonics

To facilitate synchronism with an RF field and efficient acceleration in a cylindrical guide, it is necessary to reduce the phase velocity of the wave, and a common means of doing so is via the periodic insertion of discs as shown in Figure 1.3.

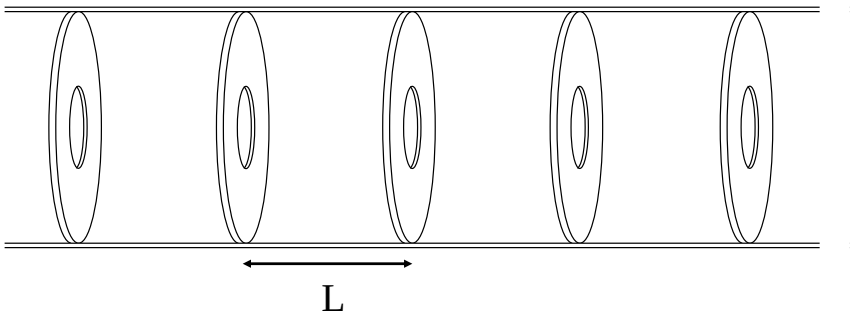

Fig. 1.3 A cylindrical waveguide section which has been periodically loaded with discs. The length of a period is given as L.

In a lossless uniform waveguide with azimuthal symmetry, the axial electric field for a TM_{01} mode may be expressed:

$$E_z(r,z,t) = EJ_0(k_c r)\cdot e^{i(\omega t - k_z z)} \tag{1.36}$$

However the addition of the discs perturbs this electric field in the z direction in a manner described by Floquet's theorem, which states that *in a given mode of an infinite periodic structure, the fields at two different cross sections that are separated by one period differ only by a constant factor, which in general is a complex number* [10]. Hence, the resulting longitudinal field may be expressed:

$$E(r,z,t) = E_L(r,z)\cdot e^{i(\omega t - k_z z)} \tag{1.37}$$

Where $E_L(r,z)$ is a periodic function with the same longitudinal period, L, as the disc loaded waveguide. As with all periodic functions, $E_L(r,z)$ can then be expanded and expressed as a Fourier series, written:

$$E_L(r,z+L,t) = \sum_{n=-\infty}^{\infty} a_n(r)e^{-i2\pi nz/L} \tag{1.38}$$

Where a_n are the Fourier coefficients. Using Equation 1.37 to solve Equation 1.22 it can then be shown that [4]:

$$a_n^{''}(r) + \frac{a_n^{'}(r)}{r} - K_n^2 a_n(r) = 0 \tag{1.39}$$

Where the prime notation refers to differentiation with respect to the radial position, r, and K_n is given [4]:

$$K_n^2 = \left(\frac{\omega}{c}\right)^2 - \left[k_z + \frac{2\pi n}{L}\right]^2 \tag{1.40}$$

For cases where $K_n^2 > 0$, the solution can be expressed as [4]:

$$E_z(r,z,t) = \sum_{n=-\infty}^{\infty} E_n J_0(K_n r)e^{i(\omega t - k_n z)} \tag{1.41}$$

Where:

$$k_n = k_z + \frac{2\pi n}{L} \tag{1.42}$$

The solution to Equation 1.41 then represents an infinite number of waves, known as space harmonics, each of which is denoted by its respective index, n. These harmonics have the same frequency but differ in their respective guide wavenumbers, and once again, a dispersion diagram may be plotted, as shown in Figure 1.4.

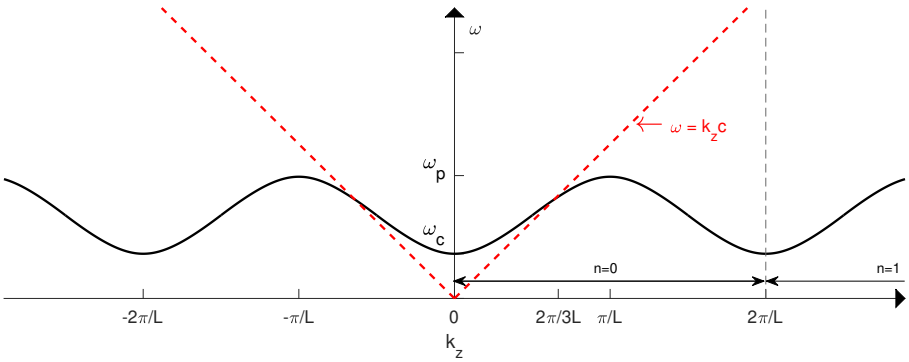

Fig. 1.4 A Brillouin diagram illustrating the dispersion relations for a perfect transmission line (dashed red line) and for an infinite, disc-loaded cylindrical waveguide (solid black line). A passband of permissible operating frequencies exists in the range of ω_c to ω_p. The dispersion curve for a disc-loaded waveguide crosses the red dashed line, indicating that operation with $v_p = c$ is possible when $k_z = 2\pi/3L$.

The resulting dispersion curve reflects the periodicity of the guide and shows that for a given mode there is a limited passband of possible frequencies in the range of ω_c to ω_p. As before, the phase velocity of a given space harmonic can then be calculated as:

$$v_{p,n} = \frac{\omega}{k_n} = \frac{\omega}{k_z + \frac{2\pi n}{L}} \tag{1.43}$$

As the dispersion curve is periodic however, the harmonics at a given frequency all have the same group velocity, calculated as:

$$v_g = \frac{d\omega}{dk_n} \tag{1.44}$$

Equation 1.43 shows that through the selection of the appropriate space harmonic, and hence appropriate design of the guide, synchronism with a relativistic particle may

be achieved. It is then assumed that a traversing charged particle is acted on by only the space-harmonic with which it remains synchronous, while the effects of the other, non-synchronous waves average to zero and may be ignored. In this way, continuous energy gain becomes possible and this is the premise by which TW LINACs generally function.

1.2 Characteristics of Travelling Wave Linear Accelerators

The concepts outlined in the preceding sections have shown that through the use of a periodically loaded cylindrical waveguide section, continuous acceleration of a traversing particle may be achieved. The disc loaded waveguide is a common design in LINACs however real structures are finite in length, and must have a means by which power can enter and exit. With this in mind, it is important to distinguish between two distinct categories of accelerating structures.

LINACS of the TW variety are comprised of an input coupler, a periodically loaded section, and an output coupler. During operation. power flows through the structure from the input to the output and it is from this characteristic that the structures derive their name. However, structures which operate in a standing wave (SW) regime also exist, with only a single coupler through which power may enter and exit. As the work carried out in this thesis pertains to TW LINACs particular attention will be paid the former, and the following design considerations are introduced in a way which pertains primarily to structures of this kind.

1.2.1 Energy Gain in an RF Gap

In a disc loaded waveguide, each periodic section is typically referred to as a cell. In the context of accelerators it is then useful to examine the established voltage and energy gain associated with a given cell. The electric field along the cavity axis can be defined generally as [4]:

$$E_z(z,t) = E(z)\cos(\omega t + \phi) \tag{1.45}$$

Where ϕ is the synchronous phase. Thus, the electric field experienced by a particle traversing the cavity on axis (i.e. r=0) can be defined [4]:

$$E_z(r = 0, z, t) = E(0, z) \cos[\omega t(z) + \phi] \tag{1.46}$$

The energy gain for a given particle traversing the cell can then be found by integrating the field between the cell walls as:

$$\Delta W = q \int_{-L/2}^{L/2} E(0, z) cos(\omega t(z) + \phi)\, dz \tag{1.47}$$

Which may be equivalently written [4]:

$$\Delta W = q V_0 T cos(\phi) \tag{1.48}$$

Where V_0 is the RF voltage on axis, given:

$$V_0 = \int_{-L/2}^{L/2} E(0, z)\, dz \tag{1.49}$$

And T is the transit time factor, a factor used to account for the sinusoidal variation in the accelerating field across the length of the gap in which the particle sees the field, (g), which may be approximated as:

$$T \approx \frac{sin\,(\pi g/\beta\lambda)}{(\pi g/\beta\lambda)} \tag{1.50}$$

This factor corresponds to the ratio of the energy gain in the RF field to that of a square field and hence is maximised for small gaps. Occasionally however, with Equation 1.49 it is useful to define an average axial electric-field amplitude, (E_0), as:

$$E_0 = \frac{V_0}{L} \tag{1.51}$$

The energy gain over the cell length, L, may then be equivalently expressed in terms of E_0 as:

$$\Delta W = q E_0 T cos(\phi) L \tag{1.52}$$

With this in mind, it is then useful to define a quantitative measurement of performance which relates the accelerating voltage established to a given cavity input power. This value is known as the shunt impedance (R_s), and is calculated:

$$R_s = \frac{|V_0|^2}{P_d} \tag{1.53}$$

Generally quoted in megaohms, this quantity is analogous to Ohm's law and provides a measure of the accelerating voltage established for a given power dissipated in the cavity via ohmic losses in the walls, (P_d), the latter of which is described in further detail in Section 1.2.2. It is important to note however, that two definitions of this quantity exist in literature, typically referred to as the LINAC and circuit definitions respectively. The former is provided in Equation 1.53 while the latter, which is more frequently used in the design of circular machines, is derived from the lumped-circuit definition of a resonator and hence is halved [9]. When determining how effectively the cavity voltage can be used to transfer energy to the beam it is also important to consider the transit time factor, and so an effective shunt impedance is often defined as:

$$R_{s,Effective} = \frac{|V_0 T|^2}{P_d} \tag{1.54}$$

For comparative purposes, it is also useful to define a quantity which is independent of both the field level and the cavity length, and for this, an effective shunt impedance per unit length ($R'_{s,Effective}$) is often quoted as:

$$R'_{s,Effective} = \frac{R_s T^2}{L} = \frac{|V_0 T|^2}{P_d L} \tag{1.55}$$

As the achievable accelerating voltage per unit length is intrinsically linked to the required machine length and input power, this factor acts as a useful means of comparing structures of varying designs and operating frequencies, and it is commonly employed in the design process for this purpose.

1.2.2 Power Loss and Coupling

In Section 1.1.2 a PEC boundary was discussed, however real-world cavity resonators are subject to power loss, which gradually reduces the energy stored in the electromagnetic

field. Examples include resistive losses in the cavity surface, dielectric and magnetic losses, external losses, and indeed the energy deposited in traversing particles, often known as beam loading [4, 7]. Though generally, surface and external losses are of the greatest practical relevance. When AC signals are applied to a real conductor, the current decays exponentially with distance from the surface, a phenomenon known as the skin effect. The distance after which the current density is reduced to 1/e of its value on the surface is known as the skin depth, and is given by [4]:

$$\delta = \sqrt{\frac{2}{\sigma \mu_0 \, \omega}} \tag{1.56}$$

Where σ is the conductivity of the cavity material. For annealed copper, the skin depth is on the order of $20.6\mu m$ at 10 MHz and $2.06\mu m$ at 1 GHz. From the skin depth for a given frequency, a corresponding surface resistance (R_{Surf}) may be calculated as:

$$R_{Surf} = \frac{1}{\sigma \delta} = \sqrt{\frac{\mu_0 \omega}{2\sigma}} \tag{1.57}$$

The average power dissipation in the cavity walls due to ohmic surface resistance can then be defined [4]:

$$P_d = \frac{R_{Surf}}{2} \iint_S \vec{H}^2 dS \tag{1.58}$$

Conversely, the energy stored in the electromagnetic field is given:

$$U_{stored} = \frac{\mu}{2} \iiint_V \vec{H} \cdot \vec{H}^* dV = \frac{\epsilon}{2} \iiint_V \vec{E} \cdot \vec{E}^* dV \tag{1.59}$$

With these quantities, the power loss of a given mode per RF period may be normalised to its total stored energy to provide a quantity known as the intrinsic Q factor (Q_0). Equivalently, this quantity may also be defined as the ratio of the mode's resonant frequency (ω_0) to its bandwidth ($\delta\omega$) and thus, may be expressed:

$$Q_0 = \frac{\omega_0 \, U_{Stored}}{P_d} = \frac{\omega_0}{\delta\omega} \tag{1.60}$$

The intrinsic Q factor only takes into account losses which occur on the cavity surface, however in practice, either for the sake of measurement or excitation, it is necessary to couple to a cavity. Similarly, a traversing particle must also have a means of entry and exit. This means that in addition to the resistive losses, there will be an outwards power flux, and a corresponding external quality factor (Q_{ext}) may be calculated in similar fashion as:

$$Q_{ext} = \frac{\omega_0 U_{Stored}}{P_{Ext}} \tag{1.61}$$

The surface and external power loss may then be combined, in the calculation of a loaded quality factor (Q_{Loaded}) given:

$$\frac{1}{Q_{Loaded}} = \frac{1}{Q_{Ext}} + \frac{1}{Q_0} \tag{1.62}$$

Generally, Q_{Loaded} encapsulates all possible mechanisms of power loss however the two aforementioned are generally of the greatest significance. It is important to note however, that in high-current accelerators the beam loading becomes significant and so this source of loss must be also considered in the design process. When designing couplers for accelerator applications it is often convenient to define a coupling factor, calculated as the ratio of the intrinsic to the external Q factor:

$$\beta = \frac{Q_0}{Q_{ext}} \tag{1.63}$$

This factor provides a measure of the coupling strength between the cavity and coupling circuit. Devices with $\beta = 1$ are said to be critically coupled while devices of $\beta > 1$ or $\beta < 1$ are referred to as being over and under-coupled respectively. Typically, cavities are designed to be critically coupled with beam, resulting in reflections when filling. It should be noted however that critical coupling is not always desirable, and the chosen β value will depend on the application. An alternative example often employed in accelerator science is the use of heavily over-coupled cavities for energy storage and this is described in detail in Sections 3.1.2 and 4.3. Also of interest is the ratio of effective shunt impedance to the intrinsic Q factor, often called the *r over Q* value, which is given [4]:

$$r/Q = \frac{R_s}{Q_0} = \frac{(V_0 T)^2}{\omega_0 U_{Stored}} \tag{1.64}$$

For a given mode, this quantity is a measure of the acceleration efficiency per unit stored energy at the operating frequency and thus, is effectively a means of quantifying the interaction of the beam with a specific cavity mode. It can also be seen that the r/Q value depends only on the cavity geometry, and is then independent of material.

Many types of coupling circuits exist and, amongst other things, the chosen design depends largely on the cavity operating mode, required power handling capacity, and tunability. For TW LINACs however, the most common type is the waveguide coupler and an example is shown in Figure 1.5.

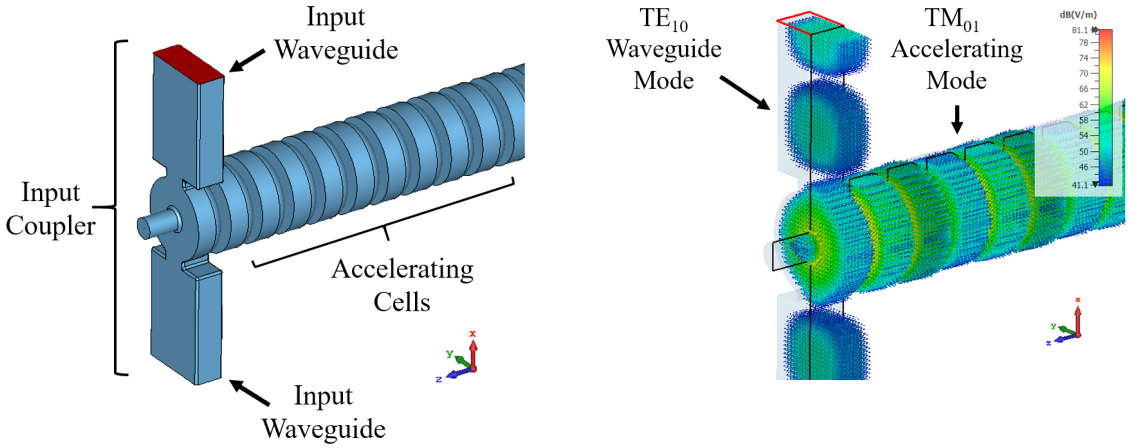

(a) (b)

Fig. 1.5 Rendering of the vacuum space of a dual-feed waveguide coupler for a TW LINAC (a) and the electric field profile during operation (b).

Although several variations exist, there required coupling is typically achieved by connecting one or several waveguide sections to a circular cell via small coupling slots as shown in Figure 1.5. To minimise reflections back to the source and ensure that the TE_{10} waveguide mode is efficiently converted to the cavity operating mode, both the cell radius and slot aperture are then optimised via the use of electromagnetic simulation codes [11]. A similar or identical coupler is then placed on the output to deliver any remaining RF power to an externally situated load.

1.2.3 Practical Design Considerations

In TW LINACS the power which is coupled into the structure propagates along its length, establishing the fields required for the acceleration of traversing charged particles. It has been shown in Section 1.2.2 however, that power is dissipated in the cavity walls and so it is then useful to examine the consequences of this effect on operation. In the simplest case, each cell in a given structure may be kept identical, and hence the attenuation per unit length will remain constant along the structure length. LINAC cavities of this kind are known as constant impedance structures, and the power of the wave is attenuated as it propagates through the structure as [4]:

$$\frac{dP}{dz} = -\frac{\omega}{Q_0}\frac{P}{v_g} \tag{1.65}$$

Correspondingly, the amplitude of the established electromagnetic fields decreases along the structure length as [4]:

$$\frac{dE_{z,0}}{dz} = -\alpha_0 E_{z,0} \tag{1.66}$$

Where α_0 is the attenuation per unit length, defined:

$$\alpha_0 = \frac{\omega}{2Q_0 v_g} \tag{1.67}$$

In constant impedance structures the attenuation per unit length is then constant, and so the absolute the power of the forward travelling wave (P_w) at any longitudinal position within the structure may be calculated:

$$P_w = P_0 \cdot e^{-2\alpha_0 z} \tag{1.68}$$

Where P_0 is the input power and z is the longitudinal position. The total attenuation (τ_0) of a structure is then dependent on its length, i.e. the number of cells, and can be calculated as:

$$\tau_0 = \alpha_0 \cdot L = \frac{\omega L}{2Q_0 v_g} \tag{1.69}$$

Hence, the power which exits the structure at the output may be given:

$$P_L = P_0 \cdot e^{-2\tau_0} \tag{1.70}$$

The value of τ_0 is also proportional to the time taken for a wave of a given frequency to propagate along the full length of the structure, a quantity known as the fill time (t_f), calculated:

$$t_f = \int_0^l \frac{dz}{v_g(z)} = \frac{L}{v_g} = \tau_0 \frac{2Q}{\omega} \tag{1.71}$$

This quantity is then the time required for the structure to fill with RF power, and is an important consideration in determining the required RF pulse length for a given machine to ensure acceleration occurs over its full length. By varying the cell designs τ_0 may be adjusted to increase the group velocity, and hence reduce the fill time, at the expense of lowered efficiency and vice versa.

The constant impedance design is commonly employed in accelerator facilities due to its simplicity and relatively low cost, however Equation 1.66 shows that the later cells in a structure of this kind are comparatively inefficient when it comes to establishing an accelerating voltage. Instead, by gradually tapering the iris radii such that the cells attenuate an increasing fraction of the incoming power this exponential decay may be eliminated and the accelerating field may instead be kept constant throughout. Travelling wave cavities where this is employed are known as constant gradient structures, where the term "gradient" refers to the accelerating voltage which is established along the structure, as given in Equation 1.51. From Equations 1.65 and 1.67 it can be seen that the power dissipation per unit length may be expressed:

$$\frac{dP}{dz} = -2\alpha_0(z)P \tag{1.72}$$

If the shunt impedance along the structure remains approximately constant, then to achieve field flatness along the structure the power dissipation must also be linear. Hence, P should decay linearly with z as:

$$P(z) = P(0) + \frac{P(l) - P(0)}{l} z \tag{1.73}$$

Through substitution, it can then be seen that

$$P(z) = P(0)\left[1 - \frac{z}{L}(1 - e^{-2\tau_0})\right] \tag{1.74}$$

Differentiating with respect to L and substituting Equation 1.72, a term for the attenuation can be found as:

$$\alpha_0(z) = \frac{1}{2L}\frac{1 - e^{-2\tau_0}}{1 - (z/L)(1 - e^{-2\tau_0})} \tag{1.75}$$

With this, the required attenuation may be calculated at each position, and in practice each cell is usually optimised individually to provide an approximately constant accelerating voltage along the full structure length. The total attenuation (τ_0), is then dependent on the number of cells and their respective attenuation constants, and may be calculated as:

$$\tau_0 = \int_0^l \alpha_z dz = \sum_{n_{cell}=1}^{N} \alpha_0(n_{cell}) \cdot L_{cell} \tag{1.76}$$

Similarly, from the group velocity of a structure's constituent cells, the fill time for a constant gradient structure may also be calculated:

$$t_{fill} = \sum_{n_{cell}=1}^{N} \left(\frac{L}{v_g(n_{cell})}\right) \tag{1.77}$$

Where N is the number of cells and L is once again the cell length. At the expense of increased complexity, the constant gradient design can make more effective use of the available structure length. Though it is important to note that a structure may be tuned to realise other goals through the above methodology, and designs which are neither constant impedance nor constant gradient also exist. Examples of such structures include a LINAC which has been tapered to provide a constant heat load to each cell by keeping the longitudinal power dissipation constant, and a hybrid design in which a constant gradient and a constant impedance section have been bonded together to form a single structure [12, 13].

1.3 Applications of High-Gradient Technology

Equation 1.52 shows that by increasing the accelerating voltage the length of accelerator may be reduced, and recent interest in future TeV scale lepton colliders and other applications where machine size is a key constraint have driven research into the achievable accelerating gradient. Modern devices are capable of operating at accelerating gradients in excess of 100MV/m and the following section provides an outline of some of the more prominent applications of the technology [14–16].

1.3.1 Light Sources

Free electron lasers, or FELS, function by way of synchrotron radiation, producing brilliant pulses of light via the undulation of electron bunches [17]. Light sources of this kind constitute a powerful diagnostic and investigative tool in the fields of microbiology, chemistry and material science. In modern FEL facilities the beam is often produced via the photoelectric effect in a specifically designed emission device, known as a photocathode gun. In the area immediately surrounding the emission site the charge density is high and the corresponding space charge effect can result in a degradation of the transverse emittance and a reduction in any subsequent photoemission, limiting the achievable FEL brilliance [18]. It is known however that the space charge effect scales inversely with the Lorentz factor, γ, defined [19]:

$$\gamma = \frac{1}{\sqrt{1-\beta^2}} \tag{1.78}$$

Where β is the ratio of the particle velocity to the speed of light. The effect may then be suppressed by rapid acceleration and the beam quality is then in part determined by the available accelerating gradient immediately after emission. In light of this, next generation FELs have driven research into the development of high-gradient photocathode guns. In 2016 a Stanford Linear Accelerator Center (SLAC) design was recorded operating with a cathode field of 200MV/m during testing, a result directly comparable to high-gradient prototypes tested at the European Organization for Nuclear Research (CERN) which regularly operate with peak surface fields on the order of 220MV/m [16, 20]. Simulations predict that via the use of high-gradient X-band technology a tenfold improvement in brightness may be achieved in addition to halving the transverse emittance [21]. Similar technology has also been implemented in the CLARA project at Daresbury Laboratory, UK, where a 3 GHz photocathode

gun was designed to operate with a cathode field of 120 MV/m at a repetition rate of up to 400 Hz [22, 23].

Alongside full scale FELs, an interest in table top machine alternatives exploiting inverse Compton Scattering for the production of X-rays has also emerged as a result of the success of the high-gradient test programmes at CERN, KEK and SLAC. Two such examples are the Tsinghua Thomson scattering X-ray source (TTX) and Smart*Light project, which plan to use high-gradient X-band structures operating at gradients of 80 MV/m and 75MV/m respectively [24, 25].

1.3.2 Radiation Therapy

Modern high-gradient devices have also found application in the medical field. The first dedicated LINAC for medical treatment was employed in Hammersmith Hospital in 1952 with the first patient being treated shortly thereafter in 1953 [26]. Following this success the device quickly spread as similar facilities were installed in Newcastle and Manchester Hospitals in 1953 and 1954 respectively [26]. Currently, approximately 30% of all tumors diagnosed in the UK are now treated by radiotherapeutic means in which a LINAC is used to deliver electron beams or high-energy x-rays to the site of the tumor resulting in the death of cancerous cells, a method referred to as external beam therapy (EBT) [27]. Such treatment also inflicts significant damage to the healthy cells surrounding the tumour and it is this aspect of the treatment which limits the deliverable dose and the extent to which the technique can be curative. However, recent studies have shown that the delivery of radiation doses beyond those conventionally used in radiotherapy treatment within a short time frame may greatly reduce radiation-induced toxicities in surrounding tissue whilst still yielding a reduction in tumour mass and this has been coined the FLASH effect [27].

The high dose rates and low delivery times required have prompted investigations into the use of Very High Energy Electron (VHEE) therapy using high-gradient machines a potential clinical solution for the treatment [28, 29] as at the present time the melting of tungsten targets due to the high irradiation rates required prevents the use of photons [30]. To date, a single patient has been successfully treated for a subcutaneous T-cell lymphoma via the use of high energy electron beams and the conceptual design of a FLASH treatment facility is ongoing as part of a collaborative effort between CERN and the Lausanne University Hospital, Switzerland (CHUV) [31].

1.3.3 Next Generation Linear Colliders

Finally, one of the main drivers in the development of high-gradient technology has been the renewed interest in physics at the TeV scale. To date the Large Hadron Collider (LHC) has contributed greatly to the field of high energy physics and the 2012 discovery of the Higgs boson marked the completion of the particle content of the Standard Model [32]. However several observations remain unexplained, namely the presence of dark matter and its relative scarcity compared to ordinary matter, neutrino masses, electroweak symmetry breaking, and indeed proposed physics beyond the Standard Model. In circular machines such as the LHC, the achievable energy is practically limited by a phenomenon known as synchrotron radiation, defined:

$$P_\gamma = \frac{2}{3}\,\frac{e^2 c}{\rho^2}\,\frac{\beta^4 E^4}{m^4} \tag{1.79}$$

Where P_γ is the emitted power, e is the charge of an electron, c is the speed of light, ρ is the bending radius of the, β is the particle velocity, E is the particle energy and m is the particle mass. An attractive alternative is then to circumnavigate this problem by through the use of a LINAC based scheme and currently two such proposals exist for a future high energy linear electron-positron collider, the Compact LInear Collider (CLIC) and the International Linear Collider (ILC) [33, 34]. Although both aim to exploit similar physics and share much of the detector technology, ILC is based on superconducting niobium accelerating structures and aims to operate with a loaded accelerating gradient of 30 MV/m while CLIC is based on normal conducting structures operating at an accelerating gradient of 100MV/m. With a proposed COM energy of 250 GeV, ILC's primary goal will be to study the Higgs boson however a potential upgrade to 500 GeV may follow to facilitate top quark production and BSM searches [34]. Conversely, the CLIC concept is to be constructed and operated in three stages at collision energies of 380 GeV, 1.5 TeV and 3 TeV respectively as shown in Figure 1.6 [33].

The first of these three stages provides reasonable coverage of the Standard Model and accurate measurements of Higgs boson couplings to fermions and bosons through the Higgs-strahlung and WW-fusion production processes. The subsequent increases allow beyond the standard model (BSM) searches and would provide access to phenomena ranging from the Higgs self-coupling and rare decays to top-Yukawa coupling. While the use of a linear scheme bypasses the constraints imposed by synchrotron losses it should be noted that such a regime also has inherent disadvantages. The inability

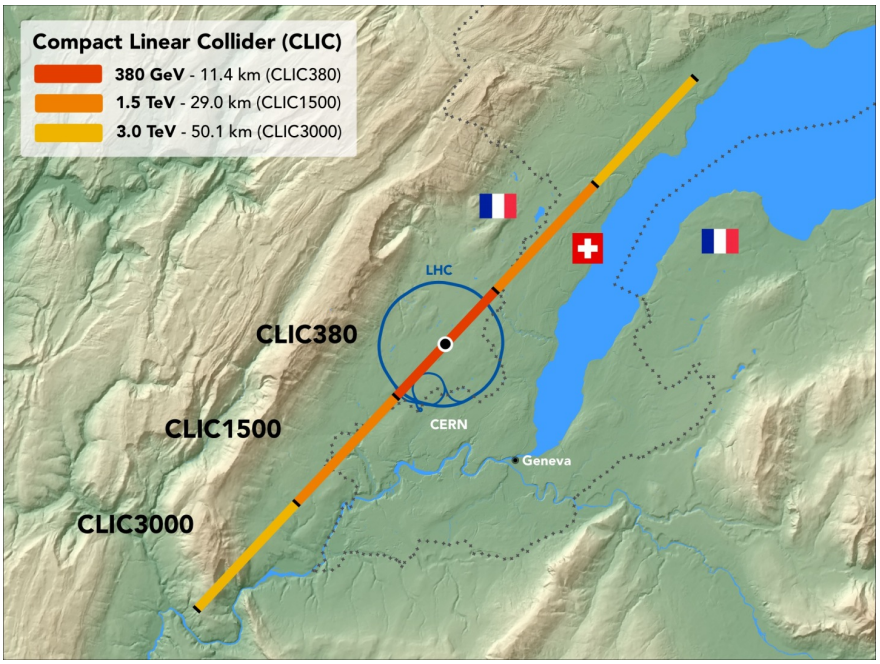

Fig. 1.6 Plan showing the footprint of the proposed 380 GeV, 1.5 TeV and 3 TeV energy stages for CLIC relative to the LHC [35].

to recirculate bunches means the energy gain must take place in a single pass and as a consequence the rapid collection large amounts of data and attainment of high luminosity are more challenging.

1.4 Thesis Outline

The underlying motivation of this thesis was the investigation of the operational challenges and high-gradient phenomena associated with operating multi-structure high-gradient arrangements via the test of a CLIC superstructure. To date, the majority of high-gradient accelerating structure tests have been performed on single structures, and to the author's knowledge no other high-gradient multi-structure arrangement has been operated with a data acquisition system as comprehensive as that of CERN's high-gradient test facility. The test of a CLIC superstructure at CERN then facilitates the investigation of collective high-field effects and is the next step in examining the feasibility of reliably operating a full multi-structure RF module. The results may also provide insight into the fundamental physics behind the phenomena themselves and highlight potential design considerations relevant in the construction and operation of future high-gradient facilities.

A brief introduction to travelling wave LINACs is presented in the current chapter followed by several emerging applications of high-gradient linear accelerators, highlighting their potential utility. Chapter 2 then provides an introduction to the phenomena associated with high-gradient operation. Chapter 3 provides a detailed overview of the Xbox-2 test stand, the experimental facility in which the work for this thesis was carried out. Following this, Chapter 4 details the design and commissioning of the test stand modifications required to facilitate a multi-structure test.

In Chapter 5 simulations pertaining to a multi-structure high-gradient arrangement are performed provide an estimation of the expected behaviour prior to the test. First, the behaviour of reflected signals in the network during vacuum arcs is investigated numerically. Full 3D particle tracking simulations of the test arrangement are then performed in CST MWS to investigate the behaviour of field emitted current during operation. Chapter 6 covers the high-power test of the first multi-structure arrangement to be tested in CERN's test stands, the CLIC superstructure, in detail. An overview of the test history is presented and a comparative analysis with previously tested high-gradient prototype structures is performed. The consequences of conditioning two structures simultaneously are also presented and measurements are performed to validate the simulations detailed in Chapter 5.

In Chapter 7 CERN's existing high-gradient test data is compiled and referenced in the creation of a Monte Carlo model of high-gradient structure conditioning and operation. The model is then used to investigate several phenomena observed in the test stands and the effects of modifying CERN's existing conditioning algorithm. Finally, in Chapter 8 the thesis concludes with an overview of the work presented and the relevant implications for any future high-gradient facility. Several suggestions for future work for which the research presented in this thesis would act as a foundation are also provided.

Chapter 2

RF Conditioning and Breakdown in High-Gradient Accelerators

To date one of the most prevalent limitations on achieving higher accelerating gradients is a phenomenon known within the accelerator community as breakdown, or vacuum arcing. Current research speculates that breakdowns may be triggered by a variety of mechanisms related to microfractures, surface imperfections and manufacture defects, the presence of contamination or adsorbed gas, and glissile dislocations within the metal [36, 37]. Additionally, while breakdown limits high-gradient operation immediately following cavity manufacture, it has been regularly observed that by gradually increasing the input power of an accelerating structure over a large number of pulses its propensity for operation at high-power without breakdown increases, an effect known as conditioning. The following chapter provides an overview of both processes, the concomitant phenomena, and the design constraints developed in the pursuit of breakdown prevention.

2.1 Field Electron Emission

In high-gradient facilities a measurable current is often observed during operation before the injection of bunches for acceleration. This is caused by the emission of electrons from the cavity surface in regions of high field and is typically referred to within the accelerator community as dark current [38–41]. While most theories about breakdown converge on the fact that the breakdown and field emission are two distinct phenomena, they are nonetheless related with field emission typically being regarded as both an important facet and potential precursor of the breakdown process [42, 43]. Recent tests at Japan's High Energy Accelerator Research Organization (KEK) have

also directly observed breakdown occurring at sites of intense field emission in test cavities and so it is important to provide an outline of the phenomenon [44]. In a metal electrons are normally incapable of leaving the bulk material if their energy does not exceed the work function of the relevant surface, however in the presence of a strong electric field the potential barrier for electrons in the conduction band is modified, making escape of the conducting electrons on the surface via quantum tunnelling possible. For a perfectly flat surface this barrier can be defined [42, 45]:

$$V(z) = \begin{cases} -V_m & z < 0, \quad \text{inside emitter} \\ -eE_S z - \frac{e^2}{16\pi\epsilon_0 z} & z \geq 0, \quad \text{outside emitter} \end{cases} \tag{2.1}$$

Where ϵ_0 is the vacuum permittivity (8.854×10^{-12} F/m) , e is the charge of an electron (1.602×10^{-19} C), V_m is the potential energy of the electron inside the metal and E_S is the surface electric field. A diagrammatic representation of this barrier is provided in Figure 2.1.

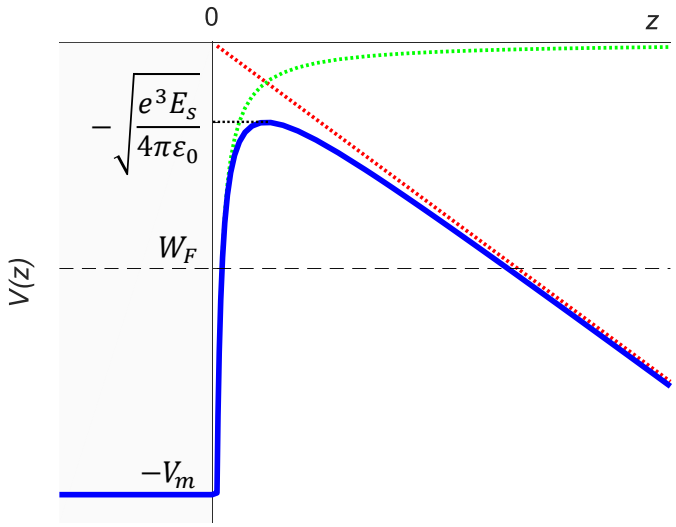

Fig. 2.1 The potential barrier, V(z), (blue) seen by the conduction band electrons in the metal with Fermi energy, W_F, as a consequence of the interaction with the image charge on the surface (green) and the surface electric field, E_S, in the vacuum (red)[46]. The effective potential height is reduced by the field as $V_m - \sqrt{\frac{e^3E_s}{4\pi\epsilon_0}}$.

This effect was described in 1928 by Fowler and Nordheim, where it was also shown that it is possible to extract the expected current density of the tunnelling electrons from the probability of the electrons tunnelling through the barrier and the number of

free electrons per unit volume [47]. In RF accelerating structures however the metallic surface is subject to fields that oscillate in time sinusoidally, by calculating the current for an RF field rather than a DC field and averaging the emitted current over one period an equivalent formula may be obtained the RF case. It is found then that the total current emitted by a given area is defined:

$$I_{FE} = (5.7 \times 10^{-12}) \cdot 10^{4.52\phi^{-0.5}} \cdot A_e \frac{(E_s)^{2.5}}{\phi^{1.75}} exp(-\frac{6.53 \times 10^9 \phi^{1.5}}{E_s}) \tag{2.2}$$

Where I_{FE} is the field emission current, A_e is the emission area, E_s is the macroscopic surface field, and ϕ is the work function of the emitting material. Given its importance in the emission process it is also important to note that the work function can vary significantly with inhomogeneities on the cavity surface including the presence of adsorbed gases, grain boundaries, and crystal orientation on the atomic scale [48, 49]. However, currents far beyond those predicted by this equation are regularly observed in high-gradient structure tests. It is often proposed then that the excess of current may result from regions of local field enhancement caused by small features or protrusions on the surface [37, 46]. The enhanced field around such a site (E_{local}) may then be expressed with the addition of an enhancement factor (β) such that:

$$E_{local} = \beta E_s \tag{2.3}$$

Where β is the ratio of the enhanced field driving the emission process to the nominal surface electric field surrounding it and $E_s$is generally taken from 3D electromagnetic simulation. Adding this enhancement factor to the Fowler-Nordheim approximation then provides:

$$I_{FE} = (5.7 \times 10^{-12}) \cdot 10^{4.52\phi^{-0.5}} \cdot A_e \frac{(\beta E_s)^{2.5}}{\phi^{1.75}} exp(-\frac{6.53 \times 10^9 \phi^{1.5}}{\beta E_s}) \tag{2.4}$$

Naturally, the inclusion of this factor facilitates fitting of both DC and RF experiments to numerical predictions and it is also possible to directly measure a corresponding β for a given experiment. In the case of the RF structure tests, the input power and hence established electric field may be swept over a given range while recording the emitted current via the Faraday cups. The value of β may then be inferred by plotting

$\log_{10} \frac{I_f}{E_s^{2.5}}$ against $\frac{1}{E_s}$ and measuring the gradient [42]. The corresponding β may then be found as:

$$\beta = -2.84 \times 10^9 \cdot \phi^{1.5} \cdot \frac{d(1/E_s)}{d(log_{10} I_f / E_s^{2.5})} \tag{2.5}$$

Experiments at CERN's test stands typically record values ranging 30 to 100 and an example of this measurement performed on a T24 structure is shown in Figure 2.2 [37, 40, 50, 38]. However, it is important to note that this is not a true enhancement factor, as it does not measure the enhancement of any individual emission site nor account for any complex electron capture and transport phenomena. Similarly the factor assumes a fixed work function and thus encapsulates the macroscopic behaviour of the cavity surface as a whole, averaged over the RF pulse. As such, real enhancement factors are expected to both be much higher and to vary between individual emission sites with the latter having been directly observed [44].

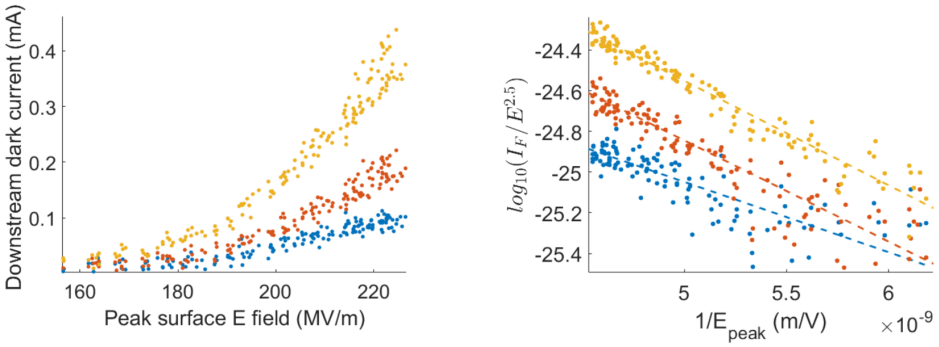

(a) (b)

Fig. 2.2 Dark current vs surface electric field (a) and $\log_{10} \frac{I_f}{E_s^{2.5}}$ plotted against $\frac{1}{E_s}$ (b) for a T24 accelerating structure for the first (yellow), central (orange) and final (blue) accelerating cells in the structure respectively [41].

The origin of features capable of establishing this level of enhancement is not entirely understood but several proposed explanations exist. Recent improvements in manufacture processes facilitate sub micron machining with achievable surface roughness of 25nm, however is still possible that small imperfections and traces may remain from the machining, cleaning and other thermal-chemical processes [40, 46]. It has also been directly observed that small deformities caused by breakdown can result in surface defects with the field enhancement factors necessary to establish significant field emission, thereby acting preferentially as the site of future breakdowns [44].

Additionally, high-power cavities are subjected to significant pulsed heating during operation. The cyclic mechanical stress induced by the accompanying thermal expansion can result micro cracking in the surface, and such behaviour has been directly observed at SLAC [51]. Recent theoretical models also propose that the formation of protrusions may be a dynamic process directly attributable to the tensile stress associated with the surface electric field. In this case glissile dislocations in the surface of the metal may be undergo plastic behaviour, forming a protrusion capable of nucleating breakdown and this theory is outlined in Section 2.3.4 [52, 53]. Such a model would then explain the dynamic conditioning of the accelerating structures. To date no such geometry with the required aspect ratio has been observed experimentally, indicating that if such geometries do exist they are destroyed upon exposure to air or occur spontaneously during operation and are immediately removed [54].

2.2 Overview of Breakdown

While no theory to date has satisfactorily explained and predicted the breakdown phenomenon, the observed characteristics have led to the proposal of a general description. This consensus is also supported by recent DC tests in which direct observation of the arc evolution with with nanosecond resolution has been made possible via the use of modern high-speed cameras [55]. It is generally accepted that the existence of some abnormality on the surface is required for breakdown nucleation, the resulting field emission then leads to substantial localised heating as will be detailed in Section 2.3.3. This, combined with the associated stress of the applied electric field can result in the onset of plastic behaviour and modification of the local geometry and emission site properties. The onset of the breakdown itself is typically accepted to have occurred with the formation of the plasma, the aforementioned serving merely as potential precursors. The progression of the arc may then be described by several distinct stages:

1. **Field Emission:** Significant emission is present as described in Section 2.1 leading to intense local heating.

2. **Neutral Atom Evaporation:** Evaporation of neutral atoms and ions from the surface occurs as a consequence of the surface electric field and growing thermal energy. Atomistic simulation has found the presence of these neutral atoms to be essential in the development of the arc [56].

3. **Ion Bombardment:** The growing density of neutrals and electrons results in substantial ionisation via collisions, producing a quasi-neutral plasma sheath

immediately outside the emission site. Ionised atoms are then attracted to and repelled by the surface resulting in continuous bombardment. Consequently, additional ions are sputtered, maintaining the plasma volume on a longer timescale.

4. **Plasma Extinction:** Following cessation of the RF pulse the plasma quenches and the molten copper cools, resulting in a modification of the cavity surface as shown in Figure 2.3.

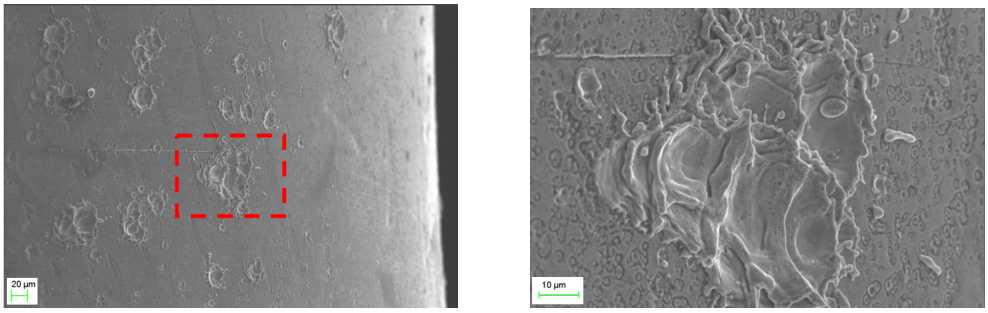

(a) SEM image showing breakdown sites on the area immediately surrounding the iris.

(b) Close-up of the breakdown site outlined in red in image a.

Fig. 2.3 Post-mortem SEM images of the CLIC crab cavity showing breakdown sites [57].

The entire event occurs within a few tens of nanoseconds and often results in the creation of a small residual crater with a diameter on the order of 5-20 μm which has been found to modify the probability of future breakdowns [58]. In RF accelerating structures, the onset of the plasma constitutes a large impedance mismatch, acting as a short circuit and reflecting a large portion of the incoming RF power back towards the source. Additionally, large emissions of current and increased x-ray production are regularly observed, indicating that a significant injection of charge carriers into the electric field occurs.

Due to the stochastic nature of the phenomenon and the fact that high-gradient accelerating structures are typically operated in a pulsed regime breakdowns are typically measured by how frequently they occur within a given number of high-power RF pulses per unit length of an accelerator. This quantity is known as the breakdown rate (BDR) and is defined:

$$\text{BDR} = \frac{\text{No. of Breakdowns}}{\text{Number of RF Pulses} \times \text{Accelerating Structure Length}} \tag{2.6}$$

Where the BDR is commonly expressed in units of breakdowns/pulse/metre, denoted bpp/m [40, 33]. The quantity is often used in the assessment of an accelerating structure's performance at a given gradient and pulse length, and the CLIC project has explicitly stated a BDR of 3×10^{-7}bpp/m as a design goal to facilitate the required luminosity [33]. Attempting to operate at higher power levels than the structure is conditioned to will then result in an increased BDR and a reduction in reliability. In extreme cases, operation at high breakdown rates or the presence of surface defects capable of nucleating breakdowns can result in cavity surface being irreparable damaged. Accelerating cells where this has occurred are known colloquially as "hot" and have been observed to limit structure performance, possibly rendering it incapable of reaching the design gradient. One example of this was observed in a study performed at SLAC in 2008 where it was noted that one cell had accumulated an order of magnitude more breakdowns than the others as shown in 2.4.

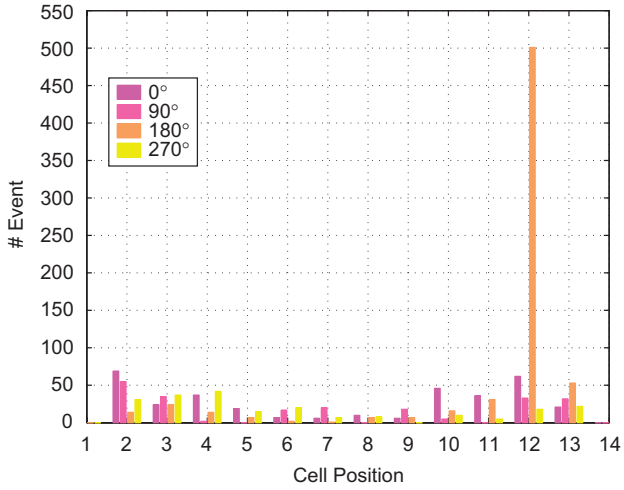

Fig. 2.4 Breakdown locations determined via an array of acoustic sensors in a SLAC H90VG5 structure showing a clear hot cell [59]. Post-mortem examination revealed a small piece of foil inside the structure.

A post-mortem visual inspection of the structure showed many craters in the predicted location in addition to a piece of aluminium foil which was believed to have been responsible for the frequent arcs.

2.3 Constraints and Underlying Physical Phenomena in Breakdown

As a result of the cumulative experimental efforts of early accelerator scientists and the more recent high-gradient test programmes several models, empirical scaling laws and design constraints have been proposed [60, 16, 61, 62]. The most prevalent of these are presented and discussed following.

2.3.1 Surface Electric Field

The surface electric field is known to play an integral role in the breakdown process, and is typically seen as necessary for the establishment of any kind of electrical arc. In 1889 Paschen studied the occurrence of electrical arcs between electrodes in gas and derived an empirical formula describing the observed behaviour [63]. The resulting relation, known as the Paschen curve, is shown for a variety of gases in Figure 2.5.

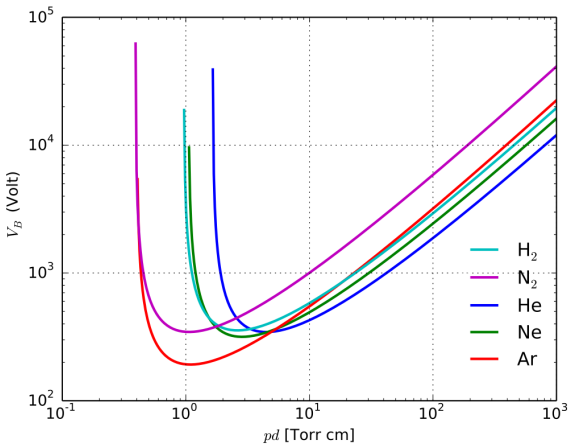

Fig. 2.5 The Paschen curves for hydrogen, nitrogen, helium, neon, and argon respectively [64].

Pachen's curve predicted that at low pressures the sustainable electric field would increase sharply, however experimental data collected from early accelerators and DC tests showed that arcing still occurred regularly under vacuum. In an attempt to quantify this behaviour, Kilpatrick established a further empirical relation from the data available at the time, defining the attainable voltage as applied to both DC tests and RF accelerating structures [60]. The relation was later reformulated by T. J. Boyd in 1982 to relate the operating frequency (f) to the maximum attainable surface electric field (E_k) as [65]:

$$f = 1.64 \times E_k^2 \cdot exp\left(\frac{-8.5}{E_k}\right) \tag{2.7}$$

Although aligning well with the available data, this new criterion still demonstrated several limitations. Notably the lack of any pulse length dependence and the inability to predict the stochastic behaviour of breakdown for a given field level. Instead, it offers only a binary indication of whether or not an arc is liable to occur as shown in Figure 2.6.

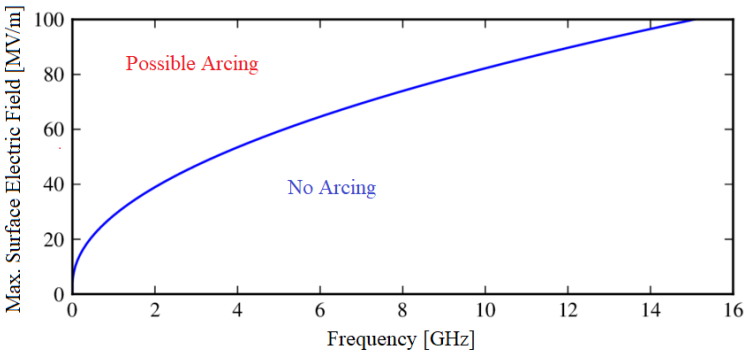

Fig. 2.6 Kilpatrick's limit showing the region in which arcing was likely to occur and below which operation without arcing was thought to be possible.

Recent structures have since been recorded operating reliably at several times the achievable field predicted by this formula [16], suggesting that it is not indicative of what is attainable with modern cavities and vacuum systems. Despite this, the trend predicted is nonetheless correct and the electric field is still regarded as an important quantity in the initiation of breakdown.

2.3.2 Power Flow and the Modified Poynting Vector

Although the surface electric field was long thought to be the quantity primarily responsible for initiating breakdowns, modern high-gradient structures have shown significant variance in the achievable gradient during testing, suggesting that it is not the only quantity which determines the limit. As a result, several other proposals have emerged, incorporating the surface magnetic field, group velocity and power flow [16, 66, 67]. In 2006 it was noted that structures with larger irises were naturally capable of sustaining greater input powers on account of the higher group velocities and hence decreased relative power dissipation in the walls. Attempts to reconcile

these discrepancies then led in the proposition that the ratio of the power flow (P) to the accelerator iris circumference (C) was fixed as [66]:

$$\frac{P \cdot t_p^{\frac{1}{3}}}{C} = Constant \tag{2.8}$$

Where t_p is the pulse length. Plotting P/C for a variety of structures demonstrated a markedly smaller spread than examples which attempted to correlate the BDR with the surface electric field however the relation also demonstrated several shortcomings. Namely, that one structure lay significantly above the others and that the quantity is unable to account for breakdowns in standing wave structures where there is no power flow through the aperture during steady state operation. Following this, in 2009 a local field quantity describing the high-gradient limit was proposed. It was noted that the local heating which occurs prior to breakdown requires power flow, of which there is no source other than the electromagnetic field. The power flow associated with the electromagnetic fields is known as the Poynting vector, and is defined:

$$S = E \times H \tag{2.9}$$

Where E is the electric field vector in V/m, H is the magnetic field vector in A/m and the units of S are W/m^2. However, this form represents the instantaneous power flow due to the concomitant time varying electric and magnetic fields and so in RF cavity design it is then more appropriate to employ the time-averaged power flow, defined:

$$\langle S \rangle = \mathrm{Re}(\tfrac{1}{2} E_m \times H_m^*) \tag{2.10}$$

Where E_m represents the sinusoidally varying electric field and H_m* denotes the complex conjugate of the magnetic component. It was proposed that a modified form of this quantity, S_c, may describe the high-gradient limit of accelerating structures, defined [16] :

$$S_c = \mathrm{Re}(S) + g_c \cdot \mathrm{Im}(S) \tag{2.11}$$

And g_c is a weighting factor calculated as:

$$g_c = \frac{\int_0^T \mid P_{rf}^{SW} \mid \cdot P_{FN} dt}{\int_0^T \mid P_{rf}^{TW} \mid \cdot P_{FN} dt} \tag{2.12}$$

Where P_{rf}^{TW} denotes the active power flow during steady state present in travelling wave structures only, P_{rf}^{SW} is the reactive power flow present in any resonant cavity, describing the oscillatory transitions between electric and magnetic stored energy and P_{FN} is the power flow associated with any field emission.

This factor accounts for the fact that the field emission only occurs during the correct electric field polarity and hence its corresponding power flow is in phase with the active power flow on the surface. Additionally, the factor accounts for the fact that the instantaneous power is lower for reactive than active power. It follows then, that field emission is 90° out of phase with the reactive power flow and as a consequence, for the same amplitude the reactive power is less effective in providing power for the field emission as shown in Figure 2.7. This factor is independent of all geometrical and material parameters, depending only weakly on the local electric field with values from 0.15 to 0.22 for fields in the range of 3 to 10GV/m [16].

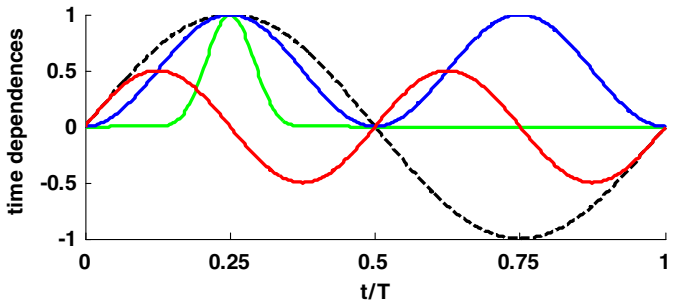

Fig. 2.7 Time dependent electric field (dashed black), active power flow (blue), reactive power flow (red), and field emission power flow (green) [16]

S_c aims to combine both the heating effect of field emitted current from an emission site and that of the RF power flow. It has been shown to align well with the results for both standing and travelling wave cavities at various frequencies and has therefore been deemed a reasonable constraint for use in the design of high-gradient accelerating structures. As a result, the quantity is now commonly referenced in modern cavity design alongside other constraints such as the peak surface electric, the peak surface magnetic fields, and the accompanying pulsed heating [68, 69].

2.3.3 Nottingham Heating

As touched upon in Section 2.2 breakdown is characterised by plasma formation, a process necessitating intense local heating which may be originate from two emission-induced phenomena. The first is Ohmic or Joule heating which occurs as a consequence of emission current and the resistance associated with the small cross section of any given emission site. As the resistivity is known to increase with temperature it has been postulated that resistive heating could result in instability at high emission densities and this was described in detail by Dyke in 1953 [70].

However in many experiments stable high-density emission is regularly observed, and indeed in several experiments involving tungsten tips under high electric fields a cooling effect providing stabilisation of the cathode-tip temperature has been noted, indicating the presence of additional mechanisms of energy exchange. For a given surface the emission of an electron from the surface is accompanied by an exchange of energy between the electrons in the conduction band and the cathode lattice. The net energy exchange is then dependent on the energy of the average emitted electron (ϵ_{emit}) and the replacement electrons supplied by the circuit (ϵ_{repl}) as:

$$\Delta\epsilon = \epsilon_{emit} - \epsilon_{repl} \tag{2.13}$$

From this equation it can be seen that the exchange can then be either exothermic or endothermic in nature, depending on the average energy of the emitted electrons and their replacements, an effect first predicted by Henderson in 1940 and discussed by Nottingham shortly thereafter in 1941 [71, 72]. It was postulated that if the energy of the emitted electron is above the Fermi level so-called Henderson-cooling occurs; conversely, when emitted from below the Fermi level then the remaining conduction band hole will scatter electrons into states above the Fermi level resulting in a local energy increase coined Nottingham-heating [73]. If ϵ_{repl} is assumed to be the Fermi level in the emitting material, $\Delta\epsilon$ can be approximated as [74]:

$$\Delta\epsilon \approx \pi k_B T_{tip} \cot 2\pi\alpha \tag{2.14}$$

In which k_B is Boltzmann's constant, T_{tip} is temperature of the emission site tip and α is given as:

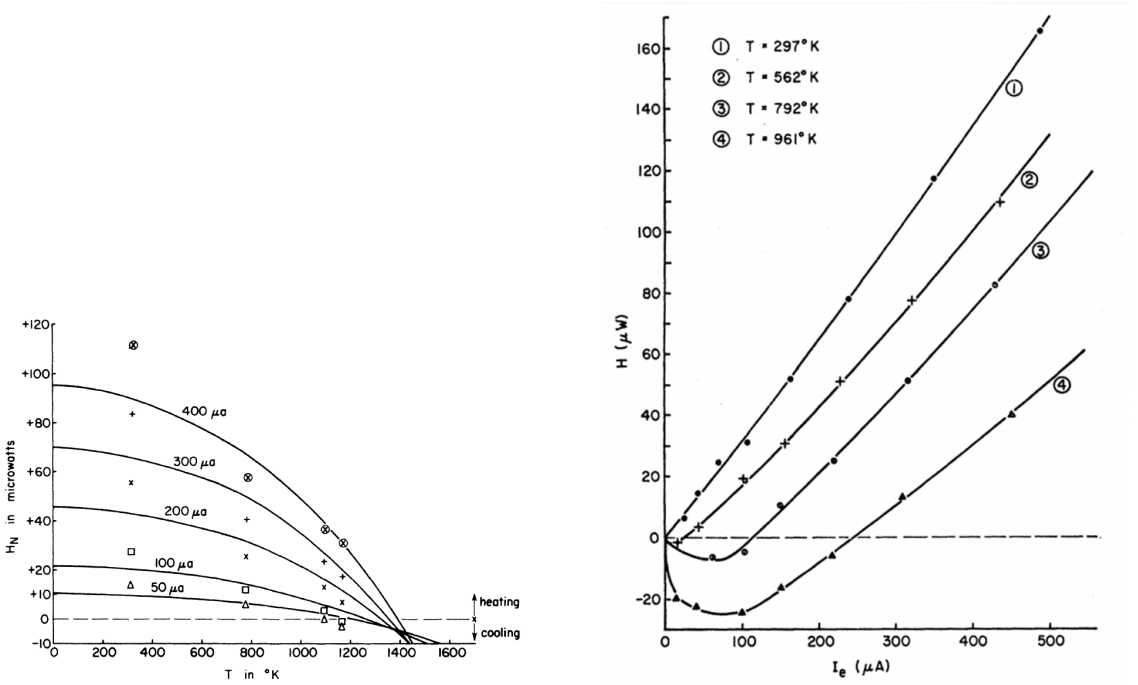

(a) (b)

Fig. 2.8 Comparison of calculated (solid curves) and measured (points) of the power transfer, H_N, during emission over a range of emission site temperatures (a) and emission currents (b). Negative values of H_N indicate a net cooling effect [75].

$$\alpha = \frac{2\pi k_B T_{tip}\sqrt{2m\phi}}{heE_{tip}} \tag{2.15}$$

here ϕ is the work function, h is the Planck constant, e is Euler's number and E_{tip} is the electric field at the tip of the emitter.

Studies on tungsten tips and carbon nanotubes have demonstrated that the magnitude and direction of the exchange is strongly dependent on the cathode temperature, the work function, and the applied electric field [74]. In pure field emission, energy levels above the Fermi level are empty and any emission then results in heating effect. However at high temperatures energy levels above E_f become populated and thus are preferentially emitted causing a decrease in the average heat transfer per emitted electron. Under the correct conditions it is then possible to reach an inversion point as shown in Figure 2.8 and this is a well known effect in devices which operate based on the principle of thermionic emission [75].

It should however be noted that the studies shown in Figure 2.8 were carried out on tungsten geometries for which the melting point is 3422°C, far beyond the melting and boiling points of copper which occur at 1085°C and 2562°C respectively. Additionally, the Fermi energy is 7eV in copper as opposed to 4.5eV for tungsten, although both materials boast comparable work functions at 4.5 and 4.7eV respectively. Modern simulations on the breakdown phenomenon have explored this effect in detail and found it to be the dominant mechanism by which heating occurs during arc formation [76].

2.3.4 Dislocation Dynamics and Breakdown Nucleation

Many attempts to explain breakdown nucleation focus solely on the arc formation, relying on the assumption of a distinct protrusion is already present on surface. Similarly, atomistic modelling has been used to simulate the migration and growth of dislocations in a metal under stress though in such simulations an arbitrary emission geometry is always initially present [77–79]. The formation of such defects however, has not yet been adequately described theoretically and to date no protrusion with the required aspect ratio has been observed experimentally. Additionally, assuming a defect is present, in modern machines breakdown nonetheless appears to occur stochastically even at fixed input power, suggesting that the nucleation of a breakdown is instead a dynamic process. A recent theory suggests that this nucleation is dependent upon the movement of glissile dislocations present in the metal in response to the mechanical stress of the applied electric field [61, 80]. The stress on the surface associated with an applied electric field may be defined [81]:

$$\sigma = \frac{\epsilon_0 E^2}{2} \tag{2.16}$$

Where ϵ_0 is the permittivity of free space, E is the applied electric field and σ is the applied stress. The theory postulates that within a metal there is an intrinsic dislocation density (ρ) and under the stress of the electric field dislocations tend to organise themselves in a cellular arrangement as shown in Figure 2.9. However, a mobile dislocation arriving at the surface may geometrically modify it, enhancing the local electric field and nucleating a breakdown. It is suggested that these dislocations undergo regular creation or depletion within the cells on the surface resulting in a change in the density ($\Delta\rho$) which oscillates about a stable value, as shown in Figure 2.9.

When the dislocation population experiences a fluctuation large enough to carry the mobile dislocation density beyond a critical value ρ_c, a critical transition occurs

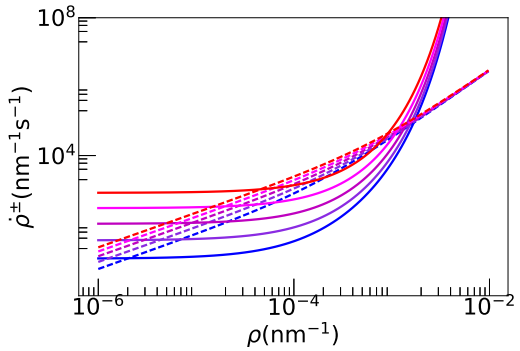

(a)

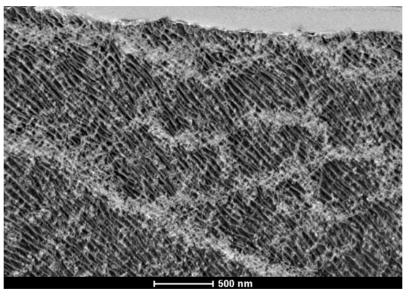

(b)

Fig. 2.9 The average birth, $\dot{\rho}_+$, (solid lines), and death rates, $\dot{\rho}_-$, (dashed lines) for electric fields of 150, 190, 230, 270, and 310 MV/m respectively from bottom to top (a). Also shown is an SEM image from a fully-conditioned OFHC soft Cu electrode in which several dislocation cells are visible (b) [36].

wherein the rate of creation exceeds the rate of depletion, resulting in plastic evolution of the surface and breakdown [61, 80]. This model is unique, as it does not rely on the assumption that defects are already present on the surface prior to breakdown and describes the regularly observed stochastic behaviour. Additionally, it suggests that it is the interlocked pattern of sessile dislocations which grants an enhanced breakdown resilience, offering a physical explanation for the conditioning process which will be outlined in Section 2.5, likening it to a hardening process.

2.4 Empirical Scaling Laws and Material Dependencies

Recent data from the CLIC test programme and other high-gradient facilities has led to the proposal of several empirically derived scaling laws and dependencies. For a structure conditioned to a given field level, the BDR has been found to vary proportionally to the gradient and hence surface electric field, and pulse length as [16]:

$$Constant = \frac{E_s^{30} \cdot t_p^5}{\mathrm{BDR}} \tag{2.17}$$

This equation constitutes an empirical scaling law which relates three parameters relevant in the evaluation of high-gradient structure performance, providing a useful basis for the comparison of cross test results where operational parameters have varied

and it is often employed for this purpose [46, 82, 83]. It should be noted however that the factors have not been derived from any kind of physical model and are simply the product of fitting to data. Similarly, a stress model has been proposed which relates the BDR to the defects present in the crystalline structure of the cavity surface [62]. This model postulates that the relationship between the BDR and the electric field (E_0) is given:

$$BDR \propto \exp\left(\frac{E_0^2 \epsilon_0 \Delta V}{k_b T}\right) \tag{2.18}$$

Where T is the temperature in kelvin, k_b is Boltzmann's constant and ϵ_0 is the permittivity of free space. ΔV is the relaxation volume of the defect, defined as the volume change of the elastic material resulting from the elastic relaxation of the position of atoms around it [84]. Hence, the relaxation volume of a vacancy would be negative as the material surrounding the vacancy relaxes towards it. This model aligns well with the empirical dependence provided in Equation 2.17 however it lacks a pulse length dependence and suggests a non-zero BDR in the absence of an electric field. Although the thermal energy to initiate the fluctuations may be present breakdown is a multi-step process and the presence of a field is nonetheless thought to be necessary to drive the emission process and eventual plasma formation.

Additionally, different materials have exhibited varying propensities for high-gradient operation. Although electrical quantities may be reduced by geometric optimisation fundamental limits of any cavity material still apply, it follows that the alternative is then to change the structure material outright. In normal conducting structures annealed copper is typically the material of choice due to its availability, machinability and favourable conductive properties. This is especially true in high frequency designs such as the prototype X-band CLIC structures where the inverse size scaling with frequency means such structures require ultra-precise milling and turning operation to achieve the required tolerances [33]. The CLIC group at CERN have however compared the performance of three identical structures manufactured from tungsten, molybdenum and copper respectively and the results of these tests are shown in Figure 2.10 [85, 86]. The copper structure was brazed under vacuum while the two latter were aligned and clamped during testing. During testing the structures reached gradients of 110 MV/m 150MV/m and 195MV/m for copper, tungsten and molybdenum respectively, record gradients at the time [85].

It was concluded from these studies that the breakdown resilience of a material is correlated with the crystal structure of the metal [87]. Face-centred cubic (FCC)

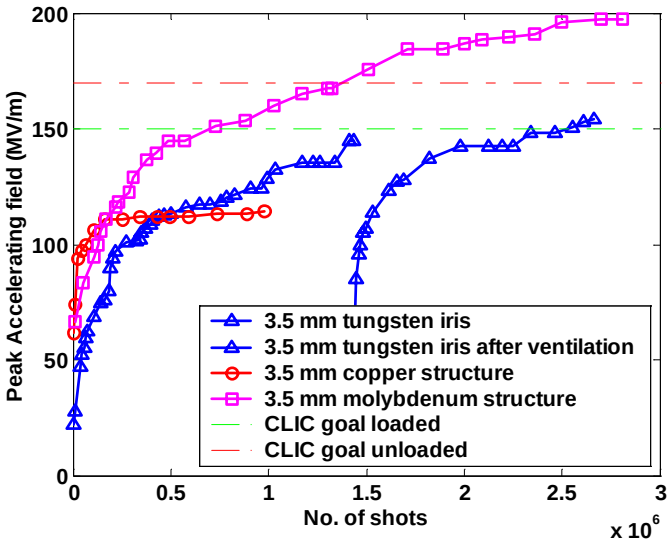

Fig. 2.10 Results of novel material structures high-gradient testing. Note the CLIC goals are given as 150MV/m and 170MV/m as this was the goal for the previously considered 30 GHz design [85]. Each sample was operated with a 15 ns RF pulse at a repetition rate of 5 Hz, "no. of shots" refers to the cumulative number of RF pulses.

metals are known to have an inherently higher dislocation mobility than metals of the hexagonal closest packing (HCP) and body centred cubic (BCC) arrangements, a result which would support with the idea that breakdowns nucleate from mobile dislocations as described in Section 2.3.4. While the results indicate that refractory metals have a higher propensity for establishing high gradients their use is not yet practicable due to the difficulty and expense associated with their procurement and manufacture. Due to its relatively simplicity however X-band waveguide has been manufactured out of various other unconventional materials such as stainless steel and gold, achieving surface field levels of 75MV/m and 50 MV/m respectively [88]. From the results of this test it was suggested that material properties such as melting temperature, yield strength and even vapor pressure may be contributing factors in breakdown constraints.

Finally, accelerating structures are often subjected to heat treatments necessitated by the bonding process during manufacture, relaxing stresses within the metal. To investigate the effect of such treatments DC experiments conducted on sets of hard copper electrodes and electrodes which have been subjected to the same softening treatments the CLIC prototype structures [89]. In these tests it was found that the ultimate performance of each electrode was comparable however the hard electrodes achieved the maximum field within fewer pulses and while accumulating fewer breakdowns. From

this study it was concluded that the conditioning is a process of micro-structural hardening and that the soft electrodes reached their ultimate performance by approaching a surface hardness comparable to that of the hard electrodes [89].

2.5 Surface Conditioning in High-Gradient RF Structures

Due to breakdown, high-gradient structure are not capable of immediate operation at the full design gradient and RF pulse length following manufacture and tuning. Attempting to do so can result in an unacceptably large number of breakdowns, hindering operation and in extreme cases irreparably damaging the structure. Typically, the high-gradient structures designed for CLIC are typically capable of establishing gradients up to 20MV/m for pulse lengths of 50-100ns before regular out-gassing events from the surface begin to compromise the vacuum integrity regularly [37]. Above this, breakdowns limit operation and the input power and pulse length are gradually increased over time while monitoring for breakdowns either manually or algorithmically. This process is known as conditioning and typically follows three main stages, increasing the input power while maintaining a constant BDR, decreasing the power to increase the pulse length then ramping back up and finally operating at fixed conditions under which the BDR drops. These stages are visible in Figure 2.11 and generally require on the order of hundreds of millions of pulses. After having been subjected to this process an accelerating structure is then typically capable of reliable operation at high-gradient.

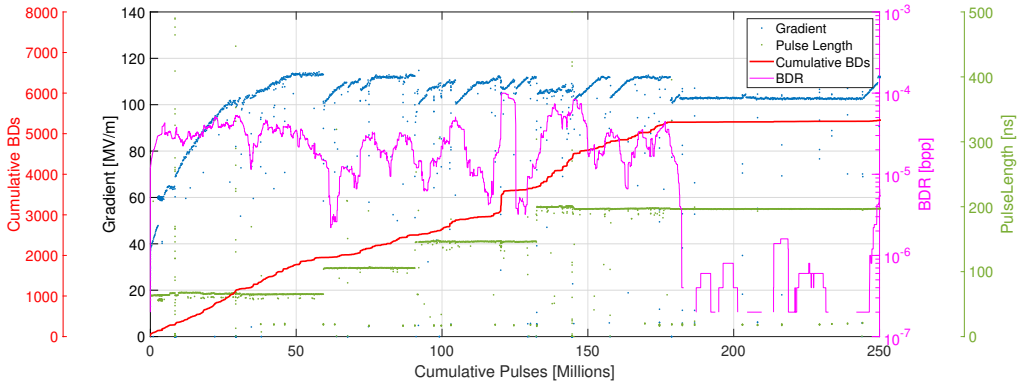

Fig. 2.11 The processing history of the T24 N2 structure tested in CERN's Xbox-2 test stand.

2.5.1 Evolution of Surface Properties during Conditioning

Historically, it was thought that breakdowns were the metric on which structures or high-power components conditioned, the accumulation of which being seen as a necessary process in the removal of surface defects or contaminants such as particulates and oxide layers on the surface. After all potential emission sites had been removed the component was then thought to be capable of operation at high power [37]. However, in 2015 it was noted that structures conditioned at different high-gradient test facilities often proceeded more comparably in pulses than in terms accumulated breakdowns and this is highlighted in Figure 2.12 [46]. This observation led to the proposal that structures then condition on the cumulative number of pulses and not the total number of accrued breakdowns [46].

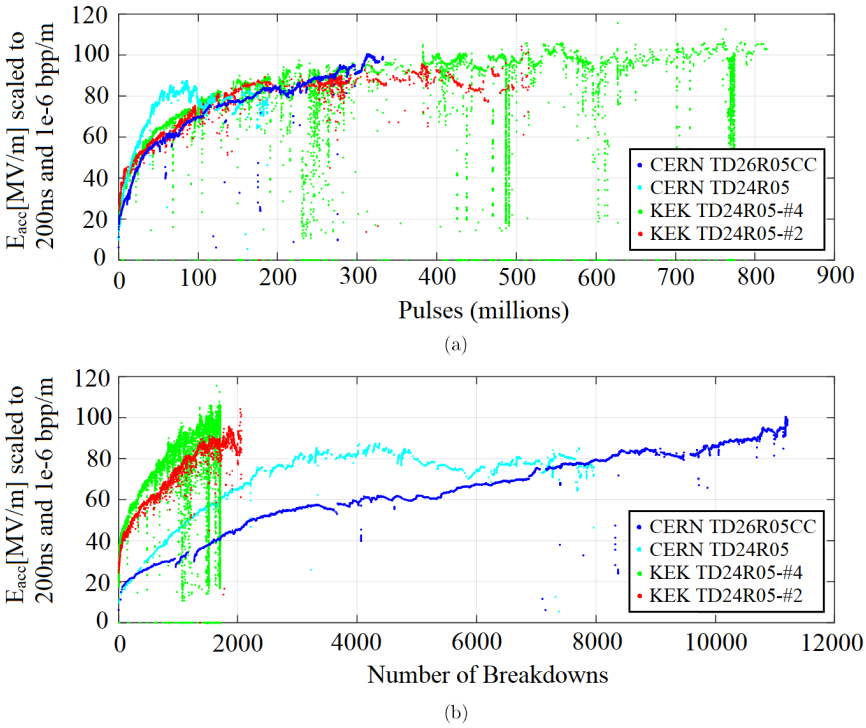

Fig. 2.12 Conditioning curves of a TD26CC (blue) and TD24R05 (cyan) tested in CERN's Xbox-1 test, and two TD24R05s (red and green) tested at NEXTEF showing the accelerating gradient scaled to a pulse length of 200 ns and a BDR of 1×10^{-6} bpp/m plotted against the cumulative number of RF pulses (a) and breakdowns (b) [46]. Image axes have been rescaled for improved readability.

It has also been noted that the handling of a structure prior to installation may contribute to such discrepancies in the accumulated breakdowns during conditioning. In 2010 two identical structures were conditioned at SLAC, one was built processed

and hermetically sealed at KEK then assembled at SLAC under the best available conditions similar to those of superconducting cavities while the other was subject to conventional methods [90]. The test results for each structure are compared in Figure 2.13.

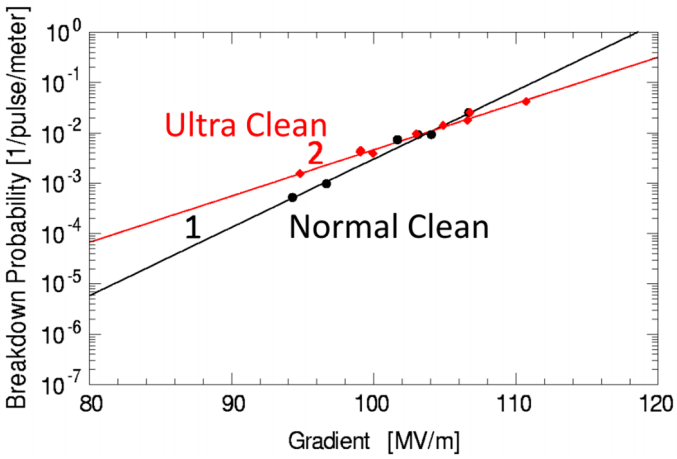

Fig. 2.13 Comparison of the breakdown probabilities for two accelerating structures, one prepared via conventional methods (normal clean) and one prepared under conditions similar to those implemented in the preparation of superconducting cavities (ultra clean) at SLAC [90].

The ultra-clean structure was conditioned over 2.4×10^5 pulses and 260 breakdowns while the latter was conditioned over 5×10^5 RF pulses and accumulated approximately 2000 breakdowns. These results suggest that breakdowns can serve to vaporise small defects acting as emission sites however once again the structures proceeded much more comparably in terms of pulses as opposed to breakdowns where they varied by an order of magnitude. Additionally, the discrepancy in pulses may be a result of the more frequent breakdowns slowing the rate at which the power was increased during conditioning. The test did however demonstrate that the ultimate gradient reached was not significantly affected by the handling techniques.

Experimental data has consistently shown that conditioning results in a modification of the surface properties of the material, namely an increased propensity for the establishment of high electric fields or an increased resistance to breakdown. However, the mechanism through which characteristic is obtained is not immediately apparent. To shed light on this, transmission electron microscopy images of a cross section of the surface of a conditioned copper cavity were taken in 2017 and compared to other copper samples. The cavity surface showed interlocked dislocation patterns identical to those associated with work hardening and an example of this work is shown in

Figure 2.14 [91]. This result aligns well with the hypothesis described in Section 2.3.4 and the suggestion that cavities condition on the number of pulses as opposed to the number of breakdowns.

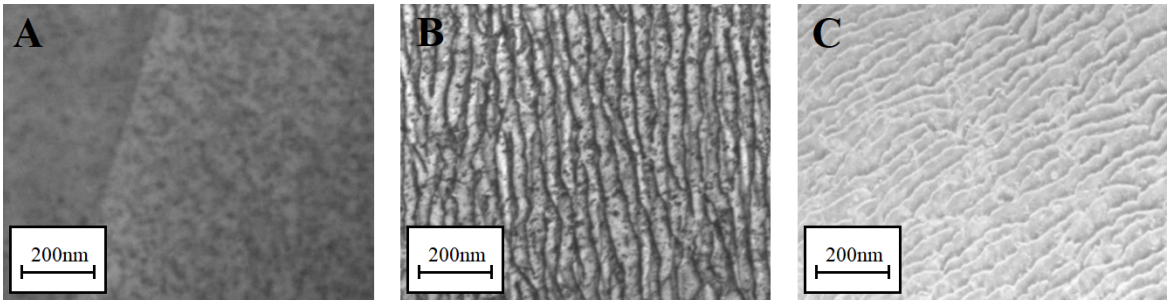

Fig. 2.14 TEM images of a copper sample (left),a work hardened sample (centre) and the surface of a copper cavity conditioned under RF pulses (right) [91]. Images have been rescaled for improved readability.

Finally, the ideal conditioning process has been shown in Figure 2.11 however it is occasionally necessary to deviate from the ideal case due to circumstances necessitating either a pause in operation or a change in the high-power waveguide network, exposing a structure to air during the conditioning. In such cases it has been shown that upon resumption of the test the structure is not immediately capable of operating at the previously achieved gradient without significant vacuum activity or breakdowns, however any previously achieved conditions are re-established in fewer pulses than were initially required and with fewer breakdowns [40, 92, 83]. This propensity for "reconditioning" agrees with the idea that some breakdowns aid in removing contaminants or oxide layers which may have migrated to the surface during exposure to air or the lack of RF. However, the ability to reestablish any previously achieved conditions more quickly indicates that a sustained modification of the properties of the material surface has nonetheless taken place.

2.5.2 Observations on Field Emission during Conditioning

As described in Section 2.1 the presence of a measurable current is also often observed in high-gradient structure tests and this current has been observed to evolve during conditioning. Due to its propensity for interaction with sensitive beam monitors, radiation production and its correlation with breakdown it is often a feature of interest in high-gradient facilities [40, 93, 38]. Figure 2.15 shows the test history of a T24 structure tested in Xbox-2 alongside the amplitude of the corresponding upstream and downstream Faraday cup signals. The amplitude of the emitted current sporadically

changes during testing and such changes typically coincide with breakdown events. Hence, it is postulated that sputtering from the plasma or the craters which form following breakdown events can produce new emission sites, altering the emission properties of the structure.

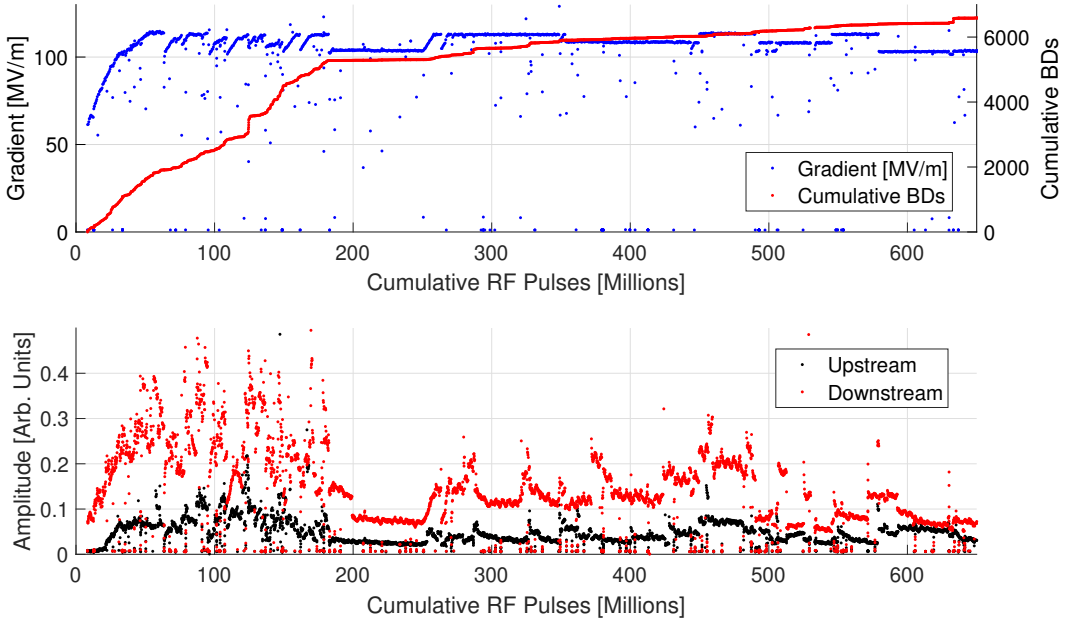

Fig. 2.15 Conditioning history of a T24 structure tested in Xbox-2. The top plot show the operating gradient and cumulative number of breakdowns plotted against pulse number. The bottom plot shows the evolution of the peak upstream and downstream Faraday cup signals during testing.

Additionally, the emission properties of structures have been resolved spatially. The high-gradient structures for CLIC have low group velocities typically on the order of 1%c and a fill time of approximately 60ns. Conversely, at gradients of 100MV/m any emitted current can reach relativistic energies within several millimetres meaning they propagate through the structure much faster than the RF pulse. By injecting an RF pulse much shorter than the fill time of the structure this effect may be exploited as the measured emission will be originate from only several cells at a time.

In 2019 it was shown by J. Paszkiewicz that a net reduction in the dark current occurs after many millions pulses and this can be seen by the bulk behaviour in Figure 2.15 [41]. However it is not yet clear if this is due to the removal of emission sites or simply a change in the emission properties. It should also be noted that this analysis found that the β value did not exhibit any clear evolution or dependence on

breakdowns, suggesting that the behaviour is instead dominated by a large number of similar field emitters whose population can vary as opposed to individual emission sites of varying aspect ratios. While no conclusion has yet been drawn, the results of the study indicated that either areas in which breakdowns regularly occur emit more current or that areas with significant emission preferentially nucleate breakdowns.

2.6 Conclusion

It is clear that breakdown is one of the key limiting phenomena in modern high-gradient accelerators and high field devices. Such events are capable of permanently altering the surface of the cavity and imparting a transverse kick on a passing bunches, resulting in a degradation of beam quality. A structure planned for operation at the gradient must then undergo conditioning process to decrease the probability of breakdown at a given gradient, typically requiring on the order of hundreds of millions of RF pulses. Doing so results in a sustained modification of the surface properties of the material and this, coupled with the reproducibility of the process implies the presence well defined underlying physical mechanism. To date, despite a wealth of experimental data neither the breakdown or conditioning phenomena have been satisfactorily predicted or explained although several models have emerged and both are areas of ongoing research.

Chapter 3

CERN's High-Gradient Test Facility

High-gradient operation poses a number of challenges which warrant investigation if widespread implementation of the technology is to become practicable and for this purpose several test facilities have been constructed worldwide [37, 94–96]. To research the breakdown and conditioning phenomena and test the novel RF components for the CLIC project, CERN has commissioned three klystron based test stands coined Xbox-1, Xbox-2 and Xbox-3 respectively [97]. The proposed CLIC RF frequency is 11.9942 GHz and so the test stands derive their name from the corresponding 8-12 GHz Institute of Electrical and Electronics Engineers (IEEE) frequency band in which they operate [98]. As much of the work presented in this thesis takes place in CERN's Xbox-2 test stand particular attention will be paid to this facility and the key design features are outlined following.

3.1 High-Power RF Generation

Xbox-2 is the second test stand to operate at CERN, constructed in 2014 following the success of the Xbox-1 experiment in order increase the number of test slots and subsequent component throughput [37]. In the test stand a Low-Level Radio Frequency (LLRF) signal is passed to a solid state amplifier capable of amplification up to several hundred watts. The output of this amplifier is then fed to the input cavity of a klystron to produce a high-power RF signal which is directed via waveguide to the device under test (DUT) inside a shielded bunker. Figure 3.1 shows the exterior of the Xbox-2 and 3 test bunker and several structures installed within.

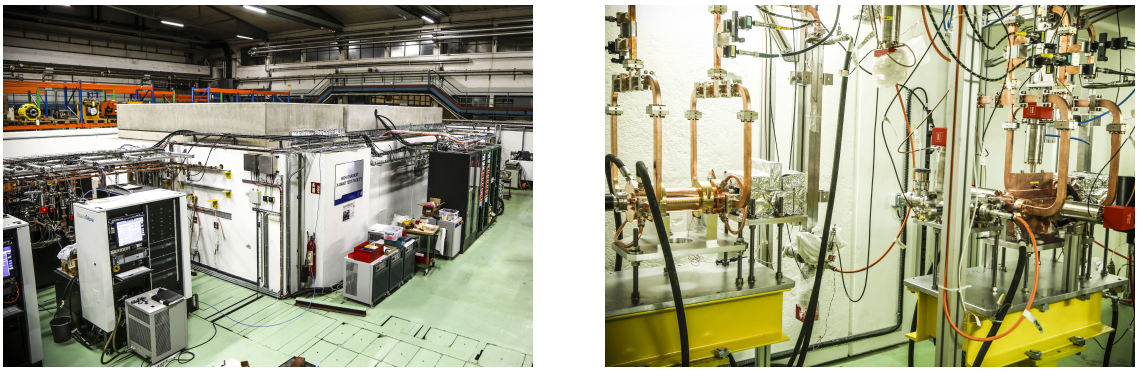

(a) (b)

Fig. 3.1 The exterior of CERN's high-gradient test facility (a) located in building 354 at CERN and two structures installed in the Xbox-3 test slots inside the bunker (b).

3.1.1 Klystron and Modulator

The high-power RF in the test stand is provided by a klystron, a type of RF amplifier which relies on the velocity modulation of an electron beam to amplify low-level signals. Typically, electrons are emitted by a thermionic cathode and accelerated by a high DC voltage in a vacuum tube. The beam is velocity modulated as it passes through one or several RF cavities excited by a LLRF input signal. While the electrons travel through the drift tube they begin to bunch and a longitudinal variation in charge density forms, the period of which matches that of the LLRF input signal. The bunched beam then passes through the extraction or "catcher" cavity where a significant portion of the energy is then extracted as an electromagnetic field, typically via waveguide. A diagram of the process is shown in Figure 3.2

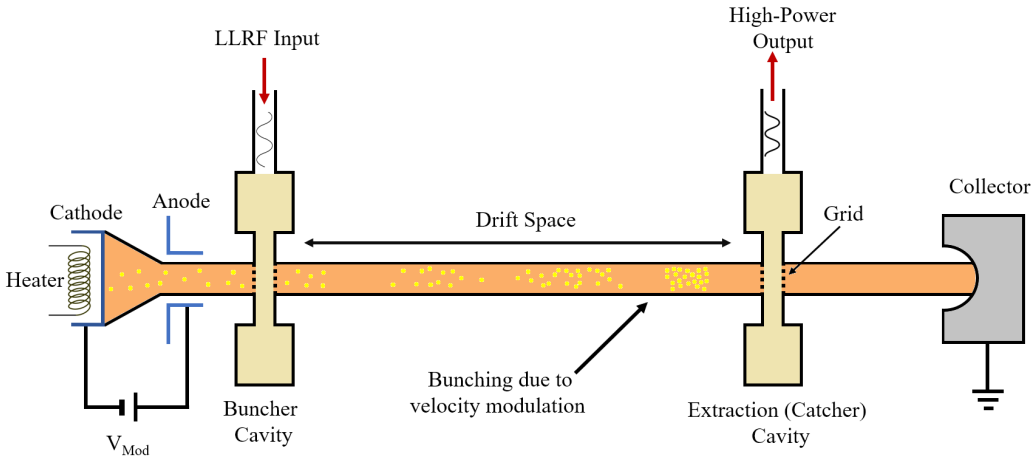

Fig. 3.2 Diagram showing the working principle of a klystron.

The first klystron was invented in 1937 by Russel and Sigurd Varian [99] and in modern commercial models beam to RF efficiencies of 30-65% are common. However novel designs capable of reaching efficiencies of up to 90% also exist, making use the core oscillation method (COM) of electron bunching or indeed higher order cavities [100, 101]. Xbox-2 uses the CPI VKX-8311A model 12GHz klystron which is capable of producing a 1.5μs 50MW RF pulse at 50Hz. The high-voltage DC pulses are provided by a Scandinova K-3 modulator which utilises a four-stage pulse forming scheme comprised of a capacitive charging power supply (CCPS), a switching network, a transformer and a tuning circuit.

3.1.2 Pulse Compressor

When operating klystrons it is generally easier and more cost efficient to construct a modulator capable of long, low-voltage pulses than one capable of producing short, high-voltage ones. As such, CERN's X-band test stands increase their peak RF power capability via a technique known as pulse compression. The first pulse compressor, coined the SLAC Energy Doubler (SLED) and now commonly referred to as the SLED-I, was invented in 1974 and consists of two heavily over-coupled RF cavities with high intrinsic quality factors connected via a 3dB 90° hybrid coupler as shown in Figure 3.3. Although the cavities themselves have been redesigned and appropriately re-scaled for use at X-band, the pulse compressor in use at Xbox-2 is principally of the same design.

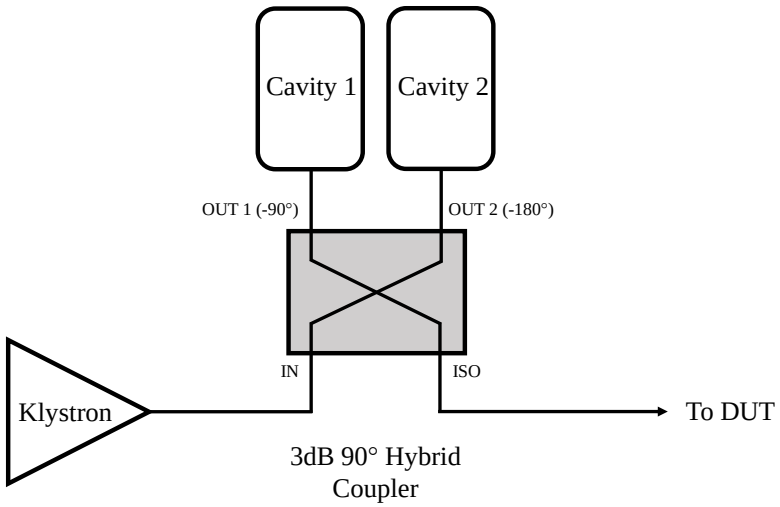

Fig. 3.3 Diagram of a SLED-I type pulse compressor.

The 3 dB hybrid coupler is a commonly used four-port device which equally splits an input signal between two output ports with a 90° phase shift between them, and a

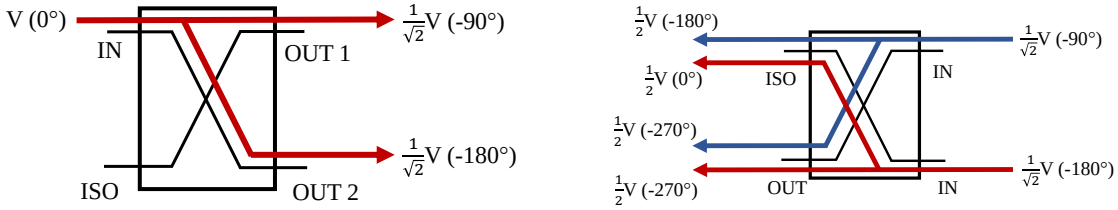

(a) (b)

Fig. 3.4 Diagram showing the operation of a 3dB hybrid in a pulse compressor. When a wave of amplitude V is introduced at the input, half the power i.e 3dB (corresponding to $\frac{1}{\sqrt{2}}$ times the voltage) is transmitted to outputs 1 and 2 with a phase shift. When a wave returns from the cavities, the process is repeated leading to complete destructive interference at the source, and all of the power being directed towards the fourth port.

high-power waveguide variant has been designed specifically for CERN's X-band test stands [102]. In the SLED-I pulse compressor, the inclusion of the hybrid means each cavity is filled with a 90° phase difference. Nominally, each cavity is identical and so by virtue of the hybrid design, any reflections from the cavities will then destructively interfere at port one and are directed entirely to port four. The process is illustrated in Figure 3.4 and this is the reason two cavities are necessary.

Each cavity is heavily over-coupled and so at the commencement of the RF pulse virtually all of the incoming power is reflected, with only a small amount entering the cavities. Simultaneously, each cavity then begins to emit a wave which can be defined relative to the klystron amplitude as [103, 104]:

$$E_{out}(t) = \frac{E_{klys}}{\sqrt{2}}\left[\frac{2\beta}{1+\beta}(1-e^{-t/t_c})-1\right] \tag{3.1}$$

Where β is the coupling factor as described in Equation 1.63 and t_c is the time constant of the cavity, calculated as:

$$t_c = \frac{2Q_0}{\omega(1+\beta)} \tag{3.2}$$

During the filling process, the total energy stored in each cavity (U_{Cavity}) steadily grows, and relative to the amplitude of the klystron pulse this energy can be calculated as a function of β as:

$$U_{Cavity} = t_c \frac{P_{klys}}{2} \frac{2\beta}{1+\beta}(1 - e^{-t/t_c})^2 \tag{3.3}$$

It can be seen then, that over a long time frame both the power to the structure and the stored energy in the SLED cavity will then tend towards a steady state solution. However, a more interesting effect occurs during dynamic changes in the klystron pulse. The second term on the right hand side of equation 3.1 refers to the reflected portion of the klystron pulse; if the incoming pulse ceases then the amplitude of the wave emitted from the cavities then instantaneously exceeds that of the klystron pulse as cancellation with the reflected wave no longer occurs. This instantaneous gain (G) may be calculated from β as:

$$G = \frac{2\beta}{1+\beta} \tag{3.4}$$

For large values of β, and hence heavily over-coupled cavities this value tends towards 2. However it this may be exploited further by modulating the phase of the incoming klystron pulse. If the klystron phase shifts quickly by 180° at time, t_{flip}, the reflected klystron pulse then constructively interferes with the emitted waves, meaning that the maximum possible amplitude is now instantaneously three times that of the klystron pulse and nine times the power.

$$E_{out}(t) = \frac{E_{klys}}{\sqrt{2}} \left[\frac{2\beta_{SLED}}{1+\beta_{SLED}}(1 - e^{-t_{flip}/t_c}) + 1 \right] \tag{3.5}$$

If for example, the klystron pulse commences at time, t=0 and the phase is flipped at time, $t_1 = 1\mu s$ before cessation of the pulse at $t_2 = 2\mu s$ the output for each region can be defined separately in terms of the reflected and emitted waves as:

$$\begin{aligned} E_{out}(t) &= \frac{E_{klys}}{\sqrt{2}} \frac{2\beta_{SLED}}{1+\beta_{SLED}}(1 - e^{-t/t_c}) - 1, && t \le t_1 \\ &= \frac{E_{klys}}{\sqrt{2}} \frac{2\beta_{SLED}}{1+\beta_{SLED}} \left[(2 - e^{-t_1/t_c}) e^{-(t-t_1)/t_c} - 1 \right] + 1, && t_1 < t \le t_2 \\ &= \frac{E_{klys}}{\sqrt{2}} \frac{2\beta_{SLED}}{1+\beta_{SLED}} \left[(2 - e^{-t_1/t_c}) e^{-(t_2-t_1)/t_c} - 1 \right] e^{-(t-t_2)/t_c}, && t > t_2 \end{aligned} \tag{3.6}$$

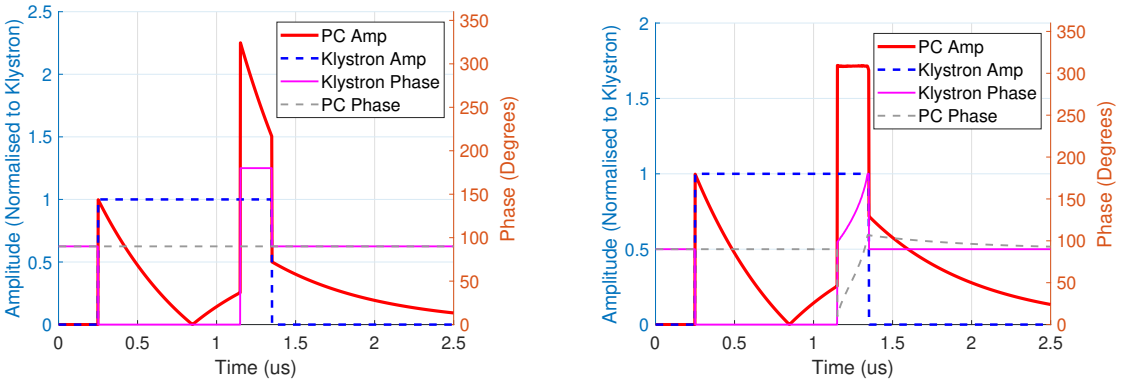

Fig. 3.5 Simulation of a pulse compressor with β=6 and $Q_0 = 1.8 \times 10^5$ showing the exponential decay resulting from operation with a fixed 180° phase flip (a) and a pulse with a flat top region achieved via phase modulation of the klystron pulse (b).

Use in this manner results in n pulse of exponentially decaying amplitude, however it is often desirable to have a pulse of fixed amplitude or phase for several hundred nanoseconds. At the expense of peak power, this is possible via phase or amplitude modulation of the klystron pulse [105]. Figure 3.5 shows a simulation of two modes of operation, one making use of a simple fixed phase flip and one using phase and amplitude modulation to provide a region which is constant in amplitude and phase.

The SLED cavities in use at Xbox-2 have a Q_0 of approximately 1.8×10^5 [37, 105]. As the klystron is capable of of delivering a $1.5\mu s$ pulse, the Q_{ext} was then set to 3×10^4 to allow filling of the cavity within the RF pulse length [105]. Figure 3.6 shows Xbox-2 modulator and klystron enclosure and the pulse compressor situated behind them.

3.2 Low-Level RF System

Controlling RF signals directly at high power is typically difficult and impractical, instead it is common to perform the necessary manipulation at low power via the use of a low-level radio frequency (LLRF) system. In the case of Xbox-2 this is comprised of a signal generation scheme and acquisition system, both of which are detailed following.

3.2.1 LLRF Generation

As described in Section 3.1.2, pulse compressor operation requires a phase modulated input pulse. As producing a modulated 12 GHz signal directly was not feasible, an up-conversion based scheme was implemented using a National Instruments NI-5793

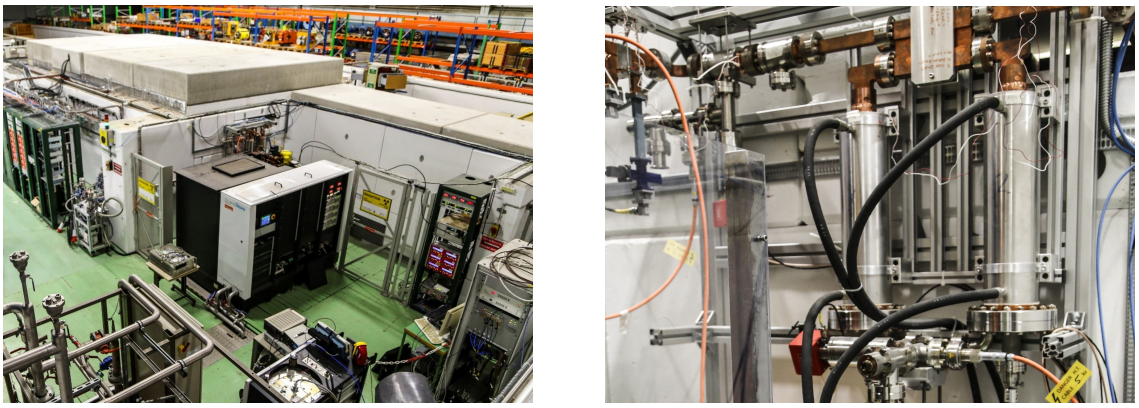

(a) (b)

Fig. 3.6 The Xbox-2 modulator and klystron enclosure located outside the test bunker (a) and the SLED-I pulse compressor situated on the bunker wall within the enclosure (b).

card. The card can accept or produce signals from 200 MHz to 4.4 GHz with a bandwidth of 200 MHz. To provide the modulation, the RF channel is split via a hybrid to produce two signals with a 90° relative phase shift. Each is then mixed with the output of a DAC to produce the in-phase and quadrature components which are then combined at to produce the desired modulation. Figure 3.7 shows a schematic of the operation.

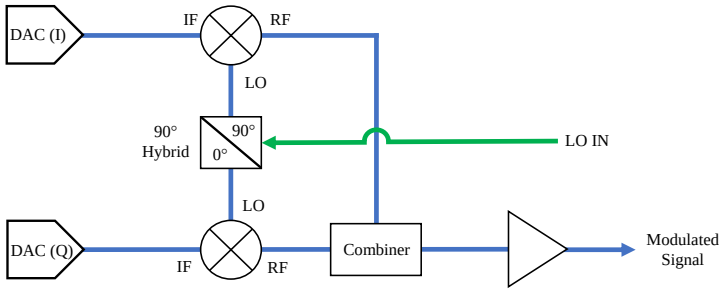

Fig. 3.7 Diagram showing how modulated signals are produced within the NI-5793 card.

In the Xbox-2 generation scheme, the output of a 2.4 GHz phase locked loop (PLL) which is locked to the PXI crates 10 MHz internal reference is amplified and split two ways. The first output is fed into a frequency multiplier and filtered to provide a clean 9.6 GHz signal for up-mixing later. The second output is amplified, filtered and once again split, with one portion being mixed directly with the 9.6 GHZ signal to provide a reference signal and the other being fed into the NI-5793 card for modulation. The

modulated 2.4 GHz signal is then mixed with the output of a frequency quadrupler to produce the modulated 12 GHz pulse which is sent to the SSA via coaxial cable, amplified to the kW level, and used to drive the klystron. As mixing produces generates components at both the sum and difference of the input signals, 12 GHz band-pass filters are also present prior to further amplification to remove the 7.2 GHz component. The full schematic is shown in Figure 3.8.

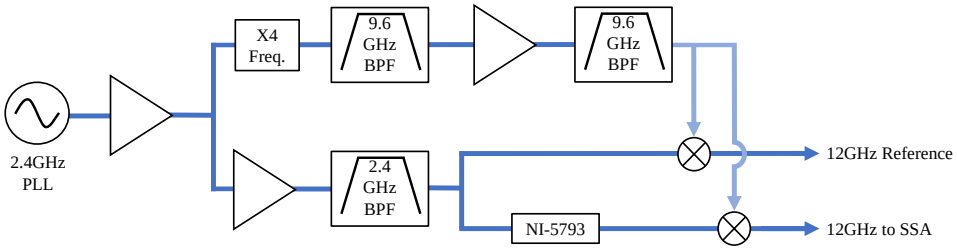

Fig. 3.8 The current Xbox-2 up-conversion scheme.

It should be noted that the output of the PLL and hence, the 9.6 GHz signal remains fixed in amplitude at all times and so the dynamic range of the LLRF pulse is controlled exclusively by the modulated 2.4 GHz output of the NI-5793.

3.2.2 Signal Acquisition

To monitor the system behaviour is it necessary to acquire the phase and amplitude of the incoming signal either by sampling directly or by reconstructive means and in Xbox-2 this is accomplished in two ways. Given the multiple channels of interest it is also convenient assign a signal naming convention and the nomenclature for this is shown in Table 3.1:

High-power directional couplers act as the interface between the high-power RF network which is held under vacuum and the acquisition system which samples the signals at low power. Two small circular coupling slots in the side of the waveguide allow a small amount of the RF power to enter the coupling section which is open to air. Ceramic inserts in the slots act as RF windows and maintain vacuum integrity in the rest of the network. Figure 3.9 shows a cross section of the mechanical design. The design generally has -60dB of coupling, where the coupling is defined as the portion of the incoming high-power RF signal which reaches the corresponding measurement port. A small portion of the incoming high-power RF does however reach the opposite measurement port too, this quantity is known as the directivity and is generally on

Channel Name	Signal Description
PKI	Klystron output
PKR	Reflection to klystron
PSI	Structure incident.
PSR	Reflection from structure
PEI	Load incident/Output of structure
PER	Reflection from load

Table 3.1 Nomenclature for the forward and reflected signals sampled at each directional coupler in Xbox-2.

the order of -30dB. Isolators and waveguide to coaxial adaptors are connected to each coupler to provide an interface for the 50 Ω coaxial cables which run from the bunker to the PXI card performing the sampling.

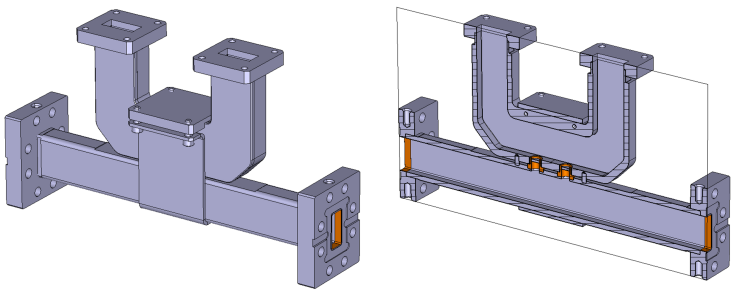

Fig. 3.9 CAD model of an X-Band 60dB direction coupler showing external geometry (left) and internal geometry with coupling slots (right).

Due to the high bandwidth and sampling speed requirements it is impractical to directly sample a 12 GHz signal; hence, where high resolution is required a down-mixing scheme is in use. A 2.9 GHz signal is provided by a PLL which is locked to the PXI crates 10 MHz internal reference. This is then quadrupled to provide an 11.6 GHz signal which may be mixed with the incoming 12 GHz RF to provide the 400 MHz Intermediate Frequency (IF) as shown in Figure 3.10.

The 400 MHz IF is then sampled by an NI 5772 card. Each card has two channels capable of sampling at 800MS/s each with a resolution of 12 bits however at Xbox-2 these inputs are interleaved to sample a single signal at 1.6GS/s, equating to four samples per cycle. In an IQ modulation and demodulation scheme the instantaneous voltage of any arbitrary signal can be written:

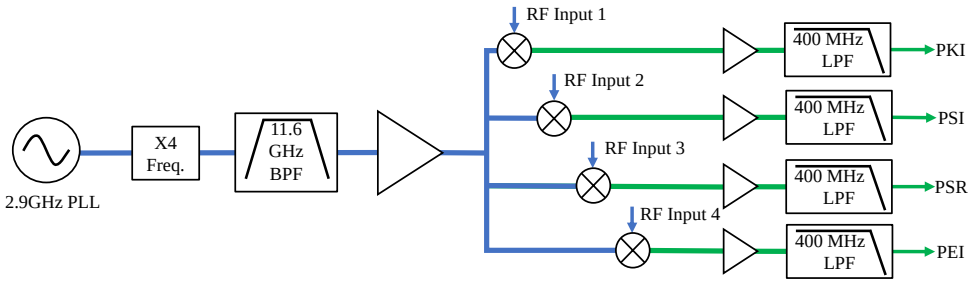

Fig. 3.10 The current Xbox-2 down-mixing scheme.

$$V_{inst}(t) = \mathrm{Re}[(I + jQ)e^{j\omega(t)}] \tag{3.7}$$

The amplitude and phase of the signal may then be recovered via basic trigonometric functions as $\sqrt{I(t)^2 + Q(t)^2}$ and $\tan\left(\frac{Q(t)}{I(t)}\right)$ respectively. However, when four times oversampling is used and synchronism is maintained the delta phase, φ, between samples becomes exactly 90°. In this special case Equation 3.7 may then be rewritten as:

$$V_{inst}(t) = \mathrm{Re}[(I + jQ)e^{jn\varphi}] \tag{3.8}$$

Where n = 0, 1, 2... and so the sampled instantaneous voltages equate to I, Q, -I and -Q in cyclic fashion. This also means no trigonometry is necessary to retrieve the I and Q components and thus the operation is well suited to being performed on an FPGA, as is the case in Xbox-2. Due to limited slot availability within the PXI chassis and cost constraints, it is not practicable nor is it necessary to implement this scheme for all RF channels. As such, channels which are of less interest in a conditioning context though still important for safety and interlocking (PER, PKR) are converted to a scaled DC voltage via the use of a log detector and sampled at 250MS/s by NI 5761 cards with 14-bits of resolution. An overview of the complete arrangement is shown in Figure 3.11.

3.3 Test Stand Operation

To interface with the PXI chassis and operate the test stand, custom software based on the LabVIEW programming language has been developed at CERN [37]. A real-

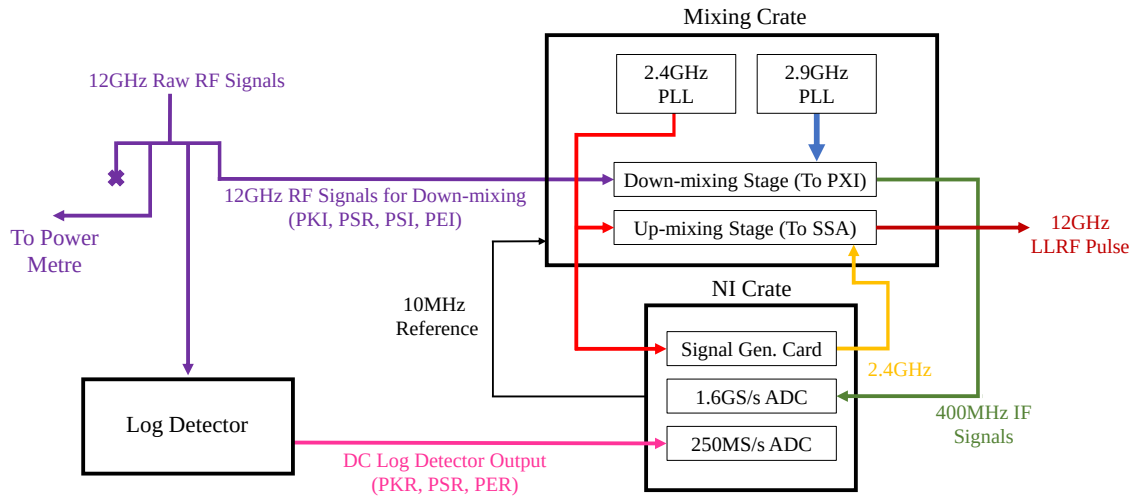

Fig. 3.11 Block diagram of the Xbox-2 LLRF system.

time program with several deterministic timing requirements runs locally on the CPU housed within the PXI chassis. A separate programme then runs on a PC, providing the operator with a GUI to monitor the signals and communicate directly with the chassis via ethernet cable. As mentioned in Section 2.5, high-gradient structures must undergo conditioning, and this is one of the key objectives of the Xboxes. To date, two main methods of doing so have emerged, conditioning on vacuum and conditioning on BDR. Each process is outlined following however a detailed overview is available elsewhere [37].

3.3.1 Vacuum Conditioning

For new components, typically vacuum tends to be the limiting factor when trying to increase in power in two ways. First, a globally raised vacuum level when RF is switched on and the second is the discrete release of gas which causes a sharp spike in vacuum levels as pictured in Figure 3.12.

The latter are prone to tripping the systems protective interlocks, particularly when the internal pressure is high throughout the system. In this case vacuum conditioning is preferred until the internal pressure improves and breakdowns become the limit on ramping to higher power. This is accomplished via a PID loop which takes the current pressure level as the process variable and the RF power level as the input variable. The system will then automatically increase or decrease the power with the objective of keeping the system pressure at a fixed user defined setpoint. Typically vacuum

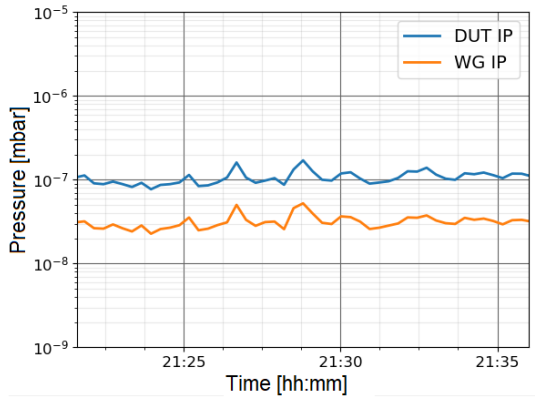

(a) Elevated vacuum levels shortly after commencing a new test as monitored by Ion pumps situated on the structure input (DUT IP) and the waveguide network approximately 1 metre prior (WG IP)

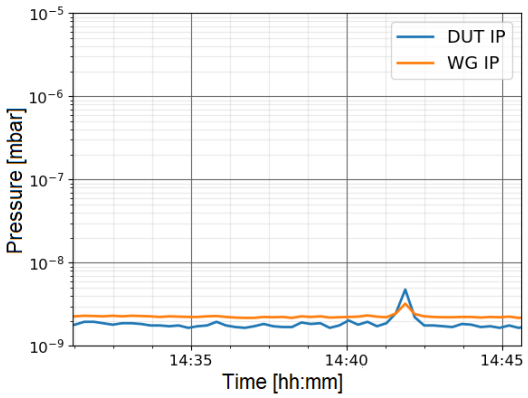

(b) Vacuum levels after several days of operation showing a small non-BD event inside the structure as monitored by ion pumps situated on the structure input (DUT IP) and the waveguide network approximately 1 metre prior (WG IP).

Fig. 3.12 Vacuum plots showing globally elevated but stable vacuum levels associated with the first high-power RF in a recently installed structure and a small non-BD outgassing event occurring several days into testing after vacuum levels have dropped.

setpoints in the range of 1×10^{-8} to 1×10^{-7} mbar are chosen for vacuum conditioning while the systems protective interlocks are set at 6×10^{-5} mbar .

3.3.2 Breakdown Rate Conditioning

Typically, after several days of operation the pressure drops to the 1×10^{-9} mbar range and the system is capable of reliably operating with RF pulses on the order of several megawatts. At this point, breakdowns begin to occur regularly and so conditioning on BDR is the preferred. In the Xbox test stands conditioning has been largely automated, facilitating 24/7 operation without the need for constant staffing [37, 106]. In Xbox-2 this algorithm is comprised of a two-stage hierarchy which monitors both the short term and long-term behaviour of the DUT. A graphical representation of this algorithm as displayed on the GUI is shown in Figure 3.13 below.

The red line scrolls to the right in real time and when it reaches the step shown in blue (at approximately 180 seconds in Figure 3.13) the power is instantaneously increased by 10kW and the position of the red line is then reset to 0. The time required for this step to be implemented is user-configurable however in Xbox-2 a cycle on the order of 10-15 thousand pulses, or 3-5 minutes at 50 Hz is typical. If a breakdown occurs soon after a step up in power, the power will be decreased by the an amount

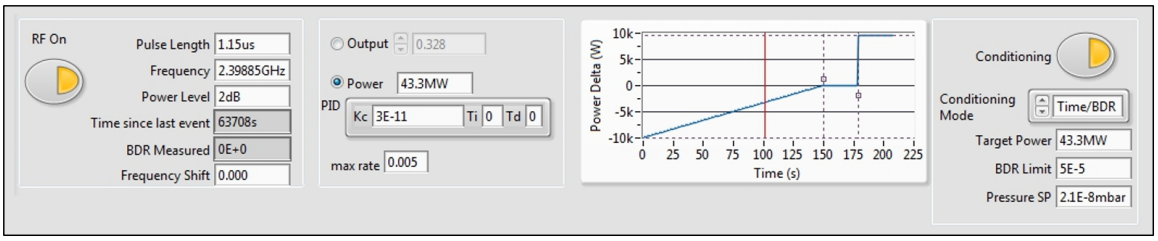

Fig. 3.13 Graphical representation of the conditioning algorithm as shown on the Xbox-2 GUI.

determined by the position of the red line. If a breakdown were to occur while the line was positioned as it is in Figure 3.13, the power would be reduced by approximately 3kW. Alternatively, if a breakdown were to occur immediately after the step up in power while the red line is positioned at time, t=0, the power would be decreased by the full 10kW. This feature then acts to increase or decrease the power based on the immediate behaviour of the structure. The second facet of the algorithm controls the long-term behaviour by monitoring a user-configurable BDR calculated as:

$$\text{BDR} = \frac{\text{No. of Breakdowns}}{\text{No. of RF Pulses in User-Defined Window}} \tag{3.9}$$

In the event that the instantaneous BDR is higher than the conditioning setpoint, the power cannot be increased. However, it should be noted that the power can still be decreased by subsequent breakdowns, depending on the position of the red line. When the BDR drops to a value below the setpoint, the steps in power will then resume. The chosen value for the calculation window is a compromise between response speed and dynamic range, and typical values range from 5×10^5 to 1×10^6 pulses to provide reasonable BDR tracking in the 10^{-6} bpp range.

3.4 Conclusion

To date the Xbox-2 test stand has successfully conditioned many prototype high-gradient accelerating structures and novel high-power RF components [37, 40, 46]. An overview of the Xbox-2 test stand at CERN has been provided and its key features have been described in preparation for the discussion of several upgrades which were implemented to facilitate the test of multiple structures simultaneously. As one of the primary purposes of the test stand is to investigate the breakdown and conditioning phenomena, both the acquisition system and the manner in which the data is logged

for future analysis have been detailed. Initially at CERN, high-gradient conditioning was performed manually. To increase component throughput and the reproducibility of tests, the process has since been automated via the implementation of a conditioning algorithm [37]. At the time of writing this algorithm is still in use and has since become standard practice in all of CERN's high-gradient test stands [106].

Chapter 4

Expansion of an X-Band Test Stand

Typically in modern high-gradient facilities, long multi-structure arrangements are necessary and so it is desirable to position structures close together to maximise the effective gradient. In CLIC, the main LINAC is comprised of superstructures, each superstructure being composed of two TD26CC accelerating structures aligned and bonded together for this purpose [33]. While the Xbox test stands have high-power tested many individual components a dual structure arrangement has not yet been conditioned to the full design gradient and pulse length.

To test two structures, the energy in the RF pulse must be doubled. Any reflected waves from breakdowns are then not only capable of interacting with the neighbouring structure, but of constructive interference resulting in local power flow and peak surface electric fields far beyond those established in previous tests. In a multi-structure arrangement, there is also an increased propensity for dark current emission and capture. Additionally, the test will shed light on the viability of conditioning multiple structures in-situ via a single power source, an important consideration in high-gradient facilities. To investigate these phenomena and meet the validation requirements for CLIC, a superstructure is scheduled for installation and testing in the Xbox-2 test stand. The following chapter provides an overview of the design, implementation and commissioning of all modifications necessary for a dual structure test.

4.1 LLRF System Upgrade

Xbox-2 is equipped with of all diagnostic capabilities necessary for a conventional single accelerating structure test. However in a multi-structure arrangement each structure must be monitored and hence additional acquisition channels are required. An example of a potential installation arrangement is shown in Figure 4.1. Additionally, a new pulse

compression scheme, a polarisable transverse deflecting structure and several other novel RF components which would benefit from such an upgrade are also scheduled for testing.

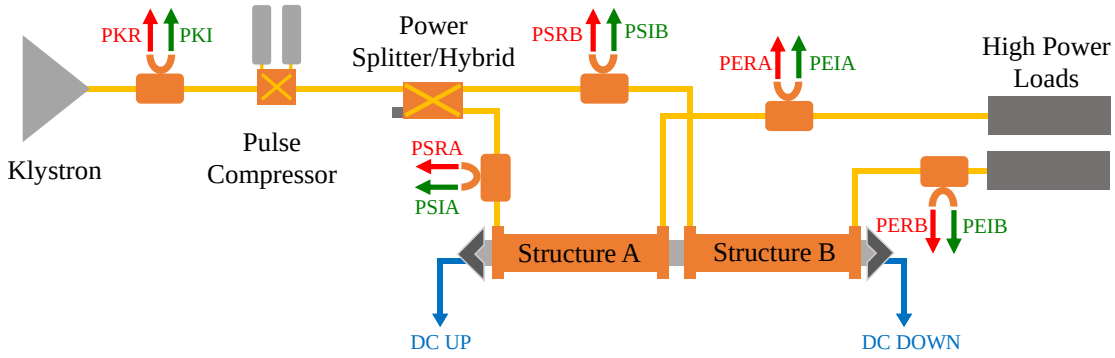

Fig. 4.1 Diagram of an example dual structure test arrangement.

4.1.1 System Requirements

Given the proven track record of the existing PXI based infrastructure it was decided that the system would be reused and expanded upon to accommodate the additional channels. Due to constraints in cost and the number of remaining acquisition card slots available in the PXI chassis it was not possible to simply duplicate the existing channels and so a partial redesign of the LLRF system was deemed necessary.

In 2019, Texas Instruments announced 12-bit ADC, the ADC12DJ5200RF, with a sampling rate of up to 10.4 GS/s and a bandwidth of 8 GHz which was marketed towards 5G testing applications and X-band sampling for radar applications [107]. As this is amongst the fastest ADCs on the market it is clear that it is still not practicable to sample the 12 GHz signals associated with CLIC structures directly with commercial hardware. Instead, a down-mixing scheme as is currently implemented must be used to recover the phase and amplitude information of the 12 GHz signals from an IF. Doing this for all channels is costly and increases system complexity so it is preferable to do so only where deemed necessary.

Waveform analysis via PEI and PSR facilitate breakdown localisation while PSI is essential for accurate inference of the power, pulse length and flatness of the pulse being sent to the structure. Additionally, it is important to accurately monitor the power and pulse shape of the klystron pulse, PKI. The addition of three additional down-mixed channels to the existing LLRF system is then necessary to monitor the

incident, reflected and transmitted signals of the second structure. Several new interlock channels are also required however as these as not typically of interest in terms of analysis the requirements may be relaxed. With this in mind a list of channels required from the LLRF system was formulated based on the resolution requirements as shown in Table 4.1.

IQ Demodulation Required		**IQ Demodulation Not Required**	
Description	Signal	Description	Signal
Klystron Incident	PKI	Reflection to Klystron (Log)	PKR Log
Structure A Incident	PSIA	Load A Reflection (Log)	PERA Log
Structure A Reflected	PSRA	Load B Reflection (Log)	PERB Log
Structure A Transmitted	PEIA	Structure A Reflected (Log)	PSRA Log
Structure B Incident	PSIB	Structure B Reflected (Log)	PSRB Log
Structure B Reflected	PSRB	Upstream Faraday Cup	DC UP
Structure B Transmitted	PEIB	Downstream Faraday Cup	DC DOWN

Table 4.1 Signals to be monitored on a pulse-to-pulse basis in Xbox-2 when running two structures simultaneously. Note that the structure reflections appear twice, this is because while a direct feed is necessary for IQ demodulation the signal must also be split and sent to a log detector for hardware interlocking.

For the RF generation the currently implemented scheme is comprised of a 2.4 GHz PLL which is fed into a two-way splitter. One output is quadrupled to produce 9.6 GHz and the other is sent to the PXI crate for modulation before being mixed with the 9.6 GHz to produce the 12 GHz pulse for amplification as shown previously in Figure 3.8. To date this scheme has an excellent track record and provides pulses of low harmonic content sufficient for klystron amplification and so modification was not deemed necessary [37].

In addition to the RF channels required, upgrades to the vacuum and temperature controls are also necessary. Due to the planned insertion of a second structure and other additional components the internal volume will increase significantly and several new ion pumps will be required. Similarly, it is important to monitor the temperature of any additional high-power components. Although expansion is necessary temperature and vacuum fluctuations are comparably long timescale phenomena and so do not require infrastructure of the same complexity of the LLRF system. Instead the outputs may sampled directly by most modern ADCs.

4.1.2 New Down-Conversion Scheme

The signals previously of interest in terms of breakdown data analysis are PKI, PSI, PSR and PEI and for demodulation of each of these channels an NI-5772 card is used. Each card contains a high-speed digitiser that can simultaneously sample two channels at 800 MS/s or sample one channel at 1.6 GS/s, the latter configuration being the one currently in use to over sample the 400 MHz IF. It was not possible to add three additional cards and FPGA modules nor was it feasible to purchase and install an additional chassis. Instead, the decision was made to use the existing four cards without interleaving the inputs, instead providing eight analogue inputs at 800 MS/s and an 800 MHz bandwidth. The sample rate will then be halved, providing a point-to-point resolution of 1.25ns. Though as this is still shorter than the fill time of the first cell in CLIC structures cell to cell resolution during breakdown localisation is still possible, particularly when combined with the phase information.

This configuration would facilitate acquisition of all seven signals of interest in addition to a spare which may be used as a reference channel at no additional cost. However, a new IF of 200 MHz is required to facilitate the use of the previously described IQ demodulation scheme and to avoid operating at the Nyquist limit. The up-conversion scheme itself may remain unchanged however due to space constraints in the rack the scheme must either be duplicated or rearranged for installation in a new crate. In order to minimise cost the latter approach was chosen.

To down-mix the RF to 200 MHz, a method of generating an 11.8 GHz signal is required. One method of doing so would be to implement a 2.95 GHz PLL and use a 4× frequency multiplier to produce an output at the fourth harmonic which can be mixed with the incoming RF signals. Alternatively, the signal may be generated directly through the use of a synthesizer. A QuickSyn FSW-0020 synthesizer with a range of 0.5 to 20 GHz was available at CERN and so the latter approach was selected. A devices phase noise i.e. the frequency-domain representation of random fluctuations in a given signals phase can be measured using a spectrum analyser provided the phase noise of the spectrum analyser's local oscillator is small in comparison. A phase noise measurement was then taken with a Rohde & Schwarz FSW26 to verify the device's performance and compared with the manufacturer datasheet. The results are shown in Figure 4.2.

Up to a 1 kHz offset the measured value actually outperforms the datasheet values by 1-2dB. However a discrepancy in the form of a peak is present between 100 kHz and 1 MHz. At its maximum it exceeded the expected value by 6dBc/Hz however as it is still under -110 dBc/Hz it was deemed fit for use. The device may be locked to a 10

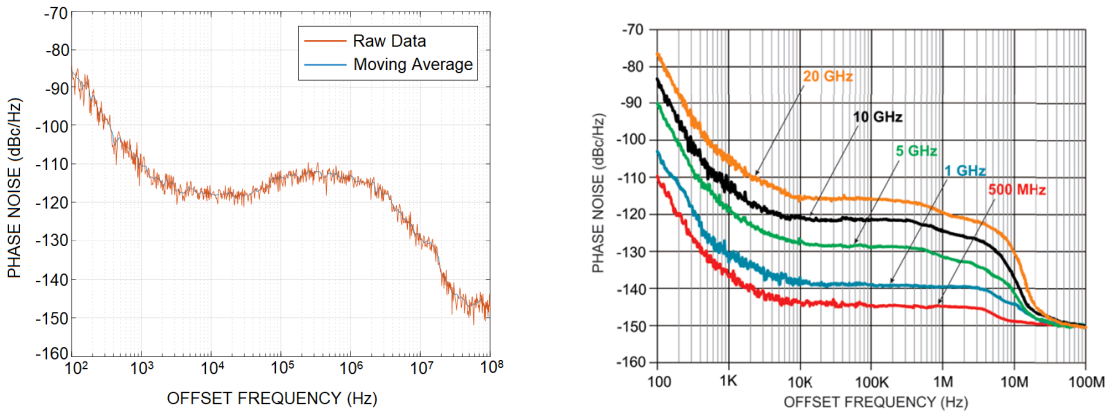

(a) (b)

Fig. 4.2 The measured phase noise of the QuickSyn FSW-0020 when programmed to produce an 11.8 GHz signal (a) and the phase noise for different frequencies as specified on the datasheet (b).

MHz clock and so is capable of using the 10 MHz master oscillator signal provided by the PXI chassis as is used by the 2.4 GHz PLL in the LLRF pulse signal generation. The 10 MHz provided by the PXI was fed into a Techniwave TWDBPD2-6G-18GA two way splitter to provide a branch for both the PLL and the synthesizer. The 10MHz signal provided is nominally $1V_{pp}$ so to ensure both devices had a signal large enough to lock to a MiniCircuits ZX60-43-S+ amplifier was also installed. The locking arrangement is shown in Figure 4.3.

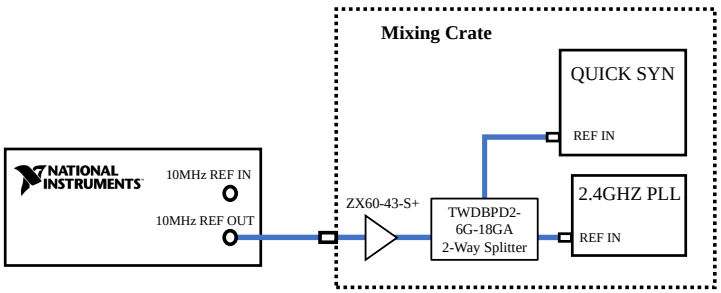

Fig. 4.3 Diagram showing how the 2.4 GHz CERN PLL and synthesizer are locked to the PXI crate's built-in 10 MHz oscillator.

The 11.8 GHz output of the synthesizer is fed through a Marki Microwave FB-1215 bandpass filter followed by a Mini-Circuits ZVA-183+ amplifier to ensure there is enough power for down-mixing all eight channels. Following this, the 11.8 GHz signal is fed into a Techniwave TWDBPD2-6G-18GA two way splitter followed by a Techniwave

TWDBPD4-6G-18GA four-way splitter. Marki Microwave M10616 mixers were then used to mix the 11.8 GHz signal with the incoming 12 GHz RF channels. These mixers operate with RF in the range of 6 to 16 GHZ to provide an IF ranging from DC to 4 GHz. The output of each mixer is then passed through a Mini-Circuits ZJL-4HG+ amplifier and a ZX75LP-216 low pass filter which provides 0.85dB rejection at 200 MHz and over 72dB at 400 MHz to suppress any harmonic content in the IF. Fixed coaxial attenuators were then used to limit the power level to acceptable levels where necessary. A 3U crate was sourced from CERN stores to mount the arrangement in existing electronics rack. The final design is shown in Figure 4.4.

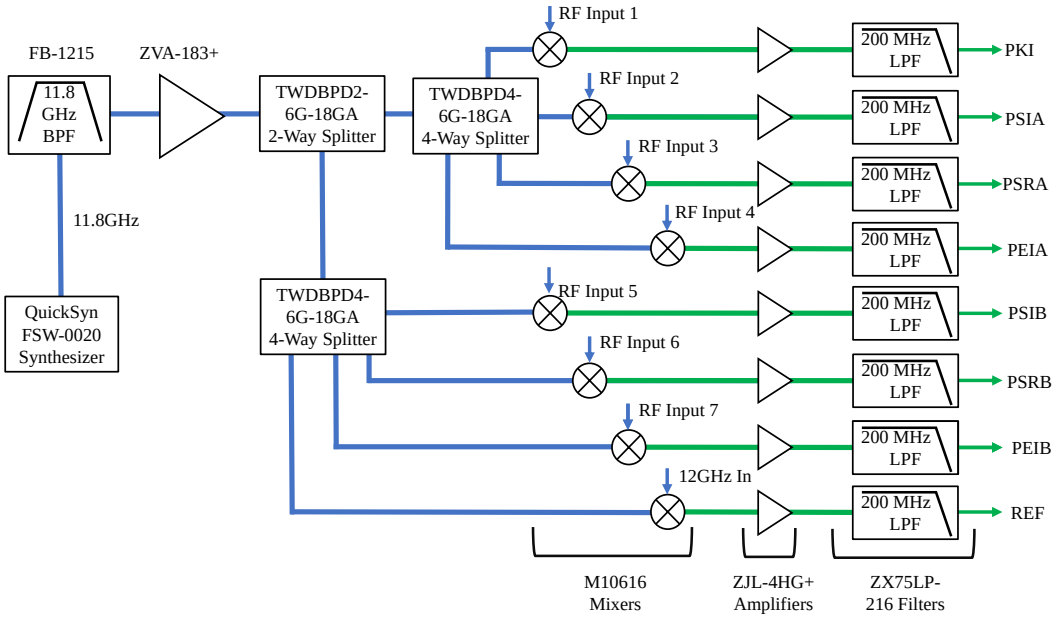

Fig. 4.4 Diagram of the new XB2 down-mixing scheme.

4.1.3 LLRF System Test and Installation

After assembly the final performance was tested using a spectrum analyser. A GPS disciplined oscillator was used to provide the 10 MHz clock and a signal generator was used to inject a 0dBm 12 GHz signal into each RF input sequentially, the 200 MHz outputs were then measured with a power meter and the results recorded in a table to construct a matrix showing the isolation between all ports. Typically isolation was in the 40-50dB range, worse on average than the previous mixing crate where the isolation was consistently better than 51dB [37]. However, the number of channels and hence components has doubled while the crate size has remained the same due to size constraints and so increased cross-talk was expected. This is still higher than the

reflection from most waveguide components and indeed exceeds the directivity of the high-power directional couplers used in the test stands which is normally on the order of -30dB and so was still deemed to be acceptable. The physical arrangement of the components in the crate is shown in Figure 4.5.

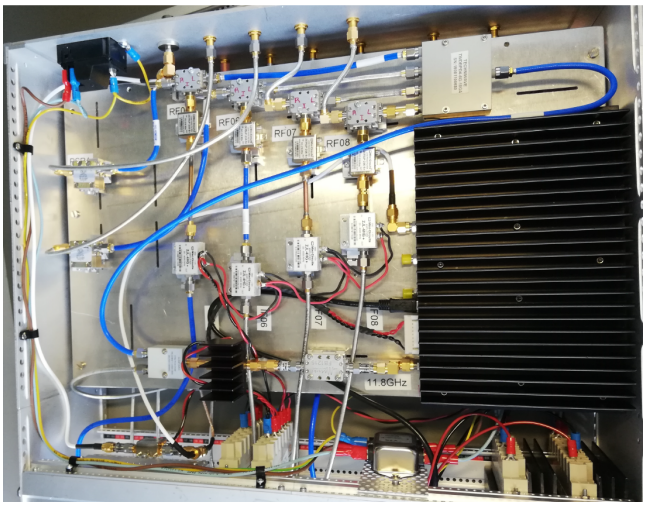

Fig. 4.5 The new down-mixing arrangement installed in the crate. The QuickSyn FSW-0020 is located on the right beneath the large black heat sink. Only four RF channels are visible, with the remaining channels being located in the lower layer of the crate.

Following this, the phase noise contribution of the mixing crate was measured with a Rohde & Schwarz FSW26 spectrum analyser. Measurements were taken of the 12 GHz output, the 2.4 GHz PLL output and the 200 MHz IF channels and the results are shown in Figure 4.6.

Here the effect of the aforementioned phase noise of the synthesizer in the 100 kHz - 10 MHz range is apparent as it is mapped onto both the 200 MHz IF channels which have mixed with the synthesizer's 11.8 GHz however not the 12 GHz signal which is a product of only the 2.4 GHz from the PLL. Notably, the noise spectral density of both the 12 GHz output and 200 MHz IF channels also generally lie 15 dB above that of the PLL output. This is in part due to the use of the 4× frequency multipliers, which also multiply phase variations and hence the phase noise by a factor of 4. This means that the resulting 9.6 GHz signal experiences an increase in noise spectral density on the order of 12 dB before being mixed with the modulated 2.4GHz signal, resulting in a total increase in phase noise of approximately 15 dB.

It can also be seen that the 200 MHz signals have phase noise spectra which are comparable to that of the 12 GHz carrier. Given the difference in frequency, this means

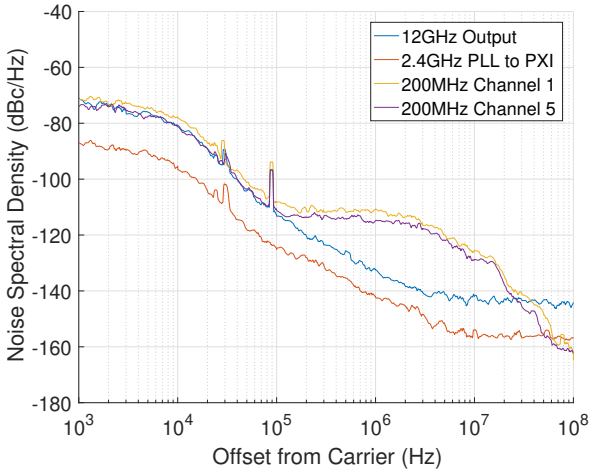

Fig. 4.6 Results of the phase noise measurement of the assembled mixing crate.

the time jitter associated with the 200 MHz signals is higher by a factor of 60. This could arise from poor coherence between the 12 GHz carrier and the 11.8 GHz LO, which relies on separate PLLs sharing a common 10 MHz clock. The expected total RMS phase noise i.e. the phase error in radians can be calculated by integrating the noise spectral density as [108]:

$$\text{RMS Phase Jitter (radians)} = \sqrt{2 \cdot \int_{f_0}^{2 \cdot f_0} S_\phi(f)\, df} \tag{4.1}$$

This may then be converted to a jitter in time as [108]:

$$\text{Time Jitter (seconds)} = \frac{\text{RMS Phase Jitter}}{2\pi \cdot f_0} \tag{4.2}$$

As the measurement was conducted only up to 100 MHz from the carrier, in order to integrate over the full 400 MHz range the noise spectral density at 100 MHz was used for all frequencies up to 400 MHz. This then relies on the assumption that the oscillator has already reached its noise floor 100 MHz from the carrier. Doing so for the 200MHz IF signals resulted in an RMS phase jitter of approximately 0.025 radians or 1.5°, corresponding to a time jitter on the order of 21 picoseconds. Finally, while both the 2.4 GHz PLL and the 12 GHz reference signal are similar in shape a notable 30 kHz spur is inherent in the CERN PLL and then mapped onto subsequent sections of the circuit. Similarly, a spur is also present on the 12 GHz reference which is then

transferred onto the subsequent down-mixing section. However, this portion of the circuit is the same configuration which has been successfully used in previous tests and as the spurious content was nonetheless below -93dB the performance was deemed acceptable and the crate was mounted in the Xbox-2 rack for testing.

An MG3692C signal generator was used to inject a -5dBm 11.9942 GHz signal into each channel and the GUI was monitored. While each channel showed a clear signal a sinusoidal amplitude variance and phase slip was present indicating a problem with the demodulation. The PXI crate has a built in 10 MHz reference signal which is distributed through the backplane and may be output to other devices. This signal was amplified and split to the PLL and synthesizer respectively, however upon inspection it was found that the latter was not reliably locking despite the 10 MHz signal falling within the 0-10dBm range required. The PXI chassis 10 MHz reference has an accuracy of ±25 ppm, however the synthesizer's internal clock falls within ±2 ppm. According to the data sheet any external reference must also fall within this range or else it may be rejected. As the QuickSyn FSW-0020's built-in oscillator outperforms the PXI crate, the decision was instead made to output the synthesizer clock for amplification, and use it as the reference for the PXI Crate and 2.4 GHz PLL. Upon rearranging the scheme the signals were once again checked with the signal generator and a signal of flat amplitude and phase was observed on the GUI. The final locking arrangement is shown in Figure 4.7.

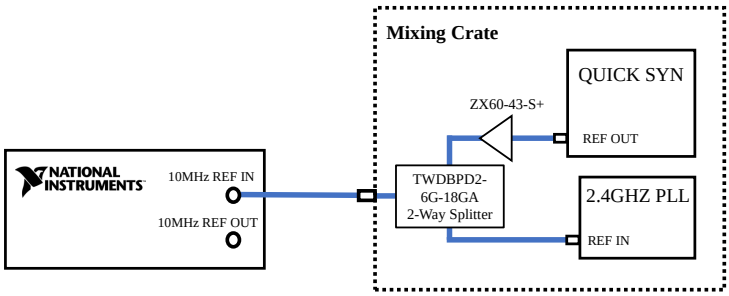

Fig. 4.7 Diagram showing how the 2.4 GHz CERN PLL and PXI crate are locked to the synthesizer's built-in 10 MHz oscillator.

Due to their high phase and amplitude stability, 13.5m RodanTech Micro-coax Utiflex UFA210A cables were selected to make the connection from the high-power directional couplers inside the bunker to the externally housed mixing crate and acquisition system for the new channels. The cables demonstrate only a 2° shift in transmitted phase when wrapped around a 3-inch diameter mandrel and provide >100dB of shielding from external signals. Given the regular changes in the test stand

and the electrically noisy environment surrounding the bunker, both are desirable properties. In the rack each signal passes through a Marki Microwave FB-1215 filter to remove unwanted spectral content, particularly any harmonics from the SSA or klystron. Attenuation was added as necessary so as to avoid saturating any mixing crate components or ADCs and each cable is then fed into a Techniwave TWDBPD4-6G-18GA four-way splitter located in the rack which provides branches for mixing, interlocking and calibration as necessary shown in Figure 4.8.

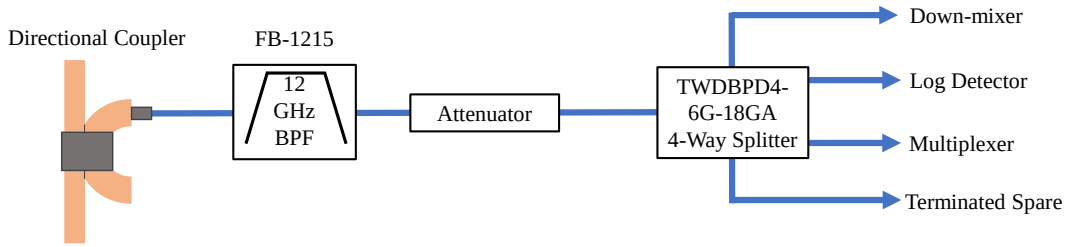

Fig. 4.8 The signal distribution scheme in Xbox-2 test stand.

To provide a means of calibration the Xbox-2 rack has a permanently installed power meter comprised of a Rohde & Schwarz NRP-Z81 power sensor and NRP-2 base unit, the input of which is fed by an 8:1, ETL systems 23166-S5S5 multiplexer. To facilitate the reading of all RF channels a second multiplexer of the same design was fed into the first as shown in Figure 4.9.

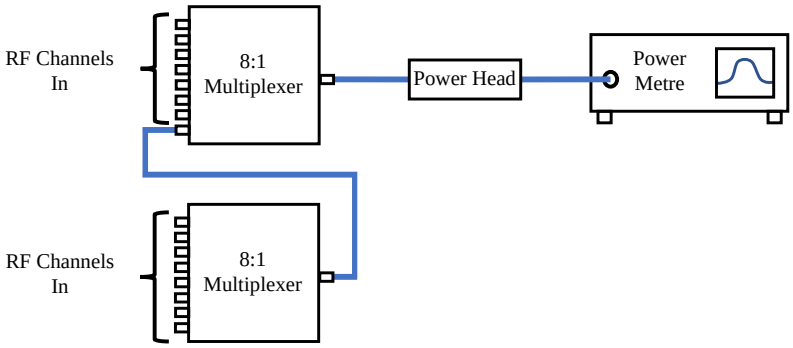

Fig. 4.9 Arrangement of the multiplexers in Xbox-2 showing how any channel may be read and calibrated non-invasively, minimising the potential for error introduction.

With this arrangement any channel can now be read by the power meter and a calibration performed without the need to unscrew cables in the rack, minimising the potential for error introduction.

4.2 Actuator Control System

A variable phase shifter and variable power splitter are also scheduled for installation and high-power testing. Each device functions by varying the position of an internal piston in a circular waveguide section to change the path length taken by the incoming RF signal [109]. The electromagnetic and mechanical design of each device is shown in Figure 4.10 and each is reported in detail elsewhere [110]. The piston on both devices is mounted on a UHV Design MPPL35-50-IS linear actuator and due to the magnetic coupling implemented, the actuator can be moved while under vacuum, without the need for direct contact. To manually position the piston on each device an operator must stop the experiment and enter the bunker. As such, operating and monitoring the device remotely is preferred and to facilitate this additional hardware and software are necessary.

Due to their strong holding torque and accurate, reproducible step sizes a stepper motor was selected as the device to provide the actuation and a complementary control circuit was designed. Due to availability within CERN a 17HS-240E motor which can provide a holding toque of 29N/cm and a step size of 1.8° was selected. When mounted on the linear actuator this corresponds to a linear step size of 0.2mm for the piston in each device. As the motor can accept up to 2.3 A per phase, driving it directly via the PXI is not possible and a motor driver is required. A Geckodrive G203V stepper motor driver was chosen to interface with the PXI chassis and provide the motor current. The G203V model can accept an input voltage of 15 to 80V DC and provide up to 7A per phase. A Traco Power TCL 120-124 AC to DC converter was selected to provide a 24V, 5A supply from the mains. To prevent damage to the devices or the possibility of exceeding the intended range of motion two contact switches were also mounted on the actuation system. Situated in the motor controller is a logic input which determines the motor direction through the use of an H-bridge circuit. In the event of an operator or software problem attempting to exceed the range of motion the relevant contact switch may then pull the direction pin on the stepper motor drive to 5V or ground respectively, forcing the motor to change the direction of motion. In order to integrate the arrangement with the existing software, a PXI SCB-68A board was selected as the interface through which the control logic could be transmitted. The final control circuit is shown in Figure 4.11.

The circuitry was tested in the lab before being mounted in a 3U crate and installed in the Xbox-2 rack above the upgraded mixing crate. Multicore cable was pulled from the back of the rack to the bunker via the cable trenches to several internally situated

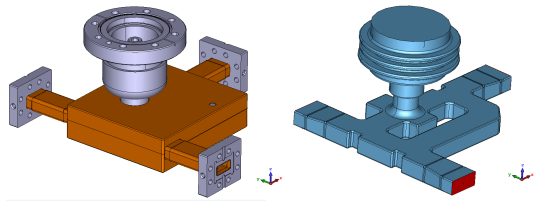

(a) Mechanical design (left) and vacuum space (right) of the power splitter.

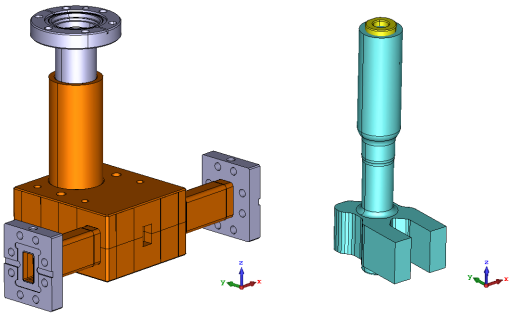

(b) Mechanical design (left) and vacuum space (right) of the phase shifter.

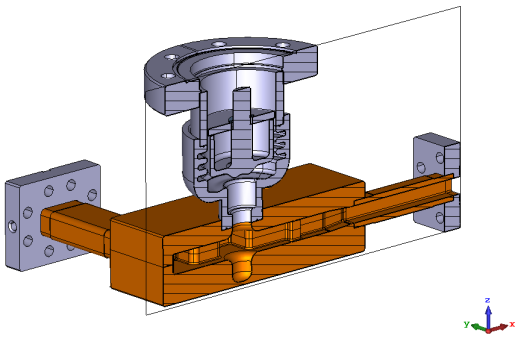

(c) Cross section of the of the power splitter mechanical design.

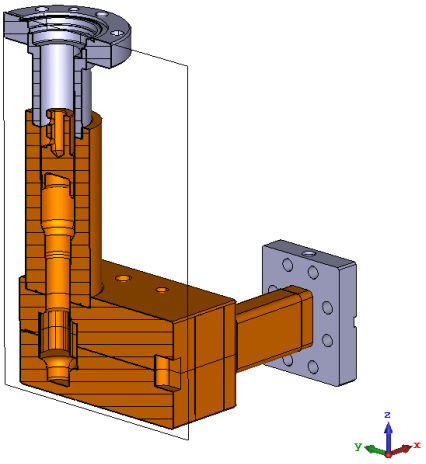

(d) Cross section of the of the phase shifter mechanical design.

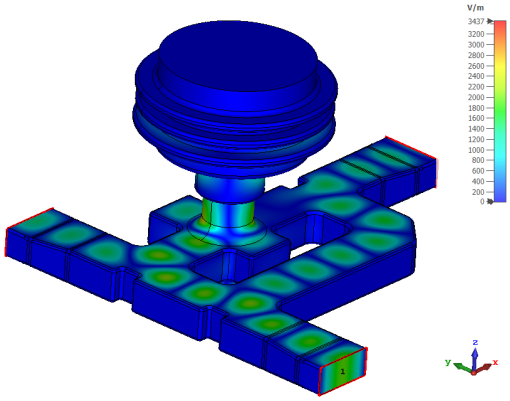

(e) CST simulation of the power splitter showing the surface electric fields at 11.9942 GHz.

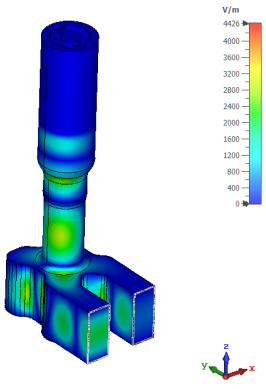

(f) CST simulation of the phase shifter showing the surface electric fields at 11.9942 GHz.

Fig. 4.10 Mechanical design and CST simulations of the variable power splitter (a,c,e) and variable phase shifter (b,d,f).

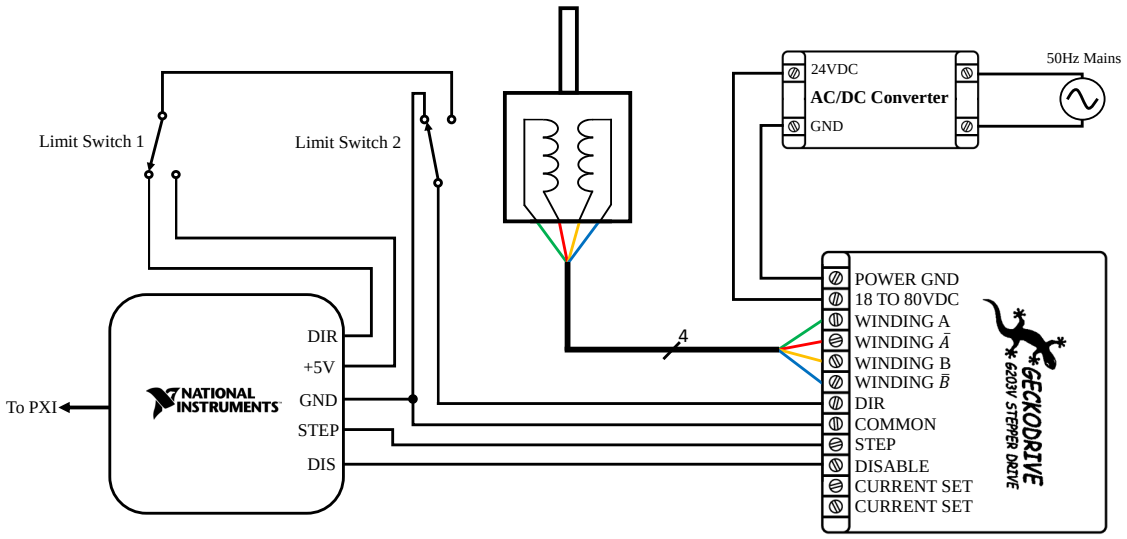

Fig. 4.11 The final stepper motor driver circuit complete with motion limiting contact switches.

screw terminals for ease of electrical connection and to provide flexibility for future installations.

4.3 New Pulse Compression Scheme

In addition to the superstructure a novel pulse compression scheme comprised of a Barrel Open Cavity (BOC) and Correction Cavity Chain (CCC) is also scheduled for testing in the X-band test stands. The scheme is an X-band variant of the C-band model already in use at the SwissFEL LINAC [111] designed for use with a novel X-band transverse deflecting structure, coined the PolariX-TDS [112]. Due to the test stand's high-power capability and the potential utility of the scheme in the upcoming tests, Xbox-2 was selected to house the experiment. Detailed following are the design, measurement and installation of the scheme.

4.3.1 BOC Design

The concept of the BOC (originally referred to as the VLEPP Power Multiplier or VPM) was first proposed in 1990 [113]. The first X-band prototype was developed and tested shortly thereafter in 1994 at KEK, Japan [114]. While the conventional SLED-I type pulse compressor utilises two storage cavities coupled by a hybrid, the

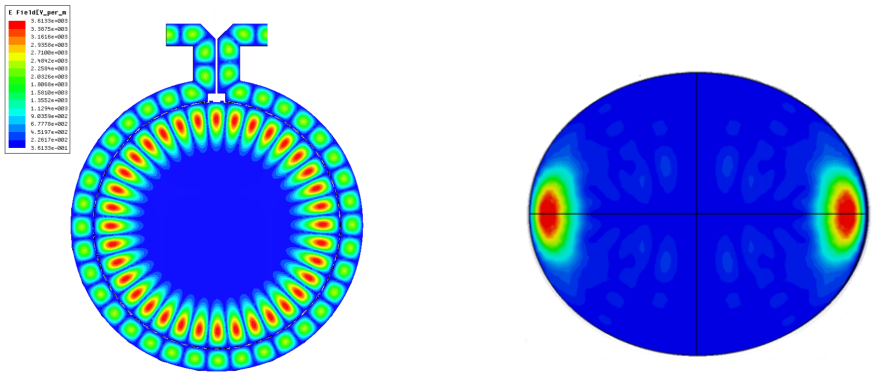

(a) (b)

Fig. 4.12 Field Distributions of C-band BOC developed and in use in the SwissFEL LINAC showing a top down view (a) and a side on view (b) of the "Whispering Gallery" $TM_{18,1,1}$ mode. It should be noted that view (b) shows only the spherical cavity and excludes the surrounding waveguide section visible in (a) [111].

BOC utilises only a single cavity operating in a resonant rotating wave regime typically referred to as a whispering gallery mode. In 1910, Lord Rayleigh noted that in a domed structure within St Paul's Cathedral, London, whispers were heard clearly elsewhere around its perimeter, even at great distances [115]. Shortly thereafter the term whispering gallery was coined and it is from this effect that the mode derives its name.

Figure 4.12 shows electric field distribution within the spheroidal cavity of the C-band BOC developed for the SwissFEL LINAC operating in this regime. The mode is excited through the coupling slots in the waveguide laying around the perimeter of the cavity as are visible in Figure 4.14 [116]. The high Q_0 of the mode means it is well suited to application in pulse compressors.

The cavity is comprised of two flat caps enclosing a characteristic convex barrel section, the geometry of which is selected such that only modes comprised of a large number of azimuthal variations can be excited (i.e. whispering gallery modes) [114]. Due to its similarity in shape, the theory of operation may be derived in the same manner as that of a cylindrical cavity, with the definitions of TE and TM modes and hence mode indices remaining the same. A parameterised elliptical cross section of the spheroidal storage cavity is shown in Figure 4.13.

The small slots placed in rectangular waveguide travelling around the equator of the geometry are spaced such that due to the multiple reflections from the cavity walls the electromagnetic field of the operating mode is concentrated close to the cavity

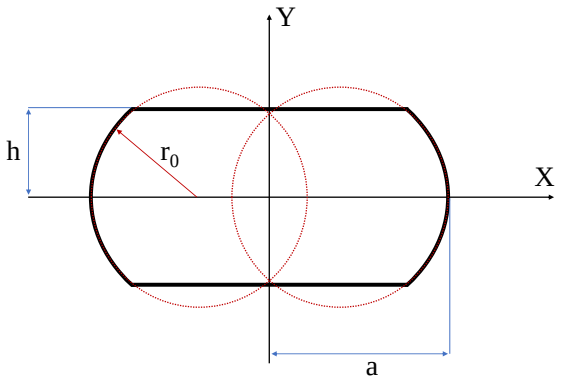

Fig. 4.13 Parameterised elliptical cross section of the BOC storage cavity.

surface. The field distribution of the whispering gallery mode in a spheroidal cavity is then classified as a TM mode and satisfies the following relation [117]:

$$ka = v_{mn} + \frac{(p - \frac{1}{2})\alpha}{\sin\theta} \tag{4.3}$$

Where k is the free space wavenumber, a is cavity radius as shown in Figure 4.13, m is the azimuthal index of the mode and p is the longitudinal index. v_{mn} is the n^{th} positive root of the Bessel function order of m for the E_{mnp} modes and its derivative for the corresponding H_{mnp} modes [116]. α is then defined:

$$\sin\alpha = \sqrt{\frac{a}{r_0}}\sin\theta \tag{4.4}$$

Where θ can be calculated from $\cos\theta = \frac{m}{v_{mn}}$ [116]. The Q_0 of the storage cavity may be approximated by taking the ratio of the cavity equator radius to the skin-depth of the cavity wall material, σ, as:

$$Q_0 = \frac{a}{\sigma} \tag{4.5}$$

For operation in a whispering gallery mode, the mode indices n and p are one while m is then determined by the desired Q factor and the operating frequency. For the X-band model a $TM_{18\,1\,1}$ operating mode and a coupling factor, β of 7.5 were selected in order to provide the required Q factor and gain for the klystron pulse length and filling time of the TDS structure for which it was originally designed [118]. Table 4.2

lists the key RF design parameters and results of low power measurement following assembly.

Parameter	Value	Unit
Diameter	246	mm
Number of coupling slots	72	-
Frequency	11995.2	MHz
Q	157800	-
Coupling factor (β)	7.88	-
Reflection coefficient	-31	dB

Table 4.2 Key geometric and measured RF parameters of the XBOC working with a $TM_{18\,1\,1}$ mode. It should be noted that the measurement was performed at a temperature of 41.2 °C while the design temperature is 40 °C [118].

The manufacture of the BOC was undertaken in-house at the Paul Scherrer Institute, Switzerland and the process was similar to that of the C-band version already in use [111]. A key aspect of both designs is that they are characterised by the absence of any features which facilitate mechanical tuning, with PSI instead opting to achieve the correct frequency through machining tolerances alone, an approach which has already been successfully implemented in structure for the SwissFEL LINAC and indeed several prototype X-band structures [82]. The storage cavity is comprised of copper, while two stainless steel cooling rings located externally provide additional mechanical support. A circular waveguide section encircles the storage cavity, while stainless steel flanges provide coupling to external waveguide sections. Figure 4.14 shows the mechanical design and the final assembly including cooling channels prior to being shipped to CERN.

4.3.2 Correction Cavity Chain Design

Cavity based pulse compressors like the SLED-I and BOC are capable of temporarily increasing the available peak power. As described in Section 3.1.2 however, in the absence of modulation the output pulse is characterised by an exponential decay. While a region of fixed phase and amplitude may be achieved via modulation of the LLRF signal, the efficiency is greatly reduced [119]; it is possible however, to circumnavigate these disadvantages passively through the use of an alternative design. One such design is the SLED-II pulse compressor which was developed at SLAC in 1990 [120]. As opposed to the cavities in use in the SLED-I design, the SLED-II is based on the use of

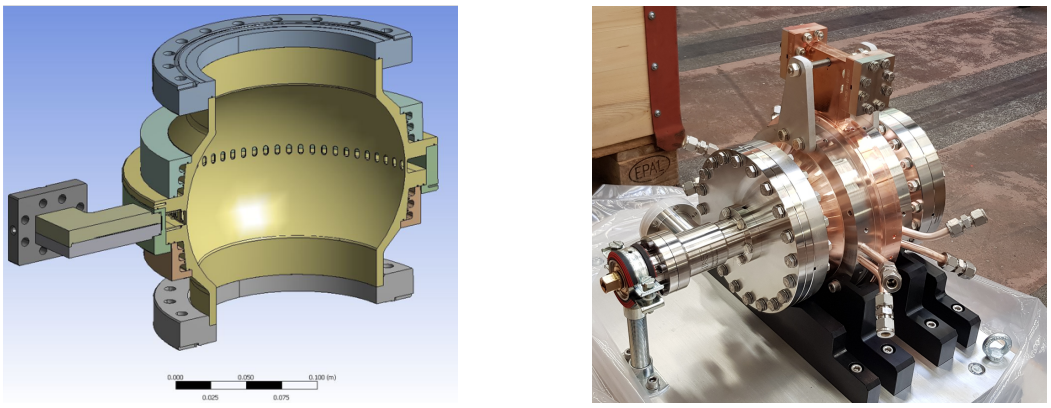

(a) (b)

Fig. 4.14 Cross section showing the mechanical design of the BOC (a) and the final assembly at PSI, prior to being shipped to CERN for installation and high-power testing (b) [118].

two identical resonant delay lines coupled via a 3dB hybrid. For a given network the response of a device to a signal at any port can be described in terms of its scattering or S-parameters. For a single two-port network, the incident voltages at each port, a_1 and a_2, are related to the reflected or outward travelling waves, b_1 and b_2, as [7]:

$$\begin{bmatrix} b_1 \\ b_2 \end{bmatrix} = \begin{bmatrix} S_{11} & S_{12} \\ S_{21} & S_{22} \end{bmatrix} \begin{bmatrix} a_1 \\ a_2 \end{bmatrix} \tag{4.6}$$

In the SLED-II arrangement the S_{21} of the device consists of a series of periodically distributed resonant peaks around the operating frequency. The interval between each peak is equal to the reciprocal of the round trip time of the RF pulse in the resonant delay line and hence, a function of its length. The principle of operation of the scheme is then similar to that the cavity based system, relying on the interference between reflected and emitted waves. However these interactions now occur at fixed intervals determined by the round trip time of the delay lines resulting in the step like change in the transmitted waveform. Both the S_{12} and output pulse shape for a input klystron pulse with a 180° phase flip are shown in Figure 4.15.

The benefit of this design is that the device passively produces a compressed pulse which is flat in amplitude however as it relies on the RF propagation time the pulse length is proportional to, and indeed fixed by, the line length, meaning it is necessarily large and potentially impracticable in some applications. More recently, it has been proposed that the same effect may be produced by employing the more compact

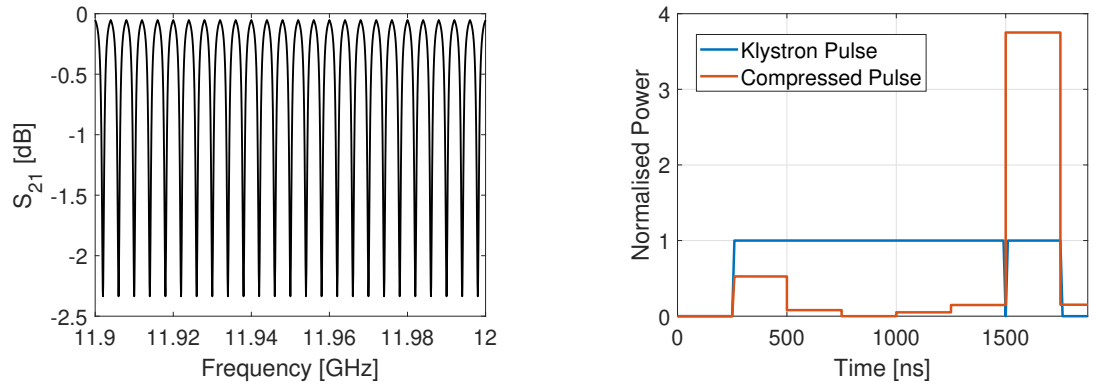

(a) (b)

Fig. 4.15 Simulated S_{21} of an X-band SLED-II pulse compressor designed to operate with a compressed pulse length of 250ns (left) and the output produced by a klystron pulse with a 180° phase flip at time t=1250ns (right). It should be noted that in reality the device is reciprocal, i.e. $S_{12} = S_{21}$.

SLED-I type pulse compressor in addition to a series of resonant cavities to imitate the frequency response of the SLED-II [121, 122]. A series of cavities for this purpose has been developed at Tsinghua University and the entire device has been named the correction cavity chain (CCC) [122]. While an infinite number of cavities is necessary for a complete reproduction of the spectrum this is clearly impracticable and so the actual number employed is the result of a compromise between pulse shape and cost. The final mechanical design and vacuum space of the cavities with field patterns are shown in Figure 4.16.

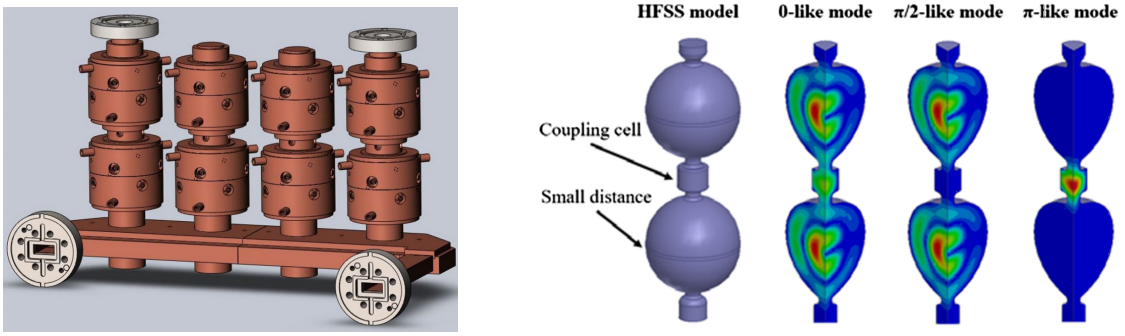

(a) (b)

Fig. 4.16 The mechanical design (a) of the correction cavity chain showing the waveguide flanges on the lower left and lower right and the vacuum pumping ports on top. Shown on the right (b) is the field patterns and operating modes in a single unit comprised of two spherical cavities and a coupling cell are also shown [122, 123].

The CCC is comprised of four units and each unit is composed of a pair of coupled spherical cavities fed from a waveguide section by a dual-mode polariser first designed at SLAC, the geometry of which is shown in Figure 4.16 [124]. Due to the symmetry of the sphere, the TE_{012} and two degenerate TE_{112} modes exist with principally the same field distributions merely rotated by 90° in space as shown in Figure 4.17, with the two latter being the operating modes. The dual-mode polariser is fed by WR90 waveguide and converts the rectangular TE_{01} waveguide mode into two circular TE_{11} modes polarised in quadrature. The two circular TE_{11} modes are then fed into the spherical cavities via a circular waveguide section. It should be noted that the definitions for circular and rectangular modes differ and so it is important to distinguish between the two. The two degenerate TE_{112} modes in the cavity effectively provide the same function as the two storage cavities in the SLED-I pulse compressor, while the dual-mode polariser may be regarded as having the same function as the 3dB hybrid.

As shown in Figure 4.16, the two spherical cells coupled by a small cylindrical cell facilitates three modes of operation, namely, the 0-like, the $\pi/2$-like, and the π-like modes. The field of the π-like mode is mainly distributed in the small cylindrical cell, meaning it is far from the operating frequency. Additionally, the field in the bottom spherical cell is small meaning any coupling to the waveguide is extremely weak. The size of the coupling cell varies in each pair; and as a consequence the field of the 0-like mode varies however the $\pi/2$-like mode remains unchanged. Thus, the small cylindrical cell can be used to tune the frequency difference between these two modes.

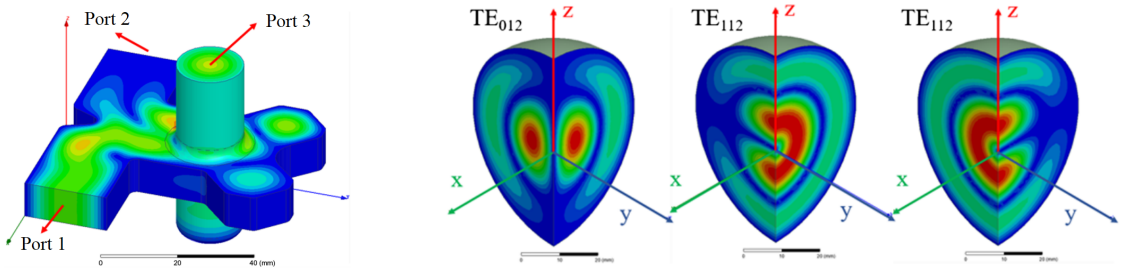

(a) (b)

Fig. 4.17 Geometry of the polariser which couples the waveguide section to the cavities showing the magnitude of the E-field distribution in an arbitrary colour scale (a) and the gield patterns seen in a section of the spherical resonant cavities with TE_{012} and two TE_{112} modes [122, 123].

Figure 4.18 shows the frequency response of a SLED-I pulse compressor when used in conjunction with a correction cavity chain alongside exemplary RF waveforms. The rectangular klystron pulse with a phase flip (blue) first passes through the CCC. The

pulse produced by the interaction with the CCC (green) then travels towards the SLED-I, providing the desired high-power flat top region (red).

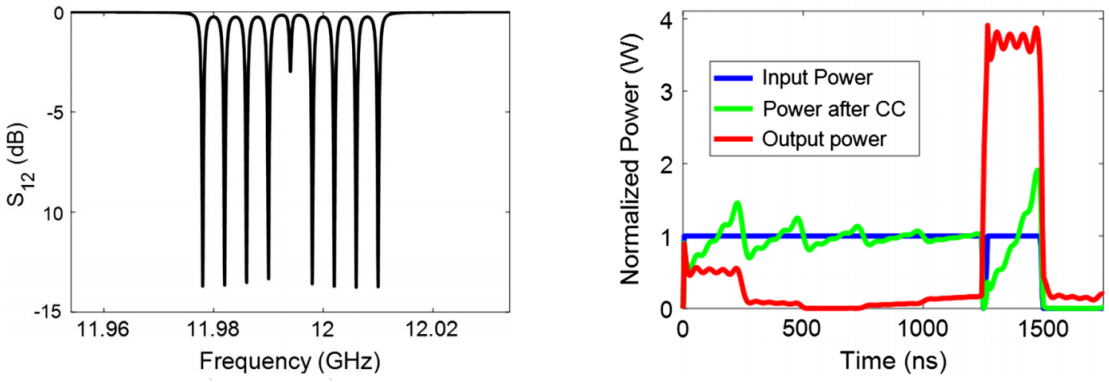

(a) (b)

Fig. 4.18 The frequency response of the SLED-I pulse compressor with correction cavities (a) and simulated waveforms at the output of the CCC and SLED pulse compressor when operating with a 1.5μs klystron pulse with a phase flip (b). The central frequency of the spectrum is 11.994 GHz and the nearby peaks are situated 4 MHz apart [122].

Due to the limited number of cavities and hence, peaks in the spectrum, several ripples are observed during the flat top region of the compressed pulse. However, it is clear that in applications requiring both pulse compression and pulse which is flat in amplitude and phase the CCC nonetheless constitutes a viable, more efficient alternative to phase and amplitude modulation. As a result, the device is now considered as a possible means of high-power RF production in the updated baseline of the CLIC project [125].

4.3.3 Tuning and Installation

Prior to brazing, the constituent components of the CCC were cold tested and tuned at Tsinghua university and this is reported in detail elsewhere [123]. Following assembly and tuning, the device was then shipped to CERN for high-power testing. Upon arrival at CERN the CCC and BOC were measured together in order to verify performance of the full pulse compression scheme. The CCC was designed specifically for use with the SLED-I type pulse compressor in Xbox-2 however due to time constraints the decision was made to test both the BOC and CCC simultaneously. As the BOC was designed for operation at 11.9952 GHz as opposed to the nominal 11.9942 GHz CLIC frequency it was clear that tuning via temperature was also necessary. The pulse

compression scheme was assembled and connected to a Rohde and Schwarz ZVA24 VNA for measurement as shown in Figure 4.19.

Temperature stabilisation was performed separately for for the BOC and CCC via the use of two SMC, HRS024-AF-20 chiller units capable of regulating the coolant temperature to within 0.1ºC. The system was held under vacuum and the chiller temperatures were then adjusted while monitoring the S-parameters to tune the BOC. Operating temperatures of 31.6 °C and 45.2 °C for the CCC and BOC respectively resulted in the centering of the spectrum at the 11.9942 GHz Xbox operating frequency under vacuum. The resulting spectrum is shown in Figure 4.19.

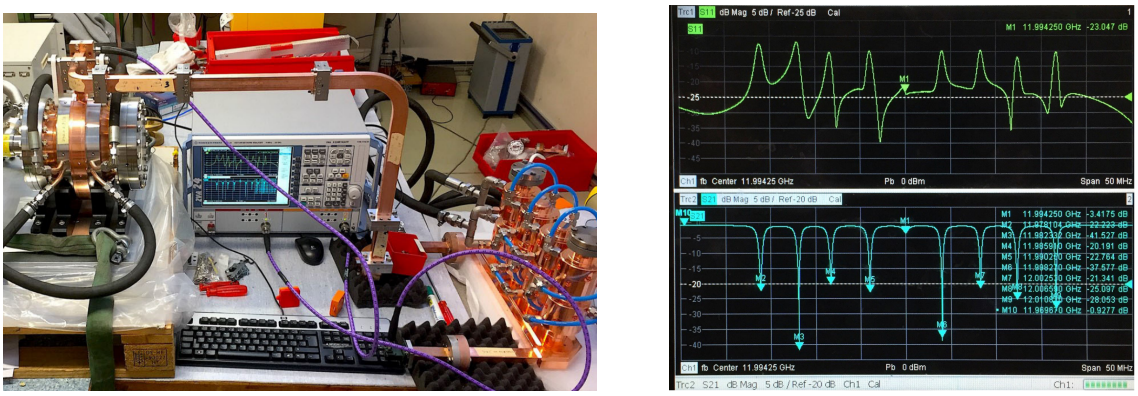

(a) (b)

Fig. 4.19 Arrangement of the BOC and CCC during VNA measurement at CERN prior to installation in the Xbox-2 test stand (a) and results of the VNA measurement of the assembled pulse compression scheme after tuning via temperature (b) [119].

The transmission coefficients of the CCC and assembled scheme including connecting waveguides were found to be -0.46dB and -0.93dB respectively, equating to a transmission efficiency of approximately 90 percent. While this was slightly worse than values from simulation it was suspected by the designers at Tsinghua University that the increased attenuation was due to the surface roughness of the CCC [119]. Prior to operation, the pulse shape which the arrangement would produce was investigated and compared to that which would be possible if it was instead employed with the SLED-I pulse compressor for which it was originally designed. A frequency domain pulse was multiplied pointwise with the S-parameters of the CCC combined with the SLED-I and CCC combined with the BOC. The resulting array was then inverse Fourier transformed (IFFT) to recover the pulse shapes in the time domain and the results are as shown in Figure 4.20 [119]. The results indicate that to produce a pulse with a flat top as is normally used in the Xbox test stands some phase modulation would then be necessary.

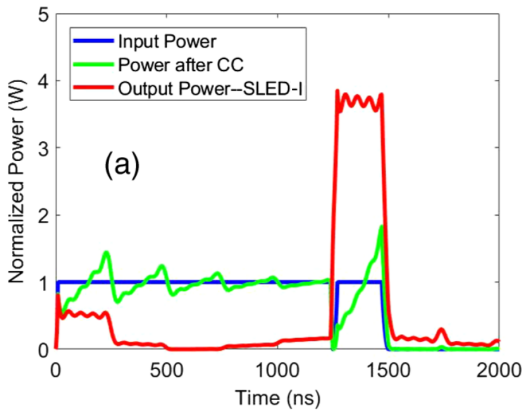

(a) IFFT of the frequency domain simulation showing the resulting waveform after passing a flat klystron pulse with phase flip through a CCC and SLED-I pulse compressor with Q_0 of 180,000 and β of 6.

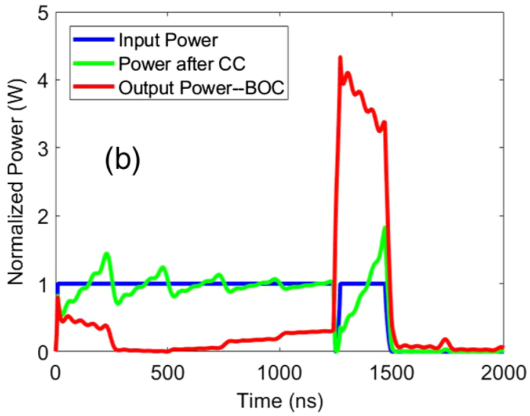

(b) IFFT of the frequency domain simulation showing the resulting waveform after passing a flat klystron pulse with phase flip through the measure spectrum of the CCC and BOC pulse compressor with Q_0 of 157,800 and β of 7.88.

Fig. 4.20 Simulated waveforms produced by a an arrangement comprised of the CCC and the SLED-I pulse compressor and the CCC and BOC respectively [119].

Following measurement, the new pulse compression scheme was deemed fit for operation and installed in the Xbox-2 test stand. Figure 4.21 shows the CCC and BOC installed in the Xbox-2 waveguide network respectively prior to high-power testing.

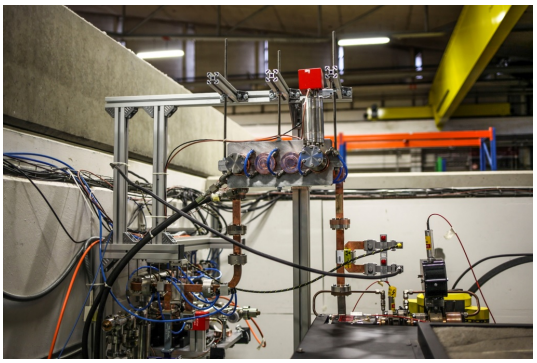

(a)

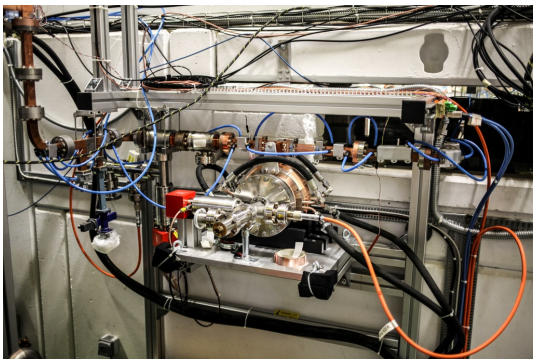

(b)

Fig. 4.21 The final installation of the CCC (a) and the BOC (b) in the Xbox-2 test stand prior to high-power testing.

4.4 Commissioning of the Upgrade

Having tested all constituent components of the updated test stand separately the final task was operation at high-power to verify that the system can operate reliably, safely and as expected while unattended. Covered following are the calibration of RF signal chains and first high-power test with the new pulse compression scheme.

4.4.1 Calibration of the RF Signal Chains

As described in Section 4.1.3 RodanTech Micro-coax Utiflex UFA210A cables were used to make the connection from the high-power directional couplers inside the bunker to the acquisition system situated outside. However it is then necessary to measure the insertion loss of each signal chain in order to accurately infer the incident power at each directional coupler. The output of an Anritsu MG3692C signal generator was measured across a range of power levels from 0 to 20dBm using a Rohde & Schwarz NRP-Z81 power sensor and NRP-2 base unit installed in the rack and recorded.

The attenuation of each RF channel was then measured by unscrewing the cable from the high-power directional coupler and injecting a low power signal produced by the generator inside the bunker. The signal was then measured at the LLRF rack through the RF multiplexers and permanently installed power meter as shown in Figure 4.22. The attenuation of each corresponding signal chain was then found as the difference between the two measurements. This method requires the unscrewing of a single connection and thus, provided no significant bending of the cables takes place, minimises the potential for error introduction. Attenuators were added as required to ensure that the power level into each mixing crate channel was around 0dBm for full power operation in order to prevent damage to the mixing crate and log detectors.

It should be noted that while this method allows accurate inference of power it does not account for the electrical length of the cables. For tests where absolute phase and timing information are required alternative procedure has been implemented which is introduced in Section 6.3.1. The total measurement must also account for the insertion loss of the directional couplers, isolators and waveguide to coaxial transitions and so each of these components was characterised in the lab via VNA measurement prior to installation.

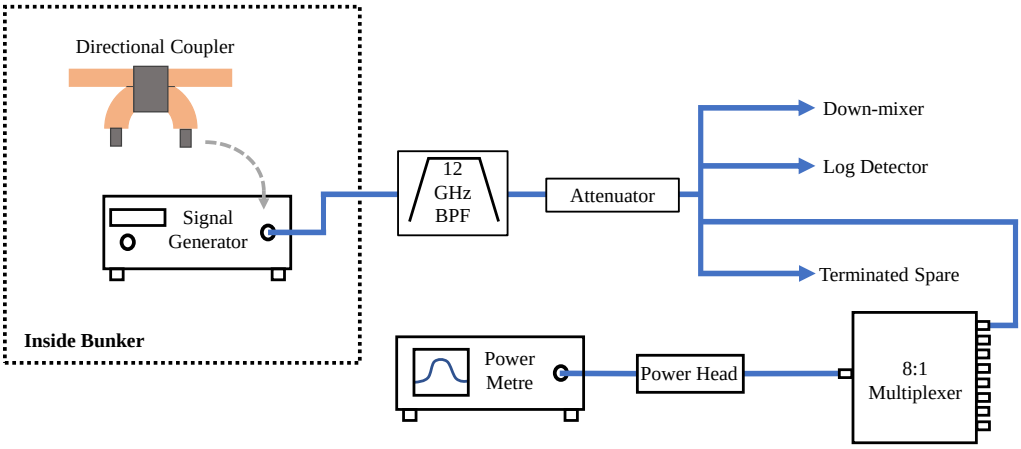

Fig. 4.22 Arrangement used for calibration in Xbox-2. The grey arrow shows the only place the signal chain must be unscrewed in order to measure the attenuation prior to operation.

4.4.2 High-Power Test

Following verification and testing of all constituent components of the new test stand arrangement the system was ready for high-power testing. The modulator voltage was set to 180kV, far below the 420kV required for full power operation at 50MW. At this voltage the saturation point of the klystron was known to be below 1MW, meaning the amount of energy in the initial RF pulses was limited to avoid damaging the system. Additionally, 10dB of attenuation was placed on the output of the SSA to ensure that the driver was not capable of saturating the klystron. The multiplexer was set to monitor the klystron pulse and the GUI was monitored simultaneously, the LLRF pulse sent to the SSA for amplification was then slowly increased until a waveform became visible on both the GUI and the power meter display as shown on Figure 4.23.

The multiplexer was then set to monitor the compressed pulse and the power was increased until a peak compressed power of approximately 1.4MW was reached, at which point significant vacuum activity limited further ramping. A calibration of the ADC values was performed by recording the power meter and the ADC value on the GUI at several points within the permissible operating range. These values were then plotted against one another and a 2nd order polynomial was fitted to provide the ADC count to watts calibration values which were then entered into software. Following commissioning, the first structure tested in this arrangement was the PolariX-TDS, ultimately reaching a compressed pulse power of 26.5MW for 100ns and this test is reported by the author in detail elsewhere [112, 118]. After conditioning at CERN

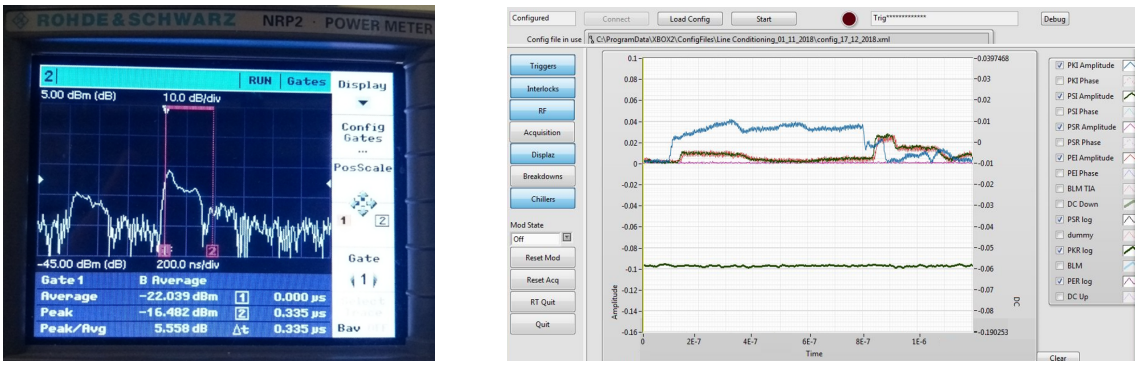

(a) (b)

Fig. 4.23 First compressed high-power RF pulses as shown on the GUI and the power meter situated in the Xbox-2 rack during calibration for the PolariX-TDS test. Details of the full test have been reported previously [118].

the structure was then installed and commissioned in the FLASHForward beamline at DESY in the summer of 2019 [118].

4.5 Conclusion

This chapter described the development and implementation of the hardware necessary to facilitate the testing of a dual accelerating structure arrangement in the Xbox-2 test stand. The new LLRF down-mixing scheme now mixes incoming 12 GHz to an IF of 200 MHz where it is sampled at 800MS/s while the signal generation portion of the test stand has remained largely unchanged save for being mounted in a new crate due to space constraints. A motor control circuit has been designed, tested and mounted in the controls rack to facilitate the remote control of several electronically actuated novel high-power RF components. Finally, the design, installation and commissioning of a novel pulse compression scheme in the test stand have been presented.

Chapter 5

Simulation of Interactions in Coupled Accelerating Structures

While both constituent TD26CCs of the CLIC superstructure are positioned on the same beamline, each structure has an independent RF input meaning the incoming power must be split between them in the test stands. The following chapter details simulations of several phenomena which may manifest during high-gradient operation in this arrangement, namely the interaction between structures during breakdown and the dependence of dark current capture on the relative phasing and gradients of the two structures. Based on the results of each study, the implications for CLIC or other high-gradient facilities planning to operate a similar arrangement are discussed.

5.1 Motivation of the Study

In previous chapters it has been reported that CLIC accelerating structures operate with accelerating gradients of 100MVm, necessitating high input powers which, depending on the design, are typically on the order of 40MW per unloaded structure. The use of separate power sources for the superstructure constituents is not a practicable option due to the cost and complexity associated with doing so. A more favourable alternative is then to derive the high-power RF required from a single source then split and distribute it via passive means, a technique which commonplace in many accelerator facilities. However, few facilities do so while operating at gradients comparable to those regularly established in CERN's X-band test stands. As the structures are effectively coupled in such an arrangement, care must then be taken to avoid interactions between them, particularly regarding where the reflected power is directed during breakdown events.

Additionally, the high accelerating gradient corresponds to surface fields in excess of 200MV/m which can result in the spontaneous emission of electrons from the cavity surface. This current can collide with the cavity irises resulting in background radiation, the dose rate of which dictates the personnel and instrumentation shielding requirements in an experimental facility. If sufficiently large such current can also affect sensitive beam diagnostics. The investigation of these effects in a dual structure arrangement is then of interest both for the planned experiment and in modern high-gradient facilities.

5.2 The Modelled Experiment Setup

The nominal input power required to establish an unloaded gradient of 100MV/m in the regular accelerating cells of the TD26CCR05 structure is 41.8MW. However in the X-band tests it is common to exceed this value with previous structures having been operated up to gradients of 115MV/m [40]. To do so in both structures simultaneously, RF power on the order of 100MW is needed for a short pulse length. As Xbox-2 has a 50MW klystron it is clear that pulse compression and a method to split the power are necessary.

If relative isolation is desired, the use of a 3dB hybrid, as shown in Figure 4.1 would allow an incoming pulse to be split evenly between structures while reflections during breakdown will be directed back to the klystron and to the hybrid fourth port which may simply be terminated. This is similar to the proposed arrangement for CLIC and indeed silicon carbide inserts have been designed specifically for terminating the fourth hybrid port [126]. In this arrangement only 25% of the total forward power can be directed back towards the source during breakdown however both structures will always receive the same input power meaning unless the performance of each is identical it will not be possible to test both to their respective limits simultaneously. Instead, the use of a high-power variable power splitter in conjunction with a high-power variable phase shifter was proposed as shown in Figure 5.1.

Both devices were also scheduled for testing and this arrangement provides mechanical control over both the ratio to which the power is split between structures and their relative phasing. If either structure develops a fault, the ratio at which the power is split between the structures may be non-invasively adjusted. Additionally, the variable phase shifter facilitates the investigation of the dark current and radiation as a function of relative phasing between the two structures.

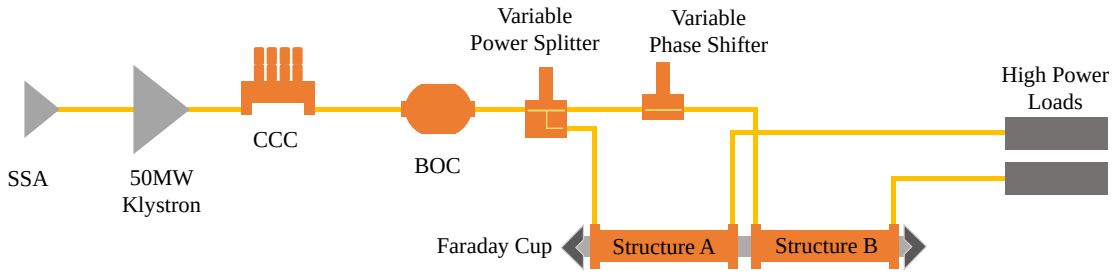

Fig. 5.1 Diagram of the planned dual structure test arrangement.

5.3 Simulation of Power Flow During Breakdown in Coupled Structures

Network theory dictates that a three-port device constructed from isotropic materials cannot be lossless, reciprocal, and matched at all three ports simultaneously [127]. A disadvantage associated with the setup shown in Figure 5.1 is that the reflected signal during breakdown may then be directed in varying ratios towards the neighbouring structure, the klystron and back to the breakdown site in a ratio dependent on the phase. An illustration of this effect is shown in Figure 5.2. The propensity for and probability of constructive interference in each location is of interest before installation to evaluate the associated risks. Additionally, the reflected signals associated with breakdown have been observed to preferentially occur on the irises and hence at integer multiples of the phase advance per cell [46, 40]. By appropriately choosing the phase advance between components the probability of surges may then be minimised.

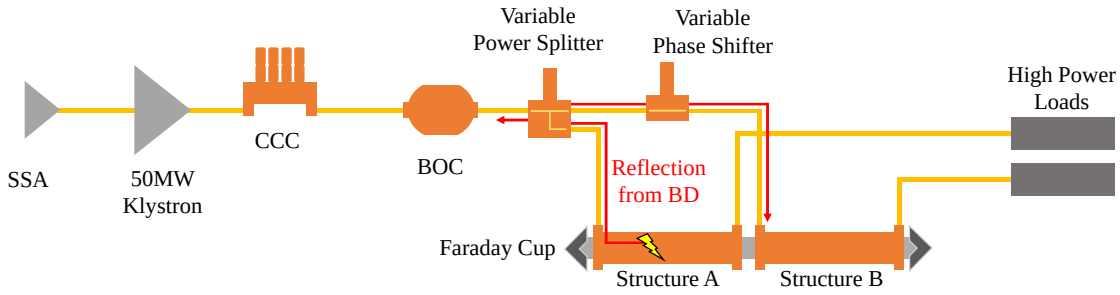

Fig. 5.2 Diagram showing how a breakdown in structure A may result in a reflection towards the klystron and to structure B.

While the desired results may be provided from 3D electromagnetic simulation, the geometry of the power splitter is large, relatively complex and such a study necessitates

several degrees of freedom, namely the load on each port and the piston position meaning the total simulation time would be substantial. Additionally, this method does not capture the effect of the other components in network, which will contribute significantly to the result. Hence, performing the entire study in 3D simulation was viewed as impracticable and so numerical methods were chosen instead.

As outlined in Section 4.3.2 the response of a given network to stimuli at any port may be captured by its corresponding S-parameters. However such matrices are not directly suitable for the analysis of many components cascaded in series. Given that the majority of existing RF networks consist of multiple components it is desirable to have a method of deriving an explicit relation between any two points in the network from the S-parameters. This can be accomplished in three ways, the first is the derivation of ABCD matrices, a two-port example of which is shown in Equation 5.1. This method also requires definition of the input and output port impedances, Z_{01} and Z_{02}.

$$\begin{bmatrix} A & B \\ C & D \end{bmatrix} = \frac{1}{2S_{21}} \begin{bmatrix} (1+S_{11})(1-S_{22}) + S_{12}S_{21} & Z_{02}(1+S_{11})(1+S_{22}) - S_{12}S_{21} \\ \frac{1}{Z_{01}}(1-S_{11})(1-S_{22}) - S_{12}S_{21} & \frac{Z_{01}}{Z_{02}}(1-S_{11})(1+S_{22}) - S_{12}S_{21} \end{bmatrix} \tag{5.1}$$

The next method involves the use of T-parameters, defined:

$$\begin{bmatrix} T_{11} & T_{12} \\ T_{21} & T_{22} \end{bmatrix} = \begin{bmatrix} S_{12} - \frac{S_{11}S_{22}}{S_{21}} & \frac{S_{22}}{S_{12}} \\ -\frac{S_{11}}{S_{12}} & \frac{1}{S_{12}} \end{bmatrix} \tag{5.2}$$

While T-parameters may be cascaded in series to examine the propagation of a wave through multiple components it can be seen that the derivations become laborious for larger networks containing devices with varying numbers of ports. The third and final method involves using the signal flow graph (SFG) method to derive the overall S-parameters for a given network. SFGs are a method of graphically mapping an RF network as a series of nodes and lines representing the S-parameters between them. The main advantage of this technique is that it provides an intuitive method of viewing and checking any existing RF network and it is possible to proceed directly to a solution. Additionally, the addition of devices with varying numbers of ports is possible without the complexity associated with the previous methods.

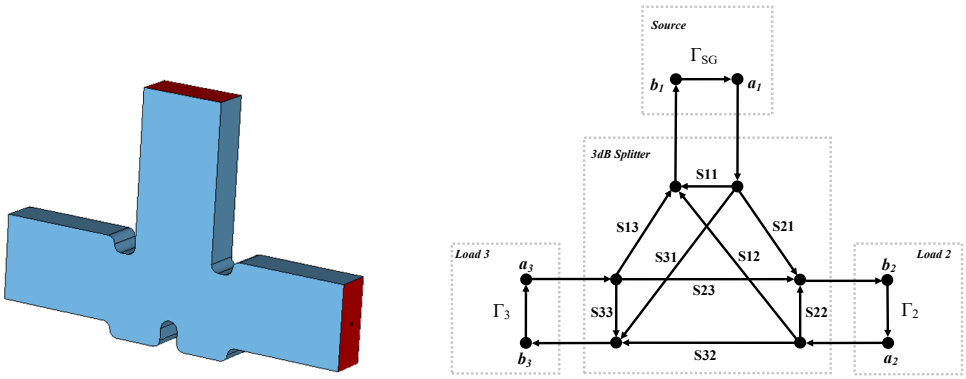

(a) (b)

Fig. 5.3 CST MWS rendering of the vacuum space in a 3dB waveguide splitter with waveguide ports in red (a) and an equivalent signal flow graph representation showing nodes as dots and the paths between them as arrows (b).

5.3.1 Solving Signal Flow Graphs

A signal flow graph consists of an arrangement of nodes and branches representing locations within the network and the paths between them respectively. For illustrative purposes a rendering of the internal vacuum space of a fixed three-port 3dB waveguide splitter is shown alongside the complementary SFG representation with two loads having reflection coefficients, Γ_1 and Γ_2 and a source reflection, Γ_{SG}, in Figure 5.3.

The transfer function of any given path in this, or any other arbitrary arrangement may then be derived from Mason's gain formula, however to apply this method several terms must first be defined [128]. A path, P_n, is defined as the product of the branches connecting any two nodes without going through the same node twice, while any path ending on its starting node will be referred to as a first order loop, L(1). For two loops or paths to be defined as non-touching, they must not share any node or path in common. A first order loop coefficient on path P_n, written as $L(1)^n$ is a loop which shares no node with path P_n. Similarly, a second order loop coefficient, L(2) is the product of two loops which do not share a common node and a second order loop coefficient on path P_n, written as $L(2)^n$ is the product of two loops which do not share a node with each other or with path P_n. By calculating these terms, Mason's gains formula then provides a transfer function between any two nodes as:

$$T = \frac{P_1[1 - \Sigma L(1)^{(1)} + L(2)^{(1)}...] + P_2[1 - \Sigma L(1)^{(2)} + \Sigma L(2)^{(2)} + ...]}{1 - \Sigma L(1) + \Sigma L(2) - \Sigma L(3) + ...} \tag{5.3}$$

If nodes a_1 and b_2 are chosen in the 3dB splitter shown in Figure 5.3 then corresponding paths and loops are given:

$$\begin{aligned} P_1 &= S_{21} & L_4 &= S_{21}S_{12}\Gamma_{SG}\Gamma_2 \\ P_2 &= S_{31}\Gamma_3 S_{23} & L_5 &= S_{31}S_{23}S_{12}\Gamma_{SG}\Gamma_2\Gamma_3 \\ L_1 &= S_{11}\Gamma_{SG} & L_6 &= S_{13}S_{21}S_{32}\Gamma_{SG}\Gamma_2\Gamma_3 \\ L_2 &= S_{22}\Gamma_2 & L_7 &= S_{23}S_{32}\Gamma_2\Gamma_3 \\ L_3 &= S_{33}\Gamma_3 & L_8 &= S_{31}S_{13}\Gamma_{SG}\Gamma_3 \end{aligned} \tag{5.4}$$

Graphical representations of all loops and paths are also provided in Figure 5.4. Substituting these terms into Mason's formula then provides the following transfer function between the nodes:

$$T = \frac{P_1[1-L_3]+P_2}{1-(L_1+L_2...L_8)+(L_1L_2+L_1L_3+L_1L_7+L_2L_3+L_2L_8+L_3L_4+)-(L_1L_2L_3)} \tag{5.5}$$

Note that in RF networks with a circulator between the source and modelled component no signals directed towards the source return meaning all terms with Γ_{SG} then reduce to zero, greatly simplifying the equation. To validate this method the reflection coefficient of the third port, Γ_3, was set as a complex impedance providing a full reflection with several different various phase shifts and Equation 5.5 was used to generate the resultant transfer function for each. Numerically, a perfect short results in a reflection coefficient of -1, however if the short does not occur immediately at the port then a phase shift will also be imparted based on propagation time of the signal. In WR90 waveguide the phase velocity of a monochromatic signal propagating in the TE_{10} mode is given:

$$v_p(f) = \frac{c}{\sqrt{1-\left(\frac{c}{2a\cdot f}\right)^2}} \tag{5.6}$$

From 11 to 13 GHz the wavelength decreases by over 21%, corresponding to an 7% percent increase in the phase velocity. Hence, if accurate results are desired over a wide band, these effects are significant and must be considered. For a length of WR90 waveguide the time delay for each frequency component may then be calculated as the length of the section divided by the phase velocity:

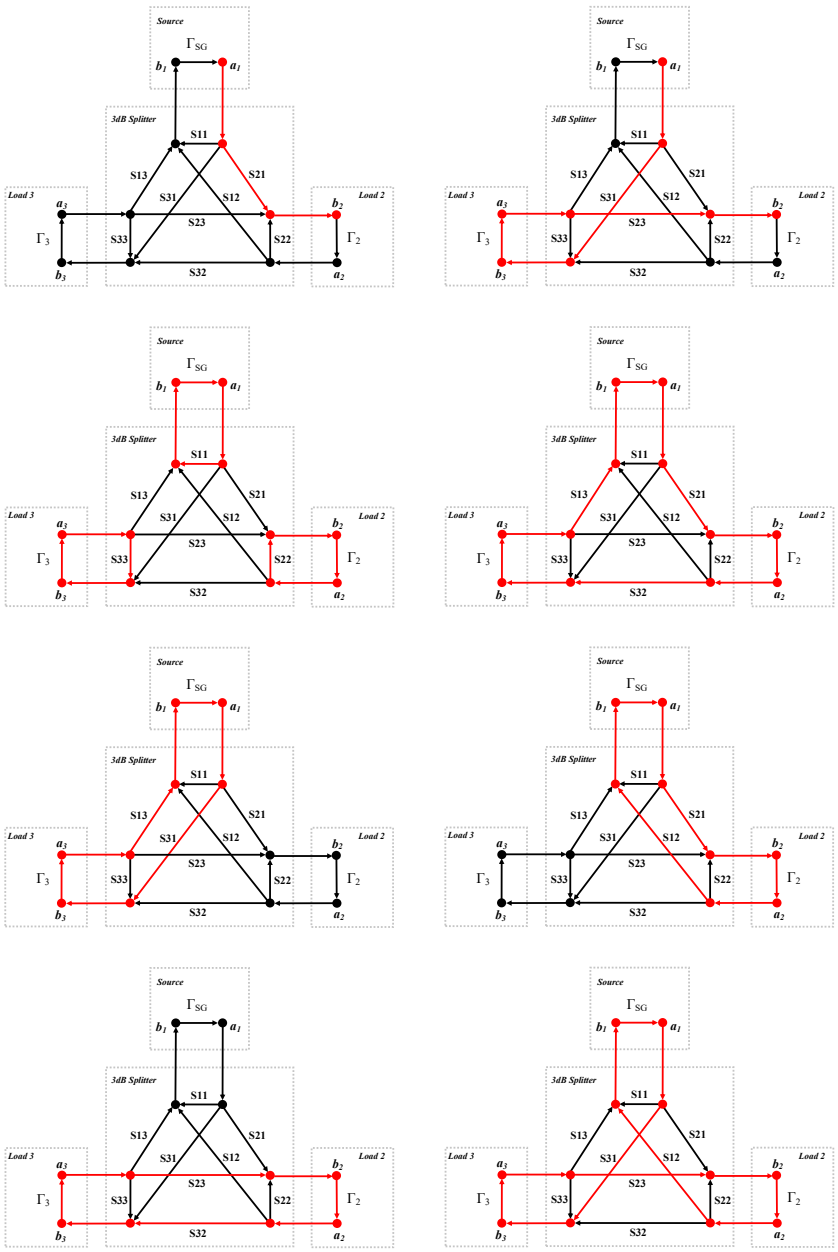

Fig. 5.4 All possible paths and loops for S21 on the 3dB splitter signal flow graph.

$$t_{delay}(f) = \frac{L}{v_p(f)} \tag{5.7}$$

For each component this can then be converted to a phase shift in degrees as:

$$\phi(f) = \frac{2\pi \cdot t_{delay}(f)}{T} = 2\pi \cdot f \cdot t_{delay}(f) \tag{5.8}$$

Where T is the period of a given frequency. For a short placed at a distance, L, downstream from one of the output ports, a complex reflection coefficient for each frequency component may then be calculated from this phase shift via Euler's formula as:

$$\Gamma(f) = -\mathrm{e}^{i \cdot 2 \cdot \phi(f)} = -\cos\left(2 \cdot \phi(f)\right) - i \sin\left(2 \cdot \phi(f)\right) \tag{5.9}$$

Where the phase shift is doubled due to the fact that the wave must make a round trip and the term is negated due to the aforementioned reflection coefficient of -1 associated with a short circuit. This equation was then used to calculate the reflection coefficients for various lengths of waveguide in the SFG method. To verify the results of the SFG method a 3D model of the splitter was then imported into electromagnetic simulation software, CST Microwave Studio. The same effect was achieved by placing an perfectly conducting boundary at various distances from the third port and running the frequency domain solver to generate the corresponding S-parameters. The results of each method are plotted in Figure 5.5.

The results of the study show that the SFG method provides accurate results over the full range of the imported S-parameters. Small differences are apparent in the depth of the minima and this is assumed to be caused by discrete changes in meshing in the 3D simulation and indeed the point to point resolution of the spectrum. While this example is solvable by hand it is clear that devices with additional ports and multi-component networks quickly become unworkable as the number of terms quickly rises. However, due to the repetitive and systematic nature of the process, counting such terms is a task well suited for code. An appropriate algorithm could then quickly provide the transfer function for large networks.

Upon production of an RF network and allocation of nodes, the determination of paths between them and any associated loops becomes a path-finding problem. Fortunately this is an active area of research in many fields of robotics and so several algorithms exist for doing so.

In conventional path-finding algorithms such as Dijkstra's algorithm and A^* it is the shortest path which is often of interest, meaning they are not well suited to this purpose [129, 130]. A viable option however is the modification of the depth-first search

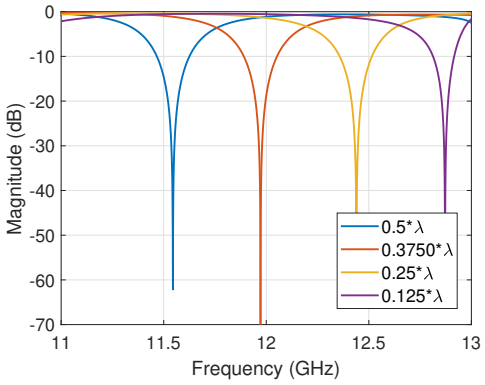

(a) Transmission of a splitter with the third port shorted at a distance of and wavelengths respectively as simulated in CST MWS.

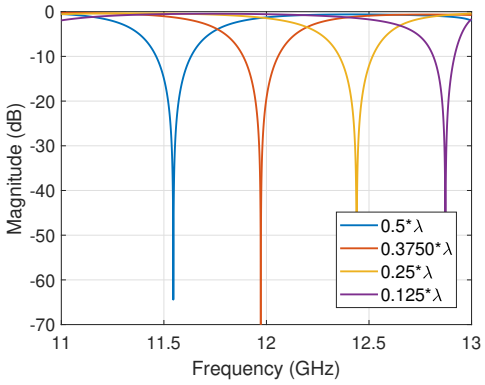

(b) Transmission of a splitter with the third port shorted at a distance of and wavelengths respectively as calculated via the SFG method.

Fig. 5.5 Comparison of the S21 of a 3dB splitter with a short circuit placed on the third port as calculated by 3D electromagnetic simulation in CST Microwave Studio and the SFG method respectively. Shorts were placed at distances corresponding to fractions of the wavelength of the 11.9942 GHz operational frequency.

(DFS), an algorithm for traversing or searching graph-like structures by exploring each series of connected nodes in succession. This can be used to produce an exhaustive list of paths but not to produce an exhaustive list of loops and so some modification is still required however the algorithm is nonetheless an appropriate choice. A signal flow chart of the planned RF network was produced by hand and the result is shown in Figure 5.6. An input file containing the name of each path and the nodes was then prepared.

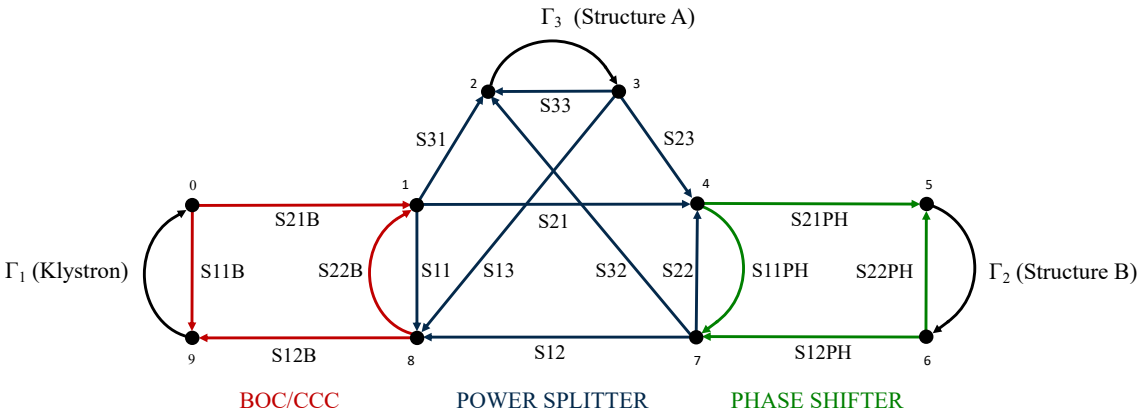

Fig. 5.6 Signal flow graph of the entire RF network planned for installation in Xbox-2.

Each path was stored in list format, with an entry for the path name and the two nodes which it connects. A recursive function was then written to perform the depth first search and store the resulting paths in an array. An empty list of length equal to the number of nodes in the network is first generated to store the nodes which have been visited. Two nodes are chosen corresponding to the start and end points of the desired transfer function. The program then commences at the start point and marks the corresponding index in the list as visited and adds the current node to the stored path, then uses simple conditional logic to exhaustively map out the potential paths. If current node is same as destination, then the current path is appended to a list which contains all successful paths. If the current node is not the destination, the function simply calls upon itself again in nested fashion, recurring for all the nodes adjacent to the current position provided they have not already been visited. Figure 5.7 shows an arbitrary network and the order in which the paths would be tracked out.

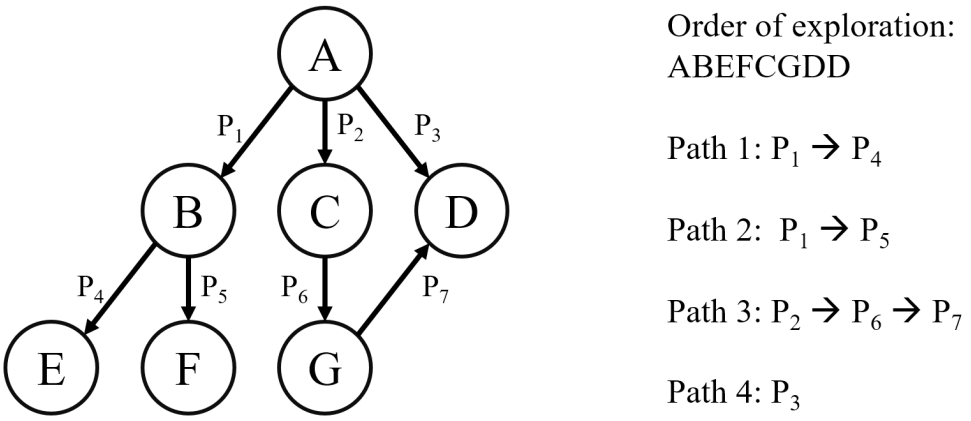

Fig. 5.7 Diagram showing the manner and order in which the recursive function would map out an arbitrary network.

The result is an exhaustive list of all viable paths from the start to the end point. While the algorithm is well suited to path generation additional logic was required to discern the loops in the network. A nested for-loop then runs the program with the start point as every node in the system and the destination as being every node which leads to the start point. The result is then an exhaustive list of closed loops within the system however due to the method in which the loops were calculated many duplicates are present. Additional logic was added to remove duplicate loops which start on different nodes. From this, the desired transfer is calculated from Mason's rule.

The code was tested with a generic two and three-port device as these particular cases are well known and defined in existing literature [131]. When running on a 3.4 GHz Intel Core i7-6700 the resulting code maps all paths and loops for a three-port device in 0.03 seconds and the full RF network comprised of the BOC, CCC, power splitter and phase shifter in 0.04 seconds, much of which is dedicated to the sequential printing of successful paths and loops for user viewing. Given the already small simulation no further optimisation was deemed necessary, however due to the exponential increase in possible paths associated with adding components adjustment may be necessary for solving larger networks.

5.3.2 Pulse Shape Variance

With the transfer functions of the system available the propagation of signals throughout the system could then be explored. A klystron pulses was generated as the product of an 11.9942 GHz sine wave and a square wave with a 10ns rise and fall time, comparable to the real klystron pulse. The time domain klystron pulse, $f_Kly(t)$, was then Fourier transformed as:

$$F_{kly}(\omega) = \int_{-\infty}^{\infty} f_{Kly}(t) e^{-j\omega t}\, dt \tag{5.10}$$

The resulting frequency domain signal was multiplied pointwise with the desired transfer function, T, and the resulting signal recovered in the time domain by taking the inverse Fourier transform as:

$$f(t) = \frac{1}{2\pi} \int_{-\infty}^{\infty} \left(T(\omega) \odot F_{kly}(\omega)\right) e^{j\omega t}\, d\omega \tag{5.11}$$

Where T is the transfer function between the two nodes of interest. Upon simulation of the full network it was noted that the pulses delivered to each port were different in shape. As this is a characteristic which is important in an operational context the effect was then examined in more detail. Compressed pulses of varying lengths were simulated with the full $1.5\mu s$ kystron pulse and a phase modulation was applied to provide an approximately flat top on the compressed pulse delivered to port 3. Figure 5.8 shows the resulting pulses delivered to each port.

Being the most apparent difference, it was initially suspected that the discrepancy was due to inclusion of the phase shifter, the S-parameters of which are shown in

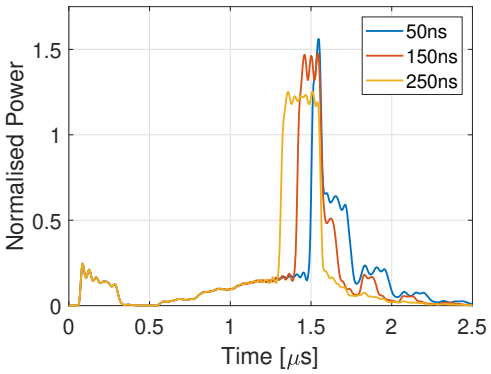

(a) The RF pulses directed to port 2.

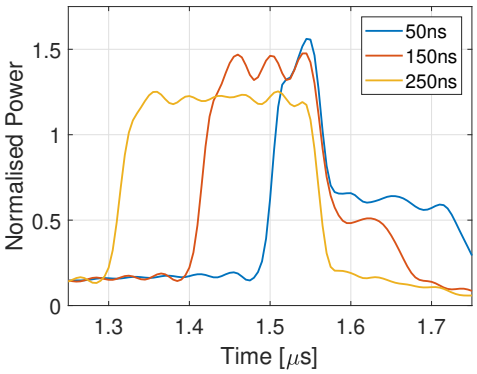

(b) Close-up of the compressed pulses delivered to port 2.

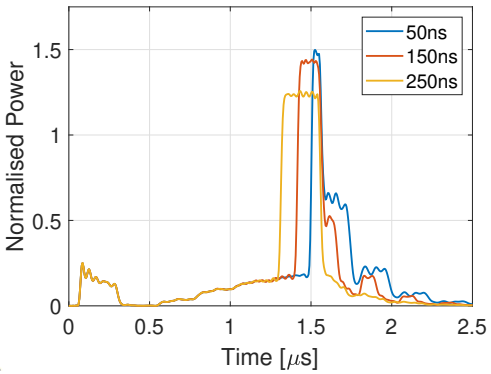

(c) The RF pulses directed to port 3.

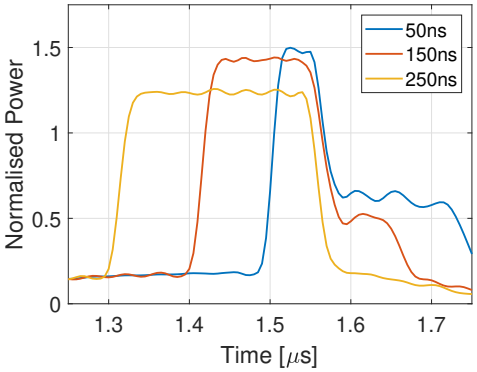

(d) Close-up of the compressed pulses delivered to port 3.

Fig. 5.8 Simulation results showing the pulses directed to port 2 (a and b) and port 3 (c and d). A full 1.5 μs klystron pulse has been used with phase modulation which has been tuned to provide an approximately flat pulse at port 3.

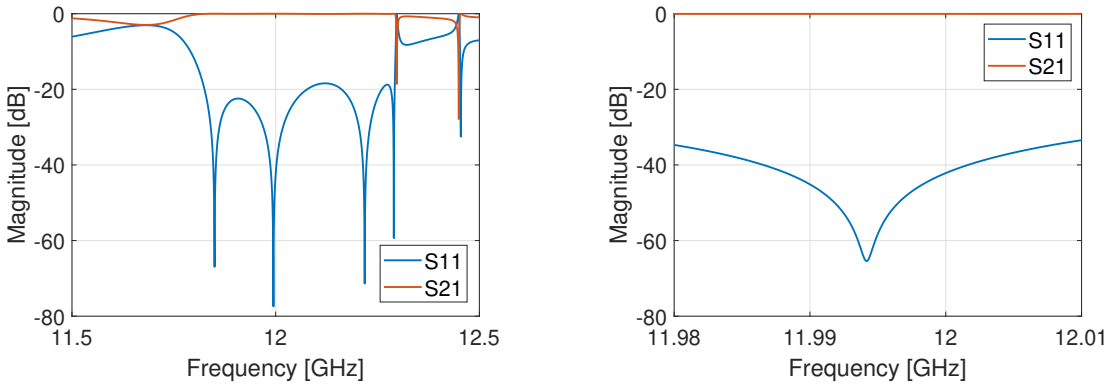

(a) Wideband view of the transmission. (b) Close-up of the operating region.

Fig. 5.9 S-parameters of the variable phase shifter with the piston in the central position showing relatively wideband transmission.

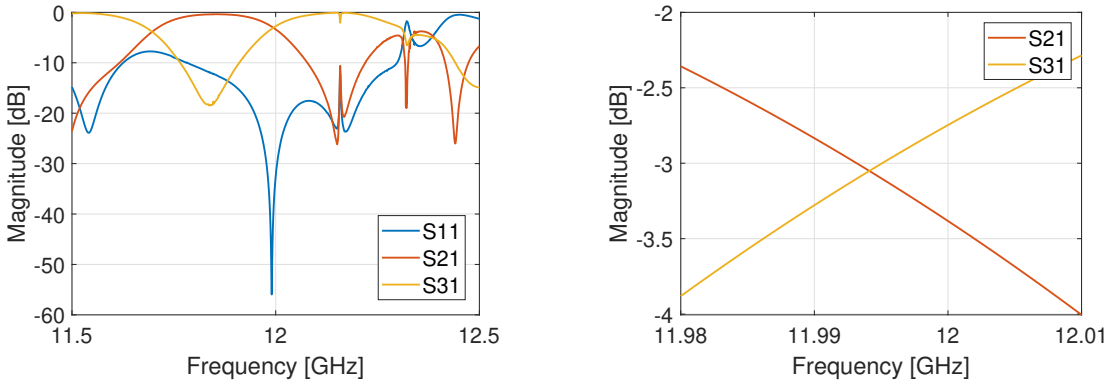

(a) Wideband view of the transmission. (b) Close-up of the operating region.

Fig. 5.10 S-parameters of the power splitter with the piston in the central position.

Figure 5.9. However it can be seen that the device boasts a relatively wideband transmission and simulations showed that it does not result in an observable change in any 12 GHz pulse.

It was instead found that this is an inherent property of the power splitter itself. In an approximately central position, the device has the S-parameters shown in Figure 5.10.

The device splits equally at the 11.994 GHz operating frequency, however the pulsed signals during operation are not monochromatic signals, instead being composed of a spectrum. The different frequency components associated with the sharp rise and fall times of the incoming pulse are then attenuated differently, with each port effectively acting as a low and high-pass filter respectively, sufficient to noticeably alter

the resulting pulse shapes. As a consequence, during operation only one structure may receive a flat pulse and this effect was later validated experimentally in Chapter 6.

5.3.3 Simulation of Power Flow During Breakdown

With a working a model an investigation was then carried out to examine the effects of breakdown during operation. The results of the study may then shed light on which relative phasing between structures provides the greatest risk and indeed what attenuation is required on each signal chain in order to provide a reasonable dynamic range while preventing damage to LLRF system. Three arrangements were investigated with the power splitter piston completely inserted, in the central position, and fully retracted. Figure 5.11 shows a rendering of the power splitter in CST MWS and the three piston positions in which simulations were performed.

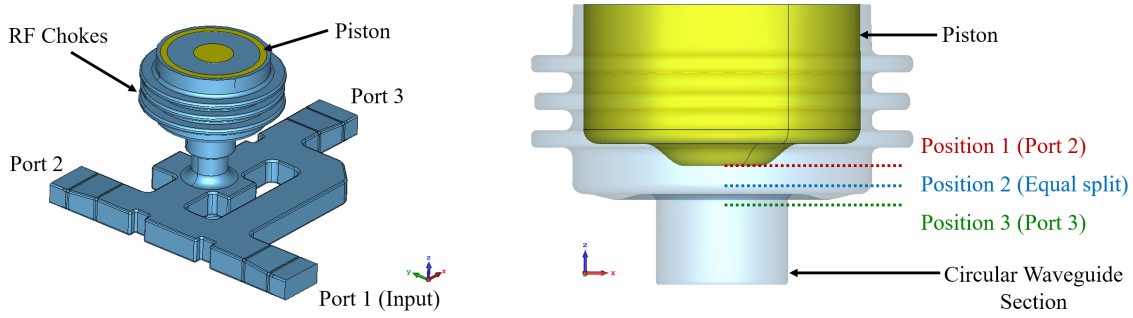

(a) (b)

Fig. 5.11 The vacuum geometry of the variable power splitter (a) and a cross section of the variable piston which acts as a short for a section of circular waveguide (b). The piston positions for which S-parameters for the SFG model were retrieved in CST MWS are also shown.

Although the model and code can quickly describe the forward and reflected waves at any node in a given system, S-parameters are time-invariant and hence not suited to modelling dynamic loads. Fortunately, several characteristics of breakdown may be exploited in order to provide a reasonable estimate of what may occur during operation. It has been shown that the thermal runaway and subsequent plasma formation during breakdown takes place on a very short timescale, typically on the order of nanoseconds [55]. Additionally, in previous high-power tests breakdowns have been observed to occur immediately upon receipt of high-power RF and an example of this occurring during the test of the CLIC crab cavity is shown in Figure 5.12.

What is of interest in the study is the manner in which the incoming power is then directed to the rest of the network during breakdown and such situations then

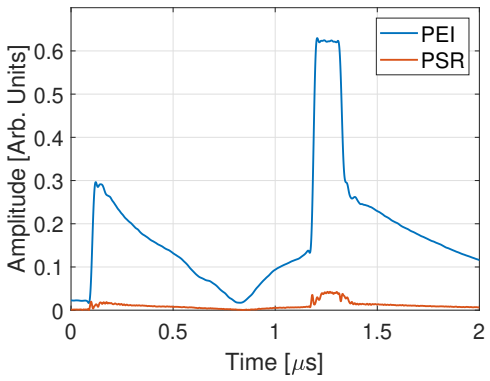

(a) Nominal transmitted and reflected signals during operation.

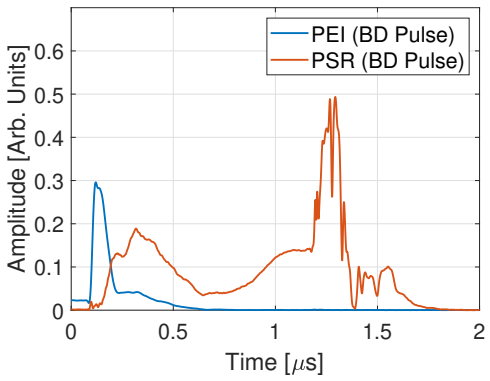

(b) Transmitted and reflected signals during a breakdown which has occurred at the beginning of the RF pulse.

Fig. 5.12 The transmitted and reflected pulses during a non-breakdown pulse (a) and a pulse in which a breakdown has occurred immediately upon arrival of the RF pulse (b). Both examples have been taken from the results of the CLIC crab cavity test.

represent the most extreme case. Hence, a reasonable approximation may be obtained by assuming that the port corresponding to one of the structures in the simulated network is shorted, calculating the corresponding transfer functions and observing the amplitude of signals directed to the other structure and back to the klystron. Various phase shifts, attenuation and dispersive effects may also be imparted on the shorted port to simulate breakdowns in any spatial position within the structure. The network then effectively acts as a two-port device and the transfer functions may be calculated with the code outlined in Section 5.3.1. With the transfer functions, the time domain reflection to the klystron (f_{PKR}) and incident signal to the non-shorted port (f_{PSI}) may then be recovered as:

$$\begin{aligned} f_{PKR}(t) &= \frac{1}{2\pi}\int_{-\infty}^{\infty} \left(T_{S11}(\omega) \odot F_{Kly}(\omega)\right) e^{j\omega t}\, d\omega \\ f_{PSI}(t) &= \frac{1}{2\pi}\int_{-\infty}^{\infty} \left(T_{S21}(\omega) \odot F_{Kly}(\omega)\right) e^{j\omega t}\, d\omega \end{aligned} \tag{5.12}$$

Where F_{Kly} is the frequency domain klystron pulse and T_{S11} and T_{S21} are the transfer functions of the system with one port shorted, serving as quasi S-parameters.

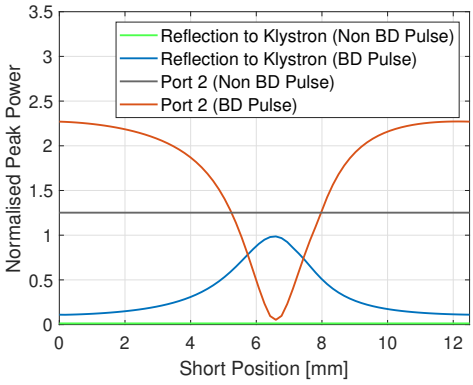

(a) Peak power delivered to the klystron and port 2 during a breakdown in port 3 as a function of the short location.

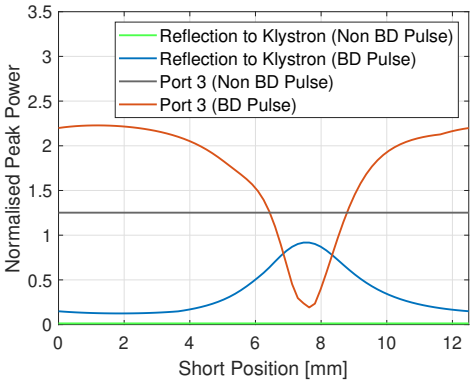

(b) Peak power delivered to the klystron and port 3 during a breakdown in port 2 as a function of the short location.

Fig. 5.13 Peak Power normalised to the klystron pulse directed to the neighbouring structure and back towards the klystron as a function of reflection phase and hence breakdown location. The power splitter piston was in the central position and hence split the power equally between port 2 and port 3. Also shown is the peak power delivered to the port during a non-BD pulse.

Central Position

It is expected that for much of the test the power splitter will split the incoming power equally, and hence the piston will be in the central position. As such, this is arguably the position of greatest interest. A loop was written to calculate the necessary transfer functions and expected waveforms for shorts on each port, while also importing a range of phase shifts (corresponding to different breakdown locations). The peak reflected power towards both the klystron and the neighbouring structure are shown for a breakdown at port 2 and port 3 in Figure 5.13. For the study the phase flip was not optimised to provide maximum compression, as it is simply the ratio between the shorted and non-shorted pulses which is of interest.

Relative to the compressed pulse which would be nominally delivered to each structure, a breakdown can result in an surge in power of approximately 80% being sent to the neighbouring structure, corresponding to a 34% percent increase in the established surface electric field. It is speculated that this surging may then result in a secondary intra-pulse breakdown in the neighbouring structure, and evidence of such intra-pulse events has previously been recorded even in single structure arrangements [37]. Conversely, if phased correctly, almost complete destructive interference occurs, with the pulse instead being partially reflected towards the klystron and the remainder

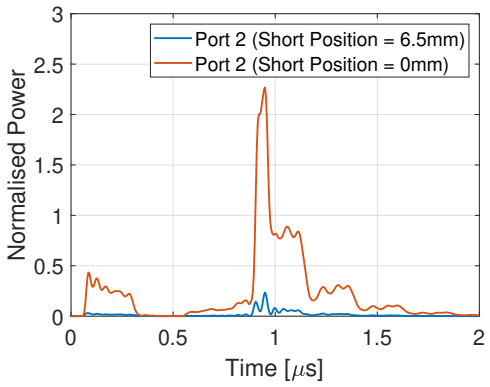

(a) Peak power delivered to the klystron and port 2 during a breakdown in port 3 as a function of the short location.

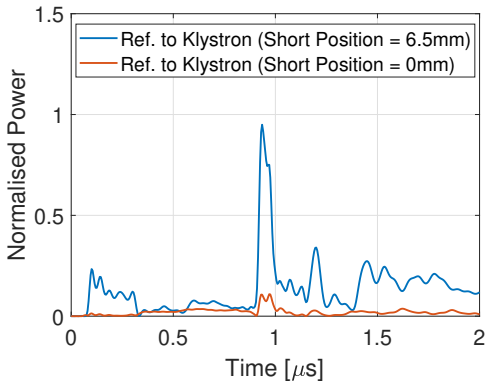

(b) Peak power delivered to the klystron and port 3 during a breakdown in port 2 as a function of the short location.

Fig. 5.14 Pulses (normalised to the klystron power) directed to the neighbouring structure and back towards the klystron for the short length in port 3 which results in the maximum and minimum value of each. The power splitter piston was in the central position and hence split the power equally between port 2 and port 3.

dissipated within the RF network. Examples of the pulse shapes for the short lengths which results maximum and minimum surges and reflections are shown in Figure 5.14.

In accelerating structures, the reflected signal during breakdowns is typically phased at integer multiples of the phase advance per cell [40, 46]. However the absolute phase advance between two given components is determined by the waveguide network. The results above show that through appropriate design choices, the propensity for surging may be minimised for a given RF network.

Full Insertion and Retraction

The next position investigated was with power splitter in its extremities. These positions are of interest as they determine whether or not arcing can result in the other structure receiving power whilst nominally in the off position. With the power splitter piston fully retracted all power is nominally directed to port 3, when fully inserted all power is nominally directed to port 2. The study was then repeated with the piston fully inserted and retracted respectively and a short placed on the port to which the power is nominally directed.

Simulations show that there is no reflected phase and hence spatial position at which a breakdown could result in the direction of power towards the structure in the off state. Monitoring the power reflected back to the klystron a clear wave pattern is present over a small range however it is clear that the majority of the power is instead

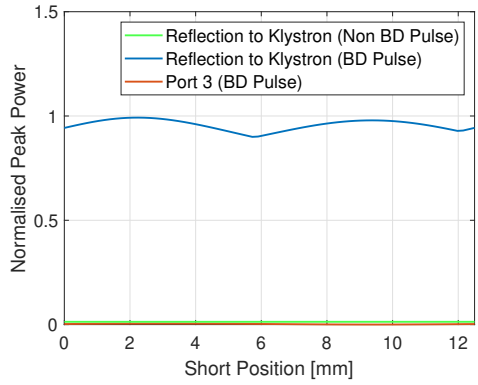

(a) Peak power delivered to the klystron and port 3 during a breakdown in port 2 as a function of the short location. The piston was in the fully inserted position and hence all power is nominally directed to port 2.

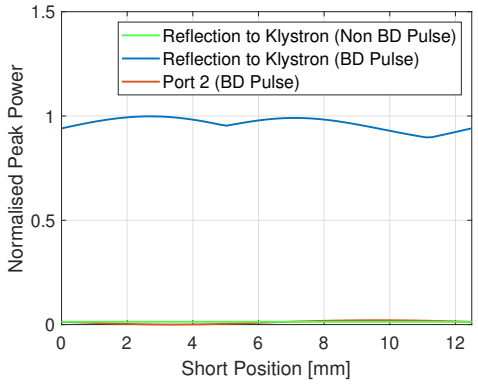

(b) Peak power delivered to the klystron and port 2 during a breakdown in port 3 as a function of the short location. The piston was in the fully retracted position and hence all power is nominally directed to port 3.

Fig. 5.15 Peak Power directed to the neighbouring structure and back towards the klystron as a function of reflection phase and hence breakdown location.

dissipated within the RF network. This result was then checked in 3D simulation by fully retracting and inserting the piston then placing a short on the port to which the power is directed. The pulse reflected to the klystron generated by the SFG model and the S21 produced by 3D simulation are both shown in Figure 5.16.

3D electromagnetic simulation confirmed that even when shorted, virtually no power is directed to the neighbouring port. Although heavily degraded a substantial portion of the compressed pulse is reflected to the klystron, with the rest being dissipated within the walls of the RF network. Notably, in Figure 5.16 several discharges following the compressed pulse are also present likely caused by the BOC and CCC being charged again by the incoming reflections and discharging in the reverse direction. However the pulse compression scheme was measured as being 45% efficient and so the energy in the pulse which reaches the klystron is nonetheless greatly reduced [119]. Additionally, unlike the previous SLED models which can reflect signals with small rise times the BOC is effectively a travelling wave device, meaning the reflection must traverse the surrounding waveguide section and cannot be reflected directly to the klystron. The results of the study then show that the device on the neighbouring port will remain largely isolated, even during breakdown events.

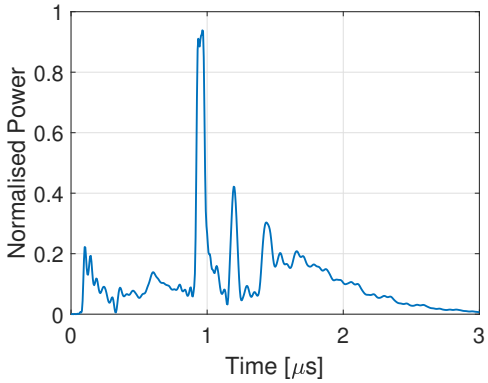

(a) Signal reflected towards klystron predicted by the SFG model when the piston is inserted (all power directed to port 2) and an arc occurs.

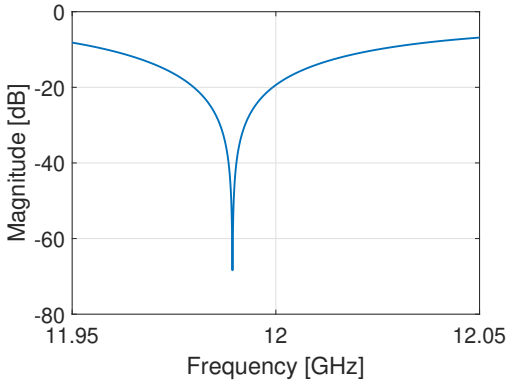

(b) Transmission to port 3 of the power splitter with the piston fully inserted and a short placed on port 2 as generated by 3D-Simulation in CST MWS.

Fig. 5.16 Pulse reflected towards the klystron. Note the secondary discharges following the main compressed pulse which occur due to the inclusion of the BOC and CCC in the simulated RF network.

Reflection During Dual Breakdowns

Finally, it was speculated previously that the propensity for surging in the neighbouring port during breakdown is liable to cause a secondary, intra-pulse breakdown. Similarly, although the probability is low, given that two structures are being tested in parallel it is also possible that both breakdown independently on a given RF pulse. To investigate the power flow during this arrangement, both ports on the power splitter were swept and the resulting S_{11} values and reflections were monitored. Figure 5.17 shows for when both ports are shorted on the output.

Sweeps were performed with both shorts in a variety of positions however as expected in each case virtually all incoming power is reflected from the power splitter with the phase of the reflections having little effect. Once again due to the losses associated with the pulse compression system, the reflected energy is one again greatly reduced and constitutes no risk beyond that which is regularly encountered in the test stands.

Conclusion

During operation breakdowns in one structure can result in an surge in power of approximately 80% percent being sent to the neighbouring structure, corresponding to a 34% percent increase in field for the remainder of the pulse. In such cases the

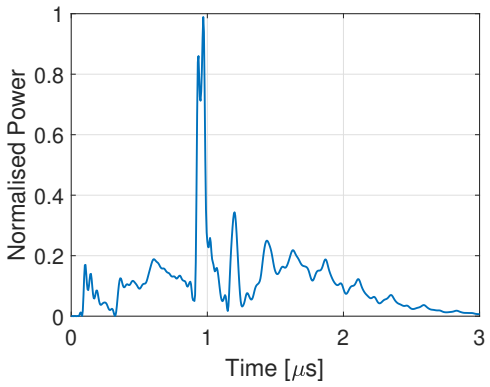

(a) Signal reflected towards klystron predicted by the SFG model when both power splitter ports are shorted.

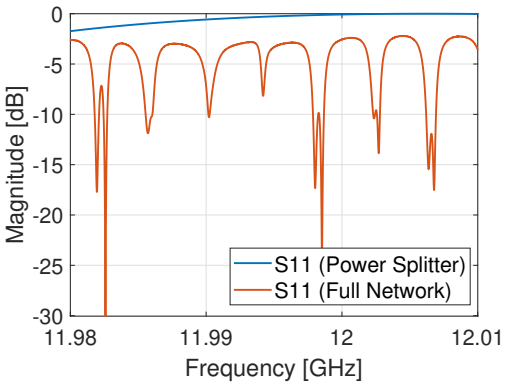

(b) S_{11} of the power splitter and the full RF network when both outputs are shorted.

Fig. 5.17 Pulse reflected towards the klystron (a) and the S_{11} of both the power splitter and the full RF network when both power splitter ports are shorted (b).

induction of a secondary breakdown on the same pulse is speculated to be a potential outcome. During breakdowns in a single structure approximately 35% percent of the total energy is directed back towards the klystron in the form of a heavily degraded pulse. Given that in previous tests the entire RF pulse is regularly reflected during breakdown the risk to the klystron associated with the potential reflections in this arrangement is thought to be lower than that which is normally encountered in the test stands.

In the event that the aforementioned dual breakdown were to occur however, full reflection is observed from the power splitter. Due to the losses associated with the other components in the network however, the peak and average power reflected to the klystron remain low. The results of the study are compared with experimental data in Chapter 6.

5.4 Simulation of Field Emission in a Multi-Structure System

CLIC accelerating structures operate with peak surface electric fields in excess of 200 MV/m. At this level, the spontaneous emission and acceleration is observed as detailed in Section 2.1. This is typically referred to as dark current and its presence has design consequences for any high-gradient facility. Due to the lack of focusing captured electrons are liable to strike the irises within the accelerating structure, leading to

generation of X-rays which will dictate the shielding requirements for the beamline and indeed this has aspect in particular has been studied in detail [38, 40]. Similarly, the current can also form a halo around main beam bunches, increasing the emittance and necessitating collimation. If sufficiently large this current can also interact with sensitive diagnostic equipment, reducing the dynamic range of the equipment and acting as a source of experimental error.

The exact conditions for capture in an accelerating structure are well defined, requiring only that an electron remains maintains synchronicity with the oscillating RF fields in the longitudinal direction while remaining sufficiently focused to avoid collimation. However the accelerating structures for CLIC are designed such that to remain synchronous passing bunches must be relativistic, a condition not met by field emitted electrons upon ejection from the surface. In travelling wave structures however, it has been shown that it is possible to inject low velocity electrons on axis into a relativistic accelerating structure such that the phase of the electron will slip relative to the wave in such a way that they asymptotically approach the synchronicity [4]. As a consequence, the injection of low energy electrons into such structures is a commonplace technique as it greatly simplifies the design process and offers flexibility in term of the structure applications. Given the phase velocity in the CLIC structures, the capture threshold for an on axis electron has been more concisely expressed in MV/m as [93]:

$$E_0 \geq \frac{1.6}{\lambda} \tag{5.13}$$

This equation demonstrates that the field required for capture then scales with frequency and in the X-band CLIC structures, this value is on the order of 65MV/m. Following this, in an accelerating structure with electric field of amplitude E_0, it has been shown that the phase of an on axis electron relative to the crest of the wave can be defined [4]:

$$\sin\theta = \sin\theta_i + \frac{2\pi mc^2}{qE_0\lambda}\sqrt{\frac{1-\beta_i}{1+\beta_i} - \frac{1-\beta}{1+\beta}} \tag{5.14}$$

Where θ and θ_i are the phase of the electron and the electron at the time of injection respectively, m is the mass of the electron, c is the speed of light, q is the electron charge, and λ is the wavelength. Finally, β and β_i refer to the ratio of the electron velocity to the speed of light at the exit and at the time of injection respectively. Due to the acceleration however, the square root term on the right is positive and increases

with electron velocity. As the electron becomes relativistic and β approaches unity, the phase asymptotically approaches a constant value given [4]:

$$\sin\theta_\infty = \sin\theta_i + \frac{2\pi mc^2}{qE_0\lambda}\sqrt{\frac{1-\beta_i}{1+\beta_i}} \tag{5.15}$$

In field emission, the majority of the current is emitted at or close to the peak of the RF crest, when the field is greatest and the energy of such current is low. Setting $\sin\theta_i$ and β_i to zero then yields:

$$\sin\theta_\infty = \frac{2\pi mc^2}{qE_0\lambda} \tag{5.16}$$

This equation predicts that for high accelerating gradients, electrons on the beam line axis remain relatively close to the phase at which they arrive relative to the RF fields. However, this only applies to electrons which are on axis, and without transverse momentum. Hence, the equations do not account for the trajectories which may be taken by electrons immediately after emission. The peak surface electric fields in the CLIC accelerating structures are much larger than those on axis, generally by a factor of two. Although these fields are then sufficiently high that electrons become reach relativistic velocities within several millimetres, it is speculated that they will accumulate significant transverse momentum and a phase delay between the time of emission and the time at which the reach the beam line axis. The time of arrival and the transverse momentum acquired then largely determine whether or not a given particle is liable to become captured i.e. continue gaining energy continuously, or rejected.

Finally, in the CLIC structures, the main beam is typically injected earlier than the crest of the RF period in order to maximise the energy gain across the cell. However, the surface electric fields in a given cell are greatest at the peak of the RF period and thus the emission is also thought to be largest at this moment. Taking both this and the aforementioned preliminary behaviour of emitted electrons into account it is expected that much of the dark current will then lag behind the main beam. The following Chapter details full 3D simulations pertaining to these effects in CST MWS.

5.4.1 Simulation Setup and Approximation of Emission Characteristics

To study the phenomenon full 3D simulations were performed in the CST Studio Suite software package. As the superstructure planned for testing in Xbox-2 is comprised of two TD26CCR05 structures, this design was chosen for simulation. The RF design is briefly outlined later in Section 6.1, however the results are thought to apply to any constant gradient design.

First, the geometry of the vacuum space within a single TD26CCR05 structure was imported into the frequency domain solver where a field monitor was deployed at at 11.9942 GHz to generate the corresponding electric and magnetic field distributions. In the CST frequency domain solver all fields are normalised to an input power of 1W, meaning renormalisation is required to examine the behaviour at high gradients. The resulting fields were then imported into the particle-in-cell (PIC) solver and the amplitude was parameterised with the inclusion an adjustment factor. A calculation line was placed along the beamline axis and used to calculate the net acceleration experienced by a fully relativistic particle, in this way the effective gradient could then be set to any desired value and checked without further calculation. A geometry which acts as the cavity surface was then generated by creating a copper block and using the built in Boolean functions to subtract the vacuum space of the structure. Field emission is a phenomenon with a strong dependence on surface field and in modern high-gradient structures the regions of peak electric field occur on the irises. As such, it is speculated that this is where emitted current density is highest during operation. The iris of each cell was then set as a homogeneous emission surface as it is not known the emission sites are actually distributed in this region. Figure 5.18 shows a cross section of the simulation geometry and the highlighted emission areas.

The built-in CST MWS field emission model was chosen as the particle source. A field enhancement factor of 30 was assigned to the emission area on the copper cavity surface, as is typically measured in high-gradient structure tests [38, 50, 132, 133]. Upon mesh generation it was noted that the imported electric and magnetic fields are automatically interpolated by the PIC solvers hexahedral meshing. This is a consequence of the fields having been generated by a tetrahedral mesh. Initial simulations showed that the interpolation between points lying inside the copper and those immediately outside in the vacuum had led to the incorrect generation of surface fields. Additionally, due to the internal curvature on one side of the cell asymmetric behaviour was observed on every iris due to the automatic adjustment of the mesh density by CST. Previous work by SLAC has shown that the capture of an electron is

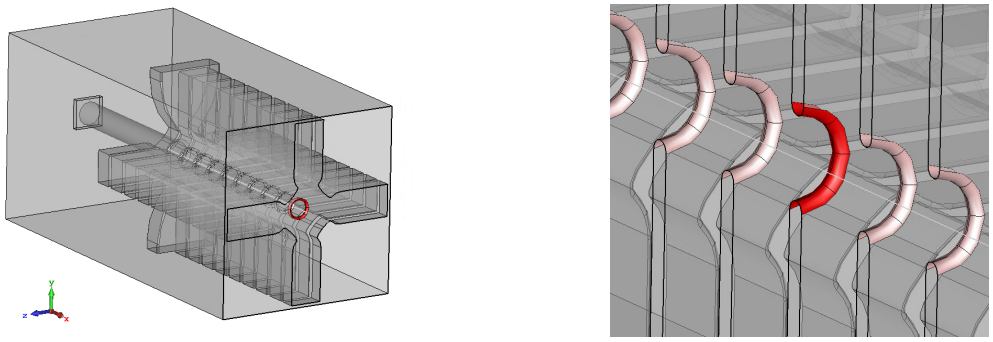

(a) (b)

Fig. 5.18 Rendering showing a cross section of the simulation geometry (a) and a close-up of the irises showing an emission area highlighted in red (b).

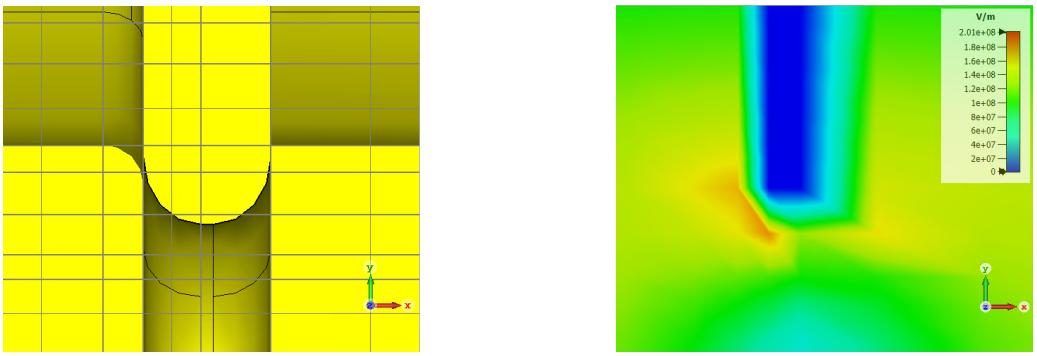

(a) Poor meshing of the cell iris.

(b) Poor E-field generation as a consequence of extrapolation between coordinates in the mesh.

Fig. 5.19 CST results showing poor meshing of the iris (a) and the heavy aliasing caused by the interpolation of the imported field (b) likely to result in emission on the left side only. Field values in (b) are normalised to a structure input power of 1W.

closely related to the position of the emission on the iris, indicating that a 3D simulation under these circumstances would not yield results representative of a real structure [134]. Figure 5.19 shows the poor surface field generation caused by interpolation of a field generated with the tetrahedral solver on to the hexahedral mesh.

This may be rectified in several ways, the first is by manually adjusting the mesh density surrounding each emission surface individually. Alternatively, if exact positioning control is desired it is also possible to place small slots internally within the volume of the iris such that they do not interact with the fields. CST includes the option to snap mesh lines to planar surfaces which if activated will then ensure meshing then occurs exactly where desired as shown in Figure 5.20.

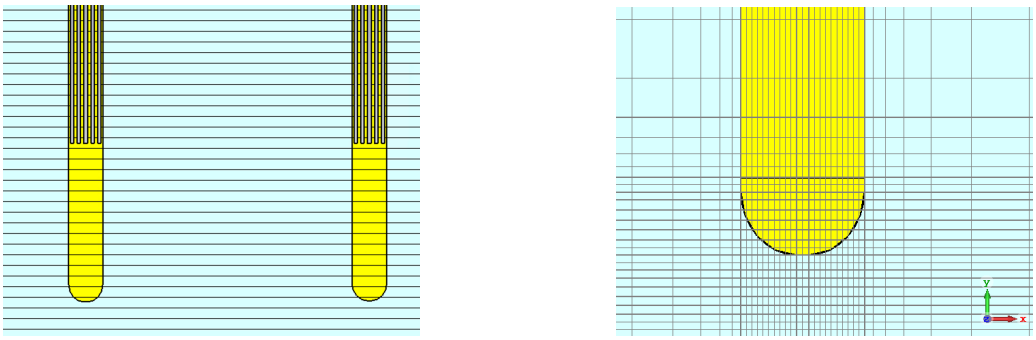

(a) Voids included within the cell walls.

(b) Improved meshing localised to the curvature of the iris.

Fig. 5.20 CST rendering showing the voids included within the copper iris (a) and the resulting increase in mesh density localised to the iris (b). As the voids are located within the copper iris they are isolated from the relevant simulation volume and have no effect on the results.

Both methods are capable of producing comparable results in terms of the final meshing however a mesh convergence study is nonetheless required. By parameterising the density in the former method it is possible to do so with relative ease and so it was taken forward for simulation. Following the mesh convergence study, a hexahedral cell boundary was set every 0.075 mm on the irises, resulting in a simulation with approximately ten million hexahedral cells for the full simulation volume. With all irises emitting and an in-simulation time of 2ns the solver run time was on the order of one day on a 3.2 GHz octa-core CPU. As this facilitated the generation of all necessary results within a reasonable time frame the setup was deemed acceptable and taken forward without further simplification or optimisation. For early simulations, four 2D monitors were placed in the beam pipe at the structures input and output. The first pair were placed where the second structure would be adjoined and were intended to monitor the current which would reach the subsequent structure. The second pair were placed several centimetres farther upstream and downstream respectively, where the detection surface of a Faraday cup would be located in a real experiment as shown in Figure 5.21, the data from these monitors could then be used to fit the results to existing experimental results.

The input of particles to the system through emission was equal to the loss of particles from the system after approximately 10 RF periods or 0.75ns. Given that the structure operates with a 120° cell to cell phase advance and has 26 cells and 2 couplers this corresponds to when the current emitted in the input coupler reaches the downstream monitor. The results quoted following were then taken by extracting the

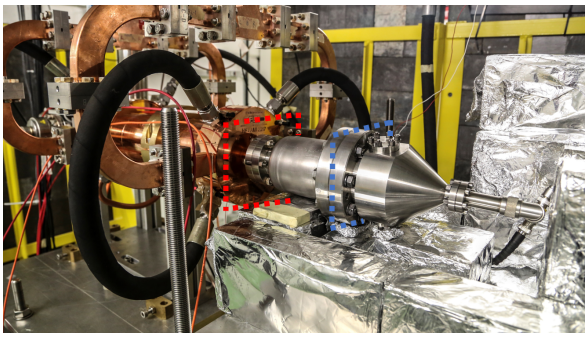

Fig. 5.21 The T24 PSI2 structure under test in the Xbox-2 test slot. Planes shown by the red and blue dashed lines indicate where the 2D monitors in simulation representing the structure output and Faraday cup detection surface correspond to experimentally.

macroparticle information logged by each monitor during the 10 RF periods after this when the system had reached a steady state solution.

Preliminary simulation results showed currents far beyond those observed experimentally, however in a real structure the emission is not truly homogeneous in nature but rather confined to discrete points on the surface with a sufficiently high field enhancement factor. As a result, only a small area is emitting at any given time. To account for this an effective emitter area factor, α, was defined as the ratio of the total area of the emission sites ($A_{emission}$) to the area of the iris (A_{iris}):

$$\alpha = \frac{A_{emission}}{A_{iris}} \tag{5.17}$$

The current density on the emission sites, J, was then scaled to reduce the total emission as:

$$J_{scaled} = \alpha \cdot J \tag{5.18}$$

Where J_{scaled} is the new emission density. Figure 5.22 shows the results of sweeping this correction factor in the range of from 1×10^{-7} to 2×10^{-5}.

Typical downstream measurements of the dark current in CERN's X-band test stands lie in the milliAmp regime while operating at an accelerating gradient of 100MV/m, and so an adjustment factor of 5.6×10^{-7} was found to be appropriate for future simulations [40]. With an approximately correct current observed at 100MV/m a preliminary sweep of gradient was then performed to ensure the results were in reasonable agreement with existing experimental data. Typically in the test stands, a

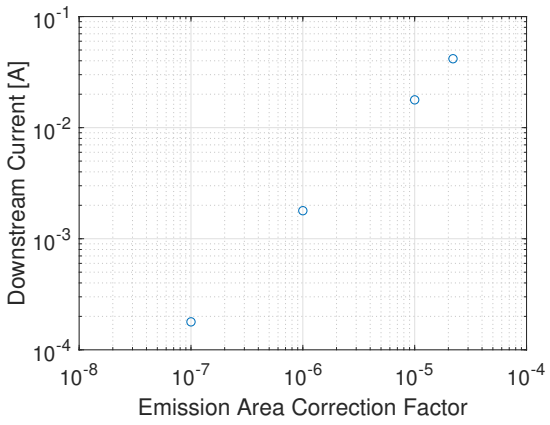

Fig. 5.22 Scan showing the downstream current averaged over eight RF periods when steady state has been reached versus the correction factor to account for fact only a small portion iris is thought to emit at a given time. Typical downstream measurements of the dark current lie in the milliAmp regime at 100MV/m and so an adjustment factor of 5.6×10^{-7} is found to be appropriate for future simulations.

measurable dark current signal emerges from the noise floor at gradients on the order of 70MV/m, equating to currents in the μA range. A sweep was performed from 70 to 110MV/m and both the absolute up and downstream currents were compared with that of existing data in addition to the ratio between them.

Simulation predicts that the upstream to downstream current ratio actually increases with gradient. In the case of the upstream signal the majority of the current is thought to be low energy and having been emitted from the first few cells as it is not phased to accelerate in this direction. Similarly the downstream will receive significant current from the neighbouring cells and these should increase comparably with increasing gradient. It was then suspected that the remaining discrepancy would be due to capture and acceleration of the electrons in the downstream direction and that any increase gradient in would would result in the downstream signal increasing more than the upstream.

Upon first glance existing experimental data shows the opposite however ramps over a long time frame accumulate breakdowns, thereby changing the emission properties of the structure and hence cannot be used as a reference. Instead it is necessary find examples of gradient changes without an intermediate breakdown. After close inspection several such regions were found in the experimental data, particularly when restarting the test stands after a pause in operation. In these regions the gradient has been slowly increased without breakdown and hence without significant changes in the characteristics of the emission sites on the cavity surface. Figure 5.24 shows a ramp

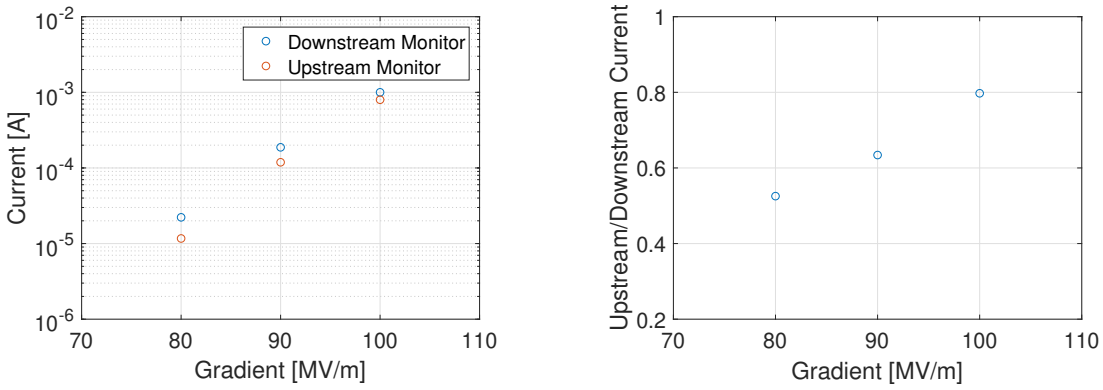

(a) (b)

Fig. 5.23 Simulation results showing the average current reaching the downstream and upstream monitors as a function of accelerating gradient (a) and the ratio between them (b).

in gradient in a T24 structure and the amplitude of the corresponding dark current signals during the process.

In such cases it can be seen that the experimentally observed characteristics agree with the simulated behaviour. If ≈ 1 mA of current is measured at the downstream Faraday cup at an accelerating gradient of 100MV/m simulations then indicate that several hundred milliamps of current is emitted within the structure itself. As the preliminary results demonstrated behaviour in agreement with existing experimental data the arrangement was taken forward for detailed analysis.

5.4.2 Capture Efficiency of a Single Structure Arrangement

As mentioned previously, the equations provided in section 5.4 describe the longitudinal behaviour of an on axis particle with no transverse momentum. However, electrons emitted from the irises are subjected to a significant transverse field component, and some time is required to reach the beam line axis. Due to the time-dependent rise of the fields, a particle traversing a given cell may experience a higher or lower transverse field component in the second half of the gap than in the first half, resulting in a net focusing or defocusing force which is dependent on the phase of the RF fields and the particle velocity. However, it is not clear whether any capture which occurs is due to such a focusing effect provided by the electric and magnetic fields or simply that the emission angle and surface electric fields result in a trajectory which does not intercept the irises downstream.

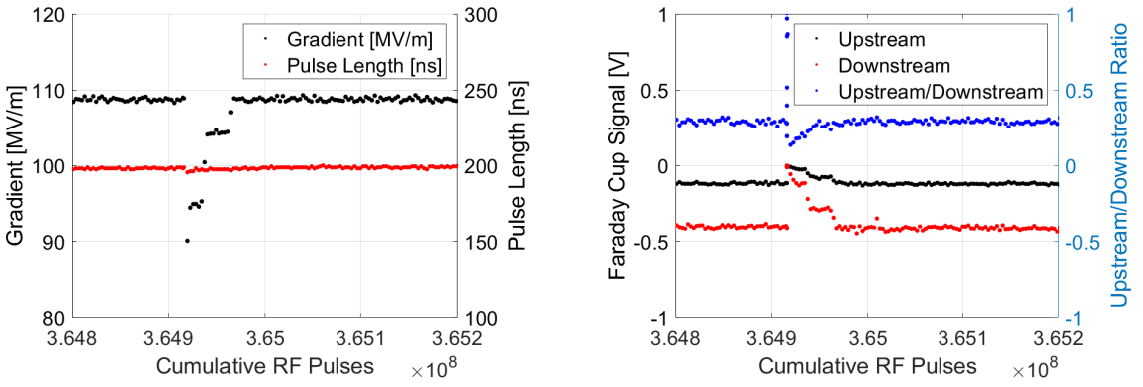

(a) (b)

Fig. 5.24 Experimental data recorded during the conditioning of the T24 PSI2 accelerating structure at CERN showing a ramp in operating gradient after a pause in operation (a) and the corresponding amplitudes of the downstream and upstream Faraday cup signals and the ratio between them (b).

To investigate this preliminary behaviour and provide an idea as to how any capture may occur, PIC simulations were performed in CST MWS. A single accelerating cell was imported in the eigenmode solver and the electric and magnetic fields were generated. Both the cell geometry and the fields were then imported in the PIC solver and repeated periodically with a phase advance of 120° between them to provide a three cell section of the full accelerating structure. As it is the preliminary behaviour of the emitted electrons which of greatest interest, a section of this length is thought to be sufficient while also greatly reducing the simulation time. It should also be noted however, that in this method the modelled section is then a constant impedance, constant gradient structure, something not possible in practice. However, given the relatively small changed in geometry and field across three cells in a full structure this is nonetheless thought to provide a reasonable approximation of the preliminary behaviour. The field in the cells was adjusted to provide an accelerating gradient of 100 MV/m for a fully relativistic particle and a small section of the iris was set to emit a single particle at different radial positions. As the objective is only to investigate the potential particle trajectories, the emission of the particles was forced, and the field emission model was not used for these simulations. The simulation was then run, with the emission commencing at different phases in the RF period. The particle trajectories associated with several emission phases of interest are shown in Figure 5.25.

In addition to the emission phase, simulations show that the position on the iris at which the emission occurs also strongly affects the probability of being transmitted

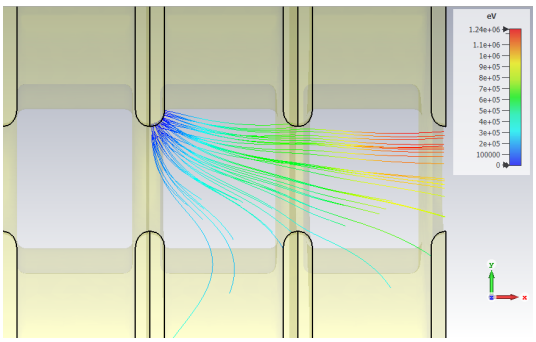

(a) Trajectories at an emission phase of 30°.

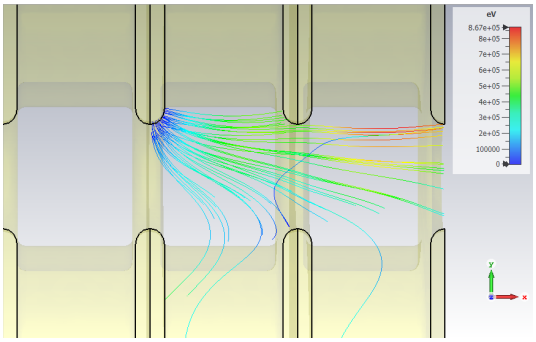

(b) Trajectories at an emission phase of 60°.

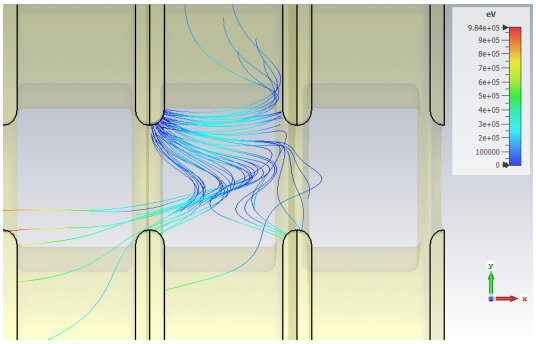

(c) Trajectories at an emission phase of 90°.

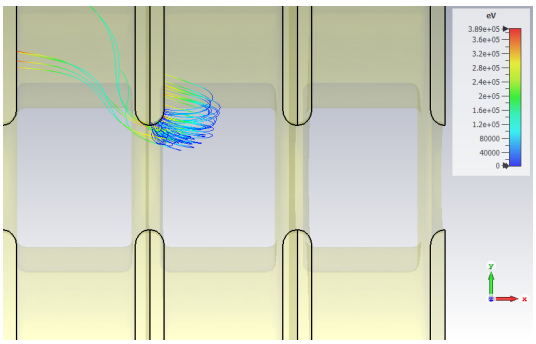

(d) Trajectories at an emission phase of 120°.

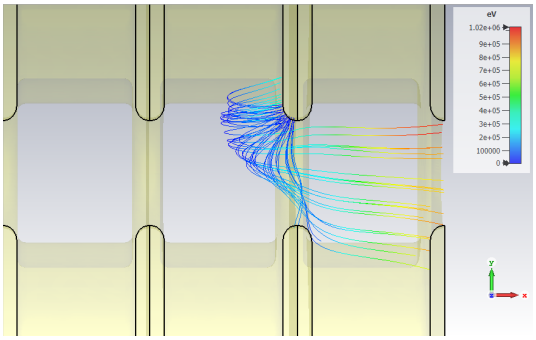

(e) Trajectories at an emission phase of 300°.

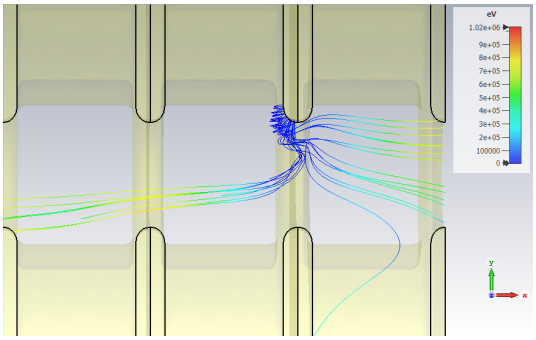

(f) Trajectories at an emission phase of 330°.

Fig. 5.25 Trajectories taken by particles emitted at various phases during the RF period. A phase of 90° corresponds to when the field in the middle cell is at its maximum. In the final two images (e, f) the current is emitted on the other side of the cell due to the reversed polarity of the field at these phases.

to the neighbouring cell and this result aligns well with work performed at SLAC in 2004 [39]. Particles emitted in the 30-60° phases showed a relatively high probability of transmission, with many of the particles reaching the subsequent cells. At each of these emission phases the maximum energy after having traversed two cells is on the order of 1MeV, corresponding to a velocity of 0.8c. As the cell lengths are fixed such that a fully relativistic beam requires a third of an RF period to traverse them, these particles will then slip relative to a fully relativistic bunch during transit until deceleration occurs or they reach an energy at which their velocity becomes ≈c.

Particles emitted at phases of 90 and 120° do not reach relativistic energies quickly as the electric field amplitude starts to decrease at these phases and thus, many are still in the cell when the field polarity changes. As a result, these particles are largely decelerated and change their direction of travel, sometimes several times, before striking the cell walls. This effect is particularly prominent at at phase of 120° where virtually all particles are immediately decelerated after emission and deflected towards the cell wall.

Notably, Figures 5.25(e-f) show that if a particle is emitted sufficiently late in the RF period, it may be completely decelerated and then accelerated in the reverse direction, with little transverse momentum. Such particles could arrive at a time which is comparable to or even slightly prior to the arrival of the main beam however due to the relatively low energy they will also be subjected to a significant slippage, similar to the cases shown Figures 5.25(a-b). These results then provide an indication as to how any emitted particles may reach the neighbouring cells, or in some cases arrive relatively close to the beam line axis with little transverse momenta. It is clear however, that the propensity for slippage due to the low velocities following emission must also be considered, and work pertaining to this is presented in Section 5.4.3, where the arrival phases, and hence the positions at which the particles' velocities stabilise, is presented.

Next, to examine the macroscopic behaviour and the characteristics of any captured current the recorded macroparticle information from each 2D field monitor was exported for examination. Figure 5.26 shows the ratio of the total emitted current from each iris, I_C to the ratio reaching the up and downstream monitors I_E at a gradient of 100MV/m.

Simulation indicates that a large fraction of the electrons emitted in the cells neighbouring the input and outputs reaches the adjacent monitors. In these regions the current has the most direct path to the output meaning the probability of striking the irises when being transported is low. Additionally, it is less reliant on the phase at

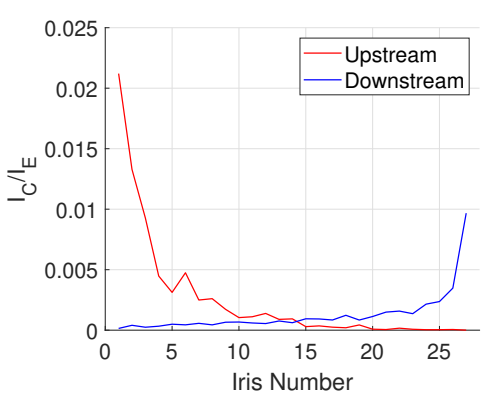

(a) Results for the monitor representing the beam pipe at the structure outputs.

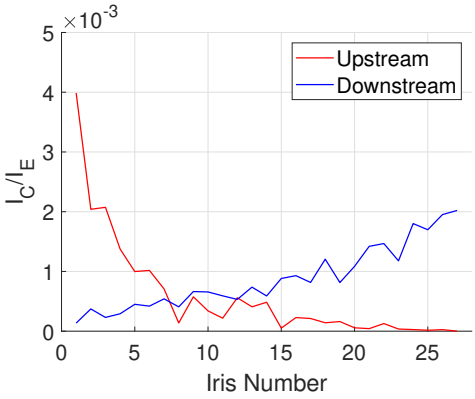

(b) Results for the monitor representing the Faraday cup detection surfaces.

Fig. 5.26 Simulation results showing the fraction of emitted current from each iris which exits the structure (a) and reaches the upstream and downstream Faraday cups (b). Electrons emitted adjacent to the input/output of the structure do not require capture to reach the 2D monitors meaning a larger fraction of current emitted in these areas reaches them.

which emission takes place. Interestingly, this effect is more prevalent in the upstream current, where a larger portion of the initial cells' current is detected despite the structure not being phased for acceleration in this direction. In later cells however, due to the structure phasing the probability of emission from later irises being kicked back without striking the copper walls or being decelerated is comparatively unlikely, meaning no current emitted in the later cells is capable of reaching the upstream monitor. Conversely, a small a portion of the emitted current from each iris is always capable of reaching the downstream monitors as synchronous acceleration is possible.

These results are in reasonable agreement with previous work carried out at SLAC and by T. Lucas however in these cases several differences should be noted [40, 39, 134]. The first is that the fraction of upstream current originating from the first few cells is larger than the fraction of downstream current which originates from the final cells, a result which is contrary to that achieved by Lucas [40]. In simulations performed by Lucas, a single cell was repeated periodically meaning the resulting simulation was representative of a structure of constant gradient and impedance, a property which is not achievable in practice. As a result of this approximation the emission, field distribution, and meshing of every cell was identical. In the CLIC structures however, the irises are tapered in the downstream direction to maintain approximate field flatness. The reduced iris radius in the later cells then appears to have resulted in a reduced probability of transmission in this region. To complement this result, the total emission

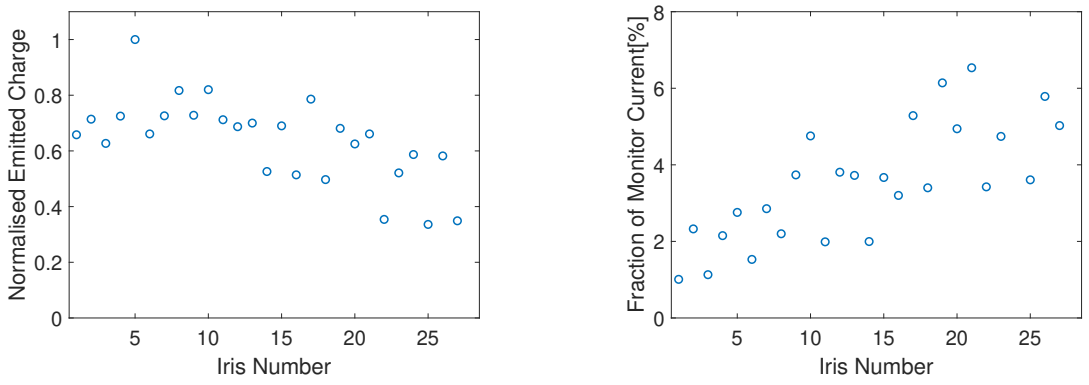

(a) (b)

Fig. 5.27 The total current emitted from each iris in simulation (a) and the contribution to that observed in the downstream monitor (b). The sporadic behaviour is caused by imperfect meshing, leading to irregularities in the emission properties however the trends are presumed to be correct.

from each cell was examined; in simulations by SLAC and Lucas, it was assumed that each iris emits equally however the results of the tapered structure simulation show that the total emission decreases in the downstream direction as shown in Figure 5.27.

The peak surface electric fields in the TD26CC increase in the downstream direction from 187MV/m to 191MV/m. As the emitted current scales with the surface electric field, $E_s^{2.5}$, the final cell may be expected to emit approximately 5% more current than the first, a prediction which conflicts with simulation results. One possible explanation for the discrepancy is that it may be due to the reduction in emission area associated with the tapering of the irises. In a given cell, the peak electric fields occur on the iris and are distributed nominally in an azimuthally symmetric fashion. However from the first to last cell the iris radius decreases from 3.15mm to 2.35mm in the downstream direction; a 25% reduction in circumference. The cell wall thickness also decreases from 1.67 to 1mm in the downstream direction. The surface area of a toroid can be calculated as:

$$A = 2\pi RC \tag{5.19}$$

Where R is the radius of the toroid and C is the circumference of its cross section. If it is assumed that the iris is where the majority of the emission occurs it can be seen that less than half the emission area is present in the final cells. Figure 5.28 shows the electric field distribution and relative sizing of the first and last irises in the TD26CC:

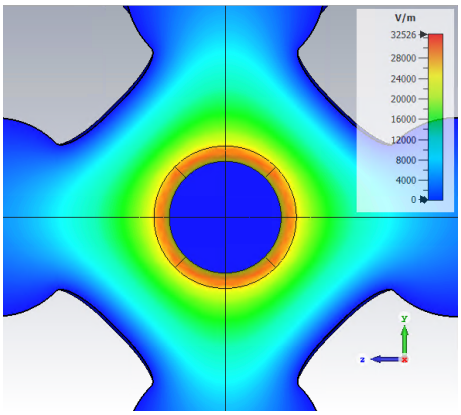

(a) E-field distribution on the first iris.

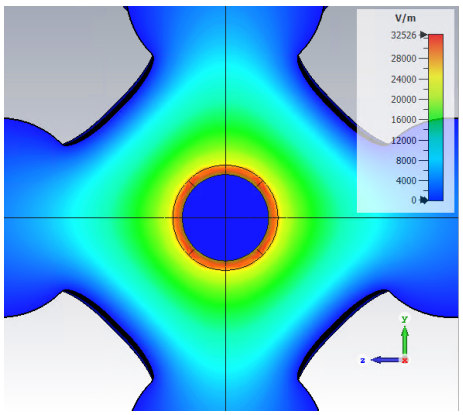

(b) E-field distribution on the final iris.

Fig. 5.28 Surface electric field on the iris of the first and final regular accelerating cells in the TD26CCR05 Structure. Fields are normalised to an input power of 1W.

Taking into account the change in iris radius and cell wall thickness it is clear that the decrease in effective emission area is the dominant effect and may offer an explanation for results presented in Figure 5.26. Assuming the emission sites are distributed evenly, the associated increase in electric field results in only a 5% increase in emission while the change in geometry predicts a 65% decrease in the total emitted current, a result which is in reasonable agreement with simulation results shown in Figure 5.27. The results shown in Figure 5.27(b) would also align with experimental observations published by J. Paszkiewicz where the current emitted from each longitudinal position within a high-gradient X-band structure cell number was monitored throughout testing [50, 135]. The results of this work showed that the majority of the downstream Faraday cup signal was found to originate from the later cells in the structure [135]. Notably however, β was found to decrease towards the end implying lower levels of field enhancement. An example of this work is shown in Figure 5.29.

Finally, in the test stands it has been noted that in the late stages of testing, the majority of breakdowns occur in the first cell of the structure under test. Given that field emission process is known to be an important precursor to breakdown, it is speculated that the increased surface area capable of sustainable significant emission in the early cells could also result in an increased probability of breakdown.

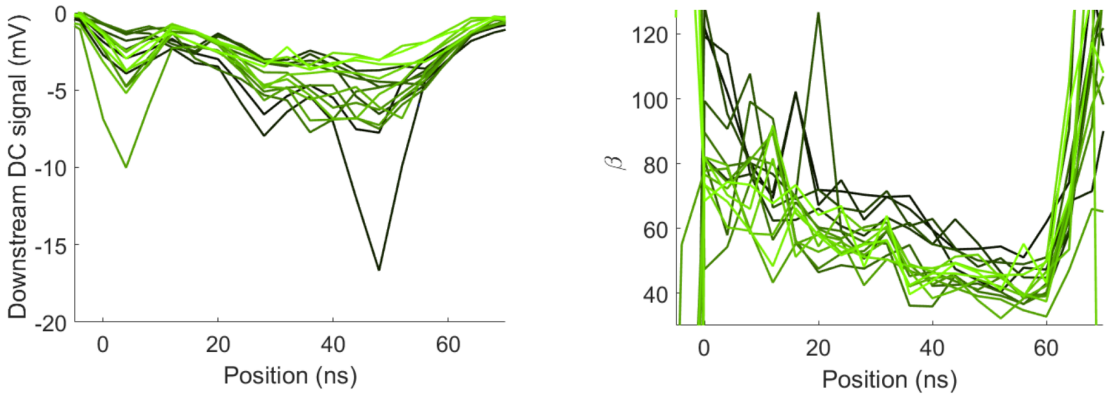

(a) (b)

Fig. 5.29 Downstream dark current signal and local β value for the T24 PSI1 structure plotted as a function of spatial position when operating at 100MV/m for different days [135]. Plots were derived by sending a short RF pulse through the structure and are hence in units of signal propagation time, where 0 represents the RF input of the structure and 60ns corresponds to the RF output.

5.4.3 Energy Spectrum of a Single Structure Arrangement

Following emission and capture the current experiences significant acceleration in the electric field. The iris from which any electrons are emitted determines the available length of structure in which they may undergo acceleration and so it is expected then, that the electron energy will be depend on the longitudinal position at which it was emitted. Additionally, the energy of the current determines whether or not the dark current can be sufficiently deflected by any magnets present in a given facility's lattice and contributes to the radiation requirements if it strikes the irises and produces X-rays. The energy spectra of the macroparticles emitted from each iris reaching the downstream monitor for a simulated accelerating gradient of 100MV/m are shown in Figure 5.30.

The highest energy current is observed at approximately 21 MeV and corresponds to that which was emitted in the first cell and has been accelerated through almost all of the structure's active length. Conversely, a comparatively large current is observed at lower energies, having been emitted by the later cells in the structure and subjected to less stringent requirements for capture and indeed a reduced probability of collimation during transport. Although Figure 5.30 demonstrates that the available energy gain is indeed determined by the longitudinal position at which a particle is emitted, it contains no temporal or spatial information about the current which reaches the monitor and so

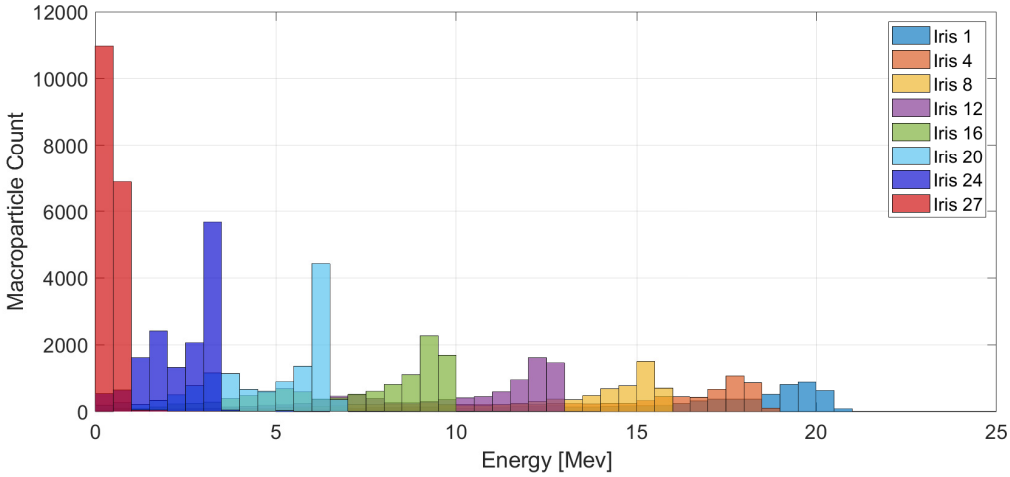

Fig. 5.30 The energy spectra of dark current emitted from every fourth iris reaching the downstream monitor in a single structure simulation with an accelerating gradient of 100MV/m. Results were taken over the course of a single RF period after the simulation had reached a steady state solution.

these facets were investigated next. A screen shot of the dark current at the structure output is shown in Figure 5.31.

While a stream of low energy current is always present, clear periodic bunching is nonetheless observed, as is visible in Figure 5.31 (b). The region in which the majority of the captured dark current lies is approximately 6.59mm long, corresponding to a length of 0.022ns in time. At an accelerating gradient of 100 MV/m, the total enclosed charge in this region is then approximately 0.084 pC. However as much of the current is not fully relativistic, the structure of the bunch is then liable to change substantially as it propagates in the beam pipe due to the variance in particle velocities. The phase space and transverse profile of the particles reaching the monitor were then examined. Figure 5.32 shows the transverse momenta and positions of the macroparticles reaching the monitor after the simulation has reached a steady state solution over the course of a single RF period.

The radius of the beam pipe at the structure output is 4mm, as the particle monitor was positioned in this pipe all particles then have a radial displacement within this range. In Figures 5.32(a-b) the current adopts the form of a tilted ellipse and a substantial energy spread is present in both the vertical (y) and horizontal (z) planes, however the highest density region is confined to within several hundred microns of the beam line axis. Approaching the extremities however, it can be seen that a small but significant number of particles have a transverse momentum of up to 300KeV/c. In regions where

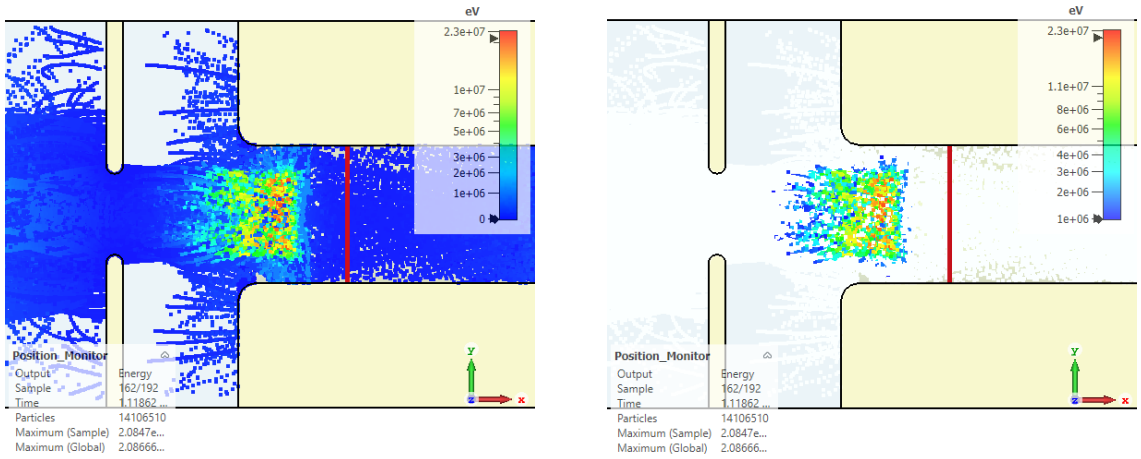

(a) (b)

Fig. 5.31 Cross section of bunched dark current approaching the 2D monitor representing the structure output (red line) in CST MWS. All particles are shown in (a) while only those with an energy greater than 1MeV, corresponding to a velocity of 0.8c or higher are shown in (b).

there are no active components, e.g. the beam pipe between structures, this current then has a propensity for spreading in the transverse planes, forming a halo around main beam bunches. Additionally, Figure 5.32(d) is approximately symmetric about the y and x axes, however this is believed to be an artifact of the non-uniform meshing in simulation. In an ideal simulation, the plots should be azimuthally symmetric though it is worth noting that such a result would not necessarily be representative real structure due as emission sites are generally distributed irregularly [136].

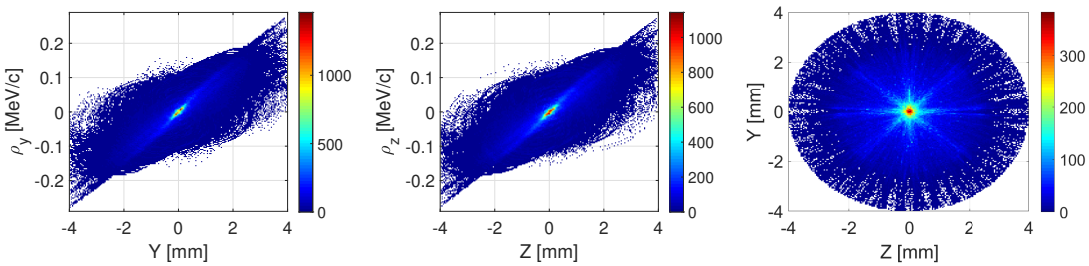

(a) (b) (c)

Fig. 5.32 Phase space diagrams (a-b) and the transverse profile (c) of the macroparticles which reach the downstream monitor over the course of a full RF Period when the simulation has reached a steady state solution. A 200 × 200 grid was used to generate the bins in each plot. The radius of the beam pipe at the structure output is 4mm, and so no current is observed with a displacement beyond this.

Following this, the arrival time of the macroparticles emitted from each iris was investigated. In the CLIC structures, the phase advance per cell is 120°. Hence, to experience the maximum energy gain a relativistic particle should be injected and enter the first accelerating cell at a phase of 30° in the RF period. For a particle to experience an energy gain close to that experienced by a relativistic beam, it must be captured and fully relativistic at a phase which is close to the nominal injection phase. Thus, it is expected that the particles with the highest energies should have been captured close to this phase. A phase of 30° (shown in red) was then used as a point of reference, and the arrival phase of the particles emitted from each iris was extracted and plotted as a function of energy. The results are shown Figure 5.33 however it should be noted that the phases shown do not correspond to the phase at which the particles were emitted, only the phase at which they reach the monitor, i.e. are exit the structure, relative to a fully relativistic bunch phased for maximum acceleration.

In simulation, the particle monitor time step was set to one twelfth of an RF period, as smaller values led to repeated crashing or freezing while transferring results back from the server. As a consequence, all particles arriving after 30° and before 60° are grouped into the same bin and this is one way in which future simulations could be improved at the expense of increased simulation time, as higher resolutions would likely yield a more complete physical picture. Despite this, it can still be seen that a significant amount of the current emitted by each cell actually arrives prior to the nominal phase, experiencing a significant and potentially close to nominal energy gain.

As expected, the current of highest energy is generally close to that of the main beam bunch however as these particles all fall into the 30°-60° bin it is unclear how close to the nominal 30° phasing they are. The variance in energies may then be partially attributed to the spread in phase within the bin, as particles at different phases experience different net accelerating voltages. Similarly, particles which are captured later than this experience gradually lower energy gains, due to the reduced net accelerating voltage they experience. Despite the propensity for slippage shortly after emission, this result nonetheless suggests that any particles which do approach fully relativistic velocities are most likely to stabilise at a position which is close to that of a fully relativistic beam which has been injected for maximum energy gain. Notably however, a small number of low energy (< 1 MeV) particles emitted from the earlier irises do arrive at the structure output at other phases. Such cases may then be particles which have experienced significant slippage, or indeed complete deceleration before being accelerated in the opposite direction during transit along the structure.

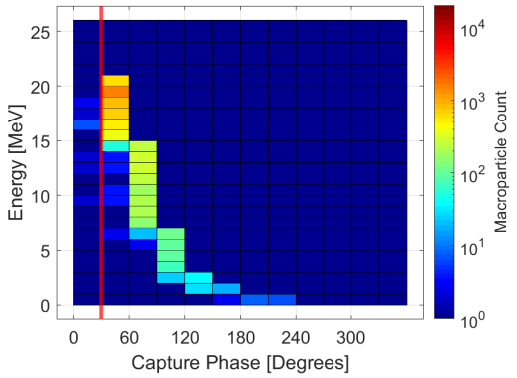

(a) Results for iris 1.

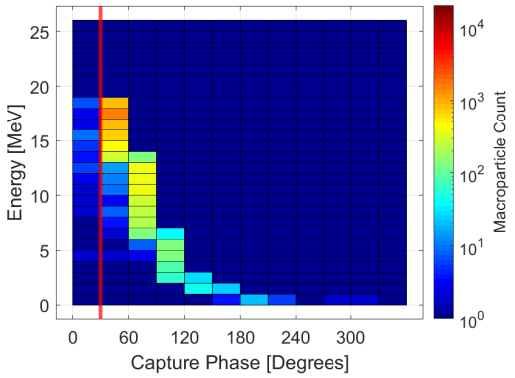

(b) Results for iris 4.

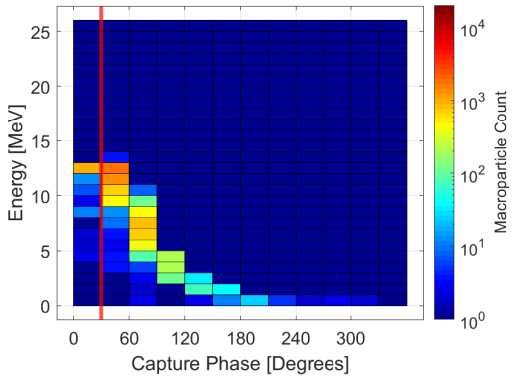

(c) Results for iris 12.

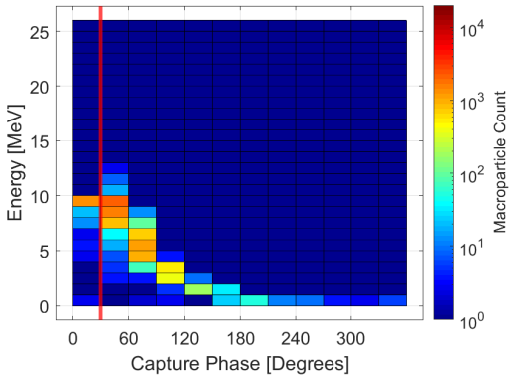

(d) Results for iris 16.

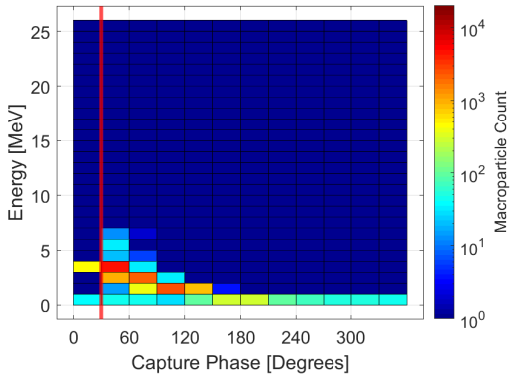

(e) Results for iris 24.

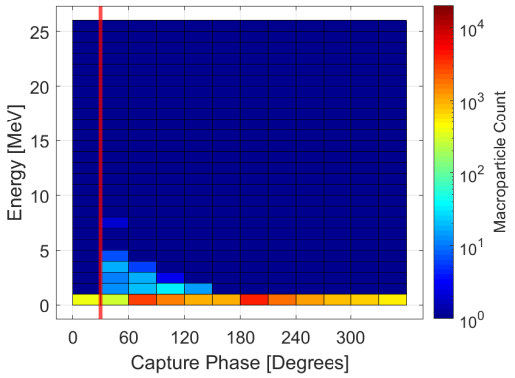

(f) Results for iris 27.

Fig. 5.33 The phase at which the current emitted from different irises exits the structure relative to a fully relativistic beam phased for maximum acceleration (shown by the red line) for various energies.

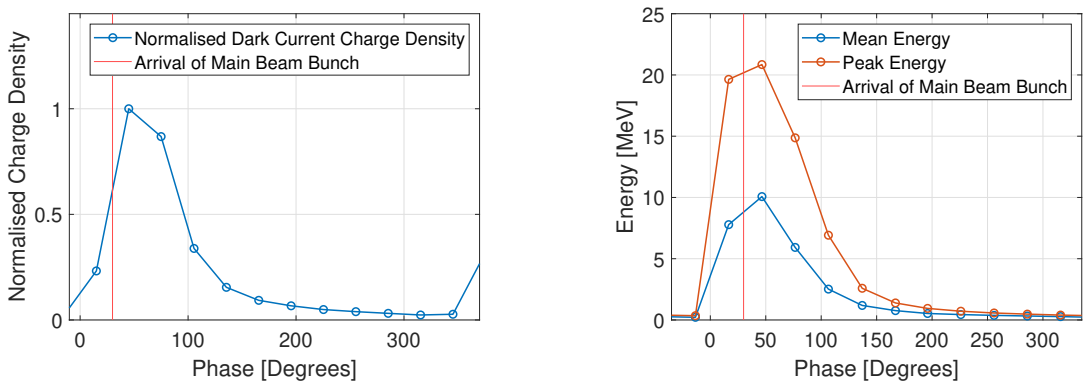

(a) (b)

Fig. 5.34 The variation in charge density (a) and mean and max energies (b) of the dark current at the output of a single structure during a single 11.9942 GHz RF period compared to the arrival time of a bunch phased for maximum acceleration. The resolution with which the structure of the current is viewed is determined by the particle monitor time step in simulation, which was set to one twelfth of the RF period. The current which arrives within the 30-60° bin is plotted as a data point at 45°.

Examining irises 24 and 27 shows that much of the current emitted by the later irises is capable of reaching the monitor at all phases due to their close proximity to the output, as was noted previously in Figure 5.26. A small number of particles also arrive with an energy gain higher than what could be achieved via acceleration over only the final cells (5-8 MeV), values which correspond to the energy gain which is achievable over 5-10 cells. This result indicates that a small number of particles have traversed several cells in the upstream direction, similar to the case shown in Figure 5.25(f), before being completely decelerated and then accelerated back towards the structure output. Finally, several characteristics of the longitudinal profile were investigated. Figure 5.34 shows the charge density, mean energy, and peak energy of the dark current which reaches the structure output relative to the arrival of a main beam bunch (shown by the vertical red line) across a single RF period.

The charge density peaks in the 30-60° bin, i.e. the 45° data point, and the current in the bin following this is comparable in amplitude, meaning that a large portion of the dark current lags the main beam somewhat as predicted in Section 5.4. Additionally, the highest average energy is also recorded in the 30-60° bin, corresponding to any current which is close to but slightly behind the nominal phase. Notably, the peak energy in the data point prior to this is also high, and close to the maximum achievable energy gain although a much lower total current is present. Once again however, the time step of the current monitors limits the resolution with which the bunch structure

can be viewed and, as mentioned previously, this is one way in which the work could be expanded upon in the future. It is also worth noting that due to the energy spread the velocities of the particles differ. The temporal charge and energy distributions are then liable to change during propagation in the beampipe, meaning that a slightly different result may be obtained if the 2D particle monitor in simulation is placed at a different longitudinal position.

5.4.4 Capture Efficiency and Energy Spectrum of a Multi-Structure Arrangement

While it is possible to perform a full dual structure simulation, the large geometry, total emission area and multiple monitors are liable to result in an unreasonably long simulation run time. Instead, the decision was made to export the results of the upstream and downstream particle monitors from the single structure simulations detailed in Section 5.4.2 and use them as the particle source in an otherwise identical arrangement. One limitation of this arrangement however, is that the imported current source will then have a time resolution equal to that of the monitors deployed in the single structure. As the time step in previous simulations was set to 30° at 12 GHz, it is expected that the results will then only be correct to within $<30°$ and this is one way in which the work could be improved upon. CST MWS has several options for particle source creation however it is not capable of directly exporting the results of a 2D monitor into another simulation as a source. It does however accept external particle sources of the .pit format. A script was written in Python to convert the results of the upstream and downstream monitors in the single structure simulation and produce a corresponding .pit file with a row detailing the relevant information for each passing particle. Each row details ten particle parameters; the coordinates in the x, y and z planes (one of which will be fixed due to the planar nature of the monitor), the momenta in the x, y and z planes, the particle mass, charge, corresponding macro-charge, and the time at which it passed through the monitor.

All emission sites were then disabled, leaving only the imported particle source in order to reduce simulation time as it is assumed that the simulated currents are low enough and become relativistic quickly enough that space charge effects will not significantly change the result. Hence, the result of the single structure simulation may simply be added to the second structure to provide the net current and energy spectrum. During operation the gap between the superstructures is fixed as shown in Figure 5.35. Ordinarily, the structures would then be phased for a synchronous beam

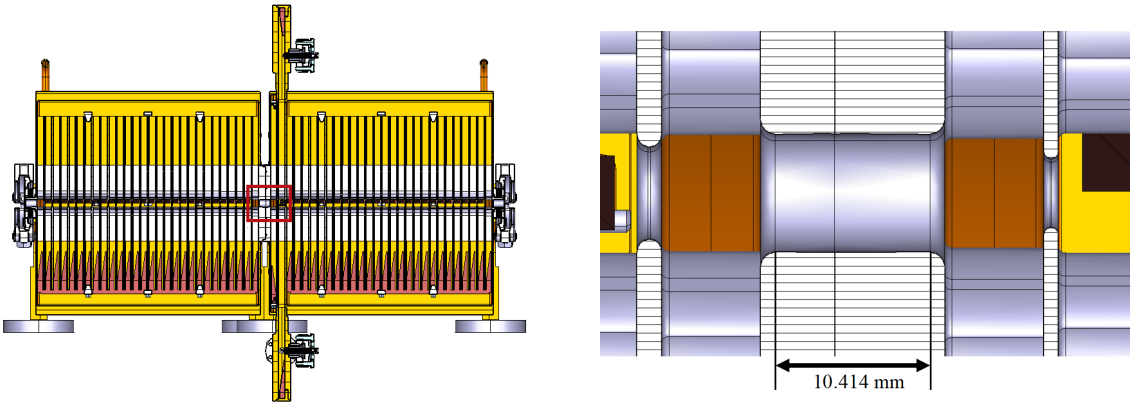

(a) (b)

Fig. 5.35 Cross section of the full superstructure assembly (a) and a close up of the section outlined in red showing the spacing between the final cell of the first structure and the first cell of the second (b).

however the planned experiment in the Xbox-2 test stand includes a phase shifter, as shown in Figure 5.1. As the relative phasing of the structures may be varied it is also desirable to investigate other phasings. The results from such arrangements will also apply to phasing errors in an arrangement with beam.

In a relativistic structure with a 120° phase advance per cell, the cell length (L_{Cell}) is calculated such that the beam stays synchronised with the fields as:

$$L_{Cell} = \frac{c}{3f} \tag{5.20}$$

In the CLIC structures where the RF period is 83.37 picoseconds, this length is approximately 8.4mm. The time taken for a relativistic bunch to traverse the 10.414mm beam pipe between structures is 34.5ps, or 150° in phase and so this, in conjunction with the fact that the total number of cells in each structure is not an integer multiple of three, must be accounted for. For maximum acceleration the second structure should then be leading in phase by 90°. In longer arrangements it is possible to vary the phasing to compensate the energy spread and this has been investigated in detail however such arrangements are not considered in this study [137]. To simplify the import process, the downstream and upstream monitors were placed at 6.207mm from the wall of each respective coupling cell and hence were situated exactly halfway between the structures. The phase of the imported electric and magnetic fields was then parameterised to investigate the effect of different phasing arrangements.

Figure 5.36 shows the results of a preliminary simulation at times of 0.1ns, 0.5ns and 1ns with the output of the single structure simulation imported as the source. As expected the bunched electrons remain synchronous with the RF fields and the maximum energy is 43 MeV, corresponding to electrons emitted in the first cell of the first structure which have experienced close to the full 100MV/m accelerating gradient across the active length of both structures.

Simulations were performed with the fields in the second structure set to different phases relative to the first. The transmission efficiency was then calculated for each relative phasing arrangement by dividing the average current reaching each monitor in the structure by the total imported current and the results are shown in Figure 5.37.

Notably, the highest transmission in Figure 5.37 occurs at 0°, as due to the long bunch length, large energy spread and phase delay relative to the main beam, this is when the largest amount of dark current falls into a window in which it continues to gain energy. The energy spectra of the dark current bunches exiting the second structure were then examined as a function of structure relative phasing and the results are shown in Figure 5.38.

The average particle energy varies approximately sinusoidally, save for a discontinuity at phases of 210° and 240° which is thought to be a consequence of the extremely long bunch structure. The maximum average energy occurs when in a phasing arrangement of 30°, an arrangement when the total transmitted current is also large. Figure 5.38(b) shows the maximum energy received by any individual macroparticle and is thus governed only by the position of the highest energy electrons in the dark current bunch. Notably, the maximum individual particle energy is then reached in an arrangement of 60°, a circumstance which requires almost on-crest acceleration on both structures. This result is once again a consequence of the time resolution of the current source which was imported from the single structure simulation. As shown in Figure 5.33, the highest energy current in the single structure arrived slightly after the nominal phase, and thus was grouped into the next monitor time step (60°). When imported into the dual structure simulation these high energy particles are then effectively "delayed" by 30° relative to nominally phase main beam bunch, and so the second structure must be phased 30° earlier than the nominal 90° relative structure phasing in order for the particles to experience the maximum energy gain. It is speculated then, that the arrangement which would result in dark current with an energy close to that of the main beam in practice lies somewhere in the 60°-90° range.

Although some particles experienced an energy gain close to that associated with on-crest acceleration in both structures, the average energy of the transmitted dark

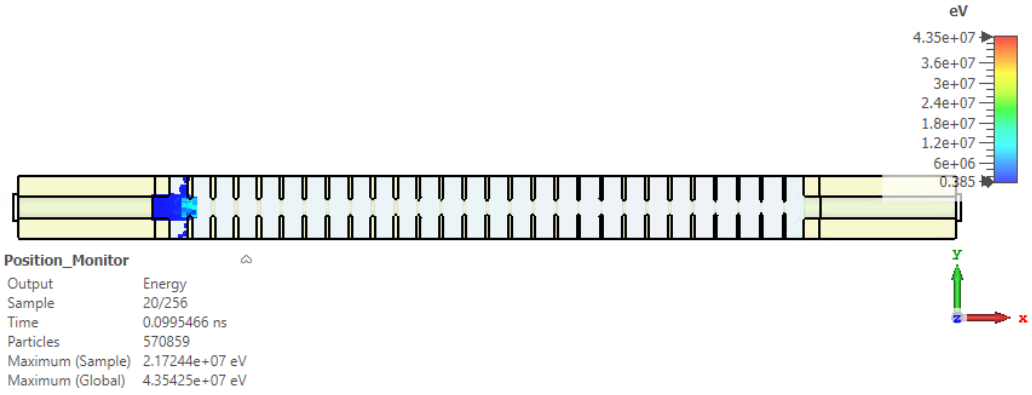

(a)

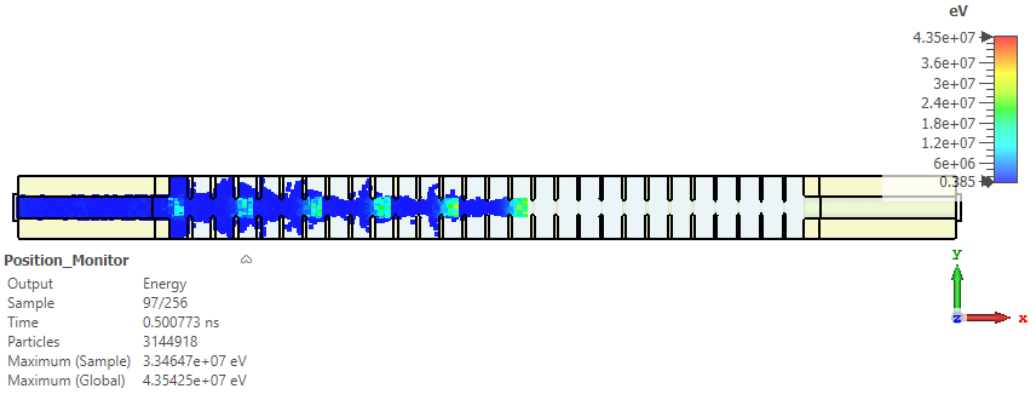

(b)

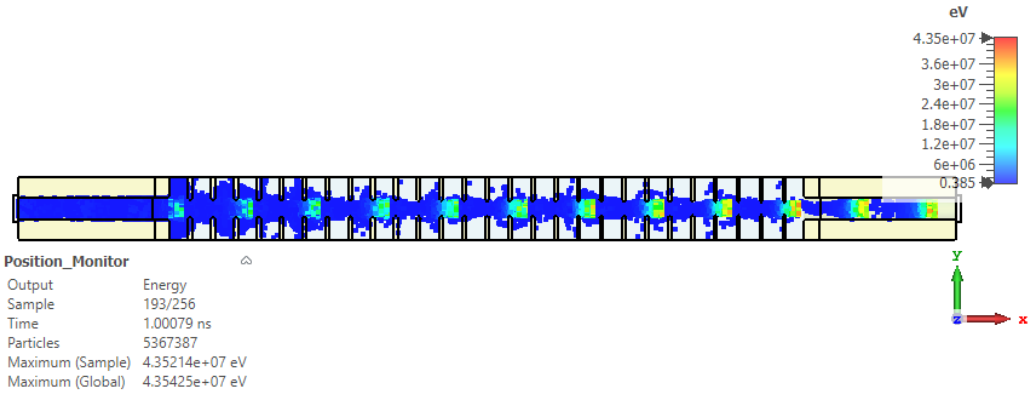

(c)

Fig. 5.36 Cross section of the PIC simulation showing the propagation of the imported current through the second accelerating structure at 0.1ns (a), 0.5ns (b) and 1ns (c) respectively. The second structure was phased at 60° relative to the first.

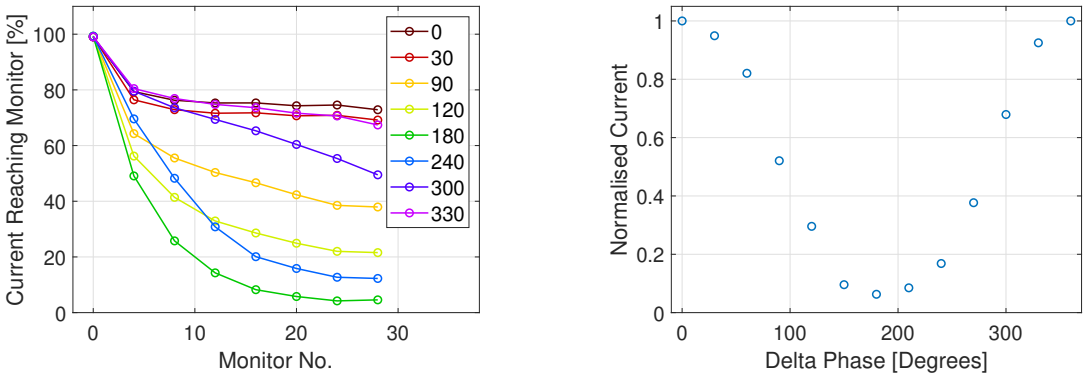

(a) (b)

Fig. 5.37 Attenuation of the current emitted from the first structure as a function of longitudinal position in the second (a) and the total current observed reaching the output of the second structure normalised to the max value (b) for various phasing arrangements. A phase of 90° corresponds to the second structure being phased at 90° relative to the first.

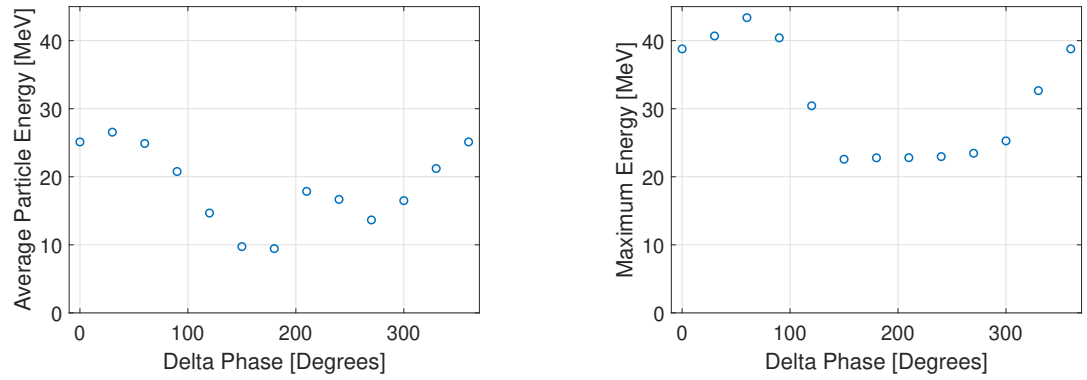

(a) (b)

Fig. 5.38 The average (a) and peak (b) particle energies in the dark current bunches observed at the output of a dual structure arrangement as a function of relative phasing. A phase of 90° corresponds to the second structure being phased at 90° relative to the first and this is the phasing in which a relativistic beam would receive the maximum energy gain. The maximum energy is governed by the arrival time of high energy particles from the first structure.

current is always much lower. The consequence of this characteristic in longer multi-structure arrangements may then be examined analytically. In Section 1.2.1, the energy gain in a particle traversing an accelerating cavity was defined:

$$\Delta W = qE_0 T cos(\phi) L \tag{1.52}$$

However, depending on the phase the dark current will be subjected a net accelerating voltage which differs from that of the main beam. The resulting discrepancy in energy gain can then be defined:

$$\Delta(W - W_s) = qE_0 T L_n \left(cos(\phi_n) - cos(\phi_{s,n})\right) \tag{5.21}$$

Where E_0 is the field amplitude, W_S is the energy of the synchronous particle i.e. the main beam, W is the energy of a particle with a given phase error and T is the transit time factor as defined in Equation 1.50. Differentiating this equation longitudinally then shows that the resulting energy discrepancy per unit length per can be expressed:

$$\frac{d(W - W_s)}{dz} = qE_0 T(cos(\phi_n) - cos(\phi_{s,n})) \tag{5.22}$$

In the CLIC structures, the bunch reaches the centre of the cell at a phase of 90° and so the $cos(\phi_{s,n})$ term becomes 0. The consequence of this, and the equations outlined in Section 5.4, is that in a relativistic structure the bulk of the dark current is incapable of reaching the same energy as the main beam. Additionally, if the particles remain fully relativistic then this divergence grows with distance, meaning that a current of a wide variety of energies may then be capable of reaching the output if not removed by the machines lattice or sufficiently collimated by other means. As mentioned briefly in Section 5.4.3 the temporal charge density and energy distribution are then also liable to change during propagation, particularly at lower energies. The energy spectrum of the imported current which reaches the downstream monitor is shown for three phases of interest in Figure 5.39.

As shown in Figure 5.39, when the second structure is phased such that the highest energy dark current from the first experiences on crest acceleration a maximum energy of 43-44MeV is obtained, corresponding to electrons which have experienced approximately on crest acceleration in both structures. However, as noted previously

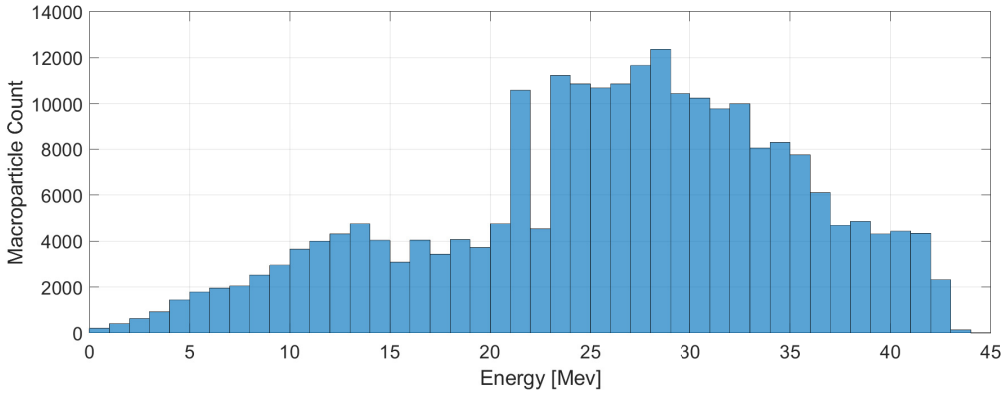

(a)

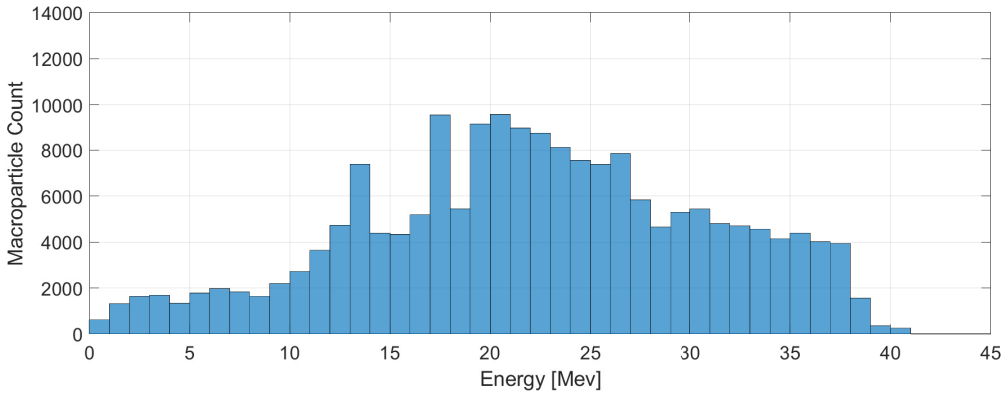

(b)

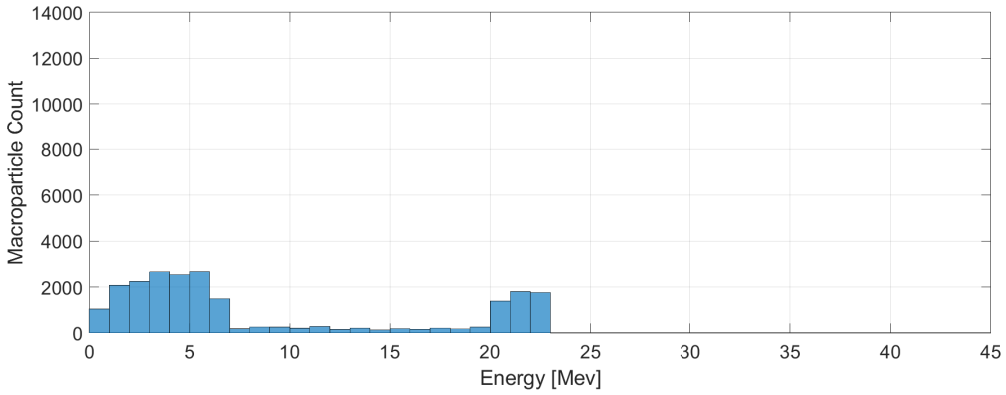

(c)

Fig. 5.39 The energy spectra of the imported current reaching the downstream monitor in the 2nd structure simulation. Structure was set to an accelerating gradient of 100MV/m and a relative phasing of 60° (a), 90° (b) and 180° (c). These results correspond to the phasing arrangements which result in the highest energy current (a), the nominal arrangement for a relativistic beam (b), and the arrangement in which the least current is transmitted (c) respectively.

this result is likely a product of the simulation time step. When phased for a relativistic beam a reduction in the maximum dark current energy is observed due to the head of the dark current bunch lagging the main beam, however a large net energy gain is still present and substantial current is transmitted. When set to 180°, a reduction in the maximum observed energy occurs as on the high energy captured electrons are now phased for declaration in the second structure and indeed lower energy electrons arriving off crest are back scattered and removed entirely. A small number of electrons reaching 23MeV are however still present, corresponding to low energy electrons from the first structure which have then been captured and accelerated in the second.

Finally, the transverse momenta and positions of the macroparticles which reached the monitor after having traversed the second structure were investigated. The acceleration provided by the structure couples the longitudinal plane with the transverse ones, meaning that the 6D emittance i.e. in the longitudinal and the two transverse directions, will be conserved however the transverse ones will not. Previously it was shown that the nominal phasing for maximum energy gain of a relativistic beam was 90°, and so this arrangement is of greatest interest in an operational context. However, it was noted that the maximum energy gain in a dual structure simulation occurred when the second structure was phased at 60° relative to the first, due to the particle monitor resolution in simuation. Thus, the results for each of these arrangements are shown in Figure 5.40 and it is assumed in practice, the correct answer would then lie somewhere between the two and that they still provide a reasonable estimation of the behaviour which may be expected.

It should be noted however that as the emission sites were switched off during the dual structure simulations the results shown in Figure 5.40 correspond only to the current which was emitted in the first structure, and was then imported into the second. If the results for a dual structure simulation are desired then it is presumed that the results shown in Figure 5.40 may simply be superimposed on to those shown in Figure 5.32.

As was the case in Figure 5.32, a significant spread in transverse momentum is present, however the extremities have been reduced somewhat, with most particles having a transverse component within 200keV/c. Additionally, an anticlockwise twist in the phase space ellipses has taken place in both cases. Although the beam pipe between structures has a radius of 4mm, the radius of the final iris is 2.35mm. Consequently, particles with substantial transverse momenta are liable to strike the irises when traversing the second structure and this is reflected in Figures 5.40(c) and (f) where the radial displacement of the majority of the transmitted current is within the latter

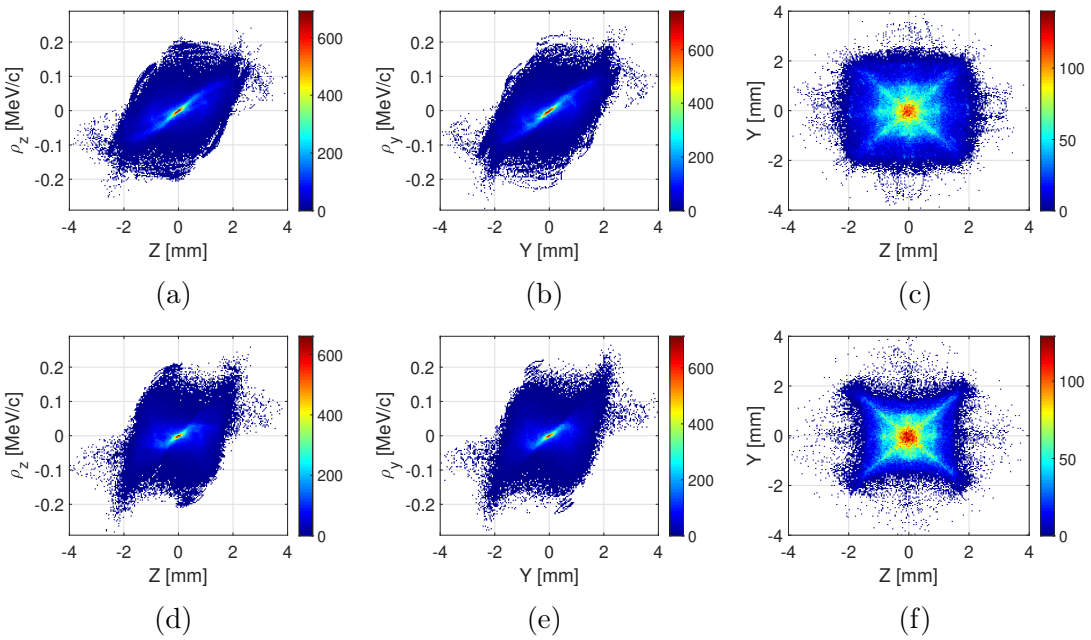

Fig. 5.40 Phase space and transverse profile of the macroparticles emitted in the first structure which reached the output of the second over a full RF Period when the second structure is phased at 60°(a-c), and 90°(d-f) relative to the first. A 200×200 grid was used to generate the bins in each plot. The radius of the final iris in the structure is 2.35mm and so most of the particles have a transverse displacement within this range.

value. Notably, the region in which the particle density is highest is markedly less focused after having traversed a second structure, suggesting that beam halo is then a likely consequence in longer, multi-structure arrangements and may warrant further consideration. Finally, Figures 5.32(c) and (f) are also approximately symmetric about the y and x axes, however this is once again believed to be an artifact caused by the non-uniform meshing.

5.5 Dark Current Considerations for High-Gradient Facilities

The results of 3D simulation have several implications modern high-gradient facilities. The first is the potential utility of the phenomenon; in high-gradient arrangements, particularly those which operate at high frequencies, the acquisition system constitutes a significant portion of the cost of the arrangement. If operation without such infrastructure is possible it is desirable to do so due to the reduced complexity and associated cost savings. However in multi-structure arrangements the relative phasing of the structures is of paramount importance and without regular phase measurement it is liable to drift due to temperature changes causing expansion of the waveguide section and modifications to the LLRF system or cabling. Additionally, if separate power sources are used the phase may also be dependent on the gain curve of the device.

The results in Figure 5.37(b) show that as the relative phasing is varied, a sinusoidal variance in the total dark current is observed. Doing so in practice then constitutes a method of in-situ phase calibration without the need for beam or an acquisition system capable of phase measurement and this has been investigated experimentally in Chapter 6. Similarly, this effect may be exploited in facilities where it is desirable to minimise the radiation produced during operation. During the conditioning process and indeed at any time without beam the structures may be kept out of phase, greatly reducing the dark current energy and accompanying X-ray production.

The results also suggest that in an arrangement like CLIC or any other facility which requires many structures in sequence there is a possibility that captured field emitted electrons may accumulate along the beamline, resulting in a substantial current and measurable beam loading. Dual structure simulations have predicted that the vast majority of dark current in such arrangements will not be capable of reaching the same energy as the main beam, however the dual structure simulations performed indicate that due to its transverse divergence it is liable to form a halo around main beam

bunches. Given the substantial transverse momenta and energy spread, it is speculated that such current may be regularly collimated with the addition of a carefully chosen magnetic lattice. However, no work has as of yet been performed by the author to model longer multi-structure arrangements and investigate this further.

5.6 Conclusion

The inclusion of a three-port device in a high-power RF network results in the potential for the energy in the RF pulse to be redirected elsewhere in the network during breakdown and this effect has been investigated for the arrangement which is planned for testing in the Xbox-2 test stand. Numerical simulations have been performed with the variable power in three positions. For the position which provides an equal split, it is predicted that during breakdown the power directed to the neighbouring structure can increase by up to 80% and it is speculated that such events could result in the occurrence of a second, intra-pulse breakdown.

Secondly, current is regularly emitted and captured within modern HG structures and 3D PIC simulations have been performed to investigate the phenomenon in both a single and dual structure arrangement. Results of the simulations reveal that in a constant gradient structure the cells situated close to the RF input emit comparatively more current than those downstream and it is speculated that this is due to the difference in surface area caused by the tapering of the irises. These observations also align with experimental data presented by J. Paszkiewicz in 2019 performed on similar high-gradient structures [135]. Additionally, it has been observed that during long term operation of high-gradient structures the breakdowns tend to occur primarily in the cells close to the input and given that emission sites are known to be precursors to breakdown the increased surface area offers a potential explanation for this phenomenon despite the marginal increase in peak fields associated with the smaller irises downstream.

Finally, the variation in capture as a function of relative phasing of neighbouring structures on the same beamline presents an opportunity for in-situ phase calibration without the need for fast acquisition systems. While some current is inevitable during operation, it is also proposed that by operating the structures out of phase during conditioning and at times without beam the amount of radiation produced may be greatly reduced, potentially lowering the shielding requirements of the facility. It is then speculated that in arrangements with many structures, the capture and accumulation

of significant current is possible and warrants further investigation in the design of future high-gradient facilities.

Chapter 6

High-Power Test of a Multi-Structure High-Gradient System

As discussed in Chapter 4, modern high-gradient facilities often require several or many LINACs in series to meet the target beam energy and if constructed, the CLIC project itself would require thousands. In the CLIC arrangement specifically, the accelerating structures are aligned and bonded together in pairs to form so-called superstructures [33]. In this context a CLIC superstructure was tested in the Xbox-2 test stand to both validate the module and investigate the operational challenges associated with a high-gradient multi-structure arrangement. The following chapter details the installation of the superstructure in the Xbox-2 test stand and the results of the test.

6.1 Structure Overview

The current baseline structure design for CLIC is the TD26CC R05 [33]. The abbreviation refers to several facets of the RF design, specifically that the irises are tapered in the downstream direction to maintain an approximately constant gradient (T), silicon carbide inserts and waveguide manifolds provide wakefield damping (D), and that the structure itself is comprised of 26 regular accelerating cells (26). Additionally, the previously employed mode launcher input couplers have been replaced with those of the compact coupler (CC) design in favour of reducing the structure length. Finally, for improved machinability, the cell edges have been designed rounding profile with a 0.5mm diameter (R05). The design of the TD26CC R05 structure is presented in detail in the conceptual design report (CDR) however as the test results of this structure form the basis of the following chapter the key RF design features are outlined following.

6.1.1 TD26CCR05 Design

Cell Design

The basic cell geometry is shown in Figure 6.1 and is comprised of a conventional circular iris surrounded by four convex walls situated between damping waveguides. To reduce manufacture costs and simplify the bonding process one side of the disc carries the features of the cell whilst the other is simply flat. While manufacture tolerances are tightly controlled, small deviations nonetheless remain which perturb the phase advance per cell, field flatness and overall transmission of the final structure. In light of this each disc has four holes on the perimeter, each of which houses brazed tuning pegs for adjusting of the cell volume and hence frequency via pulling or pushing with a slide hammer as required.

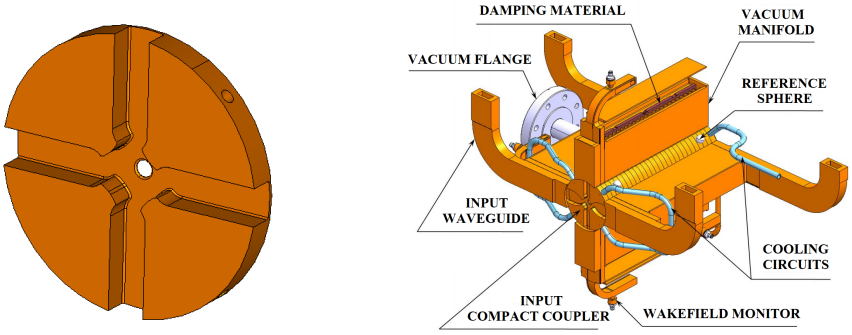

(a) Mechanical design of a single disc.

(b) Assembly of a complete TD26CC R05 structure.

Fig. 6.1 Basic cell geometry of the accelerating structure showing the waveguide damping (a) and a full structure assembly (b) [33].

The cell length is fixed by the phase advance and the other dimensions have been chosen to maximise the shunt impedance of the accelerating mode while adhering to peak surface electric field and pulsed heating. Additionally, being a revised form of the original structure proposed for the CLIC main LINAC the modified Poynting vector is also now considered [138]. In addition to the 3×10^{-7} bpp/m breakdown rate requirement these constraints are listed for the 244 ns CLIC pulse length respectively as [33, 138]:

1. Surface electric field [68]: $E^{max}_{surface} < 260 MV/m$
2. Pulsed surface heating [68]: $\Delta T^{max} < 56 K$
3. Modified Poynting Vector [16]: $S_c < 5 W/\mu m^2$

Wakefield Damping

For wakefield damping, four waveguide sections are incorporated into each disc, coupled to the central region via a tapered section as shown in Figure 6.1. A rounding corner radius of 0.5mm has been selected for the waveguides to keep pulsed heating within acceptable limits. A manifold is also brazed to each side of the structure as shown in Figure 6.1. Inside the manifold the wakefield damping sections are extended and delivered to Silicon Carbide or SiC inserts. Figure 6.2 shows a row of SiC inserts and their position within manifold on an assembled structure.

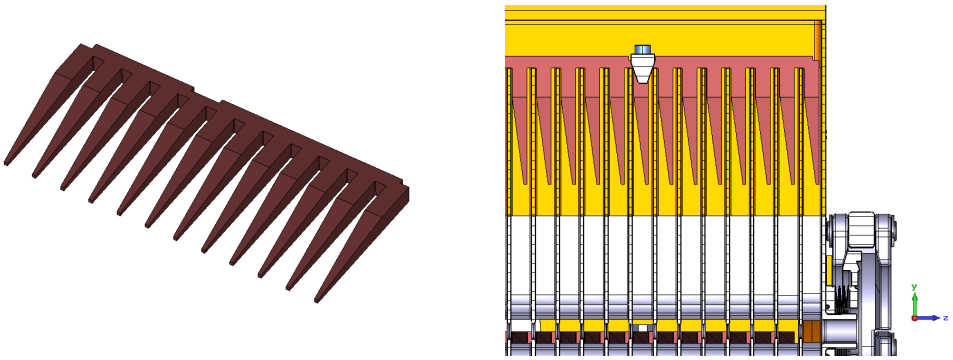

(a) (b)

Fig. 6.2 Rendering showing a row of silicon carbide inserts (a) and their final position inside the structure manifolds (b).

Each SiC spike is 3cm long and tapers linearly from a 5x5mm cross section at the base to a 1x1mm at the tip. The distance from the beamline axis to the tip of each insert is 5cm. The geometry was optimised via electromagnetic simulation to ensure reflection of any incoming RF is kept below minus 30dB for the TE_{10} mode and below minus 20 dB for TE_{01} mode [33].

Structure and Coupler Design

To provide required 100MV/m effective gradient and make efficient use of the input power the TD26CC has 26 regular cells, the irises of which are tapered linearly from 3.15 mm down to 2.35 mm, reducing the group velocity from 1.65%c to 0.83%c. In this way the attenuation of each cell changes, resulting in an approximately constant distribution of the unloaded gradient along the length of the structure as outlined in Section 1. The cells are also optimised such that the other design constraints are adhered to.

Fixed to each end the structure is a coupling cell, to match the input waveguide sections to the regular accelerating cells and convert the rectangular $TE10$ waveguide mode to the circular TM_{01} accelerating mode. The coupling cells themselves closely resemble the accelerating cells however a double feed is present, comprised of a section of WR90 waveguide tapered inwards toward the cell centre. This integrated compact coupler design allows a reduced structure length, increasing the effective gradient as opposed to the mode launcher type present in other CLIC prototypes [139, 140]. In each coupling cell, the other two damping waveguides have been included to maintain efficient wakefield damping and to minimise the quadrupole component of the established fields within the cell. The structure requires an input power of 43MW to establish an average unloaded gradient of 100 MV/m across the full 230mm active length comprised of 26 regular cells and 2 couplers, while establishing 100MV/m only over the 26 regular cells requires an input power of 41.8MW. Figure 6.3 shows several key RF parameters as a function of cell number during loaded and unloaded operation.

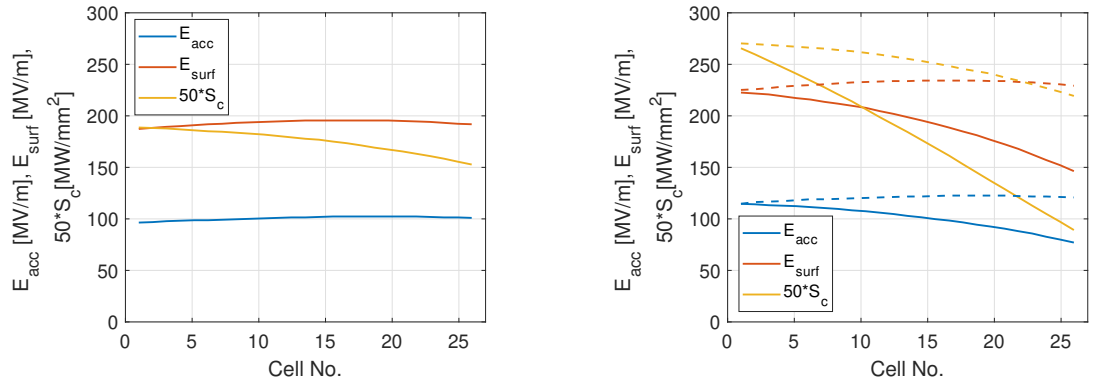

Fig. 6.3 Key RF parameters for each cell for the unloaded (a) and loaded (b) design powers. In plot b the dashed lines represent unloaded operation and solid lines are beam-loaded conditions.

The accelerating gradient, surface electric field rise and temperature rise are made to be approximately constant during unloaded operation as in the test stands. Conversely however, the modified Poynting vector decreases in the downstream direction. Table 6.1 provides a summary of the structures's key RF and geometric parameters.

6.1.2 Endoscopy and Tuning

Prior to installation in the test stands the superstructure was installed and operational in the beam line in the CLIC Test Facility (CTF3) [141]. Two superstructures were

Parameter	**Value**	**Unit**
f_0	11.9942	GHz
$\delta\phi$	120	°/cell
t_f	66.98	ns
v_g	1.68-0.83	%c
Shunt Impedance	81 - 103	MΩ/m
Q_0	5536-5738	-
$E^{max}_{surface}$	230	MV/m
ΔT^{max}	47	K
No. Cells	26	-
Iris Radii	3.15-2.35	mm
Iris Thickness	1.67-1.00	mm
Structure Length (inc. Couplers)	230	mm

Table 6.1 Key RF and geometric design parameters of the TD26CC R05 structure for the CLIC main LINAC [138].

installed in CTF3, the first being comprised of structures labelled ACS1 and ACS2, while the second was comprised of ACS3 and ACS4. The superstructure comprised of the two latter was removed for installation in the Xbox test stands. During operation in CTF3, a large reflected signal indicative of a fault was eventually noted in ACS4 as is shown in Figure 6.4. The reflection appears approximately 140ns after the arrival of the incident RF and persists for the duration of the pulse. As this is approximately twice the fill time of the structure it was speculated that there may be a problem with one of the final cells or indeed the output coupler. Following this realisation structure was removed in 2017 and placed into storage for 2 years.

The maximum drive beam current in CTF was 28A as opposed to the 101A required for CLIC and while units ACS1 and ACS2 received in excess of 40MW, neither ACS3 nor ACS4 structure were recorded as having received more than 10MW [141]. Discernment of the number of RF pulses seen by the structure was not possible however the repetition rate in CTF3 is 5 Hz, as opposed to the 50 Hz in the Xbox-2 test stand. As such, the structures are assumed to be largely unconditioned by test stand standards having received less than one quarter of the nominal input power, corresponding to less than half of the 100MV/m design gradient [141]. Additionally, although a propensity for reconditioning has been noted in previous tests after exposure to air it is not known how well conditioning is preserved after such a long period of exposure [40, 92, 83]. Due to the fault in transmission and the long storage period the structures were inspected prior to installation in the Xbox test stands. An endoscopy was first performed to

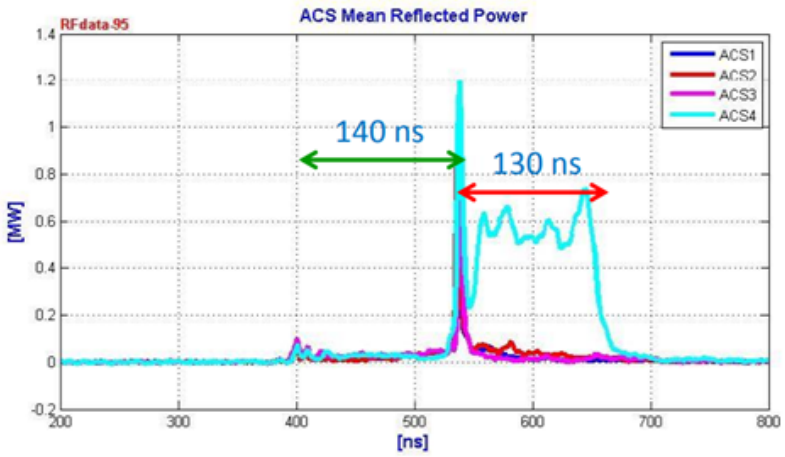

Fig. 6.4 Reflection from the superstructures observed during operation in CTF3 [141]. Note that structures ACS3 and ACS4 refer to the first and second constituents of the superstructure which was removed and later installed in Xbox-2 for high-power testing.

check for evidence of contamination in each structure and for a clear internal fault which could explain the transmission problem shown in Figure 6.4. Several images from the endoscopy are shown in Figure 6.5.

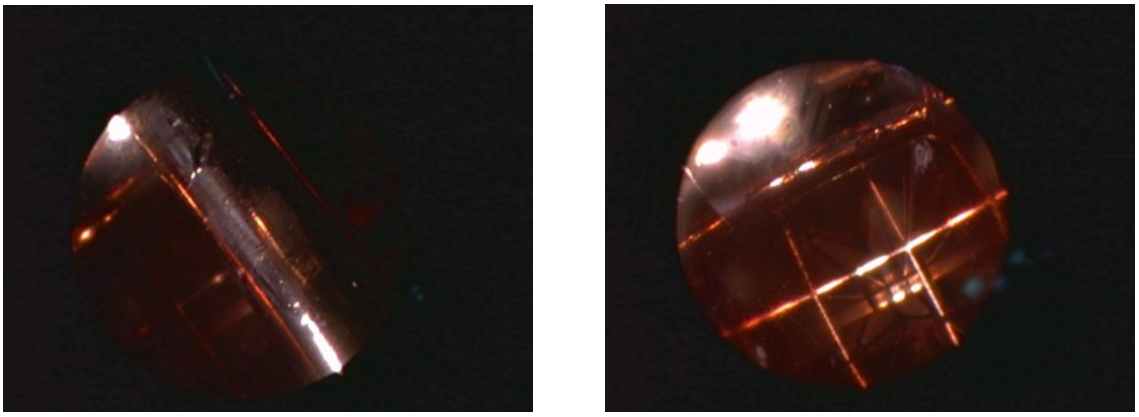

(a) Iris in the second structure.

(b) Silicon carbide spikes as seen from the beam axis in the second structure.

Fig. 6.5 Images captured during the superstructure endoscopy showing an iris (a) and a view of the silicon carbide in the damping waveguide section (b).

Several small spots indicative of breakdown sites were seen though no significant faults were visible by eye; the structures were then taken forward for RF measurement. A VNA was calibrated via the SOLT (Short-Open-Load-Through) method and used to measure the transmission of each manifold and structure in turn. As expected, structure B demonstrated poor transmission as noted in previously CTF3. To localise

the problem a bead-pull measurement was then performed. In this method, a small metallic or dielectric bead on a string is moved through the structure on the beam line axis whilst the structure S-parameters are monitored using a VNA. When well tuned, the phase advance per cell in a CLIC structure should be exactly 120° and the field profile approximately flat. The insertion of a small bead however constitutes a significant local impedance mismatch. The phase of the reflection caused by the perturbing effect of the bead is then determined by the longitudinal position while the amplitude is proportional to the weighted sum of the squares of the electromagnetic field components at its location and may be written [142]:

$$\Delta S_{11} \sim \sum_{*=x,y,z} (e_* E_*)^2 - (Z_0 h_* H_*)^2 \tag{6.1}$$

Where ΔS_{11} the change in reflection associated with the bead at a given location, e_* and h_* refer to the polarisation and magnetisation effects of bead and Z_0 is the impedance of free space, taken as $\approx 376.73\Omega$. By moving the bead longitudinally within the structure it is then possible to infer the amplitude and phase advance per cell in sequence by monitoring the reflected signal temporally [142]. When selecting a bead for the measurement it is important to consider the effect of the material choice, metals being capable of a magnetic and electric field perturbation due to the current in the surface while dielectrics only producing a significant perturbation of the electric field [143, 144]. As a result, typically a dielectric bead is favoured for accelerating structures however in cases where it is desirable to do so it has been shown to be possible to perform the measurement with both types in order to calculate each field component separately [143].

Due to having been tested with beam in CTF3 the superstructure was officially classed as radioactive material by CERN's radiation protection group. As a consequence, transporting the structure to the bead pull rig situated in CERN's dedicated tuning lab was not permitted and it was necessary to perform the measurement in air at the Xbox test facility. A makeshift bead pull rig was constructed as shown in Figure 6.6

The setup was manufactured from several small steel angle girders bolted to a composite support beam held in place by lead bricks weighing approximately 15kg in order to provide resistance to external vibrations or movement which could distort VNA measurements. A characterised bead and line were borrowed from the CERN bead-pull rig and a simple motor driver circuit was used to provide smooth motion of constant velocity. Small polyethylene inserts were machined to centre the wire as shown

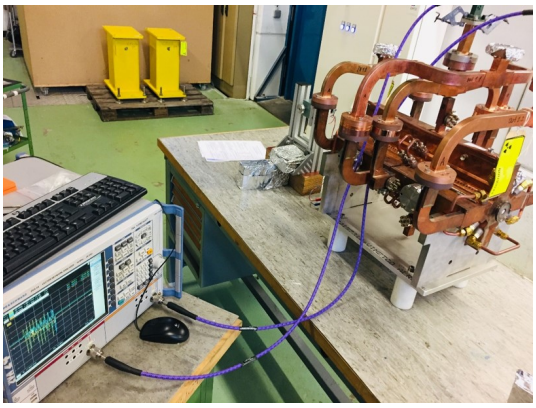

(a) Superstructure during the VNA measurement.

(b) Close-up of the plastic insert used to maintain alignment with the beam axis during the bead-pull.

Fig. 6.6 The arrangement used for the VNA measurement and bead-pull of the superstructure in CERN's high-gradient test area (a) and the dielectric wire used to move the bead through the structure (b).

in Figure 6.6 and weights were tied to each side to maintain tension and ensure the bead remained on axis throughout the measurement. The bead was then moved from the output to the input of the structure, while recording S_{11} as a function of spatial position. After each bead-pull a polar plot showing complex electric field profile was produced using a MATLAB based tuning program developed by J. Shi in 2013 [145]. The initial results of bead pulling structure B are shown in Figure 6.7.

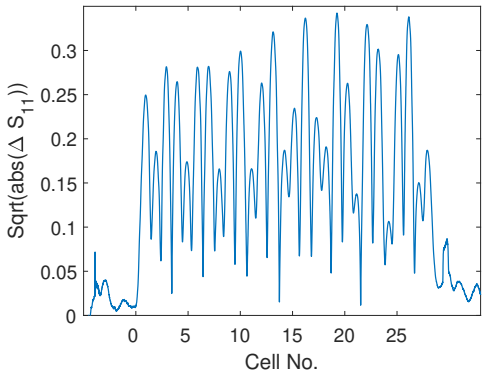

(a)

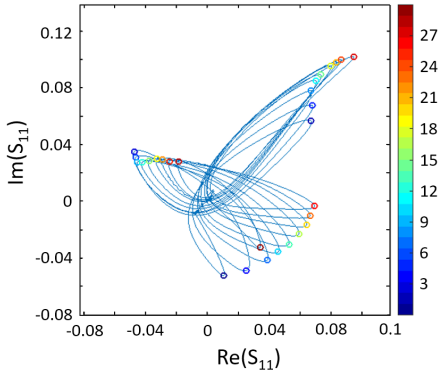

(b)

Fig. 6.7 The initial bead pull result for structure B. Shown are the field profile on the beamline axis (a) and a polar plot of S_{11} (b). The cells are counted with the bead pulled in the downstream direction i.e. from the input coupler to the output.

The 120° phase advance per cell and constant gradient design of the CLIC strucures should result in an overlapping triquetra when plotted in polar form and an approximately constant field profile. However, as is shown in Figure 6.7, a large periodic diminution in field occurs every three cells in the downstream direction indicating the presence of a standing wave within the structure. The fact that a significant field is detected in every cell shows that some coupling is present, however several of the maximum and minimum values are found near the structure output indicating that this is where the destructive and constructive interference is greatest and suggesting one of the later cells may be the cause of the poor transmission and tuning. This would also align with the observation in CTF3 where a large reflection appeared after approximately two times the fill time of the structure.

Upon inspection, small scrapes were visible beside the one of tuning pins on the final cell and it was speculated that during either installation or maintenance in CTF3 this point on the structure had been struck, leading to significant detuning of the cell. The frequency of the final cell was decreased by approximately 2 MHz, after which the transmission and field profile of the structure greatly improved. The structure was then tuned iteratively using the code developed by J. Shi until adjustments yielded no further improvement [145]. The final field profile and polar plots for each structure are shown in Figure 6.8 and Figure 6.9 respectively.

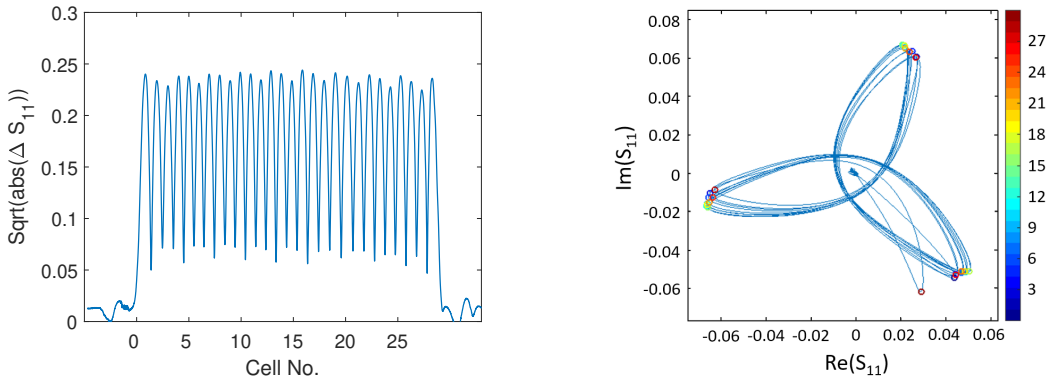

(a) (b)

Fig. 6.8 The final bead pull results for structure A showing the field profile (a) and a polar plot of S_{11} (b) with the bead pulled in the downstream direction.

The triquetra for structure B is rotated relative that of structure A due to the inclusion of spacers on the input manifold. The reflection from the bead is then delayed as the round trip is increased by two times the width of the spacers, manifesting in a fixed phase difference during the measurement. The achievable tuning is limited

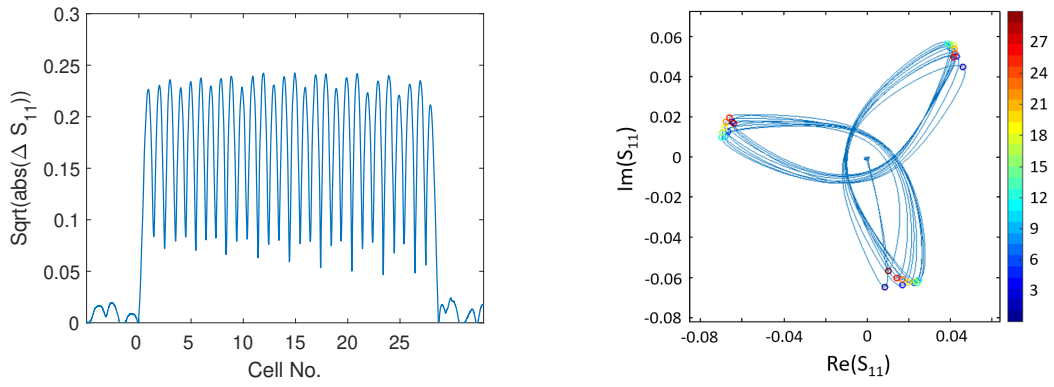

(a) (b)

Fig. 6.9 The final bead pull results for structure B after tuning showing the field profile (a) and a polar plot of S_{11} (b) with the bead pulled in the downstream direction.

by the accuracy of measurement and due to the non-ideal setup a small but notable standing wave persists in each structure. Additionally, each structure has endured some prior high-power testing and it has been documented that this results in significant degradation of the S-parameters and tuning [40, 146]. In 2018 the S_{11} for a TD26R05 structure at 11.9942 GHz in vacuum was observed to have reduced from under -58dB to -26dB whilst the field profile and phase advance for each cell were recorded as having deviated by ±5% and ±4° respectively after 900 million pulses high-power pulses and 23000 breakdowns [40]. To date no effort has been made to compensate the effects of high-power operation and so it is not known if it is possible to do so. Figure 6.10 shows the final S-parameters of each structure after tuning.

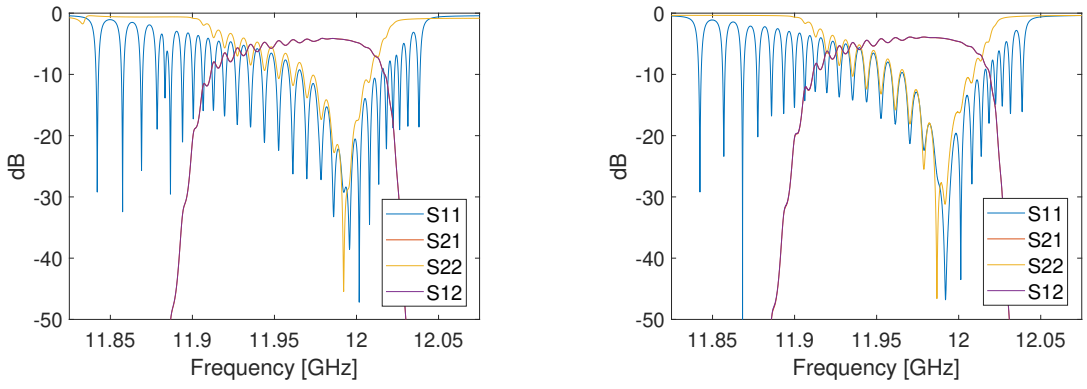

(a) (b)

Fig. 6.10 The S-parameters of structure A (a) and B (b) in air at 20.6°C prior to installation in the Xbox-2 test slot.

Although the envelopes are comparable, there is nonetheless a discrepancy between them, as expected given the difference in tuning. However, both structures remain resonant at the correct operating frequency and at this point the reflection of each is below -30dB, a value which was deemed acceptable for operation.

6.2 High-Power Test

Following tuning the structure was installed in Xbox-2 for high-power testing in the arrangement described in Section 5.2. At the time of testing Xbox-2 was equipped with a 50MW CPI klystron with a repetition rate of 50 Hz and a pulse compression scheme comprised of a BOC and CCC as detailed in Section 4.3. A high-power variable phase shifter and power splitter were installed to control the power split and relative phasing between each constituent structure. Figure 6.11 shows a diagram of the final arrangement and the signals which were acquired during testing while Figure 6.12 shows the final installation in the bunker.

6.2.1 Conditioning History

Conditioning was accomplished algorithmically in the test stand as described in Section 3.3.2 and a BDR setpoint of 3×10^{-5} bpp was selected based on the success of previous tests conditioned in the 1×10^{-5} bpp range. The breakdown rate during operation was defined as the number of breakdowns which had occurred within the previous 500k pulses, the selection of the window being a compromise between dynamic range and response speed. This provides a minimum measurable BDR of 2×10^{-6} bpp, significantly lower than intended operating range while still storing previous breakdowns long enough to prevent overly aggressive ramping in power. As the objective of the conditioning algorithm in use in the test stands is to condition and protect the system as a whole, all breakdowns in the network were taken into account in the calculation of the instantaneous BDR. As a consequence, the ramp in power and consequent conditioning can be dominated by a globally high BDR or a locally high BDR for any individual component. Given the presence of two constituent structures and a number of novel high-power RF components the performance of each structure was then assessed individually in post-processing by examining the transmitted and reflected signals recorded during breakdown events.

The electronically actuated phase shifter presented in Section 4.2 was first used during the test of the PolariX deflecting structure [147, 118]. During this test, the

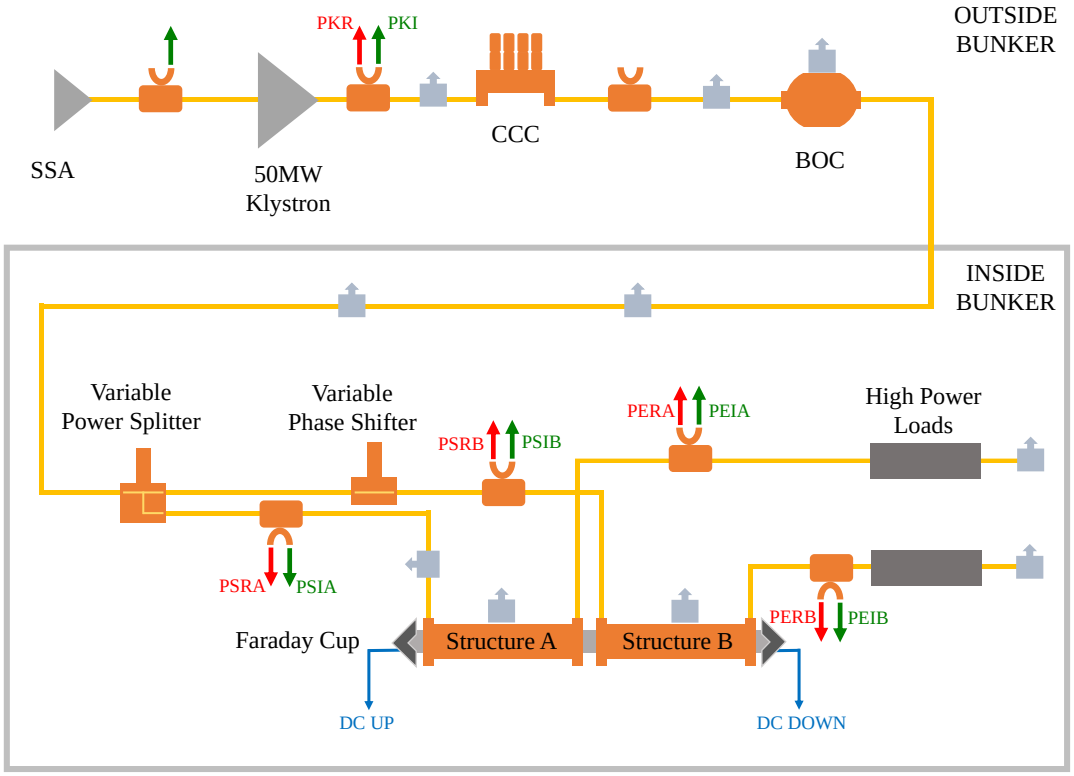

Fig. 6.11 Schematic of the superstructure test arrangement and diagnostic equipment. The green and red arrows represent the forward and reflected RF signals while the Faraday cup signals are shown in blue. The positions of the ion pumps throughout the waveguide network are shown by the grey squares with arrows.

internal piston stalled on several occasions, each necessitating an intervention to reset the device. Following the test an endoscopy was performed to examine the phase shifter internally and surface damage was found, indicating that the alignment of the internal piston had been compromised during operation [147]. To avoid such issues in the future, a power splitter and phase shifter with an alternative, manually controlled actuator were then installed in the waveguide network to control the power split and phasing between the superstructure constituents. However as the new actuators were not equipped with an encoder or motor, the circuitry presented in Section 4.2 could then not be used during the experiment.

Initially the objective was to split the power evenly between the structures, and so the power splitter was adjusted manually to provide an approximately even split based on the calibrated RF signals while the phase shifter was fully retracted to expose the entirety of the internal surface to RF. However, during subsequent calibration checks

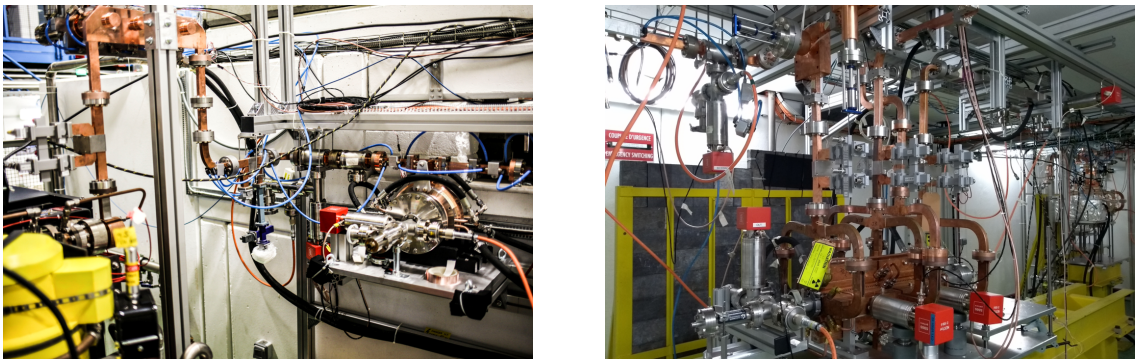

(a) (b)

Fig. 6.12 The pulse compressor arrangement at the klystron output (a) and the final installation inside the bunker prior to testing (b) showing the superstructure, power splitter and a partial view of the phase shifter. The coaxial cables for the acquisition system had not yet been connected to the directional couplers.

as high-power operation was approached several months later, a discrepancy in the amount of energy in the system was noted, indicating the presence of a calibration error. The cable chains were checked however the source of the error was not immediately clear, and during previous tests it had been noted that moving the power splitter generally necessitates a reconditioning period as the field distribution on the surface changes and a new portion of the internal surface is exposed to high-power RF.

Given the already slow conditioning, further delays were undesirable and so to facilitate the timely collection the data presented in Section 6.3, the decision was made to continue running until a substantial dark current signal emerged instead of immediately interrupting operation to verify the source of the error. The data could then corrected as required in post-processing. Following the collection of this data and the cessation of the test, the directional couplers were checked and it became apparent that a high-power directional coupler was mischaracterised, resulting in a calibration error. As outlined in Section 3.2.2 the design in use in the test stands generally has -60dB of coupling, however the directional coupler in use on the input of structure B had -53dB of coupling. Upon further investigation it was found that two X-band directional couplers at CERN had been assigned same serial number and so an incorrect calibration value had been selected during the initial calibration. As a consequence, throughout the duration of the test the power was approximately split in a 4:1 ratio, with structure B being consistently operated at approximately half the accelerating gradient of structure A. For the comparative studies following in Sections 6.2.3 and 6.3.2 the simulation work presented in Chapter 5 was then repeated

to apply to the manner in which the experiment was operated. The full conditioning history of each structure is shown in Figure 6.13.

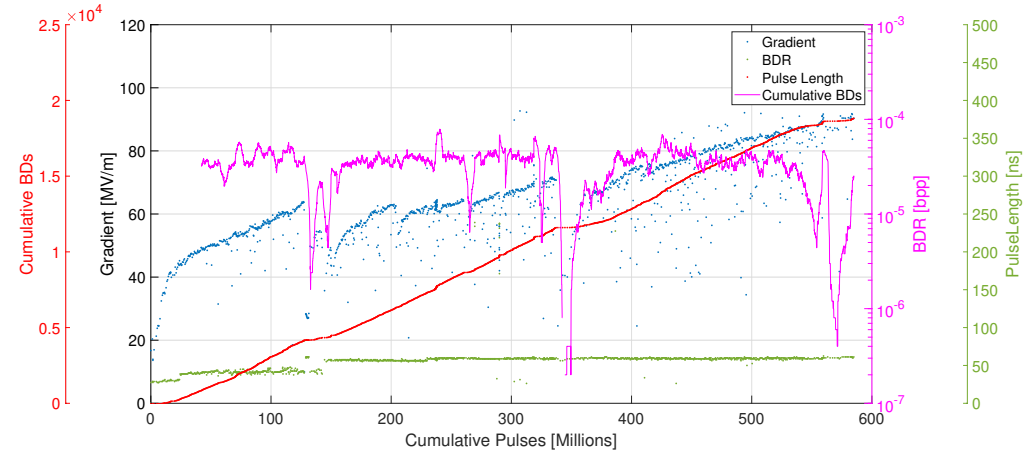

(a)

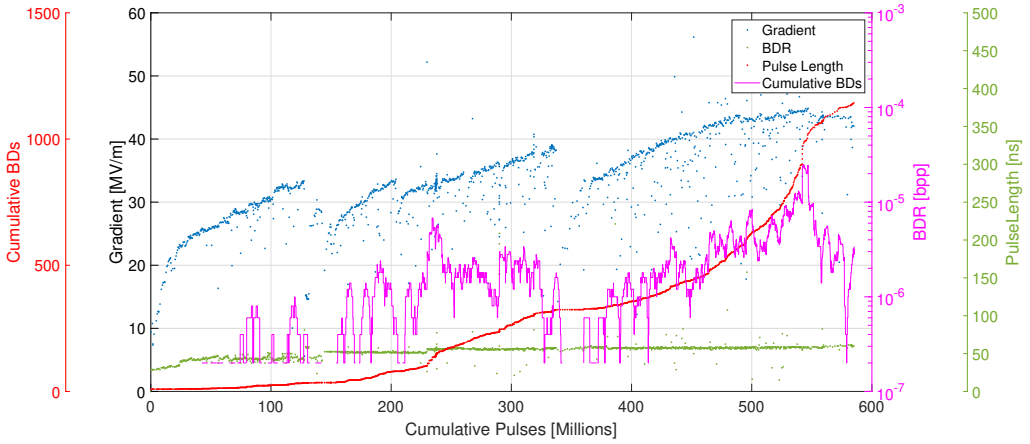

(b)

Fig. 6.13 Conditioning history of structure A (a) and structure B (b) of the super-structure respectively during high-power testing in Xbox-2 showing the accelerating gradient (blue), the pulse length (green), the cumulative breakdowns (red) and the breakdown rate (magenta).

Initially, to avoid the complications associated with pulse compressor operation a 50ns klystron pulse was used until the maximum available power from the klyston was reached. At this pulse length no compression occurs however there is some distortion of the pulse shape alongside several low power peaks following the main pulse due to the charging and discharging of the correction cavities. Additionally, as predicted in Section 5.3.2 the pulses received by each structure were not identical in shape due to difference between the S_{21} and S_{31} of the power splitter. Figure 6.14 shows the 50ns

klystron pulse delivered to each structure with a rectangular 50ns klystron pulse as the input.

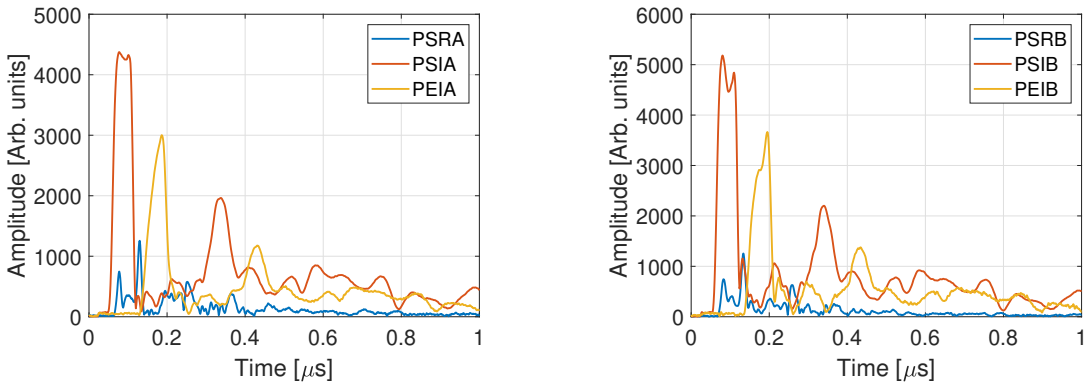

Fig. 6.14 The incident, transmitted and reflected waveforms associated with structure A (a) and B respectively (b) when using a 50ns klystron pulse. The correction cavities are tuned to 32, 16, 8 and 4 MHz respectively and so discharges in and following the main pulse are observed at 31.25, 62.5, 125 and 250ns in the time domain.

The klystron reached approximately 40MW after 140 million pulses, delivering peak powers of approximately 19 and 5MW to structure A and structure B respectively. Due to the attenuation and the dispersive effect of the pulse compression scheme the energy in the main pulse is reduced considerably and partially redistributed in the later discharges, meaning the sum of the peak powers sent to each structure was always lower than the peak power of the klystron pulse itself. As the klystron was close to the limit the decision was then made to switch to a compressed pulse and continue conditioning to higher peak power. On 22nd September, shortly after switching to the compressed pulse a high voltage power supply unit on the modulator failed, necessitating a pause in operation whilst the unit was sent for repair however during this time the vacuum integrity of the system was preserved. On 8th October 2019 the system resumed pulsing, due to the increased average power associated with the compressed pulse shape and time switched off a short reconditioning period was necessary as is visible after approximately 150 million pulses in Figure 6.13. Once again, as predicted in Section 5.3.2 it was noted that the structures received slightly different pulse shapes with efforts to produce a flat top in one structure compromising the pulse shape sent the other. To maintain fixed conditions structure A was then tuned to have an approximately flat top throughout the duration of the test. Figure 6.15 shows the

pulse shapes received by structure A and B respectively when a 700ns klystron pulse is compressed to 50ns.

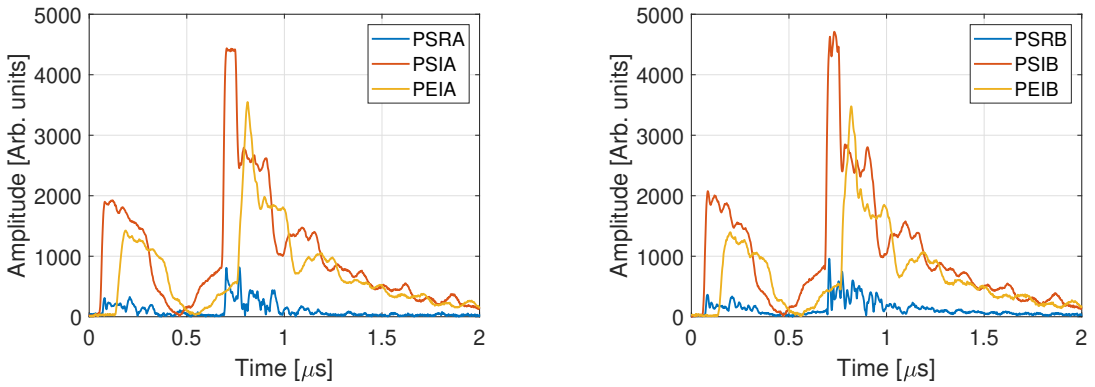

Fig. 6.15 The incident, transmitted and reflected waveforms associated with structure A (a) and B respectively (b) when a 700ns klystron pulse is compressed to 50ns.

Notably, at 250 million pulses a spike in the breakdown rate occurs, however this was due to a period of frequent access requirements and subsequent software resets in the test stand. Upon restarting the PXI crate and software the measured breakdown rate also resets, meaning upon upon each restart the system ramps until the breakdown rate setpoint is reached. Due to having occurred several times in succession a larger than usual number of breakdowns were accumulated in this period. Shortly thereafter, at the 270 million pulse mark CERN entered a two week shutdown period in late December during which the experiment was paused, necessitating a short reconditioning period upon restarting the system in January.

The constituent structures each reached gradients of 72 and 38.5MV/m respectively for a compressed pulse length of 50ns after approximately 350 million total high-power pulses however at this point a second modulator failure occurred. Immediately following repair of the modulator the decision was then made by CERN management to temporarily suspend all on site activities due to the emerging COVID-19 pandemic. The system was eventually restarted on 24th June 2020. The total time spent in the off state was then approximately 150 days however the vacuum integrity of the system was once again maintained throughout. Following this shutdown, the system ran largely uninterrupted until 9th October 2020.

Late in the conditioning a curvature emerges as the rate at which the power was increased slows. This asymptotic behaviour is a consequence of the increased probability of breakdown associated with high-field operation and the conditioning algorithm in the

test stands. As the BDR setpoint is regularly met or exceeded by groups of breakdowns the conditioning algorithm can no longer increase the power until they have fallen out of the BDR measurement window. Additionally, depending on when they occur such events may also result in a reduction in power. Notably, the rate of breakdown accumulation in structure B begins to increase, and a cluster of 65 breakdowns occurred at 4am on 24th September after approximately 540 million pulses. Following this, as a significant dark current signal was now present, ramping was paused and the BDR in both structures began to drop. The decision was then made to move the power splitter and phase shifter to test the devices and perform several experiments detailed in Section 6.3 which led to the changes observed in the conditioning plots, notably the sharp increase in power and BDR in structure A. Following the collection of this data the test was paused on 9th October 2020, pending the removal and return of the BOC to the Paul Scherrer Institute, a superconducting solenoid test and the removal of the klyston for use in an experiment at the National Institute for Nuclear Physics, Frascati, Italy (INFN).

6.2.2 Breakdown Distribution

Where possible, the breakdowns which occurred in each structure were localised via the edge method to monitor the structure performance and examine which constraints limit high-power operation [46, 148]. The plasma which forms during breakdown events constitutes a large impedance mismatch, as a consequence the incoming wave is reflected and in a travelling wave structures a truncation in the transmitted signal is also observed. In multi-cell travelling wave structures, such as those used for CLIC, if a breakdown occurs at time, t=0, then the time taken for a wave originating at any given cell (n) to propagate backwards to the input coupler (t_{ref}) can be calculated as the sum of the time taken to traverse each cell, written:

$$t_{ref} = \sum_{n_{cell}=1}^{n_{BD}} \left(\frac{L_{cell}}{v_g(n_{cell})} \right) \tag{6.2}$$

Where n_{BD} is the cell number where breakdown occurred, v_g is the group velocity for each cell and L_{cell} is the cell length. Similarly, the time taken for remaining RF power in the structure immediately after the breakdown site to reach the output of the structure (t_{tra}) may be defined:

$$t_{tra} = \sum_{n_{cell}=n_{BD}}^{N} \left(\frac{L_{cell}}{v_g(n_{cell})} \right) \tag{6.3}$$

As these events occur simultaneously, the difference in time between the detection of the falling edge of the truncated transmitted signal and the rising edge of the reflected signal may be used to infer the difference in the distance travelled between the forward and reflected waves and hence, the location in which the breakdown occurred. For a breakdown in the first cell, the truncation in power will be detected one fill time after t_{ref}. Conversely, for a breakdown in the final cell, the reflected signal will rise one fill time after the truncation in power(t_{tra}) occurs. It can be seen then, that the difference between t_{ref} and t_{tra} can adopt any value in the range of $\pm t_{fill}$. For this reason, a difference in these times associated with the location of the breakdown (t_d) may be calculated as:

$$t_d = \frac{t_{Ref} - t_{tra} + t_{fill}}{2} \tag{6.4}$$

Where the fill time is added to ensure no negative values are produced and the answer is divided by two to provide a range between 0 and the structure fill time. In this way, t_d is then zero for breakdowns which occur in the first cell and equal to the structure fill time for those which occur at the output. An illustration of the process is shown in Figure 6.16.

Additionally, on non-BD pulses the difference between the rising edges of the incident pulse and the transmitted pulse should be the fill time of the structure. With this information it is then also possible to account for any differences in cable lengths which may be present and align any given waveforms in post-processing to avoid the introduction of a systematic timing error. Alternatively, in situations where the difference in propagation times of different signal chains or absolute phase information is necessary it is possible to calibrate in an alternative manner which is described later in Section 6.3.1. To complement this method a corresponding breakdown phase may also be calculated [46]. In this method the phase difference between the incident signal and reflection from the breakdown site is sampled as:

$$\Phi_{BD} = \phi_{Ref} - \phi_{Inc} \tag{6.5}$$

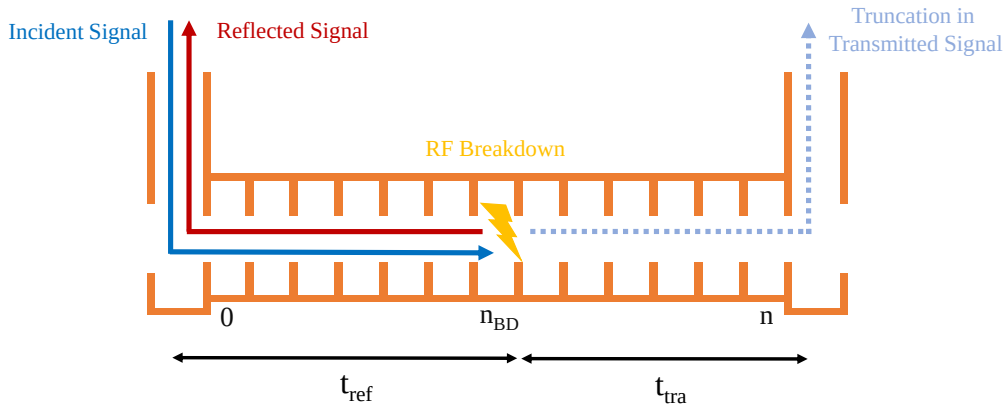

Fig. 6.16 Illustration showing how the difference in the propagation times of the rising edge of the reflection and the truncation in the transmitted signal may be used to infer the breakdown location. The resulting t_d value in this exampled would be equal to half the fill time of the structure, indicating the arc occurred in the central cell.

Where ϕ_{Ref} and ϕ_{Inc} are the phases of the reflected and incident waveforms respectively. In the CLIC structures, the phase advance per cell is fixed at 120° and breakdowns have been observed to occur preferentially on the structure irises where the fields are highest. The total phase advance calculated by this method will then be two times the phase advance to the cell in which the breakdown occurred or equivalently:

$$\Phi_{BD} = 2 \cdot \phi_{cell} \cdot n_{BD} + 180^{\circ} \tag{6.6}$$

Where ϕ_{cell} is the phase advance per cell, n_{BD} is the number of the breakdown cell as before and 180° has been added to account for the reflection coefficient associated with a short circuit. In the TD26 the cells are tapered, meaning the group velocity decreases downstream and the resulting t_d values associated with each cell in the TD26CC structure are shown in Figure 6.17 in addition to a breakdown pulse showing examples of the location of the rising and falling edges used in their calculation during analysis.

Figure 6.18 shows the resulting breakdown distribution within each structure.

During the first 150 million pulses localisation was often not possible due to the short 50ns klystron pulse which was employed. With this pulse shape, many breakdowns demonstrated no significant reflected signal with which the localisation could be performed. Additionally, after being subjected to the dispersion of the structure the transmitted signal was not well suited to the detection of sharp falling edges. Results

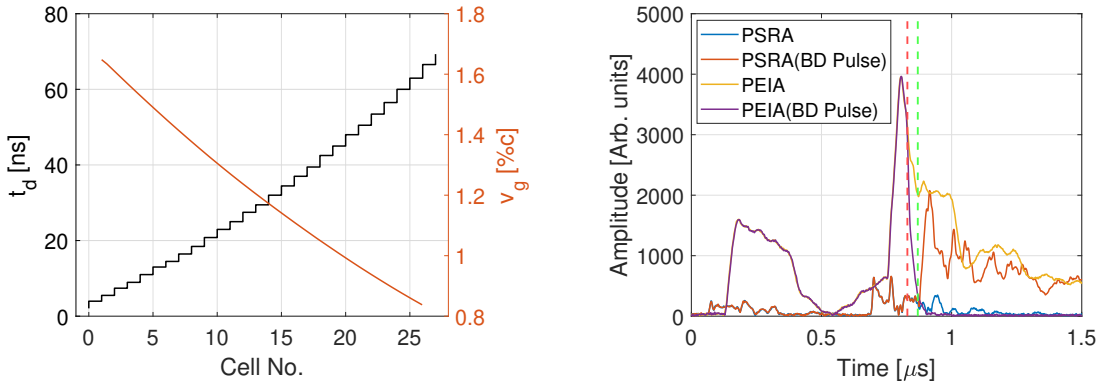

(a) (b)

Fig. 6.17 The t_d values and group velocity for each cell in the TD26CC R05 structure (a) and the transmitted and reflected waveforms on a non-BD and BD pulse (b). The truncation in the transmitted signal and rising edge on the reflected signal are shown by the vertical red and green dashed lines respectively.

from the data following this period show that a structure long spread in the breakdowns is present in structure A however the majority occurred in the final cells where the peak electric fields are highest and the modified Poynting vector is lowest. As in previous tests, the breakdown phase shows three distinct lines separated by 120°, corresponding to the phase advance per cell of the structure and indicating that breakdowns occur preferentially on the irises, where the surface electric fields are highest. Similarly, the majority of breakdowns in structure B also occurred in the later cells however due to the low number of breakdowns no significant trend emerges in the phase data. Close to the end of the test however, it can be seen that the cluster mentioned in Section 6.2.1 occurs entirely at the end of the structure and predominantly at a single phase, indicating that the events predominantly took place within a single cell, close to that which required significant tuning as described in Section 6.1.2. Virtually all breakdowns prior also occurred in this location. It is speculated that the fault observed in CT3 may have contributed to this breakdown distribution, with the cell having potentially already accumulated breakdowns and hence surface damage prior to installation in the test stands.

Notably, an increased BDR is also visible after 240 million pulses in Figure 6.13 (c). However, as outlined in Section 6.2.1 this was caused by several system restarts in quick succession, resulting in a large number of accumulated breakdowns within relatively few pulses. Given that the breakdown distribution both prior to and following this

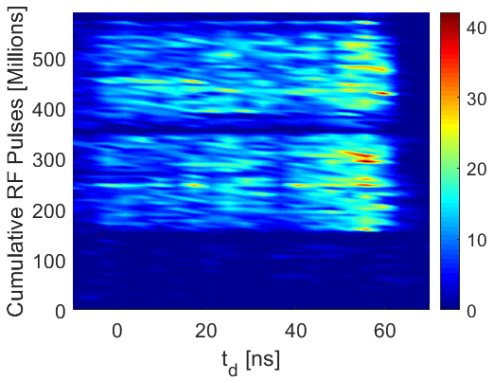

(a) Time-of-propagation vs pulses for structure A.

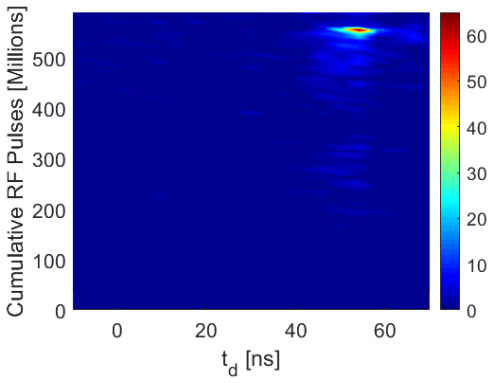

(b) Time-of-propagation vs pulses for structure B.

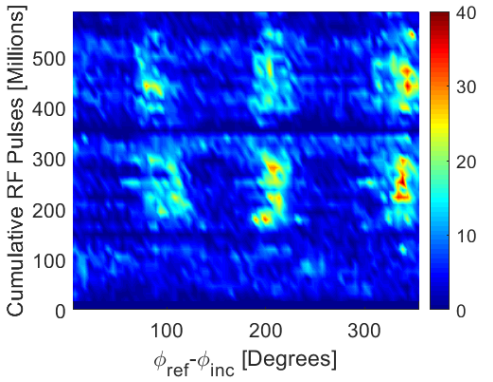

(c) BD phase vs pulses for structure A.

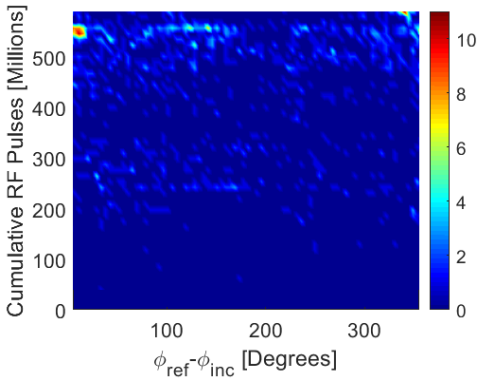

(d) BD phase vs pulses for structure B.

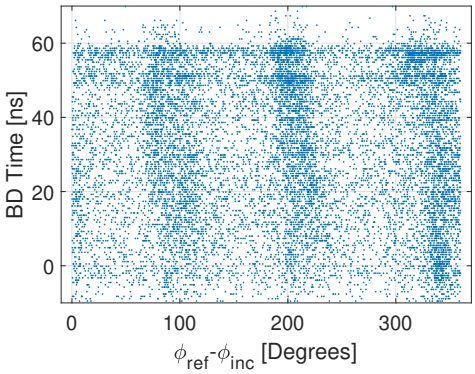

(e) Time-of-propagation vs BD phase for structure A.

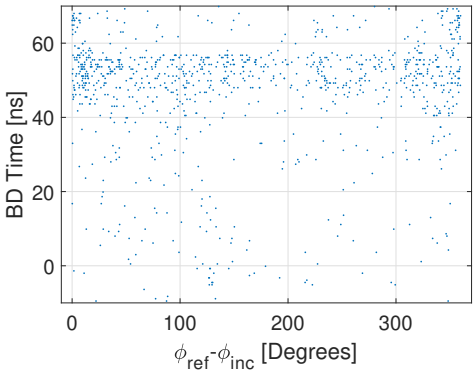

(f) Time-of-propagation vs BD phase for structure B.

Fig. 6.18 Distribution of breakdown sites within each constituent structure as calculated via the edge method. A time of 0ns corresponds to the structure input while 65ns (approximately one fill time) corresponds to the output coupler.

period are similar and that the gradient continued to increase without issue the event is not thought to have measurably altered the structure performance.

In previous tests, during the early stages of conditioning breakdowns have been observed to occur throughout the length of the structure before migrating to the front in the later stages, while operating at the full design gradient and pulse length [92]. This would then suggest that the superstructure is still in the conditioning phase. Despite this, it is important to note that the final cells in structure B still accumulated a significant number of breakdown despite the reduced input power, potentially indicating the presence of a fault. However, as the test is still incomplete no definitive conclusions may yet be drawn. Additionally, no flat runs were performed to investigate the dependence of BDR on gradient or pulse length however such experiments are planned for when testing resumes.

6.2.3 Interactions Between Structures During Breakdowns

As explored in Section 5.3, it was speculated prior to testing that the use of a three-port variable power splitter would result in interactions between structures during breakdown events as illustrated in Figure 6.19.

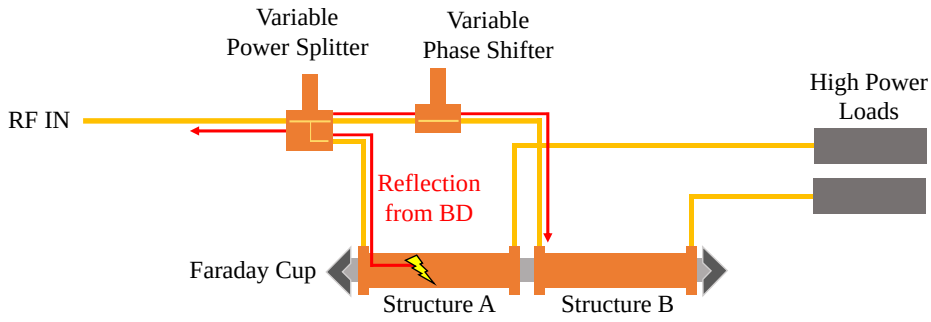

Fig. 6.19 Diagram showing how a breakdown in structure A may result in a large reflection (red) being sent back towards the klystron and to structure B, the latter being capable of provoking a secondary breakdown in structure B if constructive interference occurs.

Results of the work performed in Chapter 5 show that whether such interactions result in significant constructive or destructive interference is dependent on the phase of the reflected wave and hence the spatial location of the breakdown. Given the results of the breakdown localisation it is expected that three main regimes of interference will be observed and whether the neighbouring structure experiences an increase of decrease in incident should correlate with the location of the breakdown. As the majority of

breakdowns occurred in structure A, this effect was investigated by examining the waveforms associated with structure B during breakdown events.

During breakdowns in structure A, the incident power (PSIA) is reflected towards the klystron and structure B as shown in Figure 6.19. This reflection can then constructively or destructively interfere with the incident pulse nominally delivered to structure B (PSIB). The energy in the incident pulse for structure B during breakdowns in structure A (P_{BD}) was then calculated by integrating between the arrival of the reflection from structure A (t_{ref}) and the cessation of the RF pulse (t_c) as:

$$E_{BD} = \int_{t_{ref}}^{t_c} P_{BD}\, dt \tag{6.7}$$

A gain factor was then calculated by taking the ratio of this integral to the integral of the previous, non-BD pulse (P) between the same limits as:

$$GainFactor = \frac{\int_{t_{ref}}^{t_c} P_{BD}\, dt}{\int_{t_{ref}}^{t_c} P\, dt} = \frac{E_{BD}}{E} \tag{6.8}$$

This gain factor was calculated using both the incident (PSIB) and transmitted (PEIB) waveforms and the results of each was plotted against the breakdown phase given by Equation 6.5. Figure 6.20 shows example waveforms for a case in which constructive interference has occurred. The t_{ref} and t_c values are also included, showing the region which is integrated in the calculation of the gain factor given by Equation 6.8.

If the only source of energy loss is in the structure walls, then the gain factor calculated via the PSIB and PEIB waveforms should be equal. However, a significant current is also often observed during breakdown pulses. It is speculated then that if sufficient current reaches structure B at the correct phase measurable beam loading may occur during the breakdown pulse. As a consequence, the gain factor calculated from the PEIB waveforms would then differ from that calculated via the PSIB waveforms. This effect was then also investigated by calculating the difference between the gain factors calculated via the PSIB and PEIB waveforms. The result may then provide an estimate of the energy deposited in or extracted from the current emitted during breakdown. Finally, for comparative purposes the analysis presented in Section 5.3.3 was repeated with the power splitter set to provide a 4:1 power split, as it was set in the test stand during the collection of the experimental data. The results of the analysis and the simulated values are shown in Figure 6.21.

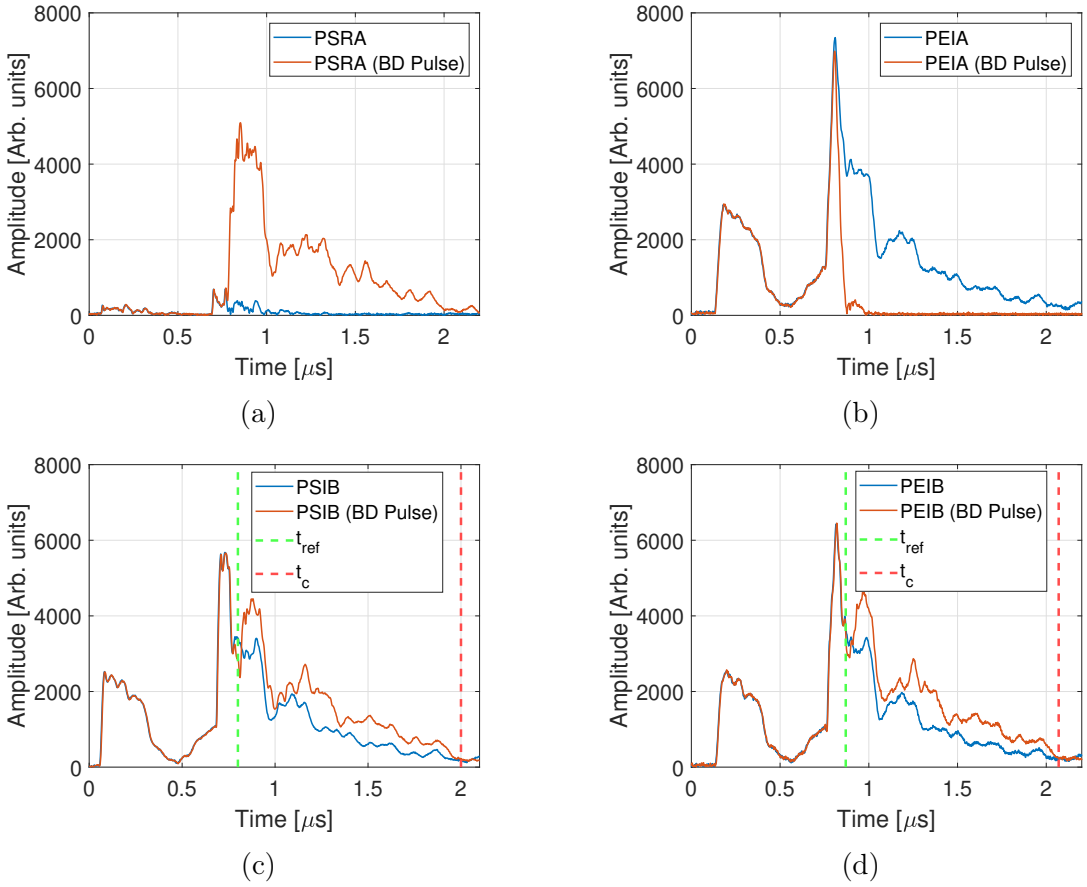

Fig. 6.20 The PSRA (a), PEIA (b), PSIB (c) and PEIB (d) waveforms during a normal pulse and a pulse in which a breakdown has occurred in structure A. The reflection from the breakdown in structure A has resulted in a power surge in structure B. The region which is integrated to calculate the gain factors is shown by the vertical green (t_{ref}) and red (t_c) lines respectively.

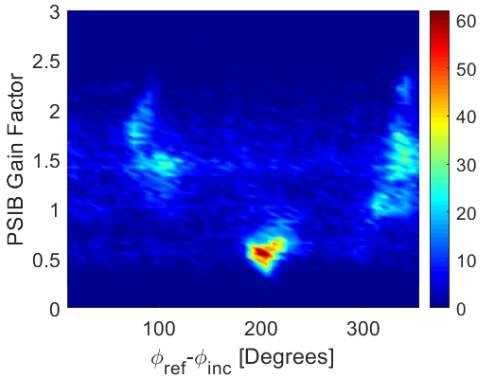

(a) The power gain observed in the PSIB signal during a breakdown in structure A plotted as a function of the phase of the reflection from the breakdown site.

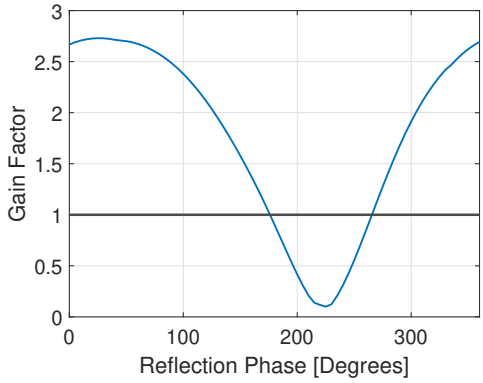

(b) The simulated power gain observed at port 3 with a short placed on port 2 as a function of the short position and hence, phase of the reflection. The power splitter used in simulation was set to the same position as in the test stand.

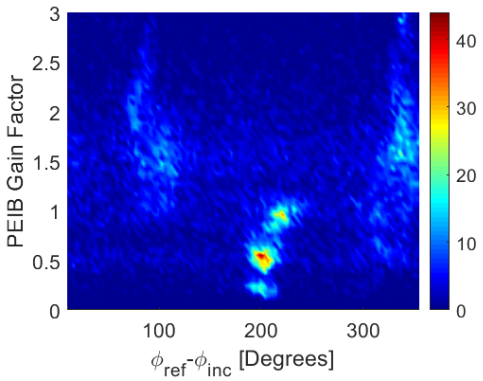

(c) The power gain observed in the PEIB signal during a breakdown in structure A plotted as a function of the phase of the reflection from the breakdown site.

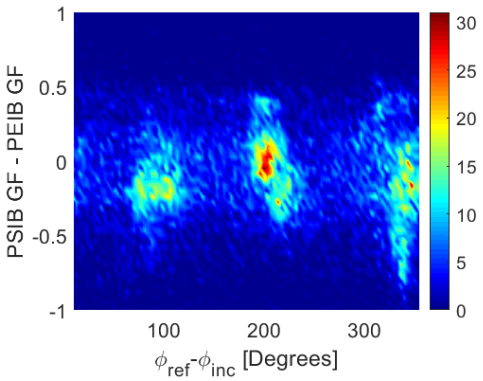

(d) The difference between the gain factors calculated via PSIB and PEIB waveforms. The discrepancy indicates that energy has been deposited in or extracted from the current emitted by structure A during breakdown.

Fig. 6.21 The change in power in structure B during breakdowns in structure A relative to a non-breakdown pulse as function of breakdown phase for the incident (a) and transmitted (c) signals and the difference between them (d). The simulation results with the power splitter in the relevant position are also shown (b). Experimental results are plotted as a heat map for improved readability and the colour scale is indicative of the number of data points lying within a given area. High density areas are shown in red and dark blue regions effectively show the noise floor of the measurement.

Three main peaks are shown, corresponding to the phase advance per cell, as shown previously in Figure 6.18. The most densely populated areas show changes in power which fall between the nominal power shown by the black horizontal line and the envelope predicted by simulation, indicating that simulation provided a good approximation of the behaviour. However, both a vertical and horizontal variance is present and this is due to two reasons. The first that breakdowns do not form a perfect short, but a complex load which results in a variance in the phase of the reflected signal. Secondly, breakdowns were logged as having occurred throughout the structure, meaning any reflected waves will also have been subjected to the attenuation and dispersion associated with the cells traversed.

Notably, the difference between the gain factors calculated via the PSIB and PEIB waveforms is approximately spread around zero, indicating that the current emitted during breakdown is equally like to extract energy from or deposit energy in the electromagnetic field. It is speculated that this is due to the nature of the emissions during breakdown, with charge carriers being emitted sporadically as opposed to a precise bunch-like structure used during nominal operation. As a consequence, whether or not notable beam loading occurs is then determined by the phase at which any charge carriers reach the neighbouring structure. It should also be noted that cases in which little downstream dark current is recorded also occur, suggesting that occasionally charge carriers emitted during breakdown may not be capable of reaching the second structure.

Depending on the time at which the arc occurs and the nature of the emitted current this phenomenon may then have several consequences during operation. In the event that an arc occurs after the main beam has already passed, a portion of the breakdown current may be captured and trial behind it however the main beam will remain unaffected. If an arc occurs prior to the arrival of a main beam, then the plasma associated with the arc is already capable of degrading the beam and thus any degradation associated with the breakdown current induced beam loading is of little additional consequence. However, if the current emitted deposits a significant amount of energy in later structures, the associated increase in surface fields then constitutes an increased risk of intra-pulse breakdowns occurring.

In Section 5.3.3 it was also speculated that a surge in power could result in the induction of a second breakdown intra-pulse breakdown in the neighbouring structure. Upon examination of the data it was found that such events occurred regularly during operation and an example is shown in Figure 6.22. For comparative purposes, the waveforms during the previous non-breakdown pulse are also shown alongside the

breakdown pulse (blue and orange respectively). In Figure 6.22, the transmitted pulse in structure A (PEIABD) is truncates immediately upon receipt of the RF pulse and a large reflection is observed (PSRABD). The incident pulse associated with structure B (PSIBBD) then becomes larger than the previous pulse, demonstrating a surge in power has occurred. At approximately $0.8\mu s$ the transmitted pulse associated with structure B (PEIBD) then truncates and a large reflection is observed (PSRBD) indicating the formation of a second, intra-pulse arc. Notably, the primary arc in structure A occurred immediately upon the receipt of the RF pulse, similar to that shown in Figure 5.12, indicating that the assumptions made during simulation were appropriate.

Conversely, a breakdown in which destructive interference occurred is shown in Figure 6.23. As before, the transmitted signal associated with structure A (PEIABD) truncates and a large reflection is observed (PSRABD). However, after $0.8\mu s$ the incident and transmitted pulses associated with structure B (PSIBD, PEIBD) are greatly reduced compared to the previous pulse, indicating that significant destructive interference has occurred.

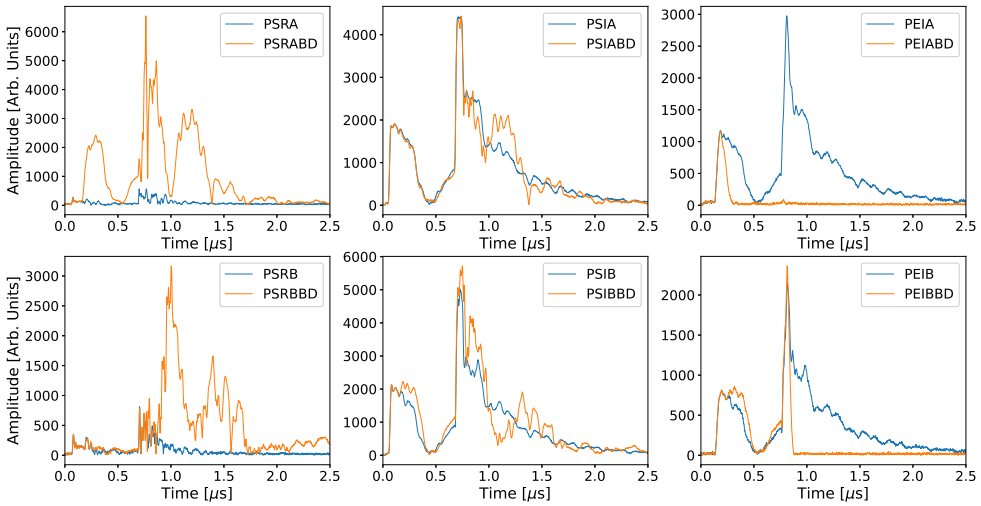

Fig. 6.22 Example of a breakdown in structure A (top) inducing a breakdown in structure B (bottom) on the same pulse. Note the surge in the incident (PSIBBD) and transmitted (PEIBBD) signals in the second structure followed by immediate truncation and a large reflection. The waveforms from the previous pulse are also shown in blue for comparison.

During the investigation, one instance in which three breakdowns occurred on a single pulse was also logged, and the resulting waveforms are shown in Figure 6.24. In

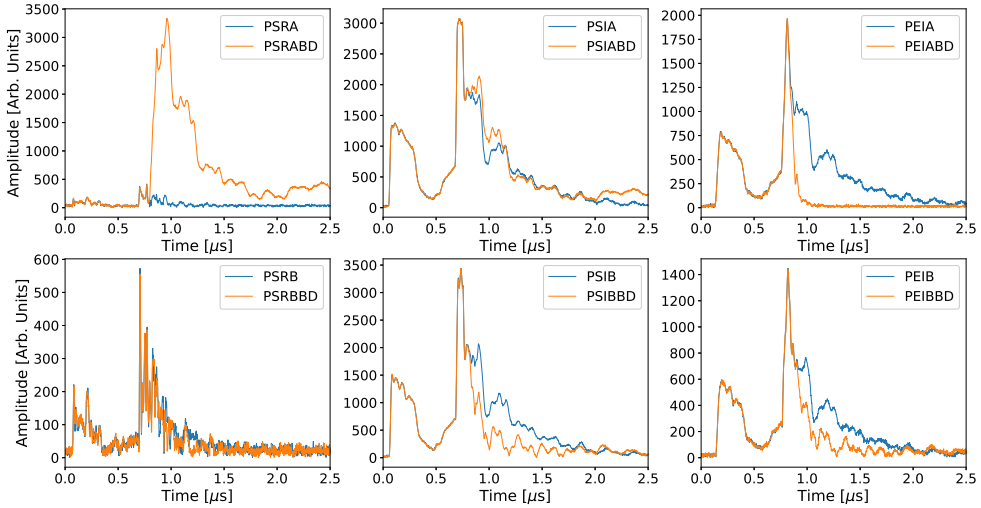

Fig. 6.23 Example showing the reflected signal from a breakdown in structure A (PSRABD) destructively interfering with the structure B incident signal (PSIBBD) causing a reduction in the incoming and transmitted power. The waveforms from the previous pulse are also shown in blue for comparison.

this example, the transmitted signal associated with structure A (PEIBD) truncates after approximately $0.75\mu s$ and a large reflected signal (PSRABD) is observed. Several nanoseconds later, a power surge is observed in the incident pulse in structure B (PSIBD). Following this, the transmitted pulse in structure B (PEIBD) truncates and a large reflection is observed (PSRBD), indicating the formation of a second intra-pulse arc. The incident and transmitted pulses for both structures then truncate simulataneously and the reflections cease, indicating that neither structure is receiving an RF pulse and that a breakdown has also occurred earlier in the network, prior to the structures. It is speculated that the breakdown occurred in the power splitter, reflecting all incoming power from the klystron and pulse compression scheme.

Approximately 100 dual breakdown events were found to have occurred during operation. Given the small number of instances relative to the total number of breakdowns such events were then relatively unlikely, and were not thought to be statistically significant. In facilities with beam, the occurrence of a single breakdown is sufficient to heavily degrade the beam and thus a secondary breakdown on the same pulse may be deemed inconsequential. The results do however constitute evidence that surges in power do not immediately result in significant damage to a structure, and that nominal operation may be resumed following such events. Results also

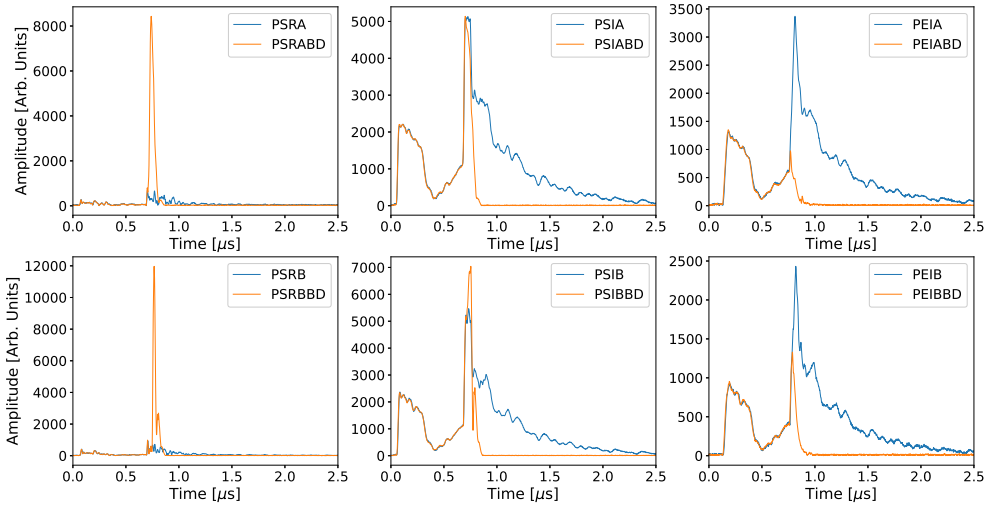

Fig. 6.24 Waveforms during a pulse in which three separate arcs have occurred. PEIA truncates first resulting in a large reflected signal. Following this, PEIB truncates and a large rise in PSRB is observed. Finally, tens of nanosends later both incident channels truncate suggesting the either the power splitter or a component earlier in the line has also arced.

suggest that by carefully selecting the length of each waveguide or indeed via the inclusion of a phase shifter it is possible minimise the propensity for power surges in this arrangement provided the phasing is not already constrained by the structures themselves. Alternatively, the use of a hybrid with a terminated fourth port as is shown in Figure 4.1 would provide effective isolation between the two components under test at the expense of having a fixed power split.

6.2.4 Comparative Analysis of Constituent Structures

Due to the discrepancy in power throughout the testing period it was noted that the breakdown rate in structure B was consistently lower than that of structure A, save for a cluster which occurred after approximately 550 million pulses. It is clear that structure A has contributed the majority of breakdowns during the conditioning period hence regulated the rate at which the power was algorithmically increased. In order to compare the superstructure to alternative designs and structures which have been tested under different conditiong, a comparative analysis was then carried out. However, it is important to note however that given the uneven power split the analysis then primarily pertains to structure A.

During conditioning a structure's performance is typically evaluated by three succinct quantities, gradient, pulse length and BDR. During the test each constituent structure operated at a vastly different breakdown rate and so to facilitate a truly qualitative comparison between both constituent structures and indeed previously tested prototypes each quantity must then be scaled to account for the other operating conditions, for this purpose there exist several dependencies in literature which may be adopted. As mentioned in Section 2.4 it has been empirically proposed that the probability of breakdown is strongly related to the accelerating gradient (E_{acc}) and the pulse length (t_p) such that the BDR at a given gradient scales as [16, 149, 46]:

$$BDR \propto E_{acc}^{30} \cdot t_p^5 \tag{6.9}$$

With these relations several means of comparison and normalisation may be derived and this is commonly performed in literature [58, 149]. Firstly, a quantity which is indicative of the conditioned state of the structure and directly related to the constant of proportionality inherent in Equation 6.9 may be calculated as:

$$E_{acc}^{*} = \frac{E_{acc} \cdot t_p^{\frac{1}{6}}}{BDR^{\frac{1}{30}}} \tag{6.10}$$

The conditioning history of a T24 Open tested at CERN's X-band facility is shown in Figure 6.25 in terms of its accelerating gradient, pulse length and BDR as a function of cumulative RF pulses. Figure 6.26 shows the history of the same structure plotted in terms of the E_{acc}^{*} quantity calculated by Equation 6.10.

Plotting E_{acc}^{*} results in a curve which is no longer segregated into regions of distinct operating conditions but a single continuous quantity which is representative of the physical state and indeed the perceived improvement of the structure as it accumulates high-power pulses. Notably, late in the conditioning process this value is much higher than the accelerating gradients which are typically achievable and so it should be noted that it is not merely a scaled gradient. Any irregularities and sharp changes of this curve are then indicative of significant changes in operating conditions i.e. in the instantaneous pulse length, BDR or input power. Alternatively, as high-gradient machines are typically designed with acceptable operating parameters in mind, the accelerating gradient may also be scaled to a reference BDR (BDR_{Ref}) and pulse length ($t_{p,Ref}$) as:

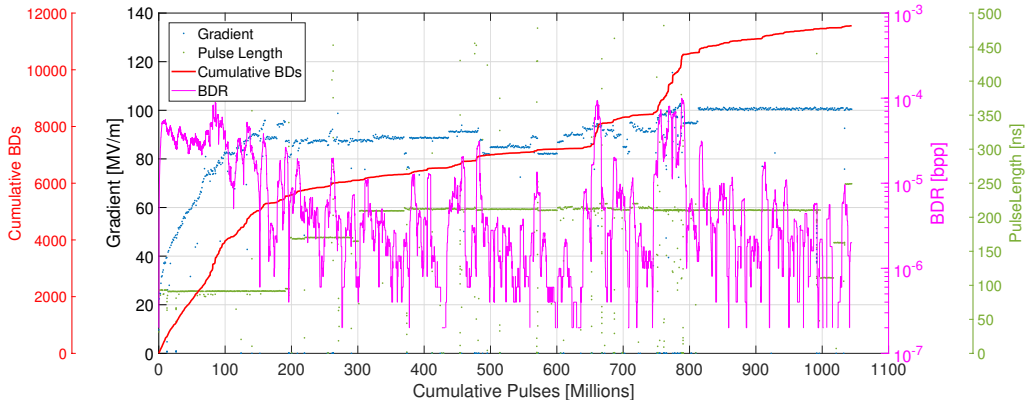

Fig. 6.25 Conditioning history of a T24-open tested at CERN's X-band test facility showing the established gradient (blue), the structure BDR (magenta), the pulse length (green) and the cumulative breakdowns (red).

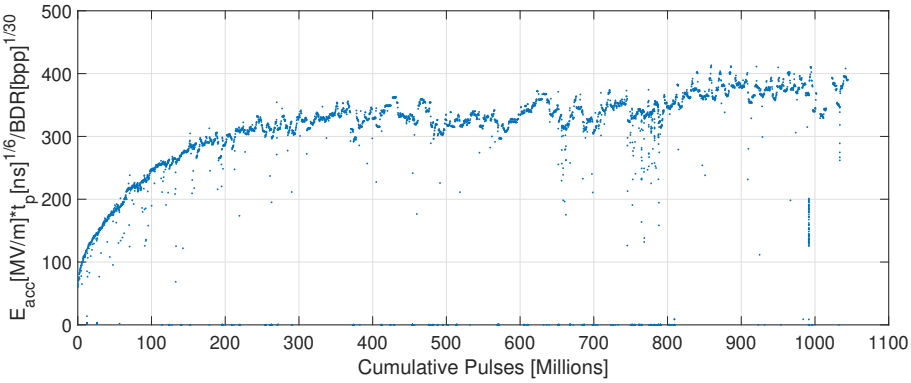

Fig. 6.26 The conditioning history of a T24-open structure tested in CERN's X-band test facility as calculated by Equation 6.10.

$$E_{acc}\{t_{p,Ref}, BDR_{Ref}\} = E_{acc} \cdot \left(\frac{t_p}{t_{p,Ref}}\right)^{\frac{1}{6}} \cdot \left(\frac{BDR}{BDR_{Ref}}\right)^{-\frac{1}{30}} \tag{6.11}$$

After having been conditioned to the reference pulse length and BDR, the scaled value is then representative of the expected ultimate structure performance. Figure 6.27 shows the conditioning history of the T24-open, scaled to a pulse length of 200ns and BDR of 1×10^{-6}, two values commonly quoted in literature [46, 82, 149].

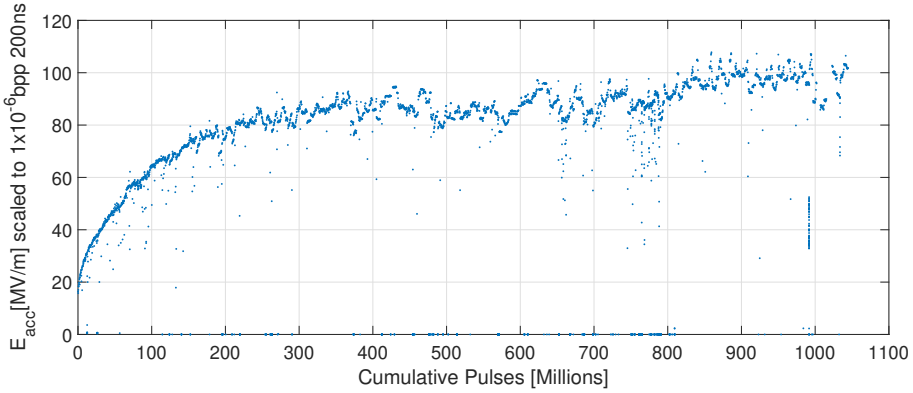

Fig. 6.27 The conditioning history of a T24-open test at CERN scaled to a pulse length scaled to a pulse length of 200ns and BDR of 1×10^{-6} with Equation 6.11.

Similarly, a scaled modified Poynting vector and BDR may be found respectively as:

$$S_c\{t_{p,Ref}, BDR_{Ref}\} = S_c \cdot \left(\frac{t_p}{t_{p,Ref}}\right)^{\frac{1}{3}} \cdot \left(\frac{BDR}{BDR_{Ref}}\right)^{-\frac{1}{15}} \tag{6.12}$$

$$BDR\{t_{p,Ref}, E_{acc,Ref}\} = BDR \cdot \left(\frac{t_p}{t_{p,Ref}}\right)^{-5} \cdot \left(\frac{E_{acc}}{E_{acc,Ref}}\right)^{-30} \tag{6.13}$$

Finally, to eliminate the effect of geometric variances between structures it is possible to normalise to a given surface electric field (E_{Surf}) as opposed to an accelerating gradient, with the two quantities differing only by a constant factor as:

$$E_{Surf} = E_{acc} \cdot k_E \tag{6.14}$$

Where k_E is a constant defined by the cavity geometry, typically ≈ 2.1 for CLIC prototype structures [150]. Using these relations, the scaled peak surface electric field, BDR and modified Poynting vector of the superstructure constituents have been compared with five other structures recently tested at CERN's high-gradient test stands in Figure 6.28. The structures chosen for comparison were two T24 structures manufactured at the Paul Scherrer Institute, Switzerland, a TD26CC which was previously tested at CERN, a T24 machined in halves and the CLIC crab cavity prototype, the latter being a traverse deflecting structure as opposed to a conventional accelerating structure like the others. It should be noted that both T24 structures were tested in Xbox-3 before being moved to Xbox-2 later in the test period and so only the data from the period spent in Xbox-3 is shown. As S_c is proportional to the input power, and hence the electric field squared, the square root of the scaled S_c is plotted to facilitate a linear comparison with the scaled surface electric field, E_{Surf}.

Similarly, the superstructure also proceed slowly in terms of the scaled modified Poynting vector, however structure A begins to approach a value which is comparable to the other structures after approximately 500 million pulses. Notably, the CLIC crab cavity generally increases more quickly than the accelerating structures. Due to operating in the TM_{110} mode deflecting structures establish necessarily high magnetic fields within their cells, which leads to a higher Poynting vector per watt of input power when compared to accelerating structures operating in the azimuthally symmetric TM_{010} mode [151]. A sharp increase in S_c was also noted during the high-gradient test of PolariX TDS, indicating that may then be a trait which is characteristic of deflecting structures in general [147].

In the early stages, the scaled BDR is an abstract and unphysical measurement, suggesting the occurrence of multiple breakdowns per pulse. The value typically becomes more appropriate in the later stages of testing as a measure of a structures ultimate performance where the scaling begins to produce more physically meaningful values. As the superstructure has not reached full pulse length or design gradient the normalisation results in a bias, however the gradient of the curve is comparable to that of previous tests and no signs of saturation are present, indicating neither structure has reached the ultimate limit. Finally, the scaled conditioning history of previously tested CLIC prototypes plotted in terms of their cumulative breakdowns is shown in Figure 6.29.

As noted previously by J.G. Navarro, when the conditioning histories are plotted as a function of the cumulative breakdowns they proceed at drastically different rates, instead progressing more comparably in terms of pulses [46]. This aligns with his

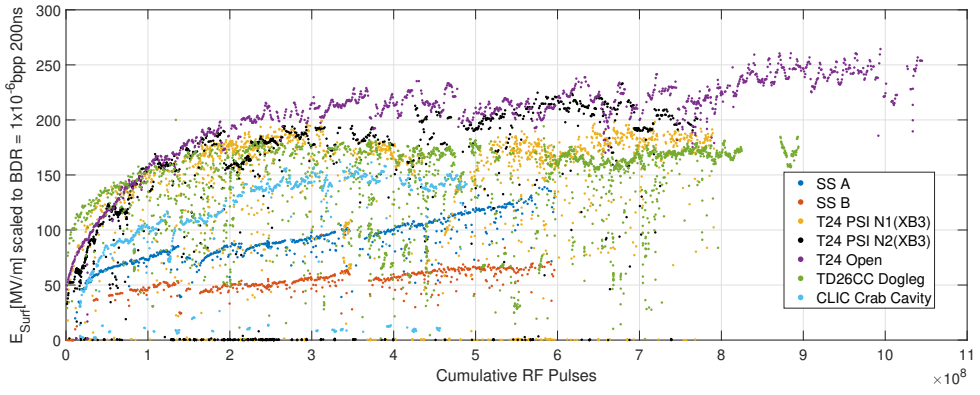

(a)

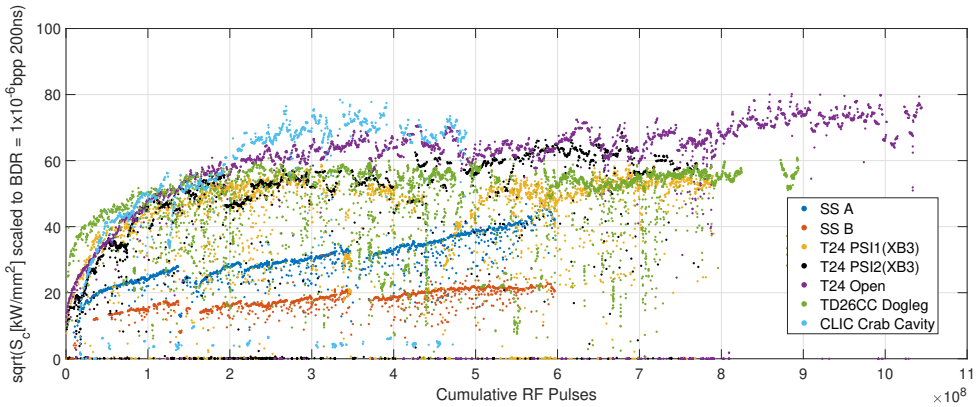

(b)

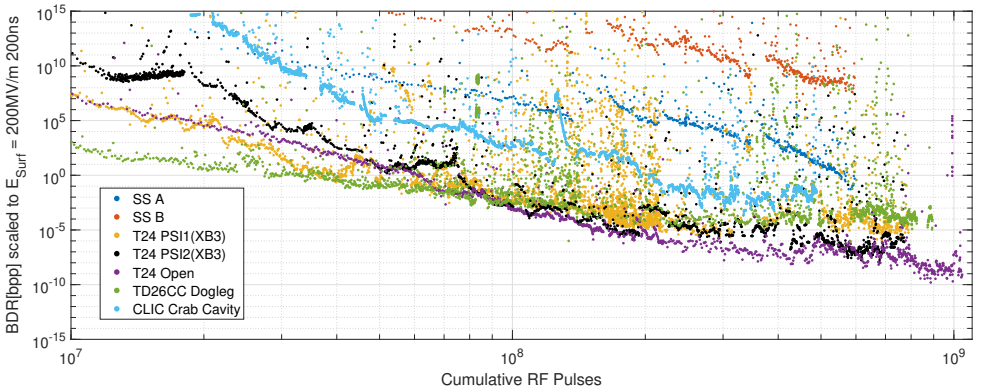

(c)

Fig. 6.28 Scaled conditioning history of superstructure constituent A (SS A) and B (SS B) plotted alongside five other high-gradient prototype structures. The conditioning is plotted in terms of the scaled peak surface electric field (E_{Surf}), the square root of the scaled modified Poynting vector (S_c), and the scaled BDR against the cumulative RF pulses in plots a, b and c respectively.

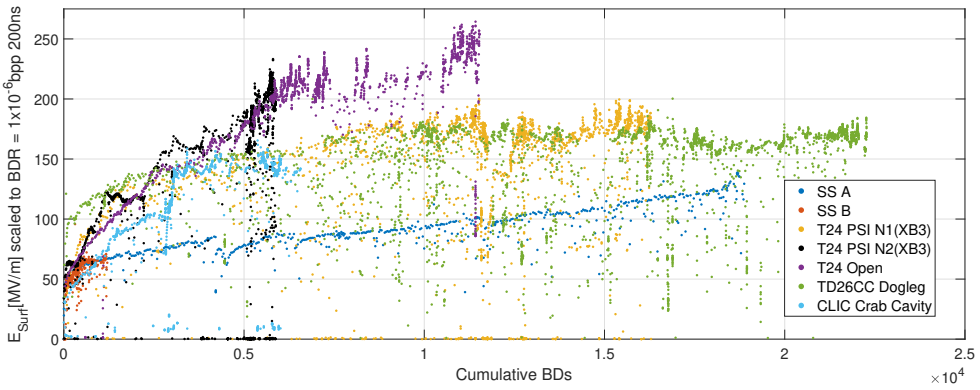

Fig. 6.29 Evolution of the scaled peak surface electric field (E_{Surf}) of superstructure constituent A (SS A) and B (SS B) when plotted against the cumulative breakdowns. Five other high-gradient prototype structures are also plotted for comparative purposes.

suggestion that cumulative RF pulses are the metric on which structures condition, and not solely the cumulative breakdowns [46]. Once again however, the superstructure constituent A proceeds more slowly than previously tested structures whilst structure B has accumulated few breakdowns to date. It is important to note however, that as mentioned previously virtually all breakdowns in structure B occurred in the final cells whilst the rest of the cells have largely been conditioned to the 45MV/m accelerating without the occurrence of arcs. As the test is ongoing no definitive conclusions pertaining to the limit of each constituent structure can be made.

6.3 Multi-Structure Emission Measurements

The inclusion of a phase shifter in one input facilitates adjustment of the relative phasing of two constituent structures. PIC simulations in Section 5.4.4 investigated how the capture and acceleration of field emitted current varies as a function of this phasing. Measurements to validate these simulations were then carried out in the test stands and the results are outlined following.

6.3.1 Phase Calibration

As the Xbox-2 test stand is a facility without beam capability it is not possible to measure the phasing of the relative structures via spectrometric methods and instead the LLRF system must be used to infer the phase difference between structures. To do so accurately it is necessary to account for the difference in electrical length of all signal

chains. In some cases, it is possible to perform time domain reflectometry to determine the electrical length of a cable and hence determine the absolute phase of two signals relative to one another however in the case of Xbox-2 this measurement is greatly complicated as the signals are not sampled directly, instead passing through a mixing crate which houses several non-linear components and for which the internal path lengths for each channel are unequal. As such, an alternative method was chosen for phase calibration. A splitter was characterised and placed on the directional coupler at the input of the first structure and the cables for both PSIA and PSIB were connected as shown in Figure 6.30. The RF was then switched on at low power for several minutes to log data.

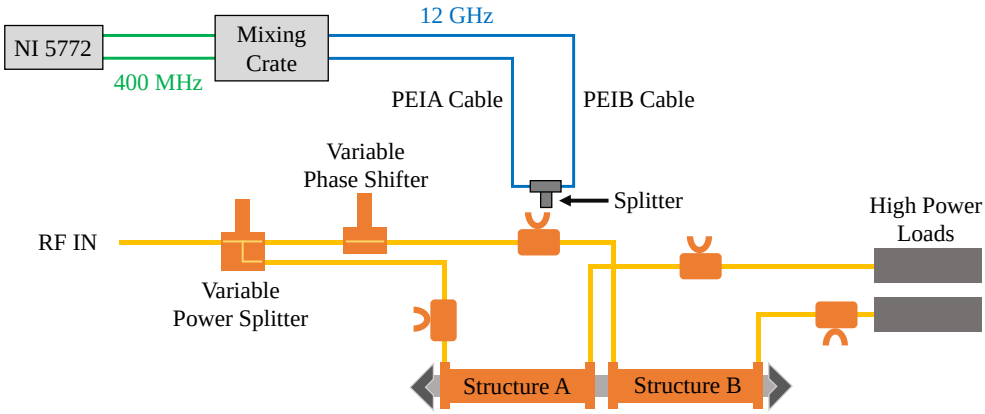

Fig. 6.30 Block diagram illustrating the setup used to calibrate the electrical length of the signal chains relative to one another.

Each cable connects to the mixing crate for down mixing to the IF at 200 MHz where it is then be sampled directly by an NI 5772 acquisition card at 800 MS/s. The acquisition trigger for this card is sent directly from the PXI backplane where it is clocked by the mains at 50 Hz. As both PSIA and PSIB are acquired by independent channels on the same card the acquisition for each data point should take place simultaneously. Any difference in cable lengths will then manifest as a fixed time and phase discrepancy between the recorded signals. Alternatively, if no splitter is available it is also possible to swap a pair of cables between their respective directional couplers and form a set of equations to be solved for the relative timing and phase. This has the added benefit of removing the need for a characterised splitter however doing so for multiple channels then becomes computationally more difficult and laborious.

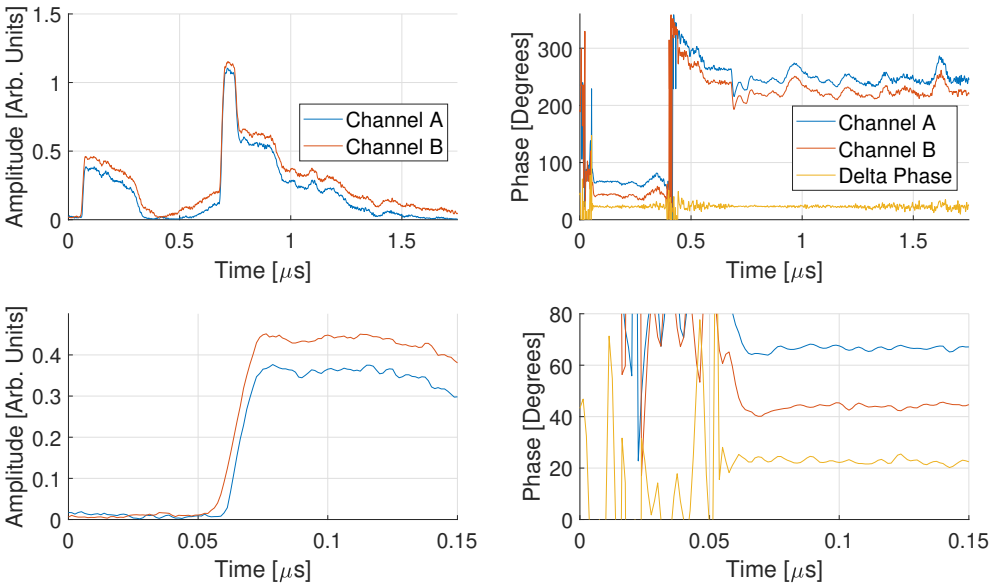

Fig. 6.31 Raw amplitude and phase data logged from the PSIA and PSIB channels when both are measuring the incident pulse on structure A (top left and top right respectively) with a close-up (bottom) illustrating the difference in electrical length of each signal chain manifesting as a phase and time discrepancy. Note, although the same signal is being sampled there is nonetheless a difference in the measured amplitude due to the difference in attenuation of each respective signal chain.

Figure 6.31 shows the resulting plots for both phase and amplitude of PEI1 and PEI2 sampling the same signal. During normal operation the data shows a time difference (Δt_{Cable}) and phase difference ($\Delta\phi_{Cable}$) between PSIA and PSIB as follows:

$$\begin{aligned} \Delta t_{Cable} &= t^r_{PSIA} - t^r_{PSIB} \approx 7ns \\ \Delta\phi_{Cable} &= \phi_{PSIA} - \phi_{PSIB} \approx 23^\circ \end{aligned} \tag{6.15}$$

Where t^r is the time at which the rising edge occurs on each signal. Results showed the PSIA signal chain to be shorter by approximately 7ns and lagging in phase by 23°. As the point to point resolution of the data is 1.25ns (approximately 15 RF periods) it should be noted that it is not possible to infer the phase difference from the timing alone. These values were therefore subtracted from all the following measurements to accurately infer the phase. Finally, although the system is calibrated up to the directional couplers, the phasing was previously corrected in CTF3 with the addition of spacers on the manifold feeding the second structure, as are visible in Figure 6.12.

While calculation of the delay associated with the spacer is possible numerically, the manifold has also been tuned via compression of the waveguide in the transverse plane meaning RF measurement is necessary to accurately infer the difference. Prior to insertion each was characterised and the difference was found to be 208° in phase at 11.9942 GHz. This difference is also visible in Figure 6.9 where it results in a rotation of the triquetra produced during the bead pull measurement.

6.3.2 Variation of Capture and Radiation with Relative Phasing

To monitor the captured current two Faraday cups were installed in the test stand, one at the input of the first structure and one at the output of the second as shown in Figures 6.11 and 6.12. Each is situated following a short section of beam pipe such that any electrons leaving the structure create a small measurable voltage upon striking the detection surface. To investigate the effect of the relative phasing on the capture of field emitted current the Faraday cup signals were monitored with the phase shifter in several different positions. To complement the measurement an ion chamber was also installed. A diagram of the arrangement is shown in Figure 6.32.

The phase shifter was fully retracted and the operating gradients in structures A and B were reduced to 85MV/m and 42.5MV/m respectively for approximately 2 minutes while the dark current signals were logged. The process was then repeated with the phase shifter in four other positions spanning the operating range of 180°. The

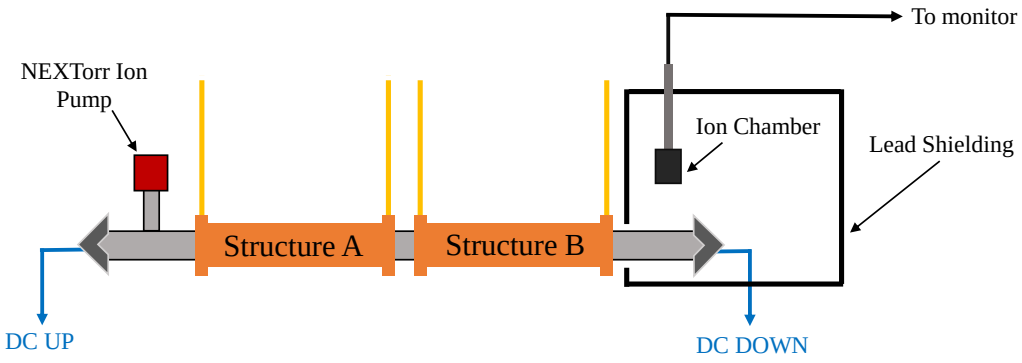

Fig. 6.32 Diagram showing the position of the ion chamber during the dose rate measurements.

reduced gradient allowed the measurements to take place without inducing breakdowns, meaning the emission properties of the structure remained unchanged. For comparative purposes, simulations were also performed in the same manner as those presented in Section 5.4.4 for structures operating at gradients 85MV/m and 42.5MV/m respectively. The results are shown in Figure 6.33.

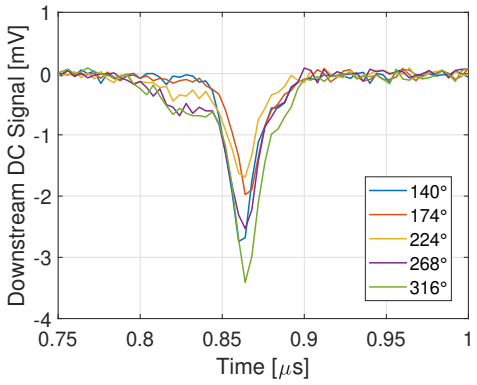

(a) Downstream Faraday cup signal logged with the structure B at different phases relative to structure A.

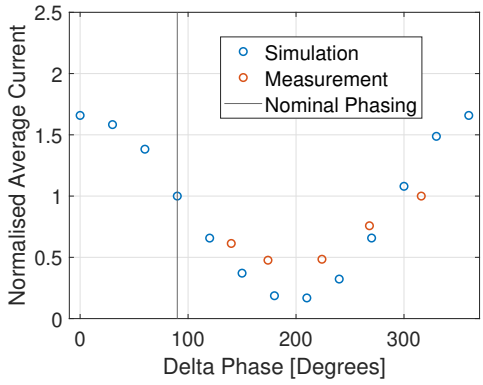

(b) Normalised average downstream dark current versus relative phasing.

Fig. 6.33 The dark current waveforms logged in each position (a) and the normalised average downstream dark current signal plotted as a function of relative phasing between structures for the simulation results and experimental data (b) for structures operating at 85 and 42.5MV/m respectively. A phase of 90° corresponds to structure B leading in phase by 90° relative to structure A. The phasing arrangement in which a fully relativistic beam would receive the maximum energy gain is shown by the black line.

A sinusoidal variation is present in the measured current over the operating range of the phase shifter. The lowest experimental measurement is higher than that predicted by simulation and the sinusoidal variance is hence reduced. This indicates that more current is emitted in the second structure than predicted by simulation. However, many of the breakdowns in structure B occurred in the final cells and an increased BDR has been shown to correlate with increased dark current signals [41]. It is speculated that high β values may be then present in the final cells of structure B. This would also align with simulation results presented in Section 5.4.2 which demonstrated that much of the current emitted in this region is capable of reaching the structure output. The locations of the minima are also in approximate agreement, indicating that the phase calibration provides a reasonably accurate measurement of the relative phasing. Results then indicate that in-situ phase measurement of the structures is possible using only the dark current.

Previously in Xbox-2 a spectrometer has been used to monitor the energy of the current observed during operation and initially it was planned that this arrangement be installed for use with the superstructure [37, 151]. However due to the additional length of the superstructure and limited space within the bunker installation of this arrangement was not possible without the removal of the Xbox-3 test slots. Instead, as mentioned previously an ion chamber and a PTW UNIDOS webline monitor were installed to record the dose rate during the measurement. Initially, the ion chamber was positioned in the bunker however during the first measurements the measured dose rate was extremely low and so the decision was made to remove a portion of the lead shielding and reposition the ion chamber beside the downstream Faraday cup as shown in Figure 6.32.

While this does not provide an inference of energy, both the total current and average energy increase with capture. As the dose rate increases in direct proportion to the current any remaining discrepancy will be due to a shift in the energy spectrum of the captured current. A dose rate measurement was then recorded in parallel to the measurements shown in Figure 6.33. During the measurement all Xbox-3 test slots were switched off to ensure only radiation produced by Xbox-2 was recorded. The three measurements which resulted in a signal exceeding the noise floor are shown in Figure 6.34.

A clear increase in the dose rate is observed over the 100° range due to the variance in capture of field emitted electrons, aligning with the increase in current shown in Figure 6.33. Additionally, while the total current approximately doubles the total dose rate increases by a factor of five, indicating that the energy of the current has also

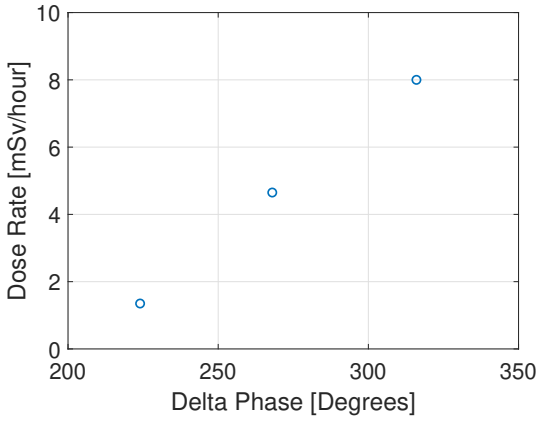

Fig. 6.34 The dose rate immediately outside the downstream Faraday cup as a function of relative phasing between the two structures.

substantially increased. Comparing the experimental results with simulations presented Section 5.4.4 also shows that the maximum dose rate was recorded in the approximate phasing arrangement in which the dark current experiences the most acceleration. As such, it is possible to exploit this effect in order to minimise the radiation produced during conditioning.

6.4 Conclusion

A superstructure comprised of two TD26CCR05 type structures bonded together has been installed in CERN's Xbox-2 test stand and constitutes the first multi-structure arrangement to be tested in the facility. The power was split between structures and the relative phasing varied through the use of a novel high-power variable power splitter and phase shifter respectively. Throughout the conditioning process the power was split between the structures in a 4:1 ratio meaning the accelerating gradient established in structure B was half of that established in structure A. Both constituent structures were capable of relatively high-power operation, with structure A and structure B having reached gradients of 90MV/m and 45MV/m respectively for a pulse length of 50ns however at the time of writing the test is still ongoing and it is clear that structure B is still comparatively unconditioned.

It was previously speculated that the inclusion of a three-port device would facilitate interactions between the structure during breakdown and the induction of breakdowns in the neighbouring structure as a consequence of this effect was regularly observed. The propensity for surging has also been investigated and simulations performed in Chapter 5

were repeated for the manner in which the experiment was operated. Experimental results demonstrated a reasonable agreement with the simulated values. During testing the dark current capture was also investigated as a function of relative phasing between the structures. Experimental results demonstrate a reasonable agreement with simulations performed in the same manner as those presented Chapter 5.

Upon distinction and comparative analysis of the structures it became clear that structure A had contributed the majority of breakdowns during conditioning due to having been operated at a higher gradient that structure B, effectively limiting the rate at which the power was algorithmically increased during conditioning. The performance of each structure has been compared with other accelerating structures which have previously been tested in CERN's X-band test stands. The conditioning of the superstructure has proceeded more slowly than the previously tested structures and it is speculated that this may be a consequence of the long storage period prior to testing and the frequent interruptions, however no signs of saturation have emerged indicating neither structure has reached its respective limit. Additionally, despite the lower operating gradient structure B still accrued approximately 1200 breakdowns, most of which occurred in a single cell at the end of the structure. As these breakdowns occurred close to where a fault was detected prior to installation it is speculated that the structure may have accumulated breakdowns and potentially surface damage while being operated in CTF3 however further testing is necessary to determine whether the structure is still capable of operation at the full design gradient. A summary of the key RF parameters achieved during the test is provided in Table 6.2.

Quantity	**Structure A**	**Structure B**	**Units**
P_{In}	33.85 (33.85)	8.4625 (7.91)	MW
E_{acc}	90 (90)	45 (43.5)	MV/m
E_{Surf}	175.5 (175.5)	87.75 (84.83)	MV/m
H_{Surf}	369 (369)	184.5 (178.35)	mA/m
S_c	3.321 (3.321)	0.8303 (0.8163)	MW/mm^2
t_p	50 (50)	50 (50)	ns
Cumulative RF Pulses	585	585	Million
Cumulative BDs	18892	1227	-

Table 6.2 Summary of key test parameters for each superstructure constituent. Values shown correspond to the maximum achieved during the test period and where relevant the values at which each structure terminated the test are also included in brackets.

Chapter 7

Monte Carlo Model of High-Gradient Conditioning and Operation

Recent test results have consistently demonstrated that modern high-gradient structures must be conditioned before reliable operation is achieved, typically requiring hundreds of millions of high-power RF pulses. The optimisation of this process is then of great interest in terms of cost reduction, increasing throughput and reducing the probability of component damage. Due to the reproducible nature of the phenomenon algorithms have also been developed to automate the process, namely at Daresbury Laboratory, SLAC and CERN [37, 152, 153]. However, such algorithms have been implemented based on empirical observations and due to the significant time and cost required, optimisation studies are difficult to perform experimentally.

The following chapter presents the development of a model capable of capturing the regularly observed characteristics of the conditioning process and the macroscopic behaviour of CERN's high-gradient test stands as a whole. The model is then used to examine phenomena observed in the test stands and the effects of adjusting several variables in CERN's current conditioning algorithm.

7.1 General Description of the Model

Recent high-power test results from the Xbox test stands suggest that conditioning proceeds on pulses [46, 149]. As such, the model is based on the assumption that the surface's propensity for high-field operation is modified on a pulse-to-pulse basis. Based on the characteristics of a given RF pulse it will also be necessary to both determine whether or not a breakdown occurs and respond accordingly while saving

all values of interest for later review. A simple recursive loop capable of encapsulating this functionality is shown in Figure 7.1.

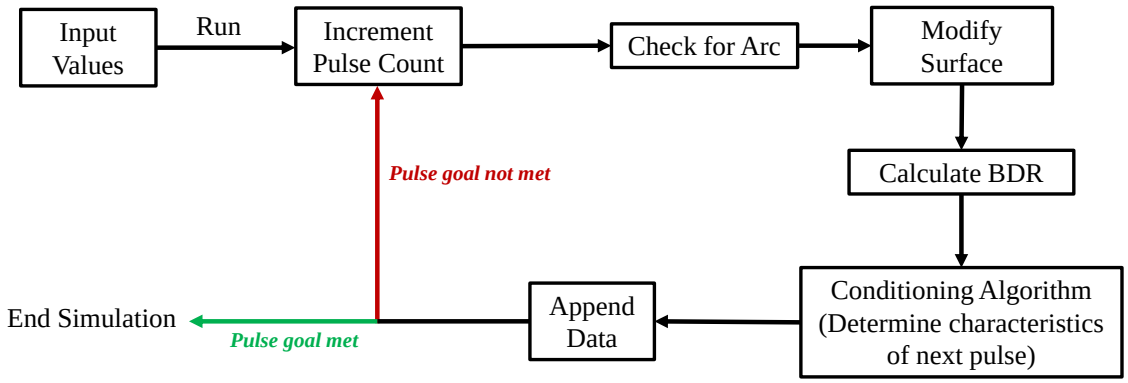

Fig. 7.1 Simplified block diagram showing the how the conditioning process and test stand behaviour may be simulated.

Many of the functions required are simplistic in nature or, in the case of the conditioning algorithm, already well defined. However, a means of capturing the probabilistic behaviour of breakdown and the conditioning process must be derived. Due to the strong empirical dependency it is convenient to define the model in terms of the electric field. It is important to note that the electric field is not the only quantity thought to be significant in breakdown, however as it scales proportionally with other electrical quantities this is nonetheless thought to be a reasonable approach [16].

7.1.1 Definition of the Model's Quantities

Given the stochastic nature of breakdown, it is convenient to define the level to which a device has been conditioned, and hence the terms used in the model, relative to a reference breakdown rate. With this in mind, terms are first required to represent the operating voltage and voltage to which the device has been conditioned i.e. the operating field at which the device has a probability of breakdown which is equal to the reference breakdown rate. Additionally, it is known that conditioning cannot take place indefinitely and instead proceeds asymptotically, slowing as high-field operation is approached. Hence, it is assumed that for a given material there is an intrinsic limit above which no further improvement takes place, or equivalently, above which the surface accumulates damage faster than it conditions. The model is then defined in terms of the following quantities:

- $P_{Baseline}$ = The instantaneous probability of breakdown for a given device operating at the level to which it has been conditioned.
- $E_{Operate}$ = The electric field level in MV/m at which the device operates.
- E_{State} = The surface electric field level to which the device has been conditioned in MV/m. Operation at this field level results in a probability of breakdown which is equal to $P_{Baseline}$.
- E_{Sat} = The saturation point for a given material in MV/m. Operation above this level does not result in any further improvement in E_{State} and thus this is the maximum surface field attainable at the reference breakdown rate after the device has been fully conditioned.

7.2 Conditioning Algorithm

As the model will be primarily used to examine CERN high-gradient test data the conditioning algorithm implemented in simulation is identical to that present in the test stands. The test stands are programmed in the National Instruments native LabVIEW format and so the algorithm was converted to a Python function which may be invoked in the model. An overview of the algorithm was provided in Section 3.3.2 and a detailed description is available elsewhere [37, 106]. However, as the adjustment of the algorithm forms the basis of several studies in Section 7.5 the key variables concerned will be outlined. A graphical representation of the conditioning algorithm is shown once again in Figure 7.2.

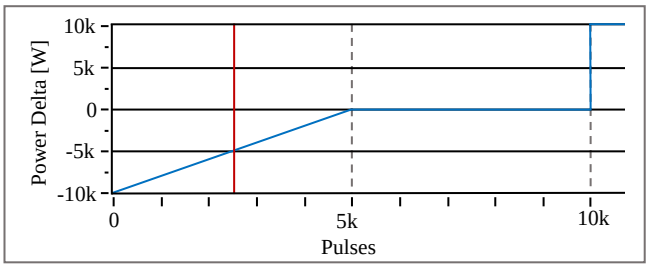

Fig. 7.2 Graphical representation of the conditioning algorithm in CERN's high-gradient test stands where the loop length is set to 10,000 pulses, the ramp length is set to 5000 pulses, and the step size is 10kW.

During operation the vertical red bar scrolls to the right as the system pulses, when it reaches the step shown by the blue curve, the power level is increased by the

step size and the red line resets to the left side. The process happens periodically at intervals determined by the loop length. If a breakdown occurs shortly after this step within the ramp length the power is then decreased by an amount determined by the number of pulses since the step was implemented. A breakdown in Figure 7.2 would then correspond to a decrease in power of 5kw. The ramp length, loop length and step size are all user-configurable variables in the test stands. Simultaneously, a BDR is calculated during operation using Equation 3.9.

If the calculated BDR exceeds the chosen BDR setpoint, the loop in Figure 7.2 continues to run however the step in power will simply not be implemented. As before the BDR measurement window and BDR setpoint are also user-configurable variables in the current conditioning algorithm. For preliminary simulations the loop and ramp lengths were set to 10k and 5k pulses respectively with a step size of 10kW. A BDR setpoint of 4×10^{-5} was also chosen with a BDR measurement window of 500k pulses as values in this range are often implemented in the test stands.

7.3 Quantification of Conditioning

Although the model is defined in terms of the electric field, the algorithm in the test stands feeds back on power. As different structures establish different surface electric fields for a given input power a conversion is then necessary. Typically, the CLIC structures require input powers on the order of 40MW to establish an unloaded gradient of 100MV/m, corresponding to surface electric fields in excess of 200MV/m. Hence, the structures establish a surface electric field of approximately 32000V/W$^{0.5}$ and a similar value $E_{Operate}$ is then calculated for a given power ($P_{Operate}$) as:

$$E_{Operate} = 32000 \cdot \sqrt{P_{Operate}} \tag{7.1}$$

In this way, in simulation the conditioning algorithm may still operate based on a power, while all Monte Carlo based conditioning and breakdown calculations may be performed in terms of the electric field. To model the conditioning process it is then necessary to determine how the surface's propensity for establishing high fields without breakdown i.e. E_{State}, evolves from pulse-to-pulse. Assuming a material dependent limit, which is approached asymptotically and operation above which yields no improvement, the conditioning rate (CR) is defined in terms of the previously proposed quantities, scaling proportionally as:

$$CR \propto \left[1 - \frac{E_{State}}{E_{Sat}}\right] \tag{7.2}$$

This term also remains unitless and is hence scalable for different materials, a characteristic which aligns with the experimental data presented in Section 2.4 in which different materials were recorded as having both conditioned at different rates and exhibited varying propensities for establishing electric fields without breakdown [85]. Previously in CERN's test stands the input power was increased by in a staircase-like fashion, with each step being on the order of megawatts and resulting in a large increase in the BDR [37]. This suggests that the rate at which the surface conditions quickly decreases at fixed voltages. Hence, to produce a significant conditioning effect the operating field must be close to the level to which the surface is conditioned. To capture this characteristic $E_{Operate}$ and E_{State} are added as:

$$CR \propto \frac{E_{Operate}}{E_{State}} \cdot \left[1 - \frac{E_{State}}{E_{Sat}}\right] \tag{7.3}$$

Finally, a constant (γ) is added to facilitate tuning of the absolute value as:

$$CR = \gamma \left[\frac{E_{Operate}}{E_{State}} - \frac{E_{Operate}}{E_{Sat}}\right] \tag{7.4}$$

Where the units of γ are V/m. The units of CR are then V/m/pulse and refer to the increase in a surface's propensity for establishing electric fields without breakdown per pulse. The conditioning effect is then modelled by the calculation and addition of CR to E_{State} on a pulse-to-pulse basis, while the total change in the conditioned state of the surface may be defined as the sum of the CR values for every previous pulse, or:

$$E_{State} = \sum_{i=0}^{N} CR(i) \qquad i = 1, 2, 3...N \tag{7.5}$$

Where i is the pulse number and N is the cumulative number of pulses. It should be noted that the that the assumption that E_{State} grows linearly with the products of both the two terms in Equation 7.3 and γ is not based on physical model, but rather a postulation based only on empirical observations. One benefit of having a functional

framework however, is that eventually alternative relations may also be simulated and investigated.

7.4 Stochastic Modelling of Breakdown

As detailed in Section 2.4 when operating at a surface to which the structure has been conditioned small changes in the electric field have been shown to strongly affect the BDR as [16]:

$$BDR \propto E^{30} \tag{7.6}$$

However, the probability of breakdown at a given field decreases as conditioning progresses. It follows that the probability of breakdown (P_{BD}) is then related to the ratio of the operating voltage to the level to which the surface has been conditioned and hence will be assumed to scale as:

$$P_{BD} \propto \left(\frac{E_{Operate}}{E_{State}} \right)^{30} \tag{7.7}$$

However, when operating at the level to which the device has been conditioned Equation 7.7 becomes unity. Thus, to provide a reasonable probability of breakdown on each pulse the $P_{Baseline}$ quantity defined in Section 7.1.1 is added as:

$$P_{BD} = \left(\frac{E_{Operate}}{E_{State}} \right)^{30} \cdot P_{Baseline} \tag{7.8}$$

In this way when the device is operating to the level to which it is conditioned it follows that:

$$P_{BD} = P_{Baseline} \tag{7.9}$$

To use this notation appropriate values for both E_{Sat} and $P_{Baseline}$ must then be selected. At CERN and KEK, X-band prototype structures regularly reach accelerating gradients in the range of 100-120MV/m, corresponding to peak surface electric fields of up to 250MV/m [154, 155]. However, save for ultra-high BDR tests performed at SLAC, relatively few high-gradient copper structures have been recorded operating at room

temperature with peak surface electric fields above this [156]. Based on these results, an E_{Sat} value of 250MV/m, corresponding to an accelerating gradient of approximately 120 MV/m, will be assumed for copper structures.

Next, a reasonable reference breakdown rate may then be selected. Amongst the most extensive structure tests to have taken place in CERN's X-band test stands was the test of the T24 PSI2 structure [157]. The structure accumulated a total of 700 million high-power pulses in the Xbox-3 test stand before being installed in Xbox-2. During the latter portion of the test the structure accumulated over 600 million pulses and several measurements were performed to investigate the dependency of the BDR on the established electric field. The results are shown in Figure 7.3.

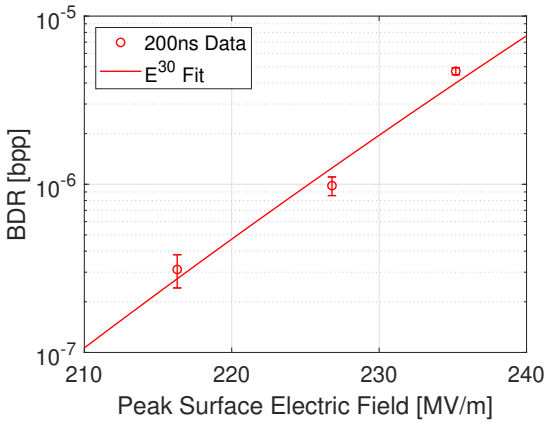

Fig. 7.3 The measured BDR as a function of peak surface electric field for the T24 PSI2 structure tested in CERN's Xbox-2 test stand at a pulse lengths 200ns. Error bars have been calculated as the square root of the number of breakdowns for each data point and the measurements are compared to the empirical E^{30} scaling. Details of the full test are available elsewhere [157].

Throughout the test the structure operated reliably at accelerating gradients above 100MV/m, corresponding to peak surface electric fields in excess of 210MV/m. This structure is then assumed to have been conditioned close to the E_{sat} quantity proposed previously and thus may be used to help provide an estimate of $P_{Baseline}$. In Figure 7.3 a BDR of $\approx 3 \times 10^{-7}$ bpp was recorded while operating at a peak surface electric field of 216.3MV/m, corresponding to an accelerating gradient of 103MV/m. Substituting these values into Equation 7.13 yields:

$$P_{BD} = 3 \times 10^{-7} = \left(\frac{E_{Operate}}{E_{State}} \right)^{30} \cdot P_{Baseline} \tag{7.10}$$

Assuming E_{state} is 250MV/m, an appropriate value for $P_{Baseline}$ then lies in the 1×10^{-5} range. Repeating the process with data from SLAC in which normal conducting structures have been tested to higher BDRs in the 1×10^{-4} bpp/m range also yields a similar value [156]. Finally, in 2018 a high-gradient T24 prototype structure was tested at CERN up to a peak surface field of approximately 240MV/m and it was noted that while operating at this level the BDR remained fixed at 5×10^{-5} bpp and did not decrease, indicating that no further improvement was taking place [40]. As such, a value of 5×10^{-5} was selected for $P_{Baseline}$. It should be noted however that the objective is merely to select a value which provides results which are in reasonable agreement with existing high-gradient prototype structure data. Hence, the value may be tuned at a later stage or adjusted to model other high-voltage devices. Additionally, the primary purpose of the model is to examine and optimise the preliminary conditioning of structures, which typically takes place at 50ns, and the BDR is known to scale with RF pulse length to the fifth power [16]. However, it is assumed that the structure referenced in Figure 7.3 was already conditioned to operate at the 200ns pulse length and so no renormalisation of $P_{Baseline}$ to account for the pulse length was deemed necessary.

7.4.1 Two-Rate Model Approach

Data has shown that breakdowns are also statistically more likely to occur in groups which are both temporally and spatially close together [46]. It is then convenient to group the breakdowns into primary events, which occur stochastically, and secondary events which occur immediately following, and are thought to be a consequence of the primary event [58]. Figure 7.4 shows the accumulation of breakdowns during a high-gradient structure test and a probability distribution plotted as function of the number of pulses since the previous breakdown. The resulting probability density functions have been described by a two-term exponential model, expressed [58]:

$$P_{BD}(n) = Ae^{-\alpha n} + Be^{-\beta n} \tag{7.11}$$

The exponential coefficients then correspond to the breakdown rate of each regime, with α referring to BDR of primary events, and β to secondaries or follow-ups. If accurate results are desired the model should then demonstrate similar behaviour. In practice, breakdowns locally alter the material surface, making future arcs more likely. In simulation, this effect may be captured in several ways, namely by the

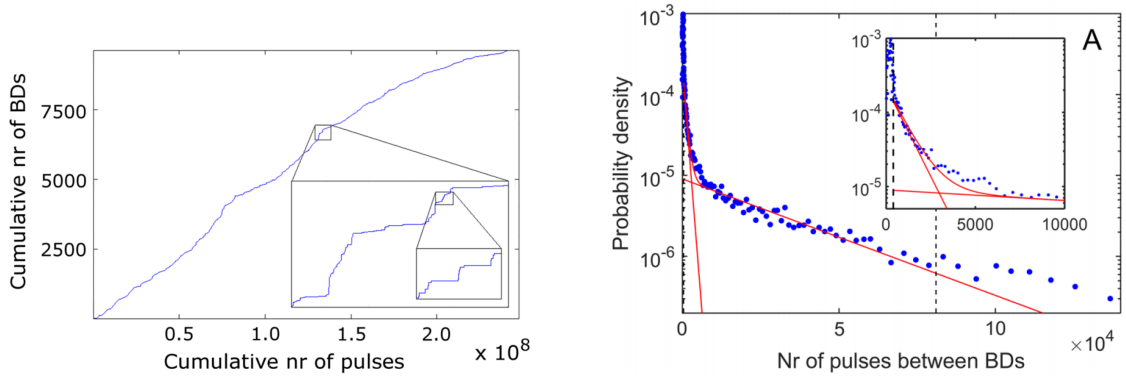

(a) (b)

Fig. 7.4 Cumulative number of breakdowns as a function of cumulative RF Pulses for a TD26CC structure tested in Xbox-1 with insets showing close-ups of the breakdown accumulation (a) and a distribution showing the number of pulses between breakdowns with a double fit in red (b) [58].

implementation of a large, negative CR value on breakdown pulses or alternatively, by adjusting the E_{State} value. However such approaches yield additional uncertainty, making tuning of the model a complex multivariate problem. As an appropriate method of modelling the effect is not known a priori, in the early stages the characteristic was enforced by recording the number of pulses since the previous breakdown, and modifying the probability of breakdown with Equation 7.11 as:

$$\begin{aligned} P_{BD} &= \left(Ae^{-\alpha n} + Be^{-\beta n}\right) \cdot \left(\frac{E_{Operate}}{E_{State}}\right)^{30}, && n \leq 10,000 \\ &= P_{Baseline} \cdot \left(\frac{E_{Operate}}{E_{State}}\right)^{30}, && 10,000 < n \end{aligned} \tag{7.12}$$

Where n is the number of pulses since the previous breakdown and factors α, β, A and B are taken from fitting to experimental data as 3.307×10^{-5}, 1.107×10^{-3}, 85×10^{-6} and 2.4×10^{-4} respectively. In this way, the probability of breakdown is temporarily increased by orders of magnitude immediately following a previous event. After 10000 pulses have elapsed the breakdown probability is then assumed to have returned to the baseline value. Alternative approaches to modelling the effect of breakdown may then be investigated later when the aforementioned equations have been validated and other variables are known to have been assigned a reasonable value. The conditioning data of five high-gradient prototype structures tested at CERN was then selected to provide a benchmark against which the model could be tuned. Figure 7.5 shows the

conditioning history of each plotted in terms of the peak surface electric field and cumulative breakdowns. Only the preliminary conditioning is shown, excluding changes in pulse shape and length. As the model is defined in terms of the peak surface electric field, the results for the structures have also been plotted in this way for comparative purposes as opposed to the more conventionally used accelerating gradient.

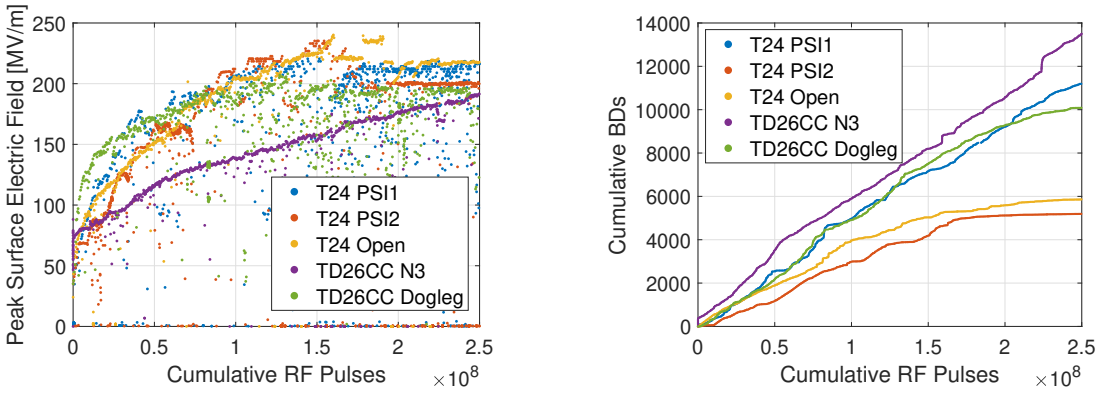

(a) (b)

Fig. 7.5 Preliminary conditioning of several high-gradient prototypes plotted as a function of cumulative RF pulses (a) and breakdowns (b). Only the preliminary conditioning is included and so the pulse length is for 50ns for the data shown.

It can be seen that in the CLIC structures are typically capable of establishing peak surface electric fields on the order of 60MV/m when conditioning commences, corresponding to accelerating gradients of the order of $\approx 30MV/m$. As such, the initial values of E_{State} and $E_{Operate}$ were set to $70MV/m$ and $60MV/m$ respectively. As mentioned previously the copper CLIC prototype structures are typically incapable of being conditioned to operate reliably in excess of 120MV/m at room temperature corresponding to peak surface electric fields on the order of 250MV/m and so E_{Sat} was set to $250MV/m$. A parameter sweep of γ was then run and a value of unity was found to produce a conditioning rate comparable to that observed in the test stands. Figure 7.6 shows the preliminary results of the model after tuning.

Notably, the probability distribution differs from that shown in Figure 7.4 as significantly fewer breakdowns are recorded as having occurred immediately following a prior event. However, as is visible in the inset on Figure 7.4(b) the fit given in Equation 7.11 does not extend to the first few hundred pulses following breakdowns where the majority of events occur. This discrepancy is then a consequence of the chosen equation however it is nonetheless thought to be sufficient for tuning purposes.

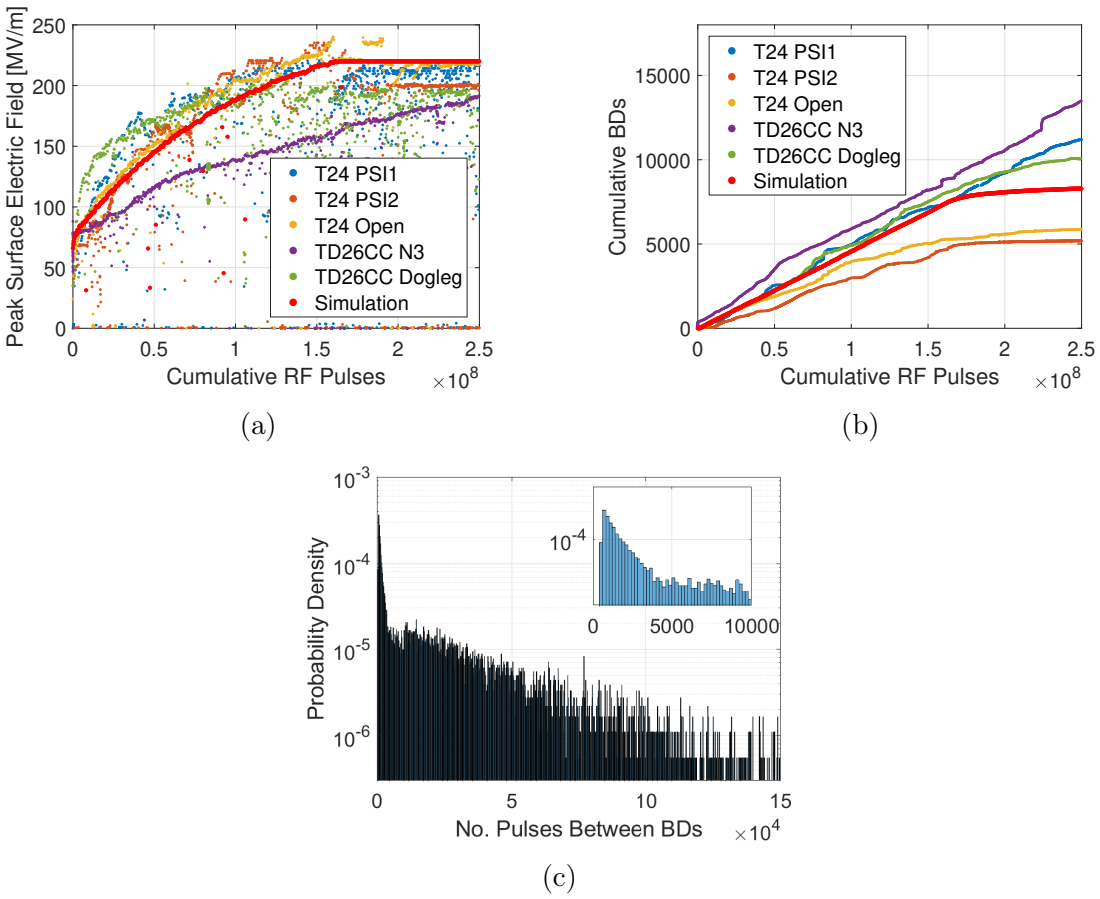

Fig. 7.6 Results of the model using the two-rate approach i.e. Equation 7.12 plotted as a function of cumulative RF pulses (a) and breakdowns (b). Results are overlaid on the conditioning curves of several high-gradient prototypes for comparative purposes. Also shown is a distribution of the number of pulses between breakdowns with a bin size of 200 pulses (c).

As the results are in reasonable agreement with the experimental data selected for benchmarking the model was then taken forward for further analysis.

7.4.2 Grid-Based Approach

The use of Equation 7.12 yields valid results provided the conditioning algorithm implemented in the code remains unchanged. However, after a breakdown occurs in the model, the probability of a subsequent event may be reduced by orders of magnitude by simply implementing several extremely low power pulses following. The latter result is unphysical and thus does not permit the investigation of means of algorithmic recovery from breakdown. Additionally, This also leaves the effect of breakdown on the surface undefined. With the other variables tuned to provide reasonable results an alternative means of producing the probability distribution shown in Figure 7.4 was investigated.

In practice, a breakdown physically alters the surface as shown in Figure 2.3. In simulation each breakdown will then be assumed to either improve or worsen the surface respectively. However, while a value of E_{State} may be assigned to the entire structure, the effect of breakdowns is a local one. In light of this a grid-based approach was adopted, with each element being representative of a portion of the surface. Each element then evolves at the standard conditioning rate and each is checked separately for the occurrence of a breakdown on every pulse. If a breakdown is logged then the corresponding grid element is then randomly improved or worsened. With this approach it is also then possible to allocate different fields to different grid points and monitor the conditioning of each individually. By doing do, the conditioning of different cells within an accelerating structure or indeed different points on a given cavity surface may also be simulated.

The exact physical scale over which breakdowns affect the surrounding surface is unknown. In accelerating structures however, groups of breakdowns typically occur in the same cell. A grid comprised of 26 elements was then selected initially, with each corresponding to the regular accelerating cells in a CLIC prototype structure. Each element is then assigned an enhancement factor, ψ, when calculating the breakdown probability as:

$$P_{BD} = \left(\frac{E_{Operate}}{E_{State} \cdot \psi} \right)^{30} \cdot P_{Baseline} \tag{7.13}$$

However, the previously chosen $P_{Baseline}$ quantity is representative of an entire CLIC prototype structure. As each grid cell must be checked individually the use of

Equation 7.13 would then greatly increase the probability of breakdown on a given pulse, skewing the results. To avoid this, the probability of breakdown when checking all grid elements should then be equal to $P_{Baseline}$. For this purpose, a new quantity, P_{Grid}, was defined. While operating at the level to which the structure is conditioned, the probability of having a non BD pulse is given as $1 - P_{Baseline}$. Hence, in a system with n grid elements the following relation should hold:

$$(1 - P_{Grid})^n = (1 - P_{Baseline}) \tag{7.14}$$

Hence, an appropriate P_{Grid} value may be recovered for any arbitrary number of cells as:

$$P_{Grid} = 1 - \sqrt[n]{(1 - P_{Baseline})} \tag{7.15}$$

The probability of breakdown for each individual grid element is thus given:

$$P_{BD} = \left(\frac{E_{Operate}}{E_{State} \cdot \psi} \right)^{30} \cdot P_{Grid} \tag{7.16}$$

Where ψ serves to improve or worsen the state of the surface at a given grid point and is initially unity. In the event that a breakdown occurs at any point, the site is then assigned a new value for ψ. Breakdowns often occur in groups however structures also regularly resume reliable operation after having accumulated several breakdown, meaning there is nonetheless a reasonable probability of improving the surface, corresponding physically to the removal of emission sites capable of nucleating future breakdowns. As such, it was decided that new values of ψ would be randomly selected from a Gaussian distribution as has previously been used in literature to examine the evolution of field emission sites [158]. An illustration of the process is shown in Figure 7.7. It should be noted however, that the implementation of other probabilistic functions is also possible, and this is one facet of breakdown which a working model may be used to investigate.

The mean and standard deviation of the distribution from which ψ is selected following breakdown will be denoted μ and σ respectively. ψ is then analogous to the field enhancement factors associated with sputtering which my occur around breakdown sites during arcing as shown in Figure 2.3. A parameter sweep of σ was run and a value of 0.1 was found to produce a probability distribution comparable to the experimental

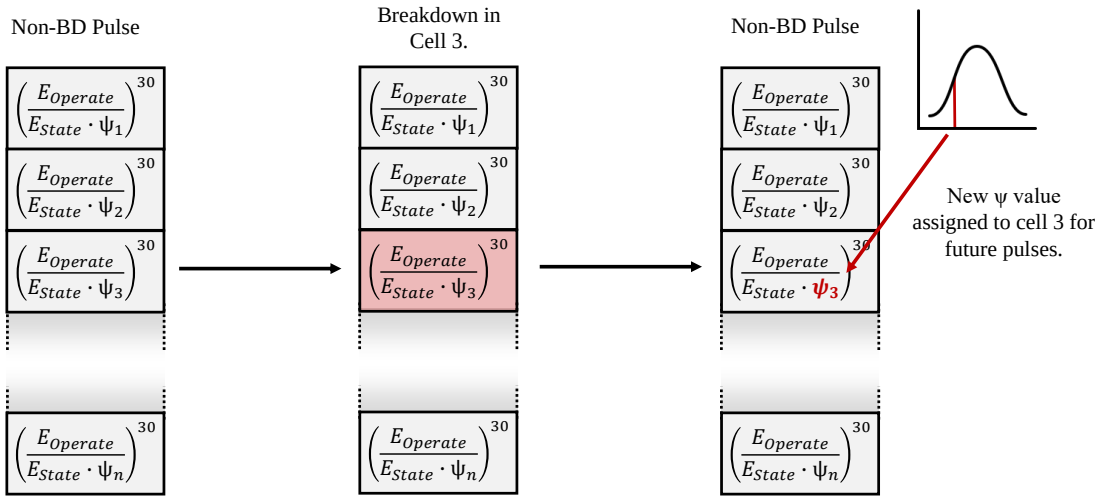

Fig. 7.7 Diagram showing an array of grid elements, each with a unique ψ value. If a breakdown is recorded in a grid element, the element is then assigned a new ψ value.

data shown previously in Figure 7.4. As each grid element evolves at the standard conditioning rate and the ψ values for each generally remain centred around the mean, μ, changes in μ have little effect on the simulation and the value was left at unity. Figure 7.8 shows a comparison between the preliminary results of the model and the high-gradient test data. Once again, the results have been plotted in terms of the surface electric field for comparative purposes.

After tuning, the grid-based approached yields a probability distribution in which breakdowns are several orders of magnitude more likely to occur immediately following a previous event, comparable to the two-rate fit shown previously. Due to the strong empirical dependency on the electric field even small changes in the denominator of Equation 7.13 significantly change the probability of breakdown. The consequence of using of an appropriately tailored Gaussian distribution breakdowns is then that a breakdown tends to result in an immediate follow up if ψ is decreased, or a very large number of pulses until the next breakdown if it is increased, resulting in the shown distribution.

The fact that many elements acting in this way still produces a distribution comparable to experimental data also indicates that the probabilistic behaviour of breakdown may be reasonably modelled by an array of elements representative of different portions of the surface as opposed to a single lumped quantity. The performance requirements for CLIC and other facilities list a target breakdown rate per metre, and so it is well known that the probability of breakdown scales with the active surface area. The use

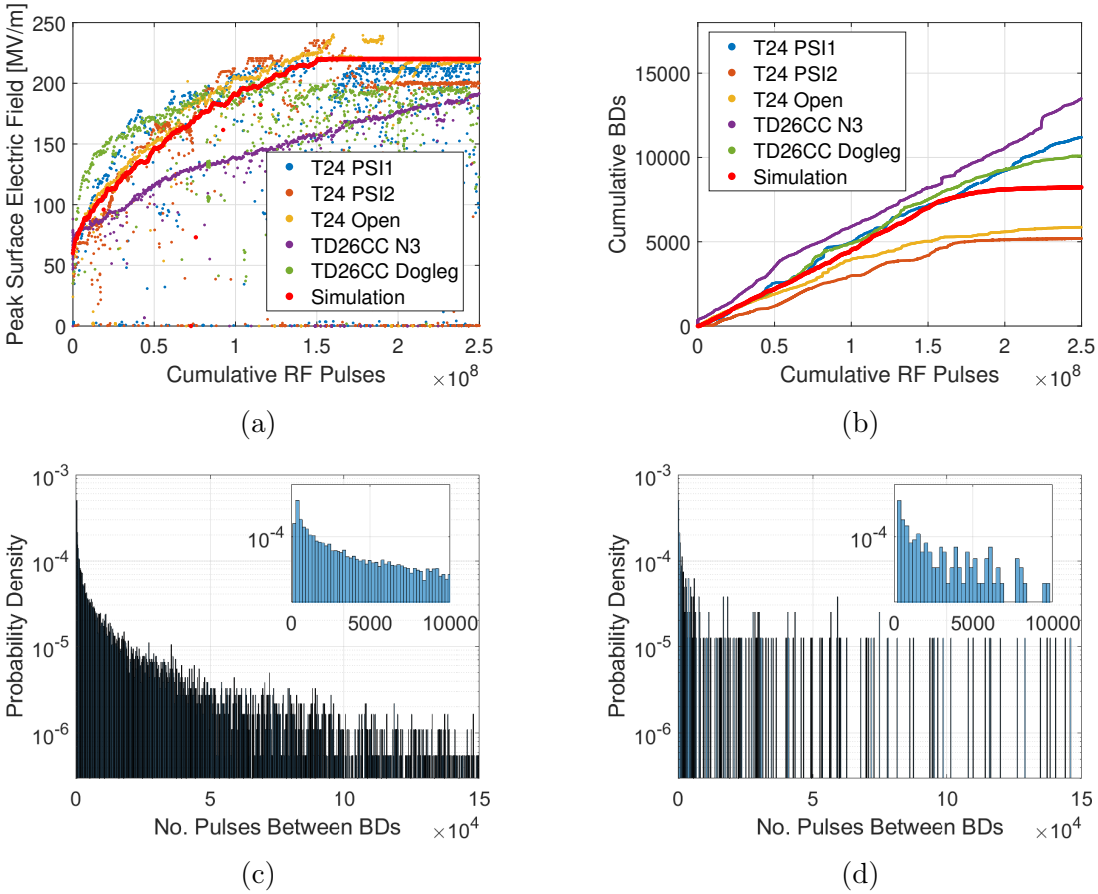

Fig. 7.8 Results of the model when using the grid-based approach shown in Figure 7.7 instead of Equation 7.12. Results are plotted as a function of cumulative RF pulses (a) and breakdowns (b) and overlaid on the conditioning curves of several high-gradient prototypes for comparative purposes. Also shown are distributions of the number of pulses between breakdowns for all grid elements (c) and for a single element (d). A bin size of 200 pulses is used in each.

of a grid-based simulation method then means it is possible to tailor the breakdown probability and chosen number of elements to represent smaller portions of a given surface, analogous to the mesh density in 3D simulation or equivalently, larger arrangements. Hence, the effect of changing the number of grid points one aspect which may be investigated further in future studies. In practice breakdown craters have a finite size and are also capable of sputtering over short distances. As the model is not yet capable of cross-talk this characteristic is not yet captured, and this is an additional feature which may be investigated.

Given the reasonable agreement with the experimental data selected for benchmarking the model was taken forward for further analysis. the final settings which produce the results shown in Figure 7.8 are summarised in Table 7.1. When running the final Python script on a 3.4 GHz Intel Core i7-6700 the code can simulate a 250 million pulse test with 26 grid elements in approximately 1.5 hours. As this facilitated the generation of all desired results within a reasonable time frame no further optimisation was deemed necessary. If higher speeds or larger simulations are desired, switching to a compiled language such as C would allow compilation of the script in its entirety and optimisation with respect to the hardware, resulting in a reduced run time.

Parameter	Description	Value	Units
E_{Limit}	Ultimate achievable field.	250	MV/m
E_{State}	Field to which structure is conditioned (initial value).	70	MV/m
$E_{Operate}$	Operating field (initial value).	60	MV/m
$P_{220MV/m}$	Input power required to establish a peak surface electric field of 220 MV/m.	40	MW
Loop_Length	Length of Conditioning Algorithm Loop.	10000	pulses
Ramp_Length	Length of ramp during which power can be subtracted following the step.	5000	pulses
Ramp_step	Power Increment.	10000	W
BDR_Setpoint	PID Loop Setpoint.	4×10^{-5}	bpp
BDR_Window	BDR Measurement Window.	5×10^{5}	pulses
PulseRange	Pulse range for which to run the simulation.	2.5E8	pulses
Goal	Target field in simulation. Algorithmic ramping ceases upon reaching this value.	220	MV/m
Grid_Size	Number of elements in the simulation grid.	26	-
γ	Constant to tune conditioning rate.	1	V/m
μ	Mean of the distribution from which ψ is selected following breakdown.	1	-
σ	Variance of the distribution from which ψ is selected following breakdown.	0.1	-

Table 7.1 Initial settings for the Monte Carlo model which produce the results shown in Figure 7.8.

7.5 Results of the Model

With the grid-based model capable of reproducing existing experimental data, several studies were carried out to examine several phenomena observed in the test stands and the effects of adjusting parameters in the existing conditioning algorithm. The results of the studies are presented following.

7.5.1 Simulation of Spatially Resolved Conditioning

Depending on the design, in accelerating structures a cell to cell variance in the electric field is typical. As a result, a variance in the number of breakdowns accumulated by each cell has been observed during high-gradient tests [37, 151]. Similarly, the field distribution varies radially within a given cell. Post-mortem examinations have shown that the regions on the iris where the surface electric field is highest accumulate a higher density of breakdown sites than the surrounding areas [40, 159, 151]. This effect was particularly prominent in the test of the CLIC crab cavity where due to operating in the TM_{110} dipole mode the surface electric field in each cell is is not azimuthally symmetric. Figure 7.9 shows the CLIC crab cavity during the post-mortem examination and the breakdown crater locations on a single cell, superimposed on the surface electric field distribution [151, 57].

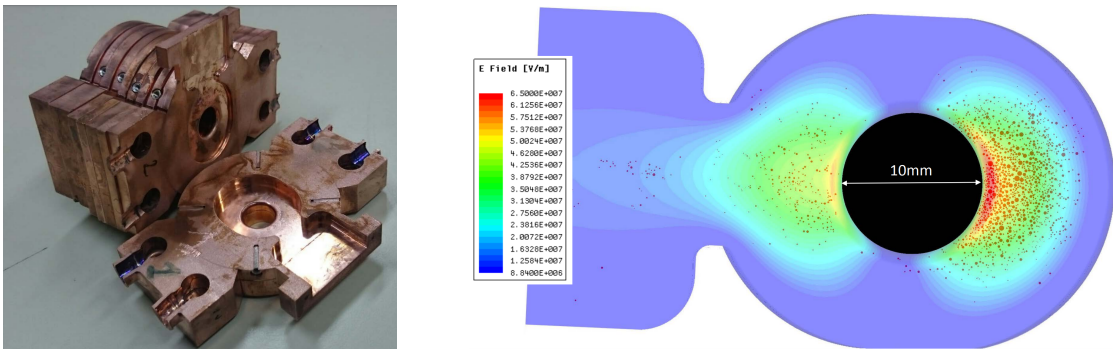

(a) (b)

Fig. 7.9 Sections of the CLIC crab cavity after high-power testing (a) and the breakdown crater locations in the input cell (marked as number 1 in the photograph) plotted over the electric field distribution from HFSS (b). The cavity was cut via electrical discharge machining (EDM) [57].

The total number of breakdown craters counted in the post-mortem for each angular position on the second iris of the first cell is shown in Figure 7.10. Notably, the density of the breakdown craters is high on the bottom of the cell. Although a perfect dipole

mode is perfectly symmetric, due to the coupler employed the dipole mode is perturbed slightly meaning the peak surface electric field on the bottom of the cell is slightly higher.

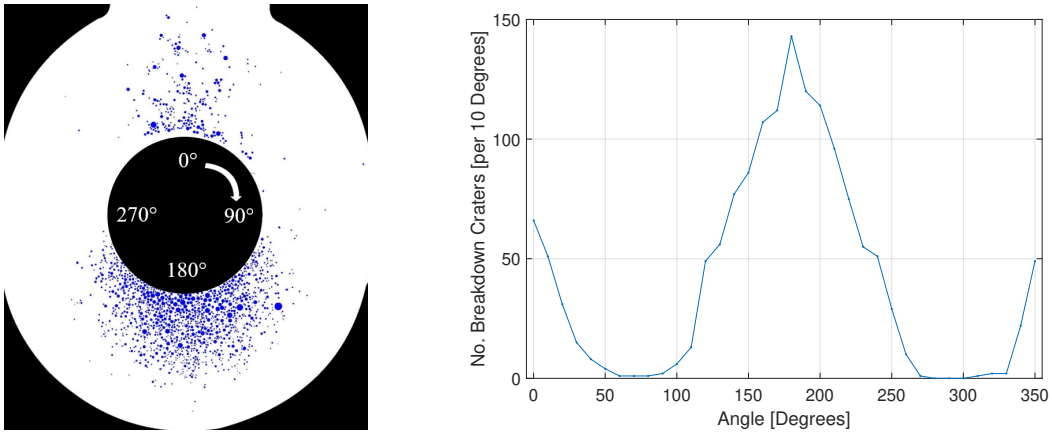

(a) (b)

Fig. 7.10 The breakdown sites on cell 2, iris 2 of the CLIC crab cavity (a) the total number of breakdown craters as a function of angle (b) [57]. The direction in which the sites were counted and hence, corresponding angular position is also labelled in (a). A total of 1305 breakdown sites were counted on the surface.

Although the probability of breakdown decreases with a reduction in field, regions in which the field is reduced are also effectively less conditioned. It is clear upon examination of that fields that the density of breakdown craters itself does not follow the proposed E^{30} scaling, however it is speculated that both of the aforementioned aspects play an important role in the observed behaviour and so the process was investigated with the model. For a given input power, the electric field at two given points on the surface of a cavity varies by a constant factor (k_n). By assigning separate k_n and E_{State} values to each point on the grid, the conditioning of each may then be monitored separately. The simulation grid was set to have 19 elements, each representing a 10° radial slice of the surface of a single cell. To provide the corresponding k_n values lines were then placed around the iris of the first cell in CST MWS and swept to produce 19 separate calculation surfaces centred at angular positions from 0 to 180 degrees as shown in Figure 7.11.

The k_n value for each element was then taken as the integrated surface electric field for each calculation area, normalised to the maximum. Two additional arrays were then produced in simulation, containing E_{State} and k_n values for each grid element.

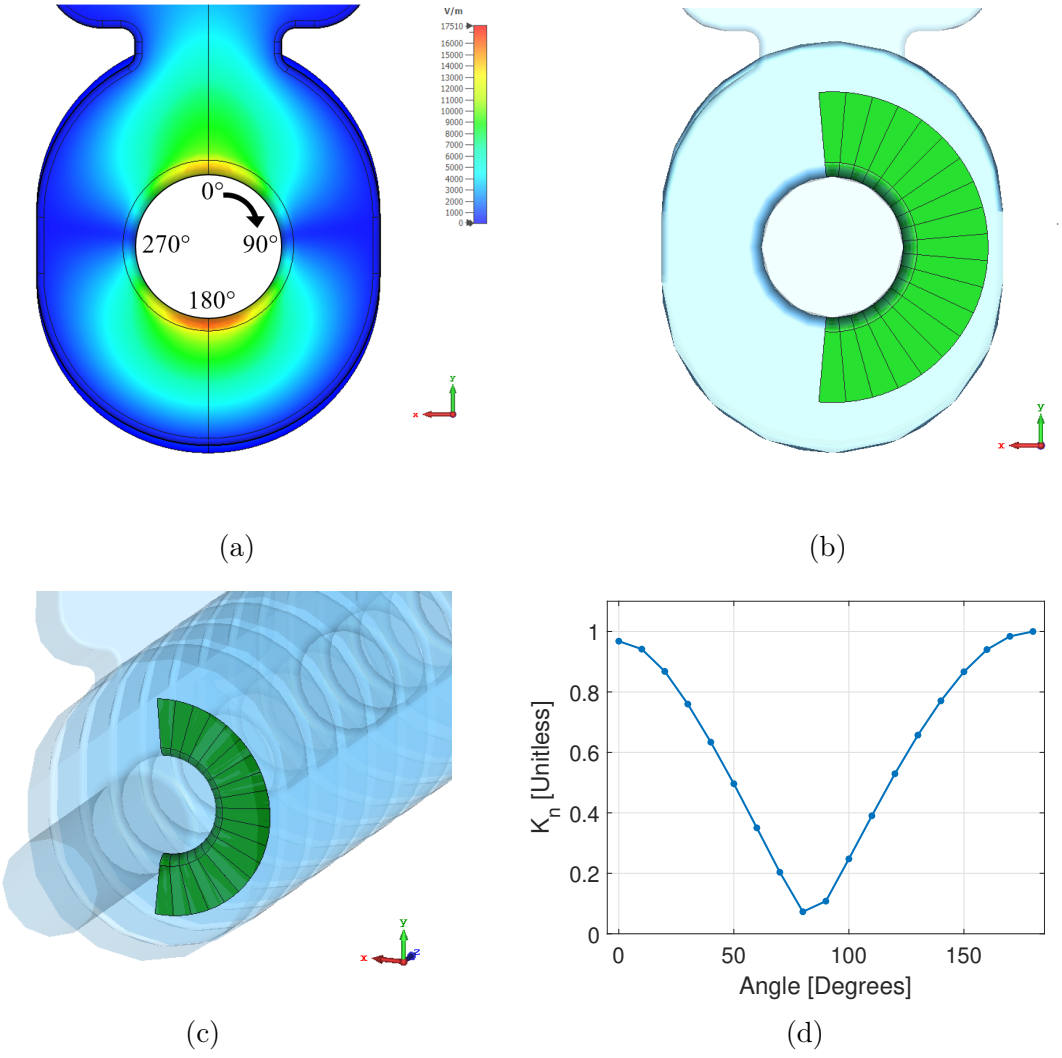

Fig. 7.11 The CLIC crab cavity surface field distribution normalised to an input power of 1W in CST MWS showing the convention in which angular positions were assigned (a) and the calculation surfaces produced by sweeping the lines radially (b). An isometric view of the calculation surfaces is also shown (c) alongside the corresponding k_n values calculated as the integrated electric field on each calculation surface normalised to the maximum (d).

Thus, the conditioning rate for the element corresponding to each radial position (ϕ) becomes:

$$CR(\phi) = \gamma \left[\frac{E_{Operate} \cdot k_n(\phi)}{E_{State}(\phi)} - \frac{E_{Operate} \cdot k_n(\phi)}{E_{Sat}} \right] \tag{7.17}$$

While the probability of breakdown is equivalently adjusted as:

$$P_{BD}(\phi) = \left(\frac{E_{Operate} \cdot k_n(\phi)}{E_{State}(\phi) \cdot \psi(\phi)} \right)^{30} \cdot P_{Grid} \tag{7.18}$$

At the design power of 13.35MW the peak surface electric field established within the CLIC crab cavity is 89.2MV/m [37]. This corresponds to a power to voltage ratio of 24413V/W$^{0.5}$ as opposed to the 35000V/W$^{0.5}$ which is typical of the CLIC accelerating structures. Additionally, during conditioning the cavity was operated up to a peak surface electric field of approximately 173 MV/m over 390 million pulses, a lower value than is typical of the accelerating structures. Much of this time was also spent running under fixed conditions in order to investigate the dependency of breakdown on pulse length and operating power, while only 60 of the first 80 million pulses were spent ramping algorithmically [37]. The full conditioning history of the CLIC crab cavity is shown in Figure 7.12.

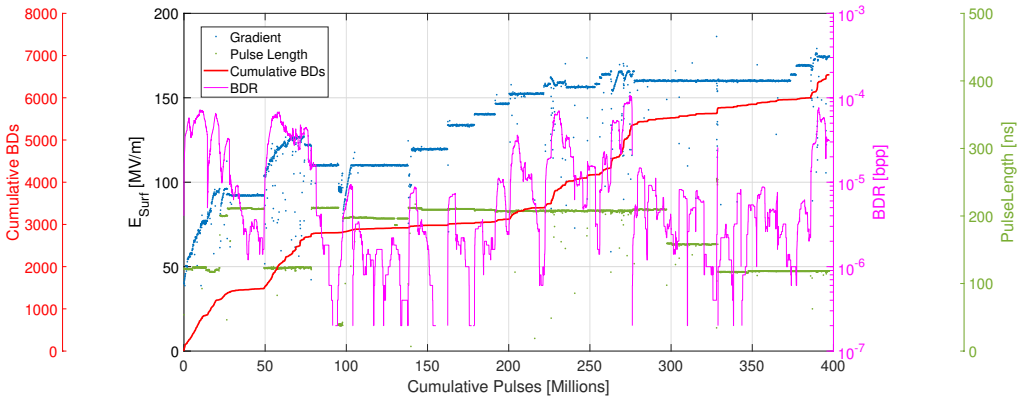

Fig. 7.12 Conditioning history of the CLIC crab cavity showing the peak surface electric field (blue), the structure BDR (magenta), the pulse length (green) and the cumulative breakdowns (red) as a function of cumulative RF pulses.

In order to yield a more result which is more representative of the test, the voltage to power ratio was adjusted in simulation to match that of the crab cavity. It should

also be noted however that the pulse length was changed several times during the test of the CLIC crab cavity and that this is one aspect of operation which is not currently captured by the model. As such, the surface electric field was scaled with Equation 6.11 to a pulse length of 100ns as:

$$E_{Surface}\{t_{p,100ns}\} = E_{Surface} \cdot \left(\frac{t_p}{100ns}\right)^{\frac{1}{6}} \tag{7.19}$$

The history in terms of the resulting scaled gradient is shown Figure 7.13.

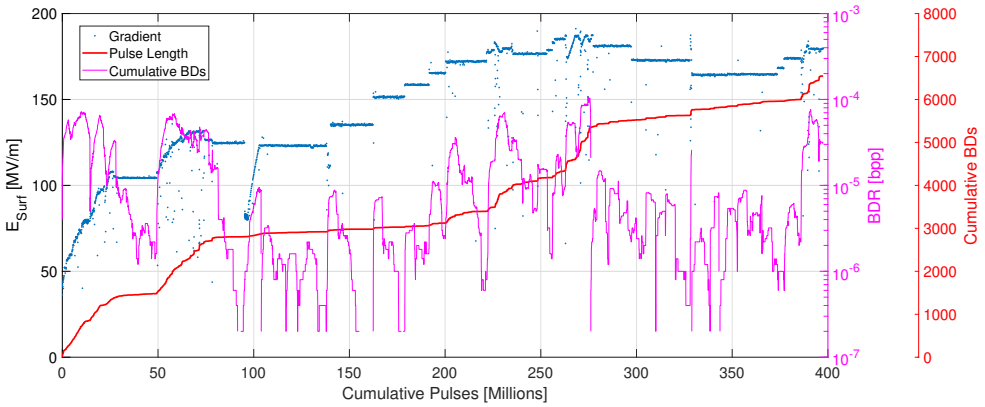

Fig. 7.13 Conditioning history of the CLIC crab cavity showing the peak surface electric field scaled to a pulse length of 100ns (blue), the structure BDR (magenta), and the cumulative breakdowns (red) as a function of cumulative RF pulses.

To provide a more reasonable approximation of the observed behaviour, an identical conditioning procedure was programmed into the model, where $E_{Operate}$ is then representative of the scaled gradient given by Equation 7.19. However it is important to note that the model was tuned to provide a reasonable agreement with preliminary conditioning data only, and as such may not yield results representative of a real test over excessively large numbers of pulses. In light of this the simulation was then run for only the first 300 million pulses of the test as this is the region in which the majority of the breakdowns occurred. The conditioning of each element was then monitored separately. Figure 7.14 shows the results of the full simulation, taking the breakdown rate and cumulative breakdowns as the sum total of all grid elements.

Notably, although the total the cumulative breakdowns in simulation is comparable to that recorded during the experiment, the majority occur within the first 100 million pulses, even limiting the rate at which the power is algorithmically increased. This may partially be a consequence of the chosen $P_{Baseline}$ value, which was selected to

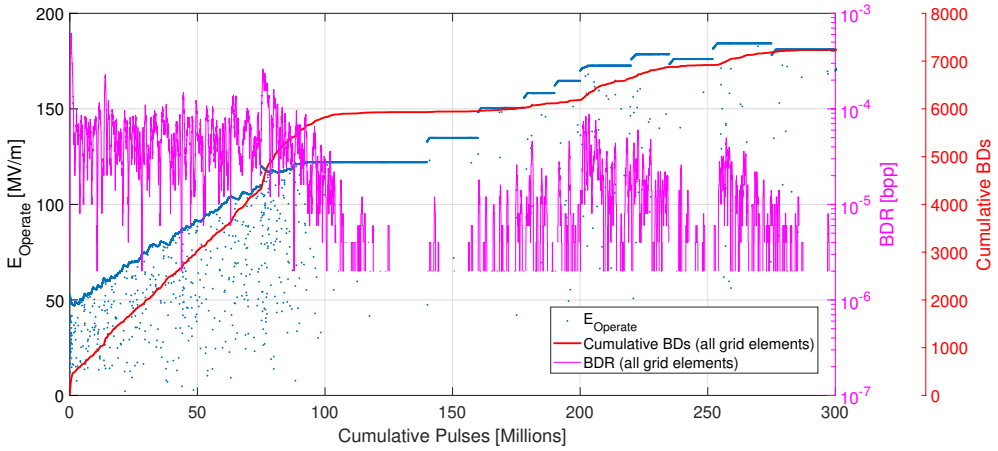

Fig. 7.14 Results of the simulation showing the nominal $E_{Operate}$ value (blue), the total BDR (magenta), and the cumulative breakdowns (red) as a function of cumulative pulses.

apply primarily to a regular CLIC accelerating structures, while the crab cavity has only 10 regular cells and thus has a much shorter active length. Similarly, it should be noted that the number of grid elements was reduced to 18 the selected $P_{Baseline}$ pertains only to full structures and was not chosen to represent a single cell test, and so each grid element is assumed to represent a radial slice of the entire structure. If results representative of a single cell are desired then it is clear that $P_{Baseline}$ must be instead be reduced. Figure 7.15 shows the evolution of E_{State} and the cumulative breakdowns for the individual grid elements corresponding to various angular slices.

The distribution of total number of breakdowns for each region is markedly more narrow than the experimental data, indicating that the E^{30} scaling does not apply to the breakdown crater density or that the k_n values were not chosen appropriately. It is also speculated that another possible reason for the discrepancy is that in practice breakdowns are capable of sputtering and modifying the surrounding surface over small distances, potentially causing secondary breakdowns in another radial slice. In simulation however, the grid elements are not capable of cross talk and this is one way in which the model may be improved. Similarly, although the breakdown craters were manually counted during the post mortem it is often not possible to distinguish between breakdowns which have occurred on top of a previous crater. It is possible then, that if many breakdowns have occurred at approximately the same location the estimated breakdown crater density for the high-field regions may be lower than the true value, a bias which would also skew the experimental distribution.

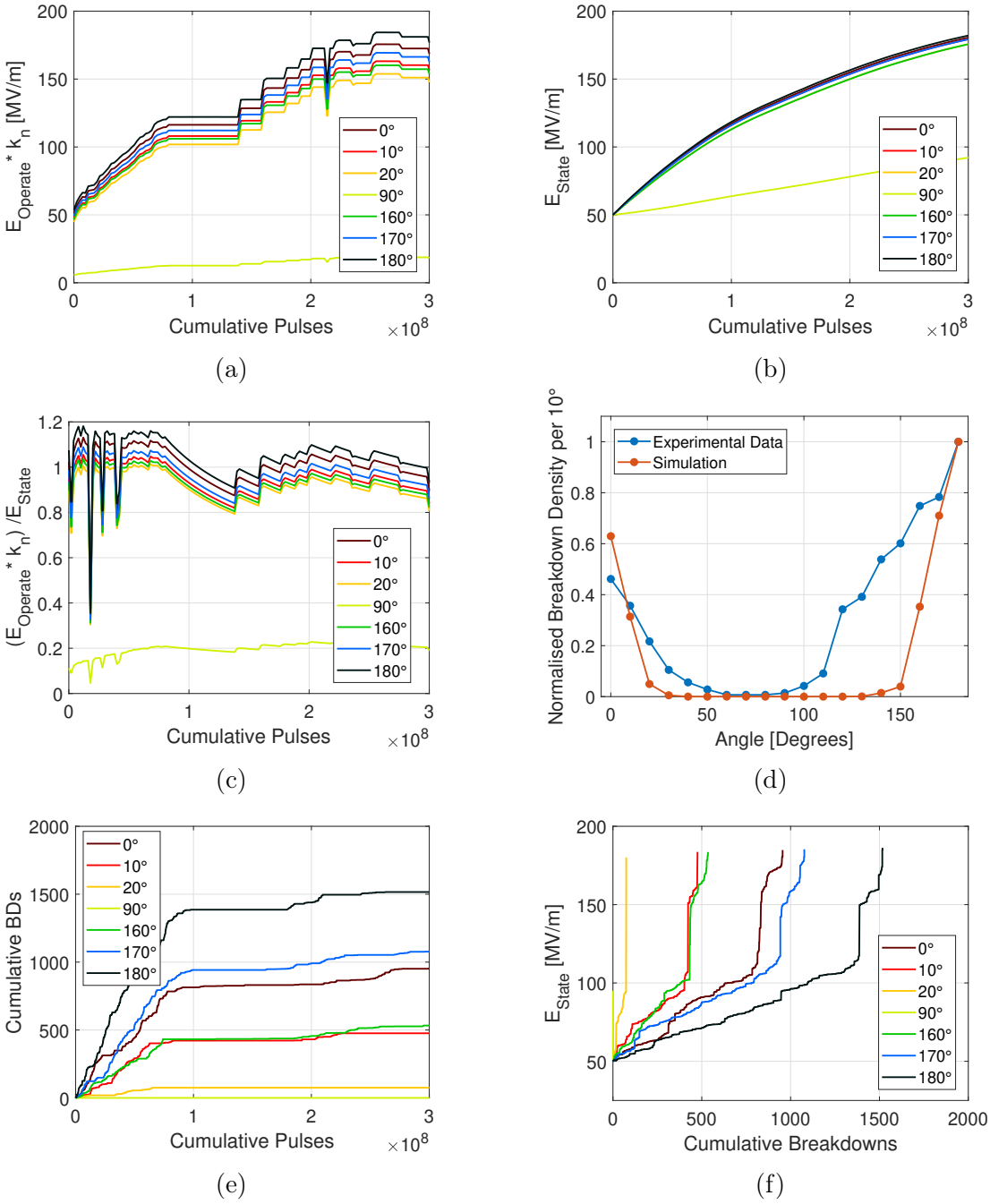

Fig. 7.15 The progression of E_{State}, E_{Op} and the ratio between them for several grid elements of interest (a,b,c) followed by the total accumulated breakdowns for each grid element normalised to the maximum and compared with experimental data (d). Finally, the breakdown accumulation and progression of E_{State} as a function of breakdowns are shown (e,f).

In the region in which the field is lowest, a comparatively small improvement in the surface is observed and no breakdowns occur. In 2019, the PolariX-TDS was tested in Xbox-2 and to date this is the only other dipole-mode structure to have undergone conditioning in the test stands [118]. In the PolariX-TDS, it is possible to rotate the orientation of the dipole mode and hence the surface electric fields established within the cavity, and this was performed several times during the test [118]. After changing the surface electric field distribution and recommencing conditioning the BDR setpoint was reached at a greatly reduced input power each time, suggesting that the regions in which the electric field was low were relatively unconditioned [147, 118]. This observation aligns well with the simulation results which show that little conditioning takes place in low field regions. The simulation results pertaining to the high-field regions also show that even a marginal reduction in the operating field significantly reduces the number of accumulated breakdowns accumulated while still producing a significant conditioning effect, suggesting that the high-field portions of the surface effectively regulate the rate at which the power may be increased during conditioning.

7.5.2 Simulation of a Multi-Structure System

During the recent superstructure test one constituent structure accumulated an order of magnitude fewer breakdowns than the other due to having been operated at a lower gradient. In future arrangements however, it will be necessary to condition multiple structures simultaneously and so the effects associated with small differences in structure performance and input powers are of interest. To investigate the effect in simulation, a second array of grid elements was created in the model to represent a second structure and the combined breakdown rate of both was then used to govern the behaviour of the conditioning.

Two scenarios were investigated, in the first the initial E_{State} value of one cavity was set $20MV/m$ higher, meaning it commenced the test in a higher conditioned state. In the second scenario, an arrangement with a less extreme power discrepancy than that present in the Xbox-2 superstructure was investigated. The $E_{Operate}$ value in one cavity was held 10% higher than the other, corresponding to a situation in which either the structures do not receive equal input powers or one cavity is designed to establish a higher field for a given input power. To avoid conflation with the previously reported superstructure test, the simulated structures have been labelled structure 1 and structure 2 respectively. The results of each study are shown in Figure 7.16.

Results for the first case show that even a small increase in the initial conditioned state of one structure is sustained throughout the duration of the test. As a result,

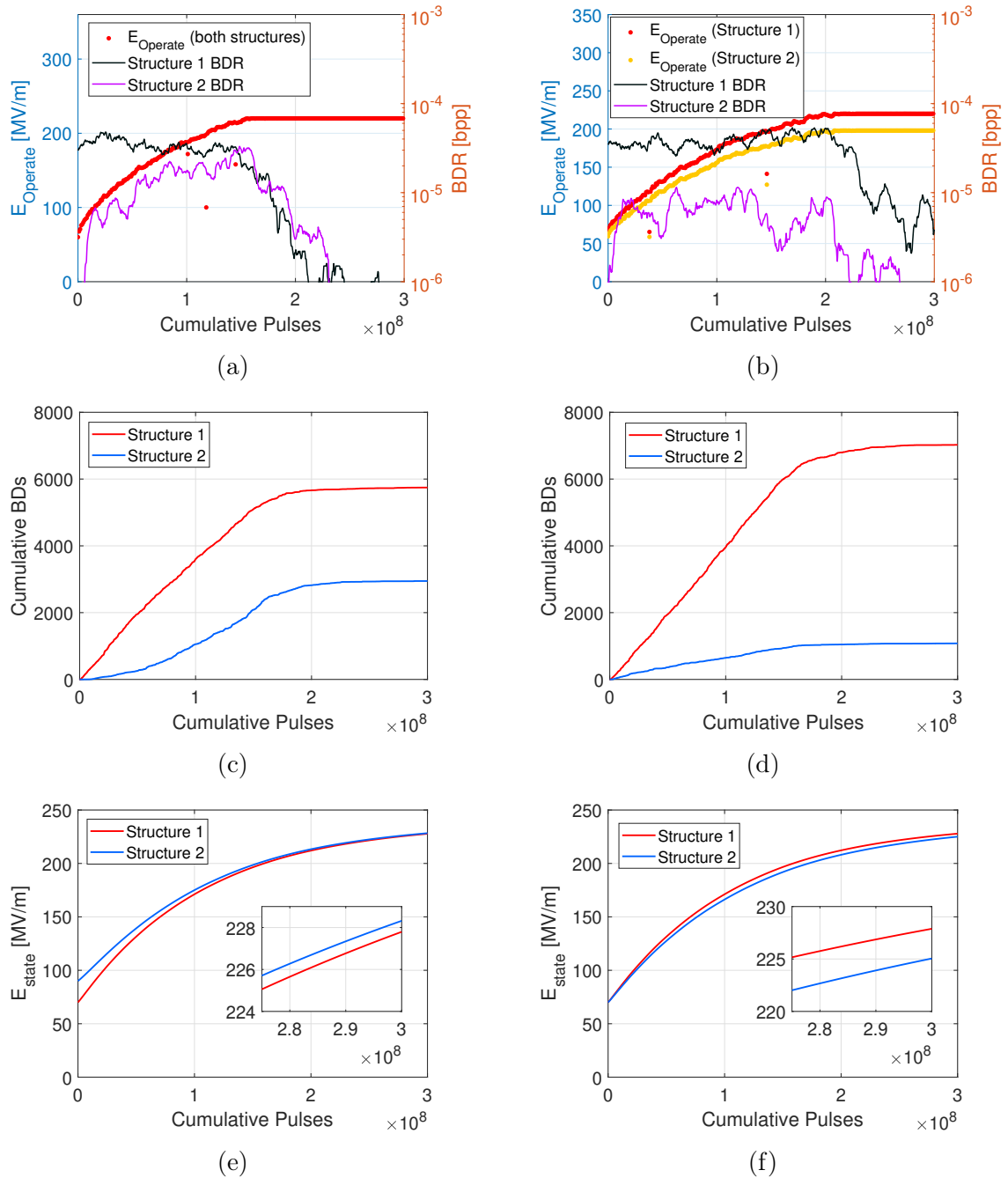

Fig. 7.16 Results of the multi-structure simulations in which the initial E_{State} value of one cavity was set $20MV/m$ higher (a,c,e) and the $E_{Operate}$ value in one cavity was held 10% higher than the other (b,d,f).

a significant difference in breakdown accumulation is present between the structures. Examining the BDR for each structure shows that structure 2, having commenced the simulation in a higher conditioned state, begins to accumulate breakdowns at a later stage. Simulation then predicts that if the superstructure resumes operation with the power split equally between the constituents then the majority of breakdowns should occur in structure B even when exceeding 90MV/m as it has commenced the test in a less conditioned state.

Although the BDR of structure 2 was generally lower than structure 1, on several occasions at the end of the preliminary ramping period an inversion occurs in which it temporarily exceeds the BDR of structure 1 despite the higher E_{State} value. This suggests that in multi-structure arrangements a conditioned structure may not necessarily always perform more reliably than a less conditioned counterpart, with the instantaneous BDR being liable to fluctuate at any given time. Additionally, simulation indicates that in a multi-component arrangement the BDR, and hence conditioning, is likely to be governed largely by a single component.

In the second case the structure which receives a higher operating field limits the rate at which the power is algorithmically increased, accruing the majority of the recorded breakdowns. This result is principally the same as that observed in Section 7.5.1, where marginal decreases in the operating field across a surface cause a significant change in the numbers of accumulated breakdowns. As a consequence, structure 2 has effectively been subjected to a slowed conditioning procedure in which the rate at which the field is increased produces a significant conditioning effect without inducing breakdowns unnecessarily frequently. This result then predicts that low-BDR conditioning may be achieved via the use of a sacrificial cavity geometrically designed to establish a higher surface electric field or indeed a virtual cavity which is simulated in parallel to regulate conditioning and avoid inducing frequent breakdowns in the primary device. However, it should be noted that it is unclear whether or not such a scheme would yield any long-term benefit. Alternatively, a similar result may be achieved without a second cavity, through the use of a specially designed conditioning method.

7.5.3 Effect of the BDR Setpoint on Conditioning

During conditioning, the operator-selected BDR defined in Equation 3.9 is tracked and limits the rate at which the power may be increased. Based on the success of previous tests, a BDR setpoint in the $1 - 5 \times 10^{-5}$ is typically selected in the Xbox test stands and little data exists on the effect of changing this value. The PolariX-TDS the

CLIC crab cavity constitute an example however which may reasonably be used for comparative purposes. During the preliminary condition of each structure the power was increased algorithmically with little operator intervention before running at a fixed input power for 10-20 million pulses, however the BDR setpoint for the PolariX-TDS 3×10^{-5} bpp whilst a value of 5×10^{-5} bpp was selected for the CLIC crab cavity [37]. Both were also exposed to air prior to installation, however it should be noted that the Polarix has a much larger internal volume and surface area.

The preliminary scaled conditioning history of each structure is shown in terms of the cumulative RF pulses and cumulative breakdowns in Figure 7.17. It should also be noted that as mentioned the orientation of the surface electric field of the PolariX-TDS was rotated several times during operation, however only the data from operation in a single orientation is shown in Figure 7.17.

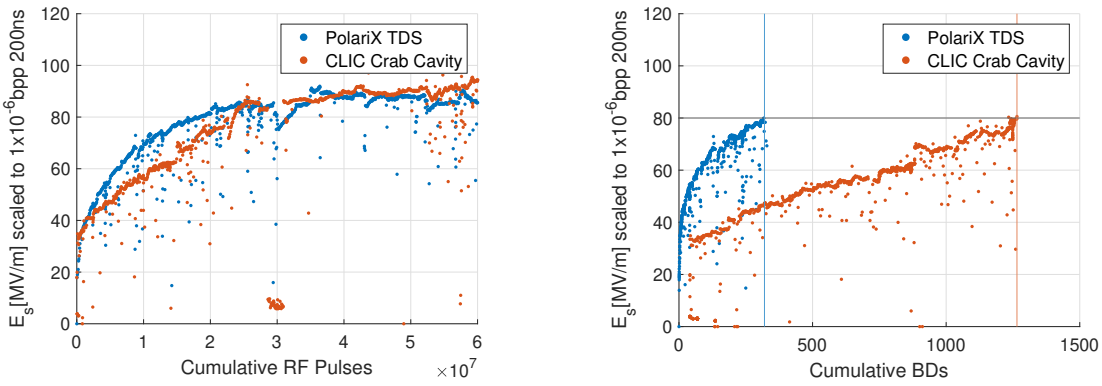

(a) (b)

Fig. 7.17 The scaled surface electric field plotted against the cumulative RF pulses (a) and cumulative breakdowns (b) for the CLIC crab cavity and the Polarix-TDS. The blue and red lines show the number of breakdowns accumulated by each structure after having reached a scaled peak surface electric field of 80MV/m.

While both structures reached the same scaled electric field value in a comparable number of pulses, each did so whilst accumulating a drastically different number of breakdowns. Despite the larger surface area and increased number of cells the PolariX reached a scaled electric field value of 80MV/m after approximately 300 breakdowns while the CLIC crab cavity accumulated over 1250. It is speculated that this may be in part due to the use of different BDR setpoints.

The CLIC crab cavity was effectively subjected to a more aggressive conditioning procedure, accumulating breakdowns more quickly. However as a consequence of the more frequent breakdowns it was also subjected to algorithmic decreases in power more

frequently, preventing it from overtaking the PolariX despite the higher permissible BDR. To investigate the effect of the BDR setpoint, a parameter sweep was performed in simulation and the results are shown in Figure 7.18.

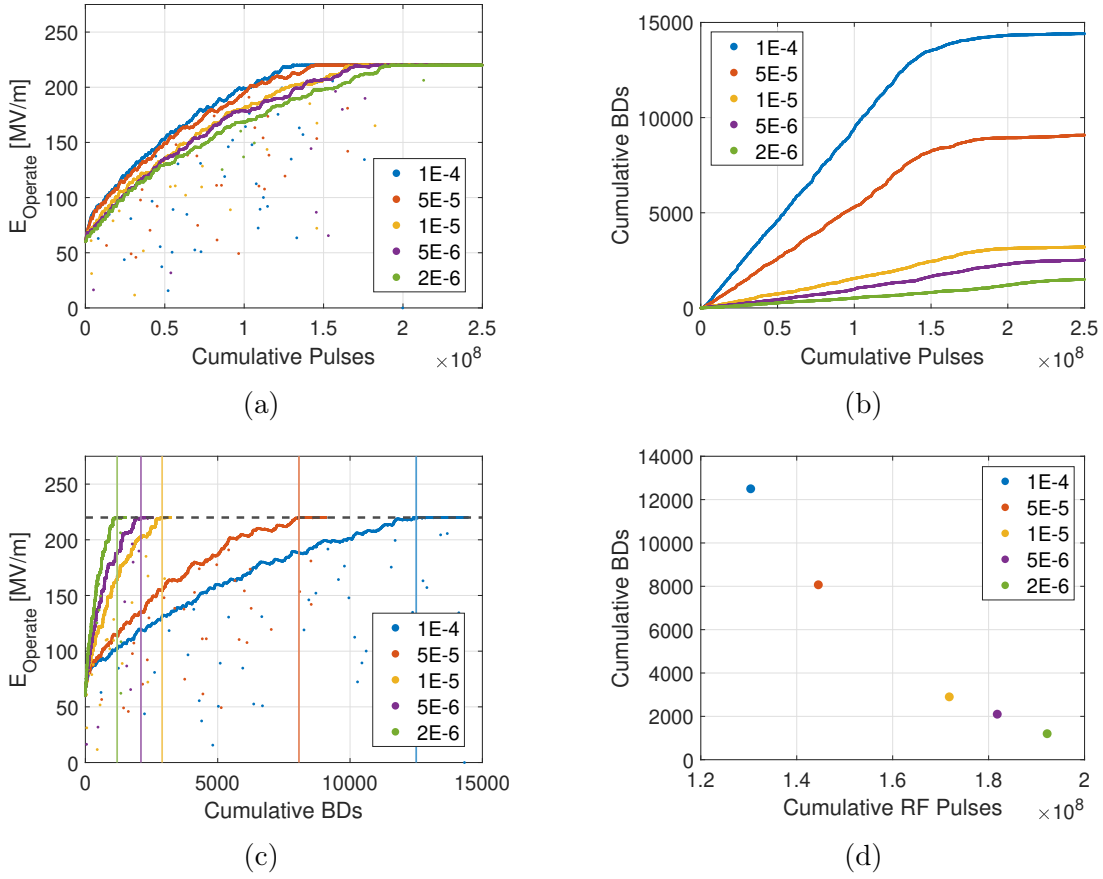

Fig. 7.18 Conditioning curves produced by the model plotted as a function of cumulative RF pulses (a) and cumulative breakdowns (b) for various BDR setpoint values. The conditioning histories are also plotted as a function of cumulative breakdowns (c) with the number of breakdowns required to reach operation at 220MV/m for each case indicated by a vertical line. Also plotted is the cumulative number of breakdowns vs the cumulative pulses required to reach operation at 220 MV/m for each setpoint (d).

Results show that reductions in the setpoint significantly decrease the cumulative number of breakdowns while having a much less pronounced effect on the rate at which the field is increased. Over the selected range the number of pulses taken to reach stable operation at 220MV/m increases by approximately 47%, while the number of breakdowns accrued decreases by a factor of 10. The model then predicts that by reducing the setpoint it may be possible to reduce the number of breakdowns accrued during a given test without significantly prolonging the conditioning period, however it

is not known by how much it would be possible to do so in practice. It has been also noted that high-power operation results in significant degradation of structure tuning and S-parameters [40]. If this effect is a consequence of breakdowns then it may be mitigated by such a reduction.

The chosen measurement window in the Xbox test stands is 500k pulses, corresponding to a minimum measurable BDR of 2×10^{-6}. Simulations suggest that this value was chosen appropriately with results indicating that to reduce the accumulated breakdowns further, the measurable breakdown rate must be decreased by a further order of magnitude. However, as the dynamic range of the BDR window is increased, the response time is also reduced, compromising the systems ability to quickly respond to large groups of breakdowns. Additionally, the time for which a given breakdown stays in the measurement window is also increased by an order of magnitude, greatly slowing the ramping. For this reason no lower values were investigated.

7.5.4 Effect of the Algorithm Loop Settings on Conditioning

During operation, an increase in power is liable to cause a breakdown if the surface is not sufficiently conditioned. In response to the breakdown the algorithm may then reduce the operating power. Additionally, as shown by Figure 7.4 primary breakdowns are typically accompanied by several further events, and so it is desirable to minimise the probability of primary breakdowns occurring. By tailoring the loop lengths and ramp lengths the surface may held at a given voltage long enough such that a step in power is unlikely to cause a breakdown but still produces a significant conditioning effect. A similar effect may also be achieved by selecting an appropriate step size for a given loop and ramp length. To provide an indication as to how these factors affect the preliminary conditioning, the loop length, ramp length, and step size were swept in simulation and the results are shown in Figure 7.19.

The results shown in Figures 7.19(a-b) predict that by increasing the loop length the number of breakdowns accrued may be reduced. When the loop length is increased, the steps in power occur less frequently however there are also fewer reductions in power in response to breakdowns, meaning that the preliminary conditioning period is not significantly prolonged. It is speculated however, that excessively long loop lengths are then liable to make reaching higher target BDR values impossible. Similarly, larger ramp lengths result in fewer accumulated breakdowns during the preliminary conditioning without significantly prolonging the process, however the potential reduction in breakdowns is much smaller than that associated with optimisation of the loop length.

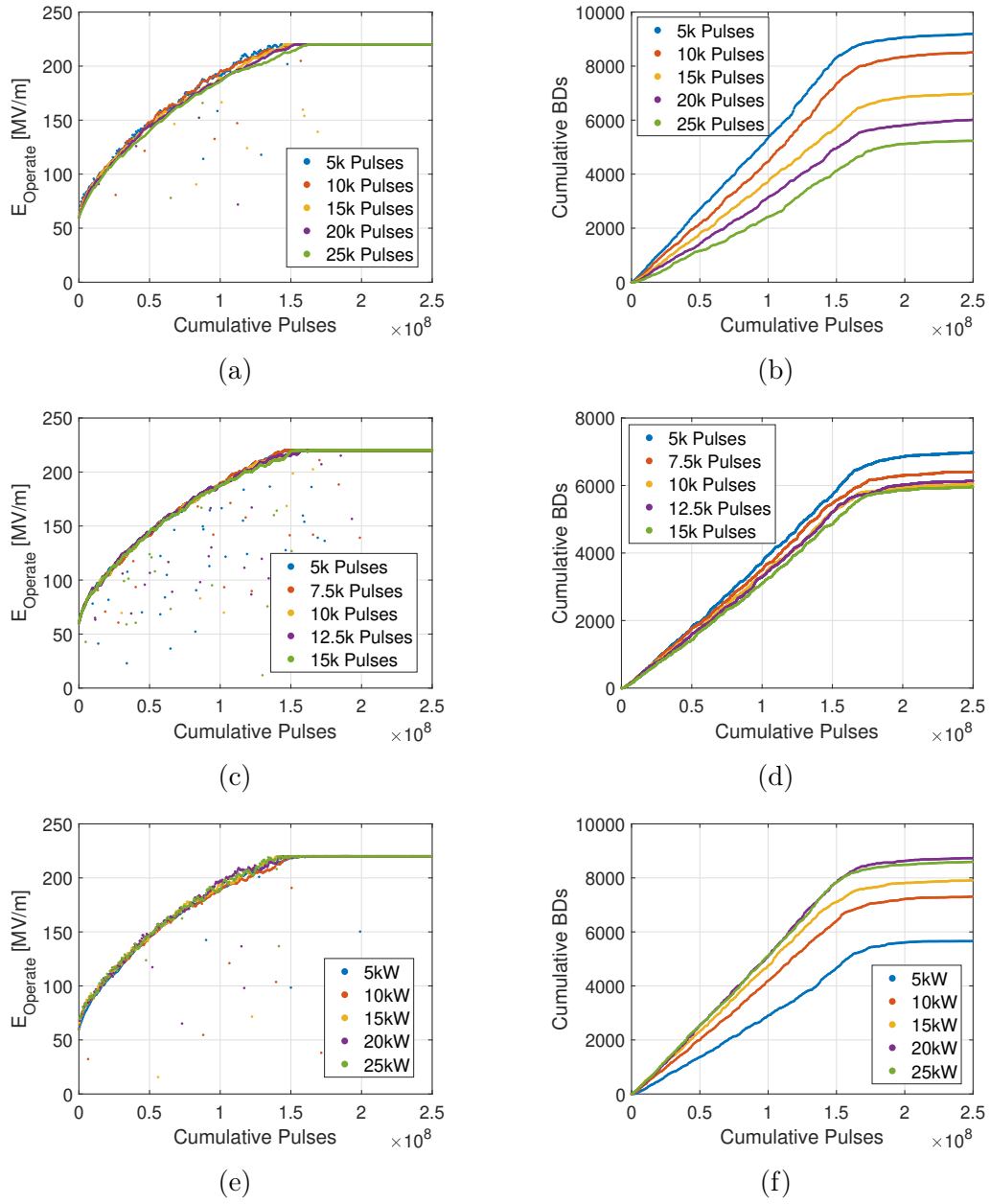

Fig. 7.19 Conditioning curves produced by the model plotted as a function of cumulative RF pulses and cumulative breakdowns for various loop lengths, ramp lengths, and step sizes. In Figures(a-b) the loop length was swept with the ramp length and step sizes fixed at 15000 pulses and 10kW respectively. In Figures(c-d) the ramp length was swept with the loop length and step size fixed at 5000 pulses and 10kW respectively. In Figures(e-f) the step size was swept with the loop length and ramp length fixed at 15000 pulses and 5000 pulses respectively. In all cases the BDR setpoint was set to 4×10^{-5} bpp.

As adjusting the step size effectively modifies the average rate at which the power is increased, the results in Figures 7.19(e-f) are also similar to those obtained by adjusting the loop length. However this nonetheless indicates that for a given loop, the step size can be tuned to minimise the probability of breakdown after each increase in power. Results in all cases then indicate that the use of a slowed, and less aggressive conditioning strategy implemented in the test stands could reduce the number of breakdowns accumulated during conditioning while having little effect on the overall duration of the conditioning period, as was shown previously when adjusting the BDR setpoint in Section 7.5.3.

Examining the conditioning curves presented in Figure 7.19 shows that in each case the average increase in power per pulse remains comparable whilst the number of breakdowns accrued varies. This result predicts that the manner in which the power is increased over short timescales is liable to affect the component behaviour during testing, and not solely the average rate at which the power is increase. As such, an optimal combination of parameters may then be derived depending on the goals of the operator. To provide an indication as to where the optimal values may lie, parameters sweeps were run of the loop length sizes for two different breakdown rate setpoints. Figure 7.19 demonstrates that changes in the ramp length had little effect, and so this quantity was fixed at 5000 pulses in each case. The first breakdown rate setpoint investigated was 1×10^{-5}, as Figure 7.18 showed that breakdown rate setpoints lower than this offered only marginal reductions in the cumulative breakdowns while significantly prolonging the test period. The second breakdown rate setpoint chosen was 4×10^{-5}, lying within the range typically employed in CERN's test stands. The results of the sweeps for each are shown in Figure 7.20.

Once again, results indicate that in general, the number of accrued breakdowns may be reduced at the expense of a prolonged preliminary conditioning period. However, parametric combinations which require a similar or equal number of pulses accrue different numbers of breakdowns, indicating that with optimally selected values conditioning may take place at a reduced breakdown rate with no additional temporal cost.

In small, single structure arrangements minimising the risk of damage to the structure is generally the priority and so a conservative approach to conditioning is likely more favourable at the expense of additional RF pulses. In large multi-structure arrangements however, or indeed in a CLIC-like scenario where thousands of structures must be conditioned, a difference of several hundred million pulses per structure constitutes a significant temporal and monetary investment during commissioning.

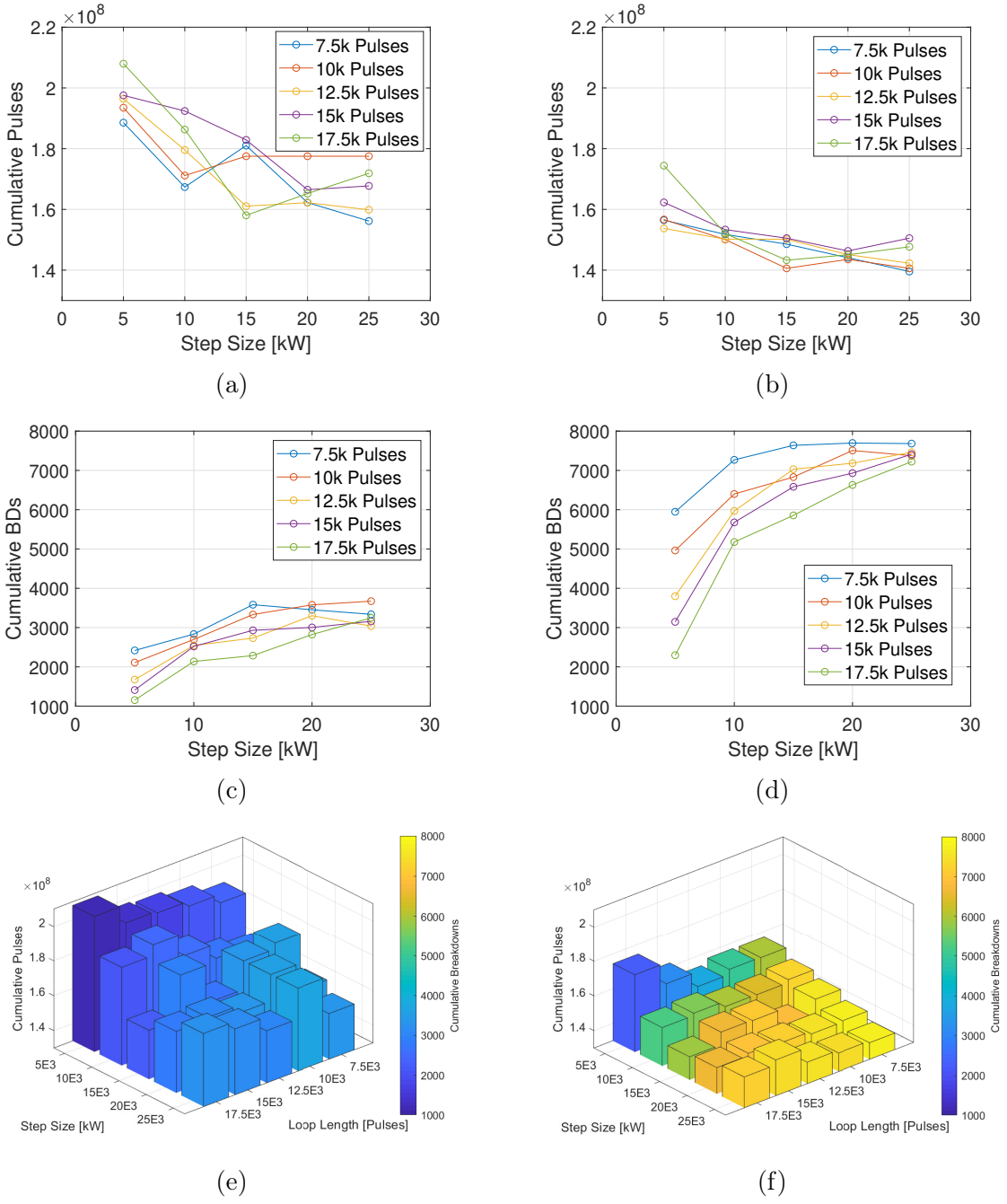

Fig. 7.20 The number of pulses and cumulative breakdowns required to reach operation at a surface electric field of 220MV/m for different step size and loop length combinations at a BDR setpoint of 1×10^{-5} (a,c) and 4×10^{-5} (b,d). It was shown previously in Figure 7.19 that the ramp length had little effect on the preliminary conditioning and so this value was fixed at 5000 pulses for all cases. For readability the 4D results are also compiled and presented as a 3D histogram for where the colour is indicative of the cumulative number of breakdowns for BDR setpoints of 1×10^{-5} (e) and 4×10^{-5} (f).

Hence, the optimal combination of values is dependent on the arrangement which must be conditioned, the time available to perform the conditioning, and the level of risk which is deemed to be acceptable. In such scenarios, the introduction of a cost function would then allow application of these results to derive approximately optimised values depending on the operator preference, and this is one way in which the work may be applied or indeed expanded upon in the future.

Finally, it is also worth noting that an additional limit of the current algorithm is that the loop length, ramp length and increases in power are fixed throughout the duration of the test, the latter resulting in gradually reduced voltage steps in the later stages of testing. An additional extension of the work may then be to use of the model to investigate of the use of an automated or dynamic step size, loop length, and ramp length during component conditioning.

7.6 Conclusion

A discretised model based on the idea of the progressive modification of the surface properties of a material on a pulse-to-pulse basis has been developed and, while relying on several assumptions, offers explanations for several results observed in the test stands. The model has been used to simulate the inhomogeneous breakdown accumulation and conditioning observed in a high-power tested dipole mode cavity. Simulation results indicate that even a marginal reduction in surface results in a significant reduction in the accumulated breakdowns while producing a comparable level of conditioning. This offers an explanation for the inhomogeneous distribution of breakdown craters observed during post-mortem examinations of cavities which have undergone high-power testing. Results also suggest that low field regions remain relatively unconditioned, a prediction which aligns with experimental results observed in the test of a polarisable transverse deflecting structure (PolariX-TDS).

In future high-gradient facilities, it will be necessary to condition several structures, potentially in parallel. To investigate the effects associated with doing so a dual structure arrangement was then simulated for two scenarios. In the first scenario the power was split evenly and one cavity commenced the test in a higher conditioned state. In the second scenario, one cavity was allocated a consistently higher operating field throughout the conditioning. Simulation results for the first scenario demonstrate that even small differences in the conditioned state of each cavity persist throughout the test duration, and a significant discrepancy in the accumulated breakdowns emerges as a consequence. Similarly, in the second scenario investigated the cavity receiving

the higher field accrues a larger number of breakdowns, regulating the rate at which the power may be increased. These results principally agree with the results of the superstructure test presented in Chapter 6 in which one superstructure constituent accumulated fewer breakdowns due to being operated consistently at a lower gradient. However, it is important to note that the discrepancy in operating gradient chosen in simulation was not as large as that which was present in the test stand. Additionally, the breakdowns which occurred in structure B in the test stand were not homogeneously distributed, potentially indicating the presence of a fault. Nonetheless, simulation results predict that the operation of a sacrificial or virtual cavity in parallel with a primary device may facilitate low or reduced-BDR conditioning, although it is currently unknown if such a conditioning regime would yield any benefit.

Parameter sweeps have been carried out in order to determine the effect of several algorithmic parameters on conditioning and results suggest that the number of breakdowns accumulated during CERN's high-gradient structure tests could be reduced without significantly prolonging the test period by selecting a lower the BDR setpoint in the test stands. A similar result may also be achieved via adjustment of the loop settings in the current algorithm. Several parameter sweeps have been performed to provide an indication of what may be expected when operating with different settings, however the optimal combination of parametric values will depend on the arrangement which must be conditioned, the time available, and the acceptable level of risk.

Lastly, it should be noted that the existing model is a work in progress and demonstrates several shortcomings, namely the lack of a pulse length dependence and that breakdowns have no permanent consequence, as is the case in real tests. Additionally, the model has been tuned to apply only to soft copper cavities and excludes the vacuum conditioning process typically required in CERN's test stands. As such, several other facets of operation could be added to provide an improved physical picture of the conditioning process. The framework provided may also be used to investigate other means of capturing the probabilistic behaviour of breakdown, alternative physical models of conditioning, and to trial entirely different approaches to algorithmic conditioning.

Chapter 8

Conclusion and Future Work

8.1 Overview of Work Presented

To date, high-gradient normal conducting technology has found numerous applications worldwide both in research facilities and industrial applications. A primary limitation of the technology however is the occurrence of vacuum arcs and to operate reliably at high-power such devices must be subjected to a conditioning process. To investigate these phenomena and the practical considerations associated with the operation of high-gradient arrangements the Xbox-2 test stand at CERN has been modified to accommodate additional RF channels and the first multi-structure arrangement has been tested at high-power. The following chapter outlines the key results of the high power test and the results of the work carried out in this thesis.

8.1.1 High-Power Test of a Multi-Structure Arrangement

The Xbox- test stand has been modified to accommodate a dual structure arrangement and a CLIC superstructure has been tested at high power. Within the available test period the constituent structures reached unloaded gradients of 90MV/m and 45MV/m respectively at an RF pulse length of 50ns. Due to the discrepancy in input power it was noted that one structure accumulated an order of magnitude fewer breakdowns than the other, and that the majority of these breakdowns occurred in a single location within the structure. A comparative analysis has been performed with previously tested HG structures however the test is still ongoing. The conditioning of structure A has proceeded more slowly than structures previously tested at CERN however it is speculated that this may be a consequence of the long storage period.

8.1.2 Simulation of a Multi-Structure Arrangement

In CERN's test stands prototype high-gradient structures regularly establish accelerating gradients above 100MV/m, corresponding to peak surface fields in excess of 200MV/m. When operating at this level a measurable current is observed due to the emission and capture of electrons within the structure, a phenomenon typically referred to as dark current. Full 3D PIC simulations of dark current in a structure with tapered irises have been performed in CST MWS and compared with experimental data. It has been observed in simulation that later cells in a tapered structure emit less current despite establishing higher peak fields, and this result is in agreement with the experimental data recorded in the test stands. It is then proposed that this effect may be attributed to the reduction in iris radius in tapered structures resulting in a reduced potential emission area, and hence fewer emission sites.

A dual structure arrangement has also been simulated by recursively feeding the output of a single structure simulation into itself. In this arrangement the total captured current and indeed the resulting radiation produced may be reduced by adjusting the relative phasing and these results were then validated experimentally in the test stands. This effect also constitutes a potential means of in situ phase calibration. Results also suggest that considerable current may accumulate in long multi-structure arrangements, forming a halo around main beam bunches and acting as a significant source of radiation. It is also speculated that such current may also result in measurable beam loading and interact with sensitive beam diagnostic equipment.

The model is principally based on the progressive modification of the properties of the cavity surface on a pulse to pulse basis

8.1.3 Monte Carlo Model of High-Gradient Conditioning

To shed light on the probabilistic behaviour of breakdown and the conditioning process a Monte Carlo model capable of replicating the macroscopic behaviour of structures installed in CERN's high-gradient test stands has been developed. The model is principally based on the assumption that a modification of the device surface takes place on a pulse to basis. Equations capturing this behaviour have been derived from empirical relations and the regularly observed characteristics of the conditioning process. The model was then tuned to give reasonable agreement with existing test stand data.

The results produced by the model offer potential explanations for several phenomena observed in recent high-gradient tests. Additionally, parameter sweeps were

performed to investigate the implications of changes in CERN's current algorithmic approach to high-gradient conditioning and the results indicate that by adjusting the algorithmic parameters, it may be possible to condition structures while accumulating fewer breakdowns without significantly prolonging the test period. However, these results have not been verified experimentally and it should be noted that is currently unknown if there is any benefit to doing so. The model nonetheless constitutes a low cost way of trialing different approaches to conditioning without the monetary and temporal expense associated with doing so experimentally.

8.2 Future Work

8.2.1 Completion of the Multi-Structure High-Power Test

The high-power test of the CLIC superstructure is ongoing, pending the return of the Xbox-2 klystron. Additionally, the BOC pulse compressor has been returned to PSI, Switzerland and the previously utilised SLED design has been reinstalled with the test being scheduled to continue in late 2021. To date, structure B remains comparatively unconditioned and so in order to verify whether both structures are capable of operation at the full design gradient and pulse length it is currently planned that the power splitter be adjusted upon resumption of the test to equally split the power between the structures.

Previously, in Chapter 7 it was speculated that it may be possible to consistently hold the field in a device high enough to produce a significant conditioning effect, yet without inducing breakdowns frequently. If the superstructure test resumes operation with the power split equally and this hypothesis is correct, then even when exceeding 90MV/m in both structures simultaneously the majority of breakdowns should occur in structure B as it has effectively commenced the test in a less conditioned state.

When all components in the high-power waveguide network have been adequately conditioned additional dark current and radiation studies to complement those in Chapter 5 may also be carried out. Additionally, the CCC was designed for use in conjunction with the SLED pulse compressor, and so this arrangement may also be validated. As mentioned, it is also important to note that prior to installation in the X-band test stands the structures were placed into storage and exposed to air. Following the removal of the klystron the structures will once again remain in storage for a significant period of time. Exposure to air and the effect of storage periods are both important facets of operation for any high-gradient facility and so the results

of further testing may shed light on each. Namely, the time taken to reestablish any previously achieved conditions and the degree to which the conditioned state of the surface has been retained.

8.2.2 Expansion of the Multi-Structure Simulations

The code in developed Section 5.3 constitutes a means of efficiently calculating the transfer function between any two points of an RF network given the appropriate signal flow graph and S-parameters. While some cases may be readily approximated by hand, the code may be used to examine the signal propagation in more complex arrangements such as a full CLIC module or larger networks.

The work performed in Section 5.4 forms the basis for subsequent multi-structure simulations. Being the target gradient for CLIC, operation at 100MV/m has been investigated however it is clear that other facilities may operate at different voltages and the simulations can be readily scaled accordingly. During operation, breakdowns also occasionally result in a measurable change in the Faraday cup signal and this effect may also be investigated in simulation by varying the local β in given cell. In this way the effect of breakdown may be approximated by fitting an appropriate change in β to experimental data. It is also postulated in Section 5.4.2 that both the total emission and breakdown rate associated with a given cell correlate with iris size and hence active area. This effect could be verified experimentally with single cell tests such as those performed at SLAC given an appropriate cavity geometry.

With the recursive method employed in Section 5.4.4 it is also possible to efficiently simulate many structures in series. Although only a single superstructure has been examined the next logical step is then to expand the simulation to a full CLIC module, or indeed other larger high-gradient arrangements. It is then also possible to export the simulated dark current and examine its propagation through the magnets associated with a given lattice and whether or not it results in any measurable beam loading in later structures, effectively reducing the accelerating voltage. Based on the lattice design of a given machine, the results of such work may then shed insight as to whether the dark current is already sufficiently collimated or merits additional consideration.

8.2.3 Verification and Expansion of the Monte Carlo Model

The Monte Carlo model has been tuned to agree with single X-band structure tests, however the results may also be compared with and fit to alternative accelerating structures and the results of DC electrode tests such as the LES at CERN in order

to provide a more generalised framework. Similarly, by adjusting the $E_{Saturation}$ value the model may be compared with the conditioning curves of alternative materials. Ultimately, the goal of the tool should be to propose an ideal means of conditioning for both accelerators and other high-voltage devices. In this context, one of the primary goals should be testing the proposed algorithmic adjustments experimentally in order to verify the predictions and improve the currently employed conditioning process. An additional way in which this may be accomplished is by running the model in parallel during high-power tests and using it to regulate the conditioning algorithm in the test stands, acting as a virtual sacrificial cavity.

While the primary goal is the improvement of the conditioning process, the model also constitutes a framework which may be used to investigate alternative scalings and probabilistic models of breakdown. A current limitation of the model is that there is no permanent effect of breakdown, and quantification of this effect is a desirable prospect. As highlighted in Section 7.4.2 the grid size may also be expanded or reduced along with the $P_{Baseline}$ value in order to fit the results to larger networks or represent smaller portions of a given surface. Additionally, as breakdowns may sputter copper over small distances it is speculated that the addition of cross talk between grid elements may improve results and offer a more complete physical picture of the process.

Finally, several other aspects of operation are still not captured by the Monte Carlo model. Namely, that modelling the effect of changes in pulse length is not possible although empirical scalings exist with which this feature may be implemented. It is also clear that the model does not capture the effect of pauses in operation or the vacuum conditioning process, features which could be investigated with the addition of a secondary extrinsic surface state in the code. While aiding in the optimisation of CERN's conditioning algorithm was intended to be the model's primary purpose, the aforementioned studies and the addition of these features is also recommended in order to improve the understanding of both the conditioning and breakdown phenomena.

References

[1] G. Ising, *Prinzip einer Methode zur Herstellung von Kanalstrahlen hoher Voltzahl*, ser. Arkiv för matematik, astronomi och fysik. Almqvist & Wiksells Boktryckeri-A.B., 1924, translated as: *Principle of a method for the Production of Canal Rays of High Voltage.*

[2] R. Widerøe, "Über ein neues Prinzip zur Herstellung hoher Spannungen", *Arch. Elektrotech.*, vol. 21, pp. 387–406, 1928, translated as: *A new principle for the generation of high voltages.* [Online]. Available: http://cds.cern.ch/record/434681

[3] J. C. Maxwell, *A Treatise on Electricity and Magnetism*, ser. Cambridge Library Collection - Physical Sciences. Cambridge University Press, 2010, vol. 1.

[4] T. P. Wangler, *RF Linear Accelerators.* John Wiley & Sons, Ltd, 1998. [Online]. Available: https://doi.org/10.1002/9783527623426

[5] D. Staelin, *Electromagnetics and Applications.* Massachusetts Institute of Technology, 2011. [Online]. Available: https://books.google.ch/books?id=E37zswEACAAJ

[6] B. Hague and D. Martin, *An Introduction to Vector Analysis for Physicists and Engineers*, ser. Methuen's monographs on physical subjects. Methuen, 1970. [Online]. Available: https://books.google.ch/books?id=LV0LMRSzM5wC

[7] D. M. Pozar, *Microwave Engineering; 3rd ed.* Hoboken, NJ: Wiley, 2005. [Online]. Available: https://cds.cern.ch/record/882338

[8] F. Gerigk, "RF Basics I and II", pp. 71–116, Feb 2013, presented at the CERN Accelerator School CAS 2011: High Power Hadron Machines, Bilbao, 24 May - 2 June 2011. [Online]. Available: https://doi.org/10.5170/CERN-2013-001.71

[9] F. Gerigk, "Cavity Types", pp. 277–298, Nov 2011, presented at the CERN Accelerator School CAS 2010: RF for accelerators, Ebeltoft, 8-17 June 2010. [Online]. Available: https://doi.org/10.5170/CERN-2011-007.277

[10] G. Floquet, "Sur les équations différentielles linéaires à coefficients périodiques [On linear differential equations with periodic coefficients]", *Annales Scientifiques de l'École Normale Supérieure*, vol. 12, pp. 47–88, 1883. [Online]. Available: http://eudml.org/doc/80895

[11] D. Alesini, "Power coupling", pp. 125–147, Dec 2011, contribution to the CAS - CERN Accelerator School: Specialised Course on RF for Accelerators; 8 - 17 Jun 2010, Ebeltoft, Denmark. [Online]. Available: https://doi.org/10.5170/CERN-2011-007.125

[12] D. Angal-Kalinin *et al.*, "Design, specifications, and first beam measurements of the compact linear accelerator for research and applications front end", *Phys. Rev. Accel. Beams*, vol. 23, p. 044801, Apr 2020. [Online]. Available: https://link.aps.org/doi/10.1103/PhysRevAccelBeams.23.044801

[13] T. Lucas, "Progress on the Smart*Light project", 2019, international Workshop on Breakdown Science and High Gradient Technology (HG2019). [Online]. Available: https://indico.cern.ch/event/766929/contributions/3448975/

[14] J. Wang, G. Loew, R. Loewen, R. Ruth, A. Vlieks, I. Wilson, and W. Wuensch, "SLAC/CERN high gradient tests of an X-band accelerating section", in *Proceedings of the 1995 Particle Accelerator Conference*, vol. 1, 06 1995, pp. 653 – 655. [Online]. Available: https://doi.org/10.1109/PAC.1995.504746

[15] V. A. Dolgashev, "Progress on high-gradient structures", *AIP Conference Proceedings*, vol. 1507, no. 1, pp. 76–84, 2012. [Online]. Available: https://doi.org/10.1063/1.4773679

[16] A. Grudiev, S. Calatroni, and W. Wuensch, "New local field quantity describing the high gradient limit of accelerating structures", *Phys. Rev. ST Accel. Beams*, vol. 12, p. 102001, Oct 2009. [Online]. Available: https://doi.org/10.1103/PhysRevSTAB.12.102001

[17] C. Pellegrini, A. Marinelli, and S. Reiche, "The physics of x-ray free-electron lasers", *Reviews of Modern Physics*, vol. 88, p. 015006, Mar 2016. [Online]. Available: https://doi.org/10.1103/RevModPhys.88.015006

[18] J. Shao, "Investigations on rf breakdown phenomenon in high gradient accelerating structures", PhD Thesis, Tsinghua University, Department of Engineering Physics, 2016.

[19] M. Ferrario, M. Migliorati, and L. Palumbo, "Space Charge Effects", pp. 331–356, Jan 2016, contribution to the CAS - CERN Accelerator School: Advanced Accelerator Physics Course, Trondheim, Norway, 18-29 Aug 2013. [Online]. Available: https://doi.org/10.5170/CERN-2014-009.331

[20] C. Limborg-Deprey, C. Adolphsen, D. McCormick, M. Dunning, K. Jobe, H. Li, T. Raubenheimer, A. Vrielink, T. Vecchione, F. Wang, and S. Weathersby, "Performance of a first generation X-band photoelectron rf gun", *Phys. Rev. Accel. Beams*, vol. 19, p. 053401, May 2016. [Online]. Available: https://doi.org/10.1103/PhysRevAccelBeams.19.053401

[21] C. Limborg-Deprey *et al.*, "An X-band Gun Test Area at SLAC", *Proceedings of the 24th Particle Accelerator Conference (PAC'11)*, pp. 133–135, 2011.

[22] B. Militsyn, L. Cowie, P. Goudket, S. Jamison, J. McKenzie, K. Middleman, M. Roper, R. Valizadeh, A. Wheelhouse, and V. Paramonov, "High Repetition Rate Highly Stable S-band Photocathode Gun for the CLARA Project", *Proceedings of the 4th International Particle Accelerator Conference (IPAC2013)*, pp. 437–439, 01 2013.

[23] B. Militsyn, L. Cowie, P. Goudket, J. McKenzie, A. Wheelhouse, G. Burt, T. Jones, V. Paramonov, and A. Skasyrskaya, "Design of the High Repetition Rate Photocathode Gun for the CLARA Project", in *27th International Linear Accelerator Conference*, 2014, p. THPP126.

[24] Y. Du, L. Yan, Q. Hua, Jianfeiand Du, Z. Zhang, R. Li, H. Qian, W. Huang, H. Chen, and C. Tang, "Generation of first hard X-ray pulse at Tsinghua Thomson Scattering X-ray Source", *Review of Scientific Instruments*, vol. 84, no. 5, p. 053301, 2013. [Online]. Available: https://doi.org/10.1063/1.4803671

[25] X. Stragier, P. Mutsaers, and J. Luiten, "Smart*Light: A Tabletop, High Brilliance, Monochromatic and Tunable Hard X-ray Source for Imaging and Analysis.", *Microscopy and Microanalysis*, vol. 24, pp. 314–315, 08 2018. [Online]. Available: https://doi.org/10.1017/S1431927618013880

[26] D. I. Thwaites and J. B. Tuohy, "Back to the future: the history and development of the clinical linear accelerator", *Physics in Medicine and Biology*, vol. 51, no. 13, pp. R343–R362, Jun 2006. [Online]. Available: https://doi.org/10.1088/0031-9155/51/13/r20

[27] J. Wilson, E. Hammond, G. Higgins, and K. Petersson, "Corrigendum: Ultra-High Dose Rate (FLASH) Radiotherapy: Silver Bullet or Fool's Gold?", *Frontiers in Oncology*, vol. 10, p. 210, 02 2020. [Online]. Available: https://doi.org/10.3389/fonc.2020.00210

[28] S. Jolly, "Technical Challenges for FLASH Proton Therapy", 2019, international Conference on Medical Accelerators and Particle Therapy. [Online]. Available: https://indico.cern.ch/event/803528/contributions/3503562/

[29] P.-G. Montay-Gruel, "Perspectives for electron Flash therapy", 2019, cLIC Workshop 2019. [Online]. Available: https://indico.cern.ch/event/753671/contributions/3279476/

[30] A. Faus-Golfe *et al.*, "First Performance Calculations for the Very High Energy Electron Radiation Therapy Experiment at PRAE", in *9th International Particle Accelerator Conference*, 2018, p. MOPML051. [Online]. Available: https://doi.org/10.1016/j.physletb.2012.08.020

[31] "CLIC lights the way for FLASH therapy", Nov/Dec 2020, *CERN Courier Volume 60, Number 6,* Nov/Dec 2020. [Online]. Available: https://cds.cern.ch/record/2743359

[32] G. Aad, T. Abajyan, B. Abbott, J. Abdallah, S. Abdel Khalek, A. Abdelalim, O. Abdinov, R. Aben, B. Abi, M. Abolins *et al.*, "Observation of a new particle in the search for the Standard Model Higgs boson with the ATLAS detector

at the LHC", *Physics Letters B*, vol. 716, no. 1, p. 1–29, Sep 2012. [Online]. Available: https://doi.org/10.1016/j.physletb.2012.08.020

[33] M. Aicheler, P. Burrows, M. Draper, T. Garvey, P. Lebrun, K. Peach, N. Phinney, H. Schmickler, D. Schulte, and N. Toge, *A Multi-TeV Linear Collider Based on CLIC Technology: CLIC Conceptual Design Report*, ser. CERN Yellow Reports: Monographs. Geneva: CERN, 2012. [Online]. Available: https://cds.cern.ch/record/1500095

[34] C. Adolphsen *et al.*, "The International Linear Collider Technical Design Report - Volume 3.II: Accelerator Baseline Design", ILC International Development Team, Geneva, Tech. Rep., Jun 2013. [Online]. Available: https://cds.cern.ch/record/1601969

[35] CERN. CLIC accelerator footprint. License: CC-BY-4.0,Accessed: 14/10/2020. [Online]. Available: https://cds.cern.ch/record/2297076

[36] E. Engelberg, "Theory of electric field breakdown nucleation: mobile dislocation population dynamics and atomic simulations", 2019, 8th International Workshop on Mechanisms of Vacuum Arcs (MeVArc 2019). [Online]. Available: https://indico.cern.ch/event/774138/contributions/3507896/

[37] B. J. Woolley, "High power x band rf test stand development and high power testing of the clic crab cavity", PhD Thesis, Lancaster University, Engineering Department, 2015.

[38] D. Banon Caballero *et al.*, "Dark current analysis at CERN's X-band facility", in *10th International Particle Accelerator Conference (IPAC2019)*, May 2019, p. WEPRB059.

[39] K. Bane, V. Dolgashev, and G. Stupakov, "Simulation of dark currents in X-band accelerator structures", in *9th European Particle Accelerator Conference (EPAC 2004)*, Jun 2004.

[40] T. Lucas, "High field phenomenology in linear accelerators for the compact linear collider", PhD Thesis, University of Melbourne, 2018.

[41] J. Paszkiewicz, "Dark Current Measurements in RF Structures", 2018, international Workshop on Breakdown Science and High Gradient Technology, SINAP, Shanghai. [Online]. Available: https://indico.cern.ch/event/675785/contributions/3022039/

[42] J. Wang and G. Loew, "Field emission and RF breakdown in high gradient room temperature linac structures", in *Joint CERN-US-Japan Accelerator School: Course on Frontiers of Accelerator Technology: RF Engineering for Particle Accelerators*, 10 1997, pp. 768–794.

[43] G. A. Loew and J. W. Wang, "Field Emission and RF Breakdown in Copper LINAC Structures", *Particle Accelerators*, vol. 30, no. SLAC-PUB-5059, pp. 225–230, Aug 1989. [Online]. Available: https://cds.cern.ch/record/201288

[44] T. Abe, T. Kageyama, H. Sakai, Y. Takeuchi, and K. Yoshino, "Direct observation of breakdown trigger seeds in a normal-conducting rf accelerating cavity", *Phys. Rev. Accel. Beams*, vol. 21, no. 12, p. 122002, 2018. [Online]. Available: https://doi.org/10.1103/PhysRevAccelBeams.21.122002

[45] J. Paulini, T. Klein, and G. Simon, "Thermo-field emission and the Nottingham effect", *Journal of Physics D: Applied Physics*, vol. 26, no. 8, pp. 1310–1315, Aug 1993. [Online]. Available: https://doi.org/10.1088/0022-3727/26/8/024

[46] J. G. Navarro, "Breakdown studies for high gradient rf warm technology in: Clic and hadrontherapy linacs", PhD Thesis, Universitat de València, 2016.

[47] R. Fowler and L. Nordheim, "Electron emission in Intense Electric Fields", *Proceedings of the Royal Society of London A*, vol. A119, pp. 173–181, 1928. [Online]. Available: https://doi.org/10.1098/rspa.1928.0091

[48] Wenli and L. D., "EFFECT OF GRAIN SIZE ON THE ELECTRON WORK FUNCTION OF Cu AND Al", *Surface Review and Letters*, vol. 11, 01 2012. [Online]. Available: https://doi.org/10.1142/S0218625X04006025

[49] E. Leiva, "On the work function changes and other properties of the gas-exposed electrode surface in the NEMCA effect", *Topics in Catalysis*, vol. 44, pp. 347–354, 06 2007.

[50] J. Paszkiewicz, P. Burrows, and W. Wuensch, "Spatially resolved dark current in high gradient traveling wave structures", in *10th International Particle Accelerator Conference*, 2019, p. WEPRB062. [Online]. Available: https://doi.org/10.18429/JACoW-IPAC2019-WEPRB062

[51] L. Laurent, S. Tantawi, V. Dolgashev, C. Nantista, Y. Higashi, M. Aicheler, S. Heikkinen, and W. Wuensch, "Experimental study of rf pulsed heating", *Phys. Rev. ST Accel. Beams*, vol. 14, p. 041001, Apr 2011. [Online]. Available: https://doi.org/10.1103/PhysRevSTAB.14.041001

[52] A. S. Pohjonen, F. Djurabekova, K. Nordlund, A. Kuronen, and S. P. Fitzgerald, "Dislocation nucleation from near surface void under static tensile stress in Cu", *Journal of Applied Physics*, vol. 110, no. 2, p. 023509, 2011. [Online]. Available: https://doi.org/10.1063/1.3606582

[53] S. Calatroni, J. Kovermann, M. Taborelli, H. Timko, W. Wuensch, A. Descoeudres, F. Djurabekova, A. Kuronen, K. Nordlund, and A. Pohjonen, "Breakdown Studies for the CLIC Accelerating Structures", in *25th International Linear Accelerator Conference*, 2011, p. MOP070.

[54] E. Z. Engelberg, J. Paszkiewicz, R. Peacock, S. Lachmann, Y. Ashkenazy, and W. Wuensch, "Dark current spikes as an indicator of mobile dislocation dynamics under intense dc electric fields", *Phys. Rev. Accel. Beams*, vol. 23, p. 123501, Dec 2020. [Online]. Available: https://doi.org/10.1103/PhysRevAccelBeams.23.123501

[55] Z. Zhou, A. Kyritsakis, Z. Wang, Y. Li, Y. Geng, and F. Djurabekova, "Direct observation of vacuum arc evolution with nanosecond resolution", *Scientific Reports*, vol. 9, no. 1, p. 7814, May 2019. [Online]. Available: https://doi.org/10.1038/s41598-019-44191-6

[56] K. N. Sjøbæk, "Avoiding vacuum arcs in high gradient normal conducting rf structures", PhD Thesis, University of Oslo, 2016.

[57] B. Woolley and E. R. Castro, "CLIC Crab Cavity Post-Mortem Analysis", 2016, mini MeVArc Meeting. [Online]. Available: https://indico.cern.ch/event/464716/contributions/1983061/

[58] W. Wuensch, A. Degiovanni, S. Calatroni, A. Korsbäck, F. Djurabekova, R. Rajamäki, and J. Giner-Navarro, "Statistics of vacuum breakdown in the high-gradient and low-rate regime", *Phys. Rev. Accel. Beams*, vol. 20, no. 1, p. 011007, 2017. [Online]. Available: https://doi.org/10.1103/PhysRevAccelBeams.20.011007

[59] F. Le Pimpec, J. Frisch, K. Jobe, D. McCormick, J. L. Nelson, M. Ross, and T. Smith, "An Acoustic Sensor System for Localizing RF Breakdown in Warm Copper Accelerating Structures", *Nucl. Instrum. Meth. A*, vol. 582, pp. 345–355, 2007. [Online]. Available: https://doi.org/10.1016/j.nima.2007.08.181

[60] W. Kilpatrick, "Criterion for Vacuum Sparking Designed to Include Both rf and dc", *The Review of Scientific Instruments*, vol. 28, pp. 824–826, 1957.

[61] E. Z. Engelberg, Y. Ashkenazy, and M. Assaf, "Stochastic Model of Breakdown Nucleation under Intense Electric Fields", *Phys. Rev. Lett.*, vol. 120, no. 12, p. 124801, 2018. [Online]. Available: https://doi.org/10.1103/PhysRevLett.120.124801

[62] K. Nordlund and F. Djurabekova, "Defect model for the dependence of breakdown rate on external electric fields", *Phys. Rev. ST Accel. Beams*, vol. 15, p. 071002, Jul 2012. [Online]. Available: https://doi.org/10.1103/PhysRevSTAB.15.071002

[63] F. Paschen, "Ueber die zum funkenübergang in luft, wasserstoff und kohlensäure bei verschiedenen drucken erforderliche potentialdifferenz", *Annalen der Physik*, vol. 273, no. 5, pp. 69–96, 1889, translated as: *About the potential difference required for the spark transfer in air, hydrogen and carbonic acid at different pressures*. [Online]. Available: https://doi.org/10.1002/andp.18892730505

[64] S. P. Das, G. Dalei, and A. Barik, "A Dielectric Barrier Discharge (DBD) Plasma Reactor: An Efficient Tool to Measure the Sustainability of Non-Thermal Plasmas through the Electrical Breakdown of Gases", *IOP Conference Series: Materials Science and Engineering*, vol. 410, p. 012004, sep 2018. [Online]. Available: https://doi.org/10.1088/1757-899X/410/1/012004

[65] T. J. Boyd, "Kilpatrick's criterion", Los Alamos National Laboratory, New Mexico, United States, Tech. Rep. Los Alamos Group AT-1 report AT-1:82-28, Feb 1982.

[66] W. Wuensch, "The Scaling of the Traveling-Wave RF Breakdown Limit", 2006, CLIC Note 649, CERN-AB-2006-013.

[67] C. Adolphsen, W. Baumgartner, K. Jobe, F. Le Pimpec, R. Loewen, D. McCormick, M. Ross, T. Smith, J. W. Wang, and T. Higo, "Processing studies of X-band accelerator structures at the NLCTA", in *Proceedings of the 2001 Particle Accelerator Conference*, vol. 1, 2001, pp. 478–480 vol.1.

[68] W. W. Alexej Grudiev, "Design of the CLIC Main Linac Accelerating Structure for CLIC Conceptual Design Report", in *Proceedings of Linear Accelerator Conference LINAC2010, Tsukuba, Japan*, 2011, pp. 211–213.

[69] S. L. Pitman, "Optimisation studies for a high gradient linac for application in proton imaging", PhD Thesis, Lancaster University, 2019.

[70] W. P. Dyke and J. K. Trolan, "Field emission: Large Current Densities, Space Charge, and the Vacuum Arc", *Phys. Rev.*, vol. 89, pp. 799–808, Feb 1953. [Online]. Available: https://doi.org/10.1103/PhysRev.89.799

[71] G. M. Fleming and J. E. Henderson, "The Energy Losses Attending Field Current and Thermionic Emission of Electrons from Metals", *Phys. Rev.*, vol. 58, p. 50, Nov 1940. [Online]. Available: https://doi.org/10.1103/PhysRev.58.887

[72] W. B. Nottingham, "Remarks on Energy Losses Attending Thermionic Emission of Electrons from Metals", *Phys. Rev.*, vol. 59, pp. 906–907, Jun 1941. [Online]. Available: https://doi.org/10.1103/PhysRev.59.906.2

[73] G. Fursey, *Field Emission in Vacuum Microelectronics*, ser. Microdevices. Springer US, 2007.

[74] J. Ludwick, W. Zhu, M. Cahay, S. B. Fairchild, T. C. Back, and P. T. Murray, "Transition from Nottingham-heating to Henderson-cooling during field emission", in *2017 30th International Vacuum Nanoelectronics Conference (IVNC)*, 2017, pp. 216–217. [Online]. Available: https://doi.org/10.1109/IVNC.2017.8051617

[75] L. W. Swanson, L. C. Crouser, and F. M. Charbonnier, "Energy Exchanges Attending Field Electron Emission", *Phys. Rev.*, vol. 151, pp. 327–340, Nov 1966. [Online]. Available: https://doi.org/10.1103/PhysRev.151.327

[76] A. Kyritsakis, "Dynamic coupling between particle-in-cell and atomistic simulations", 2019, 8th International Workshop on Mechanisms of Vacuum Arcs (MeVArc 2019). [Online]. Available: https://indico.cern.ch/event/774138/contributions/3507953/

[77] H. Timko, K. Ness Sjobak, L. Mether, S. Calatroni, F. Djurabekova, K. Matyash, K. Nordlund, R. Schneider, and W. Wuensch, "From Field Emission to Vacuum Arc Ignition: A New Tool for Simulating Copper Vacuum Arcs", *Contributions to Plasma Physics*, vol. 55, no. 4, pp. 299–314, 2015. [Online]. Available: https://doi.org/10.1002/ctpp.201400069

[78] A. Kyritsakis, M. Veske, K. Eimre, V. Zadin, and F. Djurabekova, "Thermal runaway of metal nano-tips during intense electron emission", *Journal of Physics D: Applied Physics*, vol. 51, no. 22, p. 225203, may 2018. [Online]. Available: https://doi.org/10.1088/1361-6463/aac03b

[79] M. Veske, A. Kyritsakis, F. Djurabekova, K. N. Sjobak, A. Aabloo, and V. Zadin, "Dynamic coupling between particle-in-cell and atomistic simulations", *Phys. Rev. E*, vol. 101, p. 053307, May 2020. [Online]. Available: https://doi.org/10.1103/PhysRevE.101.053307

[80] E. Z. Engelberg, A. B. Yashar, Y. Ashkenazy, M. Assaf, and I. Popov, "Theory of electric field breakdown nucleation due to mobile dislocations", *Physical Review Accelerators and Beams*, vol. 22, no. 8, Aug 2019. [Online]. Available: https://doi.org/10.1103/PhysRevAccelBeams.22.083501

[81] V. Zadin, A. Pohjonen, A. Aabloo, K. Nordlund, and F. Djurabekova, "Electrostatic-elastoplastic simulations of copper surface under high electric fields", *Phys. Rev. ST Accel. Beams*, vol. 17, p. 103501, Oct 2014. [Online]. Available: https://link.aps.org/doi/10.1103/PhysRevSTAB.17.103501

[82] R. Zennaro *et al.*, "High Power Tests of a Prototype X-Band Accelerating Structure for CLIC", in *8th International Particle Accelerator Conference*, 2017, p. THPIK097. [Online]. Available: https://doi.org/10.18429/JACoW-IPAC2017-THPIK097

[83] L. Millar, "Breakdown Measurements in High-Gradient RF Test Stands", 2019, 8th International Workshop on Mechanisms of Vacuum Arcs (MeVArc 2019). [Online]. Available: https://indico.cern.ch/event/774138/contributions/3507961/

[84] M. Gilbert, S. Dudarev, P. Derlet, and D. Pettifor, "Structure and metastability of mesoscopic vacancy and interstitial loop defects in iron and tungsten", *Journal of Physics: Condensed Matter*, vol. 20, p. 345214, 08 2008. [Online]. Available: https://doi.org/10.1088/0953-8984/20/34/345214

[85] W. Wuensch, C. Achard, S. Doebert, H. Braun, i. Syratchev, M. Taborelli, and I. Wilson, "Demonstration of high-gradient acceleration", in *Proceedings of the 2003 Particle Accelerator Conference*, vol. 1, Jun 2003, pp. 495 – 497. [Online]. Available: https://doi.org/10.1109/PAC.2003.1288959

[86] A. Grudiev, S. Heikkinen, I. Syrachev, M. Taborelli, I. Wilson, W. Wuensch, C. Adolphsen, and S. Doebert, "A high-power test of an X-band molybdenum iris structure", in *22nd International Linear Accelerator Conference*, Aug 2004.

[87] A. Descoeudres, F. Djurabekova, and K. Nordlund, "DC breakdown experiments with cobalt electrodes", Jun 2009, CERN-OPEN-2011-029. CLIC-Note-875. [Online]. Available: http://cds.cern.ch/record/1355401

[88] V. A. Dolgashev and S. G. Tantawi, "RF breakdown in X band waveguides", in *8th European Particle Accelerator Conference (EPAC 2002)*, Jun 2002, pp. 2139–2141.

[89] A. Korsbäck, F. Djurabekova, L. M. Morales, I. Profatilova, E. R. Castro, W. Wuensch, S. Calatroni, and T. Ahlgren, "Vacuum electrical breakdown conditioning study in a parallel plate electrode pulsed dc system", *Phys. Rev. Accel. Beams*, vol. 23, p. 033102, Mar 2020. [Online]. Available: https://doi.org/10.1103/PhysRevAccelBeams.23.033102

[90] V. Dolgashev, "Study of basic breakdown phenomena in high gradient vacuum structures", 2010, 15th Linear Accelerator Conference (LINAC2010), Tsukuba, Japan. [Online]. Available: https://accelconf.web.cern.ch/LINAC2010/talks/fr105_talk.pdf

[91] W. Wuensch, "Normal-conducting high-gradient rf systems part 2", 2018, cAS on Future Colliders. [Online]. Available: https://indico.cern.ch/event/643268/contributions/2610647/

[92] J. Paszkiewicz, "X-Band RF Test Stands at CERN", 2018, international Workshop on Breakdown Science and High Gradient Technology (HG2018). [Online]. Available: https://indico.cern.ch/event/675785/contributions/3022037/

[93] T. G. Lucas, T. Argyopolous, M. J. Boland, N. Catalan-Lasheras, R. P. Rassool, C. Serpico, M. Volpi, and W. Wuensch, "Dependency of the capture of field emitted electron on the phase velocity of a high-frequency accelerating structure", *Nuclear Instruments and Methods A*, vol. 914, pp. 46–52, 2019. [Online]. Available: https://doi.org/10.1016/j.nima.2018.10.166

[94] R. J. Loewen, A. Menegat, A. E. Vlieks, J. W. Wang, and T. Higo, "SLAC high gradient testing of a KEK X-band accelerator structure", in *Proceedings of the 1999 Particle Accelerator Conference (Cat. No.99CH36366)*, vol. 5, 1999, pp. 3420–3422 vol.5.

[95] A. Vnuchenko, T. Argyropoulos, C. Blanch Gutiérrez, N. Catalán Lasheras, D. Esperante Pereira, A. Faus-Golfe, J. Giner Navarro, G. McMonagle, I. Syratchev, and W. Wuensch, "Design and Construction of a High-Gradient RF Lab at IFIC-Valencia", in *8th International Particle Accelerator Conference*, 2017, p. THPIK081. [Online]. Available: https://doi.org/10.18429/JACoW-IPAC2017-THPIK081

[96] S. Matsumoto, M. Akemoto, S. Fukuda, T. Higo, N. Kudoh, H. Matsushita, H. Nakajima, T. Shidara, K. Yokoyama, and M. Yoshida, "Nextef: The 100MW X-band Test Facility in KEK", *Conf. Proc. C*, vol. 0806233, p. WEPP096, Jun 2008.

[97] N. Catalán Lasheras, T. Argyropoulos, D. Esperante Pereira, C. Eymin, J. Giner Navarro, G. McMonagle, S. Rey, A. Solodko, I. Syratchev, M. Volpi, B. Woolley, W. Wuensch, and J. Tagg, "Commissioning of XBox-3: A very high capacity X-band test stand", in *28th International Linear Accelerator Conference*, 2017, p. TUPLR047. [Online]. Available: https://doi.org/10.18429/JACoW-LINAC2016-TUPLR047

[98] Institute of Electrical and Electronics Engineers, "IEEE Standard Letter Designations for Radar-Frequency Bands - Redline", *IEEE Std 521-2019 (Revision of IEEE Std 521-2002) - Redline*, pp. 1–22, 2020.

[99] R. H. Varian and S. F. Varian, "A High Frequency Oscillator and Amplifier", *Journal of Applied Physics*, vol. 10, no. 5, pp. 321–327, 1939. [Online]. Available: https://doi.org/10.1063/1.1707311

[100] D. Constable, A. Baikov, G. Burt, I. Guzilov, V. Hill, A. Jensen, R. Kowalczyk, C. Lingwood, R. Marchesin, C. Marrelli, and I. Syratchev, "High Efficiency Klystron Development for Particle Accelerators", in *58th ICFA Advanced Beam Dynamics Workshop on High Luminosity Circular e^+e^- Colliders*, 2017, p. WET3AH2. [Online]. Available: https://doi.org/10.18429/JACoW-eeFACT2016-WET3AH2

[101] D. A. Constable, C. Lingwood, G. Burt, A. Y. Baikov, I. Syratchev, and R. Kowalcyzk, "MAGIC2-D simulations of high efficiency klystrons using the core oscillation method", in *2017 Eighteenth International Vacuum Electronics Conference (IVEC)*, 2017, pp. 1–2. [Online]. Available: https://doi.org/10.1109/IVEC.2017.8289633

[102] G. Riddone, I. Syratchev, S. Atieh, A. Solodko, M. Filippova, A. Olyunin, and V. Soldatov, "Engineering Design and Fabrication of X-band RF Components", *Proceedings of the 2nd International Particle Accelerator Conference (IPAC2011)*, vol. 110904, pp. 196–198, 2011.

[103] P. G. Tenenbaum, "A Brief Introduction to RF Power Sources", 2003.

[104] Z. Farkas, H. Hoag, G. Loew, and P. B. Wilson, "Recent Progress on SLED, the SLAC Energy Doubler", *IEEE Trans. Nucl. Sci.*, vol. 22, pp. 1299–1302, 1975. [Online]. Available: https://doi.org/10.1109/TNS.1975.4327871

[105] B. Woolley, I. Syratchev, and A. Dexter, "Control and performance improvements of a pulse compressor in use for testing accelerating structures at high power", *Phys. Rev. Accel. Beams*, vol. 20, p. 101001, Oct 2017. [Online]. Available: https://doi.org/10.1103/PhysRevAccelBeams.20.101001

[106] L. Millar, "Conditioning and Operational Algorithms", 2020, RF Development Meeting, CERN. [Online]. Available: https://indico.cern.ch/event/719535/

[107] Texas Instruments. ADC12DJ5200RF Product Page. Accessed: 25/06/2020. [Online]. Available: https://www.ti.com/product/ADC12DJ5200RF

[108] W. Kester, "Converting Oscillator Phase Noise to Time Jitter", 01 2005.

[109] V. del Pozo Romano, H. Bursali, N. Catalán Lasheras, A. Grudiev, S. Pitman, C. Serpico, I. Syratchev, and M. Volpi, "High power conditioning of X-band variable power splitter and phase shifter", *10th Int. Particle Accelerator Conf. (IPAC2019)*, p. WEPRB064, 2019. [Online]. Available: https://doi.org/10.18429/JACoW-IPAC2019-WEPRB064

[110] A. Grudiev, "Design of compact high power rf components at x-band", in *CLIC-Note-1067, CERN, Geneva, Switzerland*, 2016.

[111] R. Zennaro, M. Bopp, A. Citterio, R. Reiser, and T. Stapf, "C-band RF Pulse Compressor for SwissFEL", in *Proceedings of the 4th International Particle Accelerator Conference*, Shanghai, China, 2013, pp. 2827–2829. [Online]. Available: https://accelconf.web.cern.ch/IPAC2013/papers/wepfi059.pdf

[112] P. Craievich *et al.*, "The PolariX-TDS Project: Bead-Pull Measurements and High-Power Test on the Prototype", in *39th International Free Electron Laser Conference*, 2019, p. WEP036. [Online]. Available: https://doi.org/10.18429/JACoW-FEL2019-WEP036

[113] V. Balakin and I. Syrachev, "Status VLEPP RF power multiplier (VPM)", in *Proceedings of the3rd European Particle Accelerator Conference (EPAC 92),*, vol. 920324, 1992, pp. 1173–1175.

[114] I. Syratchev *et al.*, "The Results of RF High Power Tests of X-Band Open Cavity RF Pulse Compression System VPM(JLC).", in *Proc. 1994 Linear Accelerator Conf. (LINAC'94),Tsukuba, Japan*, 8 1994, pp. 475–477.

[115] Lord Rayleigh O.M. F.R.S., "Cxii. the problem of the whispering gallery", *The London, Edinburgh, and Dublin Philosophical Magazine and Journal of Science*, vol. 20, no. 120, pp. 1001–1004, 1910. [Online]. Available: https://doi.org/10.1080/14786441008636993

[116] Z. Li, W. Fang, A. Grudiev, Q. Gu, and Z. Zhao, "A new spherical pulse compressor working with degenerated "whispering gallery" mode", in *29th International Linear Accelerator Conference*, 2018, p. THPO109. [Online]. Available: https://doi.org/10.18429/JACoW-LINAC2018-THPO109

[117] I. Syratchev, "Barrel Open Cavity RF Pulse Compression System", 2003, CLIC Note 580, CERN-OPEN-2003-054. [Online]. Available: http://cds.cern.ch/record/692469

[118] P. Craievich *et al.*, "Novel x-band transverse deflection structure with variable polarization", *Phys. Rev. Accel. Beams*, vol. 23, p. 112001, Nov 2020. [Online]. Available: https://doi.org/10.1103/PhysRevAccelBeams.23.112001

[119] Y. Jiang, H. Zha, P. Wang, J. Shi, H. Chen, W. L. Millar, and I. Syratchev, "Demonstration of a cavity-based pulse compression system for pulse shape correction", *Phys. Rev. Accel. Beams*, vol. 22, p. 082001, Aug 2019. [Online]. Available: https://doi.org/10.1103/PhysRevAccelBeams.22.082001

[120] P. B. Wilson, Z. Farkas, and R. Ruth, "SLED-II: A New method of RF pulse compression", in *15th International Linear Accelerator Conference*, 9 1990, pp. 0204–206.

[121] S. Y. Kazakov, "Pulse Shape Correction for RF Pulse Compression System", in *Proc. 3rd European Particle Accelerator Conf. (EPAC'92), Berlin, Germany*, Mar 1992, p. 1247.

[122] P. Wang, H. Zha, I. Syratchev, J. Shi, and H. Chen, "rf design of a pulse compressor with correction cavity chain for klystron-based compact linear collider", *Phys. Rev. Accel. Beams*, vol. 20, no. 11, p. 112001, 2017. [Online]. Available: https://doi.org/10.1103/PhysRevAccelBeams.20.112001

[123] P. Wang, D. Cao, H. Chen, J. Shi, Z. Wang, and H. Zha, "Fabrication and Cold Test of the Correction Cavity Chain for Klystron-Based CLIC", in *9th International Particle Accelerator Conference*, 2018, p. THPAL155. [Online]. Available: https://doi.org/10.18429/JACoW-IPAC2018-THPAL155

[124] J. Wang *et al.*, "R&D of a Super-compact SLED System at SLAC", in *7th International Particle Accelerator Conference*, 2016, p. MOOCA01. [Online]. Available: https://doi.org/10.18429/JACoW-IPAC2016-MOOCA01

[125] M. J. Boland *et al.*, *Updated baseline for a staged Compact Linear Collider*, ser. CERN Yellow Reports: Monographs. Geneva: CERN, Aug 2016. [Online]. Available: https://doi.org/10.5170/CERN-2016-004

[126] C. Serpico, "Rf Developments for the CLIC Module", 2018, cLIC Workshop 2018. [Online]. Available: https://indico.cern.ch/event/656356/contributions/2838064/

[127] F. Caspers, "RF engineering basic concepts: S-parameters", CERN, Tech. Rep. arXiv:1201.2346, Jan 2012, contribution to the CAS - CERN Accelerator School: Specialised Course on RF for Accelerators; 8 - 17 Jun 2010, Ebeltoft, Denmark. [Online]. Available: https://cds.cern.ch/record/1415639

[128] S. J. Mason, "Feedback Theory-Further Properties of Signal Flow Graphs", *Proceedings of the IRE*, vol. 44, no. 7, pp. 920–926, 1956. [Online]. Available: https://doi.org/10.1109/JRPROC.1956.275147

[129] E. Dijkstra, "A note on two problems in connexion with graphs", *Numerische Mathematik*, vol. 1, pp. 269–271, 1959. [Online]. Available: https://doi.org/10.1007/BF01386390

[130] P. E. Hart, N. J. Nilsson, and B. Raphael, "A formal basis for the heuristic determination of minimum cost paths", *IEEE Transactions on Systems Science and Cybernetics*, vol. 4, no. 2, pp. 100–107, 1968. [Online]. Available: https://doi.org/10.1109/TSSC.1968.300136

[131] M. N. O. Sadiku and C. M. Akujuobi, "S-parameters for three and four cascaded two-ports", in *Proceedings of IEEE SoutheastCon, 2004*, 2004, pp. 410–412. [Online]. Available: https://doi.org/10.1109/SECON.2004.1287952

[132] A. Vnuchenko *et al.*, "High Gradient Performance of an S-Band Backward Traveling Wave Accelerating Structure for Medical Hadron Therapy Accelerators", in *9th International Particle Accelerator Conference*, 2018, p. MOPML043. [Online]. Available: https://doi.org/10.18429/JACoW-IPAC2018-MOPML043

[133] A. Descoeudres, Y. Levinsen, S. Calatroni, M. Taborelli, and W. Wuensch, "Investigation of the DC vacuum breakdown mechanism", *Phys. Rev. ST Accel. Beams*, vol. 12, p. 092001, 2009. [Online]. Available: https://doi.org/10.1103/PhysRevSTAB.12.092001

[134] K. L. F. Bane, V. A. Dolgashev, T. Raubenheimer, G. V. Stupakov, and J. H. Wu, "Dark currents and their effect on the primary beam in an X-band linac", *Phys. Rev. ST Accel. Beams*, vol. 8, p. 064401, 2005. [Online]. Available: https://doi.org/10.1103/PhysRevSTAB.8.064401

[135] J. Paszkiewicz, "Dark Current Mapping, Fluctuation and Evolution", 2019, CLIC Workshop. [Online]. Available: https://indico.cern.ch/event/753671/contributions/3274408

[136] T. Abe, T. Kageyama, H. Sakai, Y. Takeuchi, and K. Yoshino, "Breakdown study based on direct in situ observation of inner surfaces of an rf accelerating cavity during a high-gradient test", *Phys. Rev. Accel. Beams*, vol. 19, p. 102001, Oct 2016. [Online]. Available: https://link.aps.org/doi/10.1103/PhysRevAccelBeams.19.102001

[137] N. B. Kraljevic, "Energy spread optimisation in the CLIC ML at 380 GeV", 2018, international Workshop on Future Linear Colliders, University of Texas. [Online]. Available: https://agenda.linearcollider.org/event/7889/contributions/42600/

[138] A. Grudiev and W. Wuensch, "Design of an X-Band Accelerating Structure for the CLIC Main Linac", CERN, Geneva, Tech. Rep. CERN-OPEN-2009-016. CLIC-Note-773, Oct 2008. [Online]. Available: https://cds.cern.ch/record/1216862

[139] I. V. Syratchev, "Mode Launcher as an Alternative Approach to the Cavity-Based RF Coupler of Periodic Structures", CERN, Geneva, Tech. Rep. CERN-OPEN-2002-005. CERN-PS-RF-NOTE-2002-013. CLIC-Note-503, Jan 2002. [Online]. Available: https://cds.cern.ch/record/533650

[140] S. Doebert, J. Raguin, I. Syrachev, and W. Wuensch, "Coupler studies for CLIC accelerating structures", in *8th European Particle Accelerator Conference (EPAC 2002)*, Jun 2002, pp. 2187–2189.

[141] W. Farabolini, "CLEX module results and CALIFES experiments", 2016, cLIC Workshop 2016. [Online]. Available: https://indico.cern.ch/event/449801/contributions/1945305/

[142] C. W. Steele, "A nonresonant perturbation theory", *IEEE Transactions on Microwave Theory and Techniques*, vol. 14, no. 2, pp. 70–74, 1966. [Online]. Available: https://doi.org/10.1109/TMTT.1966.1126168

[143] B. Hall, "Designing the Four Rod Crab Cavity for the High-Luminosity LHC Upgrade.", PhD Thesis, Lancaster University, September 2012.

[144] R. Wegner, W. Wuensch, G. Burt, and B. Woolley, "Bead-Pull Measurement Method and Tuning of a Prototype CLIC Crab Cavity", in *27th International Linear Accelerator Conference*, 2014, p. MOPP035.

[145] J. Shi, A. Grudiev, and W. Wuensch, "Tuning of X-band traveling-wave accelerating structures", *Nucl. Instrum. Meth. A*, vol. 704, pp. 14–18, 2013. [Online]. Available: https://doi.org/10.1016/j.nima.2012.11.182

[146] T. G. Lucas, M. Volpi, P. J. Giansiracusa, R. P. Rassool, T. Argyropoulos, H. Bursali, N. Catalan-Lasheras, A. Grudiev, G. Mcmonagle, I. Syrachev, R. Wegner, B. Woolley, W. Wuensch, D. Esperante-Pereira, and M. J. Boland, "High power testing of a prototype CLIC structure: TD26CC R05 N3", CERN, Geneva, Tech. Rep. CERN-ACC-2018-0030. CLIC-Note-1080, Sep 2018. [Online]. Available: http://cds.cern.ch/record/2642425

[147] L. Millar, "Results of the Polarix TDS High Power Test at CERN", 2019, international Workshop on Breakdown Science and High Gradient Technology (HG2019). [Online]. Available: https://indico.cern.ch/event/766929/contributions/3439308/

[148] R. Rajamaki, "Vacuum arc localization in CLIC prototype radio frequency accelerating structures", Master's thesis, Aalto University, March 2016.

[149] A. Degiovanni, W. Wuensch, and J. Giner Navarro, "Comparison of the conditioning of high gradient accelerating structures", *Phys. Rev. Accel. Beams*, vol. 19, p. 032001, Mar 2016. [Online]. Available: https://doi.org/10.1103/PhysRevAccelBeams.19.032001

[150] W. Wuensch, "A review of vacuum breakdown in high-gradient accelerators", in *2018 28th International Symposium on Discharges and Electrical Insulation in Vacuum (ISDEIV)*, vol. 2, 2018, pp. 747–752. [Online]. Available: https://doi.org/10.1109/DEIV.2018.8537005

[151] B. Woolley, G. Burt, A. C. Dexter, R. Peacock, W. L. Millar, N. Catalan Lasheras, A. Degiovanni, A. Grudiev, G. Mcmonagle, I. Syratchev, W. Wuensch, E. Rodriguez Castro, and J. Giner Navarro, "High-gradient behavior of a dipole-mode rf structure", *Phys. Rev. Accel. Beams*, vol. 23, p. 122002, Dec 2020. [Online]. Available: https://doi.org/10.1103/PhysRevAccelBeams.23.122002

[152] L. Cowie, G. Burt, W. Millar, and D. Scott, "High Power RF Conditioning on CLARA", in *9th International Particle Accelerator Conference*, 2018, p. THPAL085.

[153] P. McIntosh, A. Hill, and H. Schwarz, "An automated 476 MHz RF cavity processing facility at SLAC", in *Proceedings of the 2003 Particle Accelerator Conference*, vol. 2, 2003, pp. 1273–1275 Vol.2.

[154] K. N. Sjobak, A. Grudiev, and E. Adli, "New Criterion for Shape Optimization of Normal-Conducting Accelerator Cells for High-Gradient Applications", in *27th International Linear Accelerator Conference*, 2014, p. MOPP028.

[155] P. Burrows *et al.*, *The Compact Linear Collider (CLIC) - 2018 Summary Report*, ser. CERN Yellow Reports: Monographs, P. Burrows, Ed. CERN, Dec 2018, vol. 2. [Online]. Available: https://cds.cern.ch/record/2652188

[156] V. A. Dolgashev, S. G. Tantawi, Y. Higashi, and B. Spataro, "Study of Basic Breakdown Phenomena in High Gradient Vacuum Structures", in *15th Linear Accelerator Conference (LINAC2010), Tsukuba, Japan*, 2010, pp. 1043–1047.

[157] L. Millar, "Behaviour of High Gradient RF Structures During Long-Term Operation", 2018, workshop on Mechanisms of Vacuum Arcs (Mini MeVArc), Uppsala University, Sweden. [Online]. Available: https://indico.cern.ch/event/750619/contributions/3206320/

[158] Y. I. Levinsen, A. Descoeudres, S. Calatroni, M. Taborelli, and W. Wuensch, "Statistical Modeling of DC Sparks", in *Proceedings of the 23rd Particle Accelerator Conference*, 2009, pp. 833–835. [Online]. Available: https://accelconf.web.cern.ch/pac2009/html/auth0918.htm

[159] E. R. Castro, "Recent Microscopy at CERN", 2018, 7th International Workshop on Mechanisms of Vacuum Arcs (MeVArc 2018). [Online]. Available: https://indico.cern.ch/event/680402/contributions/2976643/

Appendix A

Published Work

A.1 Co-Author Publications

A.1.1 Peer Reviewed Journal Articles

1. "High-Gradient Behaviour of a Dipole-Mode RF Structure", Physical Review Accelerators and Beams 23, 122002 (2020), https://doi.org/10.1103/PhysRevAccelBeams.23.122002.

2. "Novel X-band Transverse Deflection Structure with Variable Polarization", Physical Review Accelerators and Beams 23, 112001 (2020), https://doi.org/10.1103/PhysRevAccelBeams.23.112001.

3. "Effect of DC Voltage Pulsing on High-Vacuum Electrical Breakdowns Near Cu Surfaces", Physical Review Accelerators and Beams 23, 113101 (2020), https://doi.org/10.1103/PhysRevAccelBeams.23.113101.

4. "Demonstration of a Cavity-Based Pulse Compression System for Pulse Shape Correction", Physical Review Accelerators and Beams 22, 082001 (2019), https://doi.org/10.1103/PhysRevAccelBeams.22.082001.

A.1.2 Non-Peer Reviewed Conference Proceedings

1. "The PolariX-TDS Project: Bead-Pull Measurements and High Power Test on the Prototype", in Proc. FEL'19 (Hamburg, Germany), pp. 396-399, https://doi.org/10.18429/JACoW-FEL2019-WEP036

2. “Dark Current Analysis at CERN’s X-Band Facility", Proc. IPAC’19 (Melbourne, Australia) pp. 2944-2947, https://doi.org/10.18429/JACoW-IPAC2019-WEPRB059

3. “K_a-Band Linearizer Studies for a Compact Light Source”, in Proc. IPAC’19 (Melbourne, Australia), pp. 2976-2979, https://doi.org/10.18429/JACoW-IPAC2019-WEPRB068

4. “An X-Band Lineariser for the CLARA FEL”, in Proc. IPAC’18 (Vancouver, Canada), pp. 3848- 3851, https://doi.org/10.18429/JACoW-IPAC2018-THPAL084

5. “High Power Conditioning on CLARA”, in Proc. IPAC’18 (Vancouver, Canada), pp. 3852-3855, https://doi.org/10.18429/JACoW-IPAC2018-THPAL085

A.2 Invited and Contributed Talks

1. “Monte Carlo Model of High-Gradient Conditioning and Operation”, 9th International Workshop on Mechanisms of Vacuum Arcs (MeVArc 2021), Virtual Conference, https://indico.cern.ch/event/966437/contributions/4245454/

2. “Monte Carlo Model of High-Gradient Conditioning and Operation”, National Vacuum Electronics Conference (NVEC2020), Virtual Conference

3. “High Power Conditioning and Breakdown Studies in Coupled Accelerating Structures”, 30th International Linear Accelerator Conference (LINAC2020), Virtual Conference

4. “Breakdown Measurements in High-Gradient RF Test Stands”, 8th International Workshop on Mechanisms of Vacuum Arcs (MeVArc 2019), Padova, Italy, https://indico.cern.ch/event/774138/contributions/3507961/

5. “Lessons Learned from CERN’s High-Gradient RF Test Stands”, International Workshop on Future Linear Colliders (LCWS 2019), Sendai, Miyagi, Japan, https://agenda.linearcollider.org/event/8217/contributions/44703/

6. “Results of the PolariX TDS High Power Test at CERN”, International Workshop on Breakdown Science and High Gradient Technology (HG2019), Chamonix, France, https://indico.cern.ch/event/766929/contributions/3439308/

7. “High Gradient Test Results at CERN”, CLIC Workshop 2019, Geneva, Switzerland, https://indico.cern.ch/event/753671/contributions/3274399/

8. “Experience with Long-Term Operation of High-Gradient Accelerating Structures”, International Workshop on Future Linear Colliders (LCWS 2018), University of Texas Arlington, USA, https://agenda.linearcollider.org/event/7889/contributions/42668/

9. “Behavior of High Gradient RF Structures During Long Term Operation”, Mechanisms of Vacuum Arcs Meeting (Mini MeVArc) 2018, Uppsala University, Sweden, https://indico.cern.ch/event/750619/contributions/3206320/

10. “Long Term Breakdown Studies in a CLIC Test Structure”, National Vacuum Electronics Conference (NVEC2018), University of Oxford, UK